

material into a leathery or rubberlike substance. Once the material has cooled below the glass transition temperature, T_g , the polymer becomes stiff and brittle. At the glass transition temperature, the specific volume and enthalpy curves experience a significant change in slope. This can be seen for polystyrene in the enthalpy-temperature curve shown in Fig. 8.1. With semi-crystalline thermoplastics, at a crystallization temperature near the melting temperature, the molecules start arranging themselves in small crystalline and amorphous regions, creating a very complicated morphology. During the process of crystalline structure formation, a quantum of energy, often called *heat of crystallization* or *heat of fusion*, is released and must be conducted out of the material before the cooling process can continue. The heat of fusion is reflected in the shape of the enthalpy-temperature curve as shown for polyamide 6.6, polyethylene and polypropylene in Fig. 8.1. At the onset of crystalline growth, the material becomes rubbery yet not brittle, since the amorphous regions are still above the glass transition temperature. As seen earlier, the glass transition temperature for some semi-crystalline polymers is far below room temperature, making them tougher than amorphous polymers. For common semi-crystalline polymers, the degree of crystallization can be between 30 and 70%. This means that 30–70% of the molecules form crystals and the rest remain in an amorphous state. The degree of crystallization is highest for those materials with short molecules since they can crystallize faster and more easily.

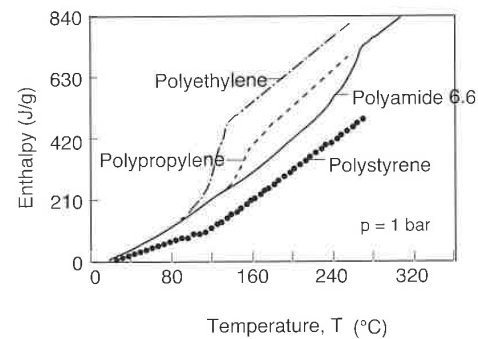


Figure 8.1 Enthalpy as a function of temperature for various thermoplastics.

Figure 8.2 [1] shows the volumetric temperature dependence of a polymer. In the melt state, the chains have “empty spaces” in which molecules can move freely. Hence, undercooled polymer molecules can still move as long as space is available. The point at which this free movement ends for a molecule or segment of chains is called the glass transition temperature or solidification point. As pointed out in Fig. 8.2, the free volume is frozen-in as well. In the case

of crystallization, ideally, the volume should jump to a lower specific volume. However even here, small amorphous regions remain which permit a slow flow or material creep. This free volume reduces to nothing at absolute zero temperature at which heat transport can no longer occur.

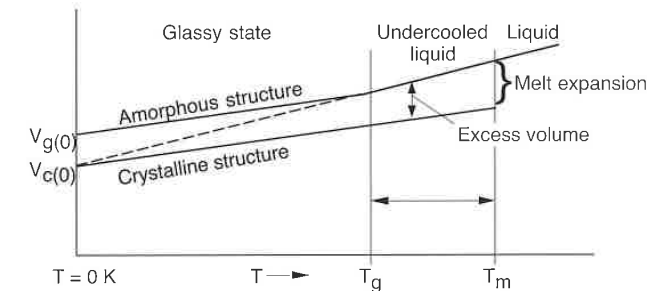


Figure 8.2 Thermal expansion model for thermoplastic polymers.

The specific volume of a polymer changes with pressure even at the glass transition temperature. This is demonstrated for an amorphous thermoplastic in Fig. 8.3 and for a semi-crystalline thermoplastic in Fig. 8.4.

It should be noted here that the size of the frozen-in free volume depends on the rate at which a material is cooled; high cooling rates result in a large free volume. In practice this is very important. When the frozen-in free volume is large, the part is less brittle. On the other hand, high cooling rates lead to parts that are highly permeable, which may allow the diffusion of gases or liquids through container walls. The cooling rate is also directly related to the dimensional stability of the final part. The effect of high cooling rates can often be mitigated by heating the part to a temperature that enables the molecules to move freely; this will allow further crystallization by additional chain folding. This process has a great effect on the structure and properties of the crystals and is referred to as *annealing*. In general, this only signifies a qualitative improvement of polymer parts. It also affects shrinkage and warpage during service life of a polymer component, especially when thermally loaded.

All these aspects have a great impact on processing. For example, when extruding amorphous thermoplastic profiles, the material can be sufficiently cooled inside the die so that the extrudate has enough rigidity to carry its own weight as it is pulled away from the die. Semi-crystalline polymers with low molecular weights have a viscosity above the melting temperature that is too low to be able to withstand their own weight as the extrudate exits the die. Temperatures below the melting temperature, T_m , however cannot be used due to solidification inside the die. Similar problems are encountered in the

thermoforming process in which the material must be heated to a point so that it can be formed into its final shape, yet has to be able to withstand its own weight.

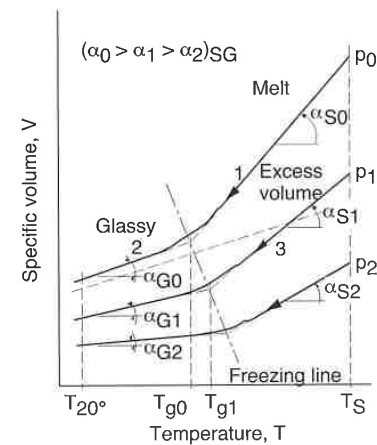


Figure 8.3 Schematic of a p-v-T diagram for amorphous thermoplastics.

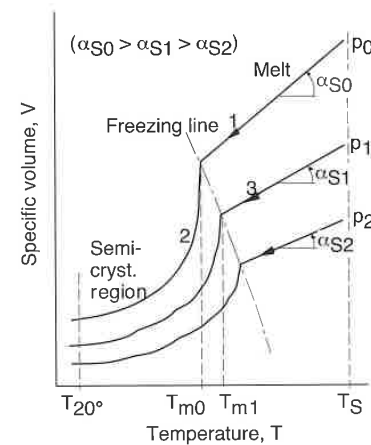


Figure 8.4 Schematic of a p-v-T diagram for semi-crystalline thermoplastics.

Semi-crystalline polymers are also at a disadvantage in the injection molding process. Because of the heat needed for crystallization, more heat must

be removed to solidify the part; and since there is more shrinkage, longer packing times and larger pressures must be employed. All this implies longer cycle times and more shrinkage. High cooling rates during injection molding of semi-crystalline polymers will reduce the degree of crystallization. However, the amorphous state of the polymer molecules may lead to some crystallization after the process, which will result in further shrinkage and warpage of the final part. It is quite common to follow the whole injection molding process in the p-v-T diagrams presented in Figs. 8.3 and 8.4, and thus predict how much the molded component has shrunk.

8.1.2 Morphological Structure

Morphology is the order or arrangement of the polymer structure. The possible "order" between a molecule or molecule segment and its neighbors can vary from a very ordered highly crystalline polymeric structure to an amorphous structure (i.e., a structure in greatest disorder or random). The possible range of order and disorder is clearly depicted on the left side of Fig. 8.5. For example, a purely amorphous polymer is formed only by the non-crystalline or amorphous chain structure, whereas the semi-crystalline polymer is formed by a combination of all the structures represented in Fig. 8.5.

The image of a semi-crystalline structure as shown in the middle of Fig. 8.5, can be captured with an electron microscope. A macroscopic structure, shown in the right hand side of the figure, can be captured with an optical microscope. An optical microscope can capture the coarser macro-morphological structure such as the spherulites in semi-crystalline polymers.

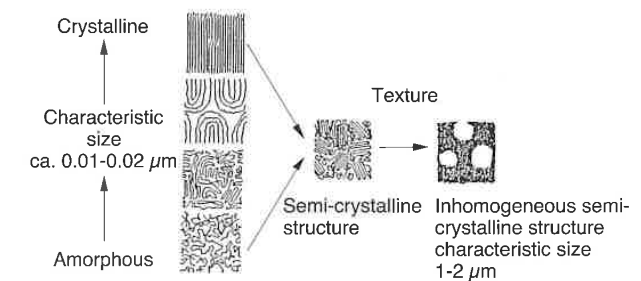


Figure 8.5 Schematic diagram of possible molecular structure which occur in thermoplastic polymers.

An amorphous polymer is defined as having a purely random structure. However it is not quite clear if a "purely amorphous" polymer as such exists. Electron microscopic observations have shown amorphous polymers that are

composed of relatively stiff chains, show a certain degree of macromolecular structure and order, for example, globular regions or fibrillic structures. Nevertheless, these types of amorphous polymers are still found to be optically isotropic. Even polymers with soft and flexible macromolecules, such as polyisoprene which was first considered to be random, sometimes show band-like and globular regions. These bundle-like structures are relatively weak and short-lived when the material experiences stresses. The shear thinning viscosity effect of polymers sometimes is attributed to the breaking of such macromolecular structures.

8.1.3 Crystallization

Early on, before the existence of macromolecules had been recognized, the presence of highly crystalline structures had been suspected. Such structures were discovered when undercooling or when stretching cellulose and natural rubber. Later, it was found that a crystalline order also existed in synthetic macromolecular materials such as polyamides, polyethylenes, and polyvinyls. Because of the polymolecularity of macromolecular materials, a 100% degree of crystallization cannot be achieved. Hence, these polymers are referred to as semi-crystalline. It is common to assume that the semi-crystalline structures are formed by small regions of alignment or crystallites connected by random or amorphous polymer molecules.

With the use of electron microscopes and sophisticated optical microscopes the various existing crystalline structures are now well recognized. They can be listed as follows:

- *Single crystals.* These can form in solutions and help in the study of crystal formation. Here, plate-like crystals and sometimes whiskers are generated.
- *Spherulites.* As a polymer melt solidifies, several folded chain lamellae spherulites form which are up to 0.1 mm in diameter. A typical example of a spherulitic structure is shown in Fig. 8.6 [2]. The spherulitic growth in a polypropylene melt is shown in Fig. 8.7 [3].
- *Deformed crystals.* If a semi-crystalline polymer is deformed while undergoing crystallization, oriented lamellae form instead of spherulites.
- *Shish-kebab.* In addition to spherulitic crystals, which are formed by plate- and ribbonlike structures, there are also shish-kebab, crystals which are formed by circular plates and whiskers. Shish-kebab structures are generated when the melt undergoes a shear deformation during solidification. A typical example of a shish-kebab crystal is shown in Fig. 8.8 [4].

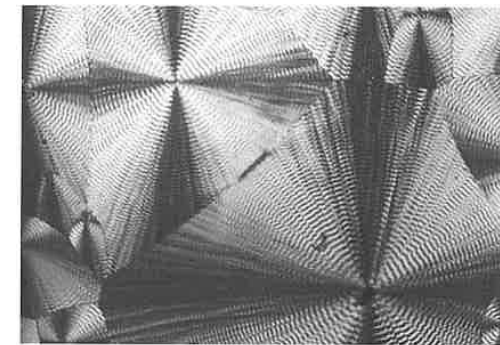


Figure 8.6 Polarized microscopic image of the spherulitic structure in polypropylene.

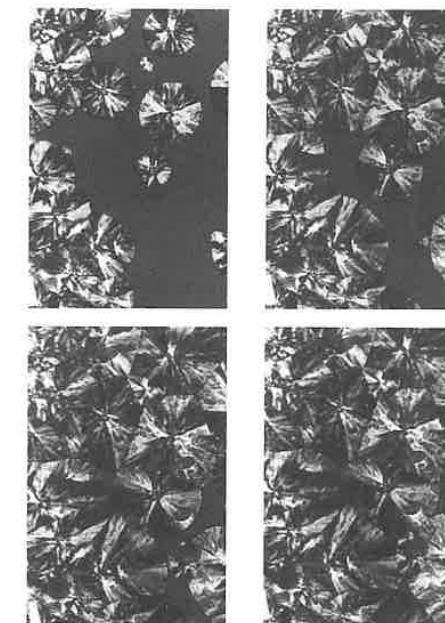


Figure 8.7 Development of the spherulitic structure in polypropylene. Images were taken at 30 s intervals.

The crystallization fraction can be described by the *Avrami equation* [5], written as follows:

$$x(t) = 1 - e^{-Zt^n} \quad (8.1)$$

where Z is a molecular weight and temperature dependent crystallization rate and n the Avrami exponent. However, since a polymer cannot reach 100% crystallization the above equation should be multiplied by the maximum possible degree of crystallization, x_∞ .

$$x(t) = x_\infty (1 - e^{-Zt^n}) \quad (8.2)$$

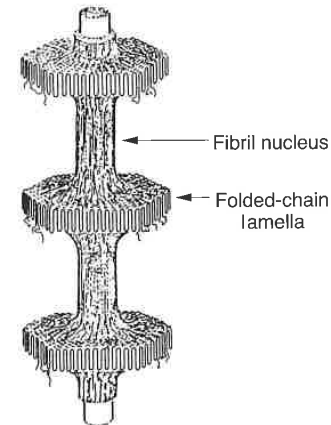


Figure 8.8 Model of the shish-kebab morphology.

The Avrami exponent, n , ranges between 1 and 4 depending on the type of nucleation and growth. For example, the Avrami exponent for spherulitic growth from sporadic nuclei is around 4, disclike growth 3, and rodlike growth 2. If the growth is activated from instantaneous nuclei, the Avrami exponent is lowered by 1.0 for all cases. The crystalline growth rate of various polymers differ significantly from one to another. This is demonstrated in Table 8.1 which shows the maximum growth rate for various thermoplastics. The crystalline mass fraction can be measured experimentally with a differential scanning calorimeter (DSC).

A more in-depth coverage of crystallization and structure development during processing is given by Eder and Janeschitz-Kriegl [7].

Table 8.1 Maximum Crystalline Growth Rate and Maximum Degree of Crystallinity for Various Thermoplastics

Polymer	Growth rate (μ/min)	Maximum crystallinity (%)
Polyethylene	>1000	80
Polyamide 66	1000	70
Polyamide 6	200	35
Isotactic polypropylene	20	63
Polyethylene terephthalate	7	50
Isotactic polystyrene	0.30	32
Polycarbonate	0.01	25

8.1.4 Heat Transfer During Solidification

Since polymer parts are generally thin, the energy equation¹ can be simplified to a one-dimensional problem. Thus, using the coordinate description shown in Fig. 8.9 the energy equation can be reduced to

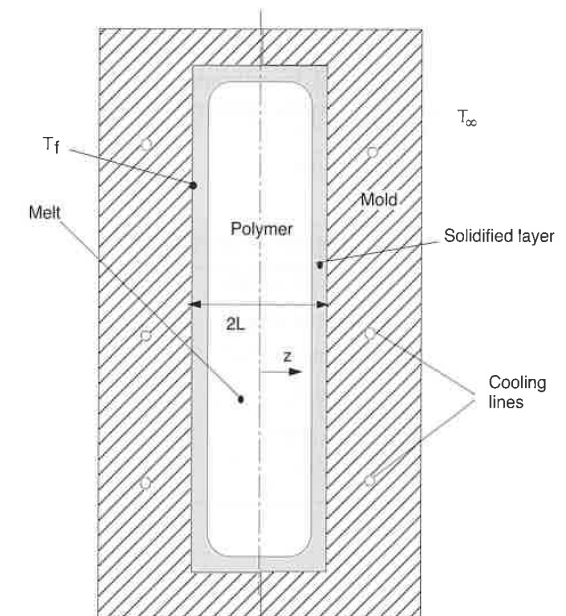


Figure 8.9 Schematic diagram of polymer melt inside an injection mold.

¹ The energy equation is discussed in Chapter 3 and can be found in its complete form in Appendix A.

$$\rho C_p \frac{\partial T}{\partial t} = k \frac{\partial^2 T}{\partial z^2} \tag{8.3}$$

Another assumption— and to reduce warpage, usually a requirement— is a symmetry boundary condition:

$$\frac{\partial T}{\partial z} = 0 \text{ at } z=0 \tag{8.4}$$

If the sheet is cooled via forced convection or the part is inside a perfectly cooled mold, the final temperature of the part can be assumed to be the second boundary condition:

$$T = T_f \tag{8.5}$$

A typical temperature history for a polystyrene plate, its properties presented in Table 8.2 [8], is shown in Fig. 8.10. Once the material's temperature drops below the glass transition temperature, T_g , it can be considered solidified. This is shown schematically in Fig. 8.11. Of importance here is the position of the solidification front, $X(t)$. Once the solidification front equals the plate's dimension L , the solidification process is complete. From Fig. 8.10 it can be shown that the rate of solidification decreases as the solidified front moves further away from the cooled surface. For amorphous thermoplastics, the well-known *Neumann solution* can be used to estimate the growth of the glassy or solidified layer. The Neumann solution is written as

$$X(t) \propto \sqrt{\alpha t} \tag{8.6}$$

Table 8.2 Material Properties for Polystyrene

K	=	0.117 W/mK
C_p	=	1185 J/kgK
ρ	=	1040 kg/m ³
T_g	=	80 °C
E	=	3.2E9 Pa
ν	=	0.33

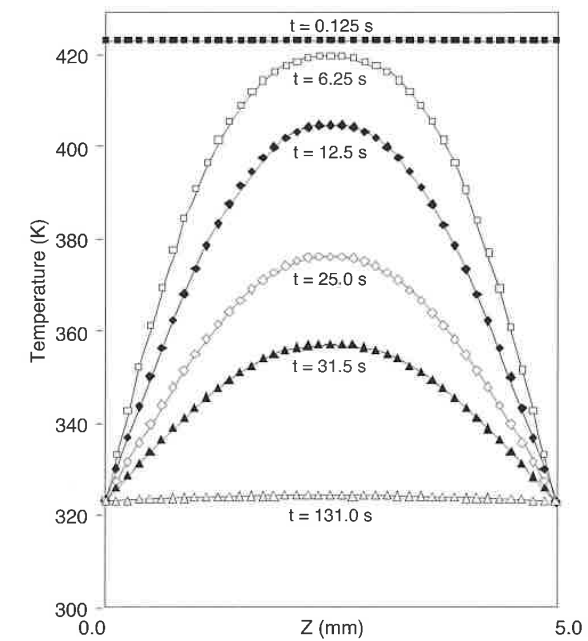


Figure 8.10 Temperature history of polystyrene cooled inside a 5 mm thick mold.

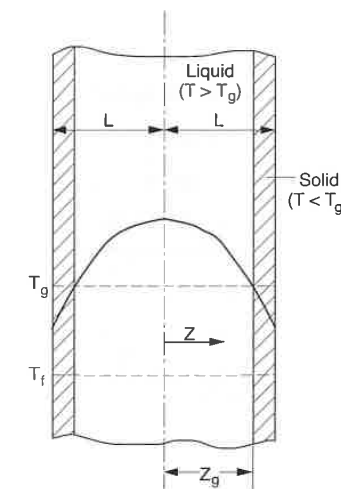


Figure 8.11 Schematic diagram of the cooling process of a polymer plate.

where α is the thermal diffusivity of the polymer. It must be pointed out here that for the Neumann solution, the growth rate of the solidified layer is infinite as time goes to zero.

The solidification process in a semi-crystalline materials is a bit more complicated due to the heat of fusion or heat of crystallization, nucleation rate, etc. When measuring the specific heat as the material crystallizes, a peak which represents the heat of fusion is detected (see Fig. 4.12). Figure 8.12 shows the calculated temperature distribution in a semi-crystalline polypropylene plate during cooling. The material properties used for the calculations are shown in Table 8.3 [8]. Here, the material that is below the melting temperature, T_m , is considered solid². Experimental evidence [9] has demonstrated that the growth rate of the crystallized layer in semi-crystalline polymers is finite. This is mainly due to the fact that at the beginning the nucleation occurs at a finite rate. Hence, the Neumann solution presented in Eq. 8.6 as well as the widely used *Stefan condition* [10], do not hold for semi-crystalline polymers. This is clearly demonstrated in Fig. 8.13 [10] which presents measured thickness of crystallized layers as a function of time for polypropylene plates quenched at three different temperatures. For further reading on this important topic the reader is encouraged to consult the literature [11, 12].

Table 8.3 Material Properties for Polypropylene

K	= 0.117 W/mK
$C_{p, \text{solid}}$	= 1800 J/kgK
$C_{p, \text{melt}}$	= 2300 J/kgK
ρ	= 930 kg/m ³
T_g	= -18 °C
T_m	= 186 °C
λ	= 209 kJ/kg

² It is well-known that the growth of the crystalline layer in semi-crystalline polymers is maximal somewhat below the melting temperature, at a temperature T_c . The growth speed of nuclei is zero at the melting temperature and at the glass transition temperature.

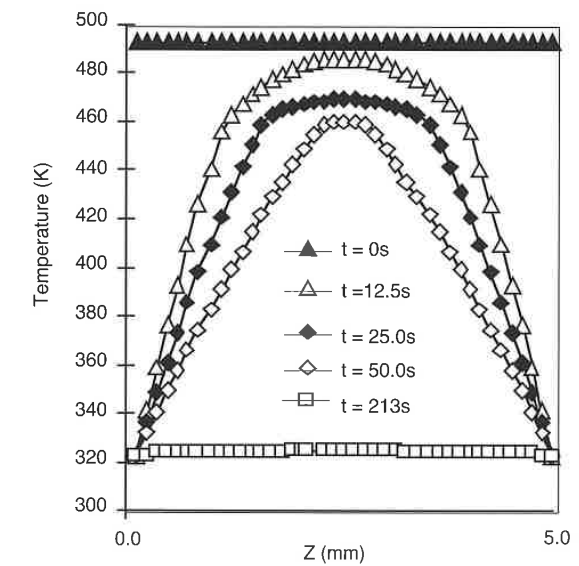


Figure 8.12 Temperature history of polypropylene cooled inside a 5 mm thick mold.

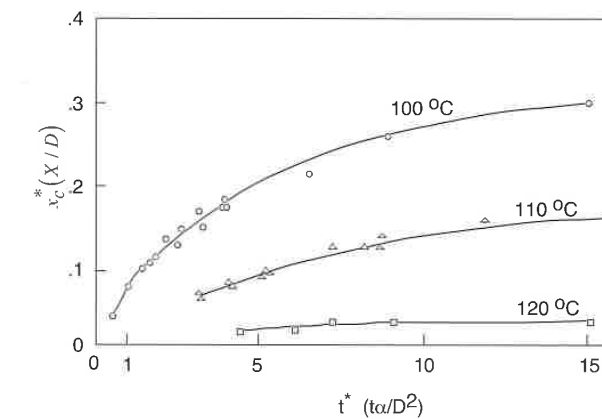


Figure 8.13 Dimensionless thickness of the crystallized layers as a function of dimensionless time for various temperatures of the quenching surface.

8.2 Solidification of Thermosets

The solidification process of thermosets, such as phenolics, unsaturated polyesters, epoxy resins, and polyurethanes is dominated by an exothermic chemical reaction called curing reaction. A curing reaction is an irreversible process that results in a structure of molecules that are more or less cross-linked. Some thermosets cure under heat and others cure at room temperature. Thermosets that cure at room temperature are those for which the reaction starts immediately after mixing two components, where the mixing is usually part of the process. However, even with these thermosets, the reaction is accelerated by the heat released during the chemical reaction, or the *exotherm*. In addition, it is also possible to activate cross-linking by absorption of moisture or radiation, such as ultra-violet, electron beam, and laser energy sources [13].

In processing, thermosets are often grouped into three distinct categories, namely those that undergo a *heat activated cure*, those that are dominated by a *mixing activated cure*, and those which are activated by the absorption of humidity or radiation. Examples of heat activated thermosets are phenolics; examples of mixing activated cure are epoxy resins and polyurethane.

8.2.1 Curing Reaction

In a cured thermoset, the molecules are rigid, formed by short groups that are connected by randomly distributed links. The fully reacted or solidified thermosetting polymer does not react to heat as observed with thermoplastic polymers. A thermoset may soften somewhat upon heating and but then degrades at high temperatures. Due to the high cross-link density, a thermoset component behaves as an elastic material over a large range of temperatures. However, it is brittle with breaking strains of usually 1 to 3%. The most common example is phenolic, one of the most rigid thermosets, which consists of carbon atoms with large aromatic rings that impede motion, making it stiff and brittle. Its general structure after cross-linking is given in Figs. 3.22 and 3.23.

Thermosets can be broken down into three categories: thermosets which cure via *condensation polymerization*, those that undergo *addition polymerization* and those that cure via *free radical polymerization*.

Condensation polymerization is defined as the growth process that results from combining two or more monomers with reactive end-groups, and leads to by-products such as an alcohol, water, an acid, etc. A common thermoset that polymerizes or solidifies via condensation polymerization is phenol formaldehyde, discussed in Chapter 3. The by-product of the reaction when

making phenolics is water. Examples of addition polymerization are polyurethanes and epoxies.

An example of a cross-linking reaction of a thermoset by *free radical reaction* is the co-polymerization of unsaturated polyester with styrene molecules, shown in Fig. 8.14. The molecules contain several carbon-carbon double bonds which act as cross-linking sites during curing. An example of the resulting network after the chemical reaction is shown in Fig. 8.15.

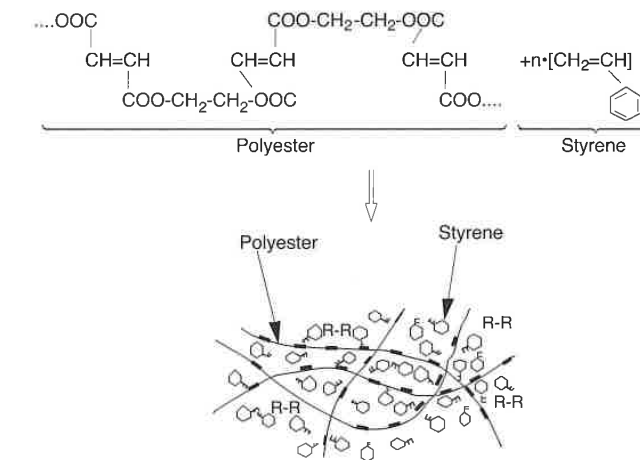


Figure 8.14 Symbolic and schematic representations of uncured unsaturated polyester.

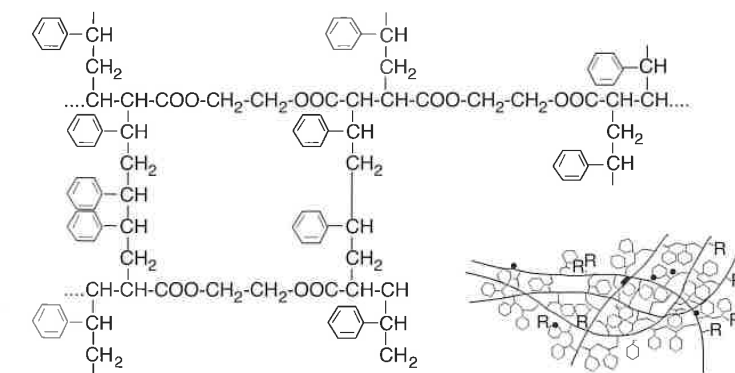


Figure 8.15 Symbolic and schematic representations of cured unsaturated polyester.

8.2.2 Cure Kinetics

As discussed earlier, in processing thermosets can be grouped into two general categories: *heat activated cure* and *mixing activated cure* thermosets. However, no matter which category a thermoset belongs to, its curing reaction can be described by the reaction between two chemical groups denoted by *A* and *B* which link two segments of a polymer chain. The reaction can be followed by tracing the concentration of unreacted *As* or *Bs*, C_A or C_B . If the initial concentration of *As* and *Bs* is defined as C_{A_0} and C_{B_0} , the degree of cure can be described by

$$C^* = \frac{C_{A_0} - C_A}{C_{A_0}} \quad (8.7)$$

The degree of cure or conversion, C^* , equals zero when there has been no reaction and equals one when all *As* have reacted and the reaction is complete. However, it is impossible to monitor reacted and unreacted *As* and *Bs* during the curing reaction of a thermoset polymer. It is known though that the exothermic heat released during curing can be used to monitor the conversion, C^* . When small samples of an unreacted thermoset polymer are placed in a differential scanning calorimeter (DSC), each at a different temperature, every sample will release the same amount of heat, Q_r . This occurs because every cross-linking that occurs during a reaction releases a small amount of energy in the form of heat. For example, Fig. 8.16 [14] shows the heat rate released during isothermal cure of a vinyl ester at various temperatures.

The degree of cure can be defined by the following relation

$$C^* = \frac{Q}{Q_r} \quad (8.8)$$

where Q is the heat released up to an arbitrary time τ , and is defined by

$$Q = \int_0^\tau \dot{Q} dt \quad (8.9)$$

DSC data is commonly fitted to empirical models that accurately describe the curing reaction. Hence, the rate of cure can be described by the exotherm, \dot{Q} , and the total heat released during the curing reaction, Q_r , as

$$\frac{dC^*}{dt} = \frac{\dot{Q}}{Q_r} \quad (8.10)$$

With the use of Eq. 8.10, it is now easy to take the DSC data and find the models that describe the curing reaction.

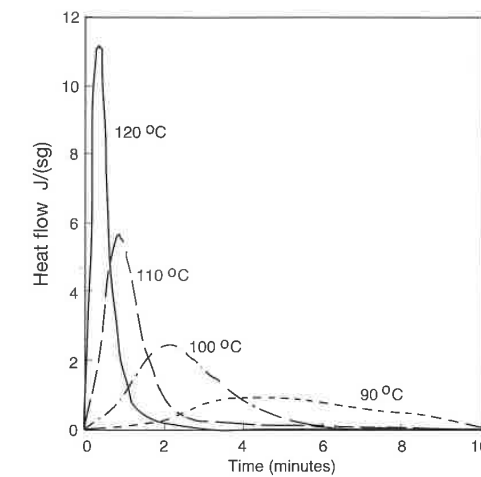


Figure 8.16 DSC scans of the isothermal curing reaction of vinyl ester at various temperatures.

During cure, thermoset resins exhibit three distinct phases; viscous liquid, gel, and solid. Each of these three stages is marked by dramatic changes in the thermomechanical properties of the resin. The transformation of a reactive thermosetting liquid to a glassy solid generally involves two distinct macroscopic transitions: molecular gelation and vitrification. Molecular gelation is defined as the time or temperature at which covalent bonds connect across the resin to form a three-dimensional network which gives rise to long range elastic behavior in the macroscopic fluid. This point is also referred to as the gel point, where $C^* = C_g$. As a thermosetting resin cures, the cross-linking begins to hinder molecular movement, leading to a rise in the glass transition temperature. Eventually, when T_g nears the processing temperature, the rate of curing reduces significantly, eventually dominated by diffusion. At this point the resin has reached its vitrification point. Figure 8.17, which presents degree of cure as a function of time, illustrates how an epoxy resin reaches a maximum degree of cure at various processing temperatures. The resin processed at 200 °C reaches 100% cure since the glass transition temperature of fully cure epoxy is 190 °C, less than the processing temperature. On the other hand, the sample processed at 180 °C reaches 97% cure and the one processed at 160 °C only reaches 87% cure.

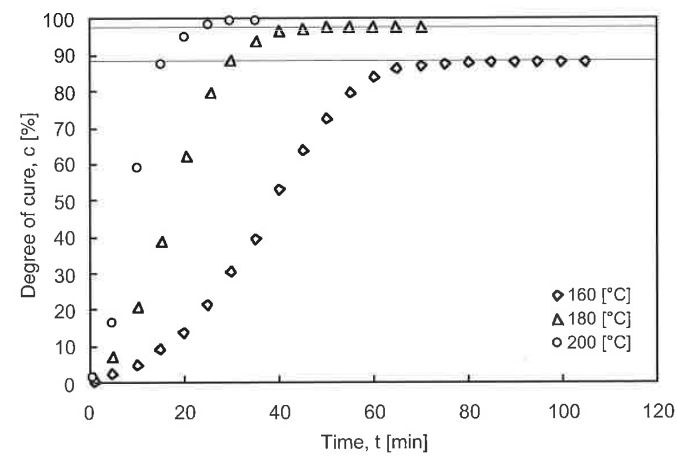


Figure 8.17 Degree of cure as a function of time for an epoxy resin measured using isothermal DSC.

Figures 8.16 and 8.17 also illustrate how the curing reaction is accelerated as the processing temperature is increased. The curing reaction of thermally cured thermoset resins is not immediate, thus the blend can be stored in a refrigerator for a short period of time without having any significant curing reaction.

The behavior of curing thermosetting resins can be represented with the generalized time-temperature-transformation (TTT) cure diagram developed by Enns and Gillham [16]; it can be used to relate the material properties of thermosets as a function of time and the processing temperature as shown in Fig. 8.18.

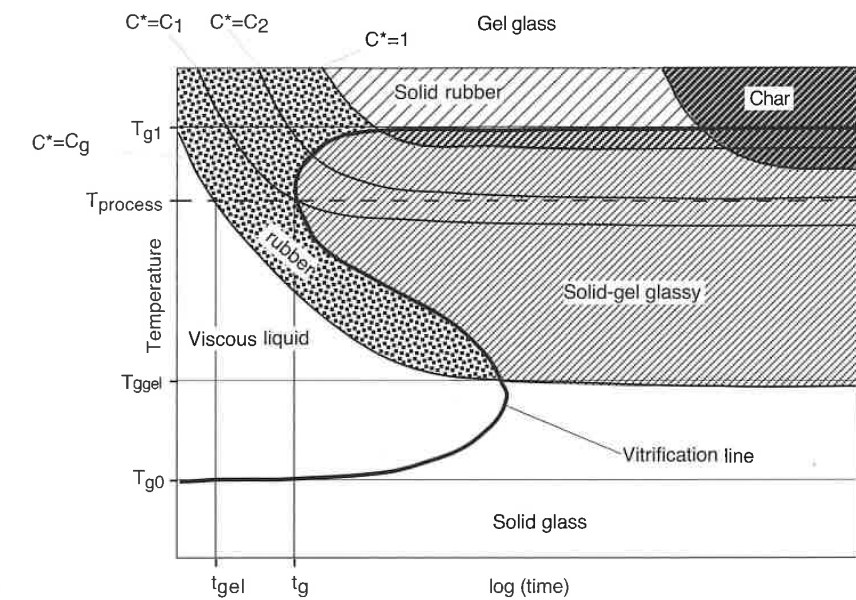


Figure 8.18 Time-temperature-transformation (TTT) diagram for a thermoset

The diagram presents various lines that represent constant degrees of cure. The curve labeled $C^* = C_g$ represents the gel point and $C^* = 1$ the fully cured resin. Both curves have their corresponding glass transition temperatures, T_{g1} and $T_{g_{gel}}$, for the glass transition temperature of the fully cured resin and at its gel point, respectively. The glass transition temperature of the uncured resin, T_{g0} , and an S-shaped curve labeled "vitrification line," are also depicted. The *vitrification line* represents the boundary where the glass transition temperature becomes the processing temperature. Hence, to the left of the vitrification curve the curing process is controlled by a very slow diffusion process. The TTT-diagram shows an arbitrary process temperature. The material being processed reaches the gel point at $t = t_{gel}$ and the vitrification line at $t = t_g$. At this point the material has reached a degree of cure of C_1 and glass transition temperature of the resin is equal to the processing temperature. The material continues to cure very slowly (diffusion controlled) until it reaches a degree of cure just below C_2 . There are also various regions labeled in the diagram. The one labeled "viscous liquid" is the one where the resin is found from the beginning of processing until the gel point has been reached. The flow and deformation that occurs during processing or shaping must occur within this region. The region labeled "char" must be avoided during processing, since at high

processing temperatures the polymer will eventually undergo thermal degradation.

The model that best represents the curing kinetics of thermosetting resins as reflected in a TTT-diagram is a diffusion modified Kamal-Sourour reaction model [17, 18, 19]. To model autocatalytic cure kinetics, the model can be applied as

$$\frac{dC^*}{dt} = (k_1 + k_2 C^{*m})(1 - C^*)^n \quad (8.11)$$

where m and n are reaction orders, and k_1 and k_2 are constants defined by

$$\frac{1}{k_i} = \frac{1}{k_i^c} + \frac{1}{k_D} \quad (8.12)$$

Here, k_i^c are Arrhenius overall rate constants defined by

$$k_1^c = a_1 e^{-E_1/RT} \quad (8.13)$$

and

$$k_2^c = a_2 e^{-E_2/RT} \quad (8.14)$$

where a_1 and a_2 are fitting parameters, E_1 and E_2 , activation energies and R the ideal gas constant. The constant k_D in Eq. 8.12 is the diffusion rate constant defined as

$$k_D = a_D e^{-E_D/RT} e^{-b/f} \quad (8.15)$$

where a_D and b are adjustable parameters, E_D is the activation energy of the diffusion process, and f is the equilibrium fractional free volume given by

$$f = 0.00048(T - T_g) + 0.025 \quad (8.16)$$

where T_g is the instantaneous glass transition temperature during cure. Equation (8.12) shows that the overall rate constant is governed at one extreme by the Arrhenius rate constant when $k_D \gg k_i^c$, which is the case prior to vitrification, and at the other extreme by the diffusion rate constant when $k_D \ll k_i^c$, which is the case well after vitrification. For a system exhibiting a unique one-to-one relationship between the glass transition temperature and conversion, DiBenedetto's equation [20] is one of the easiest approaches for stoichiometric ratios to express this relationship using only a single parameter as

$$T_g = T_{g0} + \frac{(T_{g1} - T_{g0})\lambda C^*}{1 - (1 - \lambda)C^*} \quad (8.17)$$

where T_{g0} is the glass transition temperature of the uncured resin, T_{g1} is the glass transition temperature of the fully reacted network, and λ is a structure dependent parameter theoretically equated to

$$\lambda = \frac{\Delta C_{p0}}{\Delta C_{p1}} \quad (8.18)$$

The values of ΔC_{p0} and ΔC_{p1} are the differences in the heat capacity between the glassy and rubbery state for the uncured resin and the fully cured network, respectively. However the parameter λ can also be used as fitting parameter.

Mixing activated cure materials such as polyurethanes will instantly start releasing exothermic heat after the mixture of its two components has occurred. The proposed *Castro-Macosko curing model* accurately fits this behavior and is written as [15]

$$\frac{dC^*}{dt} = k_0 e^{-E_0/RT} (1 - C^*)^2 \quad (8.19)$$

8.2.3 Heat Transfer During Cure

A well-known problem in thick section components is that the thermal and curing gradients become more complicated and difficult to analyze since the temperature and curing behavior of the part is highly dependent on both the mold temperature and part geometry [21, 22]. A thicker part will result in higher temperatures and a more complex cure distribution during processing. This phenomenon becomes a major concern during the manufacture of thick components since high temperatures may lead to thermal degradation. A relatively easy way to check temperatures that arise during molding and curing or demolding times is desired. For example, a one-dimensional form of the energy equation that includes the exothermic energy generated during curing can be solved:

$$\rho C_p \frac{\partial T}{\partial t} = k \frac{\partial^2 T}{\partial z^2} + \rho \dot{Q} \quad (8.20)$$

Assuming the material is confined between two mold halves at equal temperatures, the use of a symmetric boundary condition at the center of the part is valid:

$$\frac{\partial T}{\partial z} = 0 \quad \text{at } z = 0 \quad (8.21)$$

and

$$T = T_m \quad (8.22)$$

at the mold wall.

With the use of the finite difference technique and a six constant model that represents dC^*/dt , Barone and Caulk [23] solved Eqs. 8.20-8.22 for the curing of sheet molding compound (SMC). The SMC was composed of an unsaturated polyester resin with 40.7% calcium carbonate and 30% glass fiber by weight. Figures 8.19 and 8.20 show typical temperature and degree of cure distributions, respectively, during the solidification of a 10 mm thick part as computed by Barone and Caulk. In Fig. 8.19, the temperature rise resulting from exothermic reaction is obvious. This temperature rise increases in thicker parts and with increasing mold temperatures. Figure 8.21 is a plot of the time to reach 80% cure versus thickness of the part for various mold temperatures. The shaded area represents the conditions at which the internal temperature within the part exceeds 200 °C because of the exothermic reaction. Temperatures above 200 °C can lead to material degradation and high residual stresses in the final part.

Improper processing conditions can result in a non-uniform curing distribution which may lead to voids, cracks, or imperfections inside the part. It is of great importance to know the appropriate processing conditions which will both avoid the over-heating problem and speed up the manufacturing process.

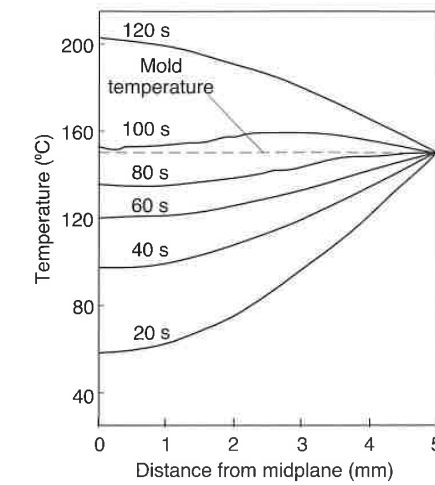


Figure 8.19 Temperature profile history of a 10 mm thick SMC plate.

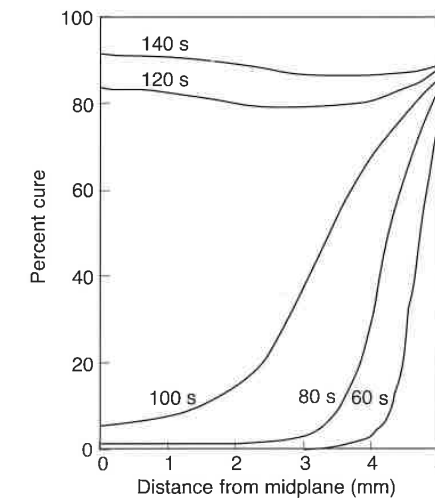


Figure 8.20 Curing profile history of a 10 mm thick SMC plate.

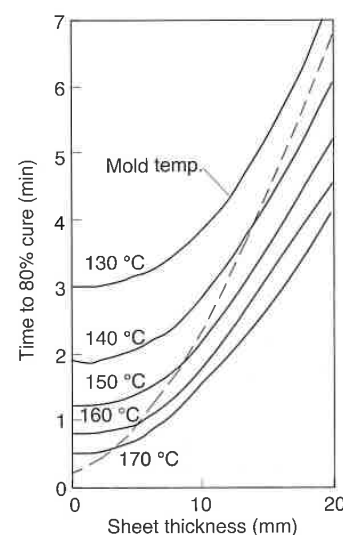


Figure 8.21 Cure times versus plate thickness for various mold temperatures. Shaded region represents the conditions at which thermal degradation may occur.

8.3 Residual Stresses and Warpage of Polymeric Parts

Some major problems encountered when molding polymeric parts are the control and prediction of the component's shape at room temperature. For example, the resulting *sink marks* in the final product are caused by the shrinkage of the material during cooling³ or curing. A common geometry that usually leads to a sink mark is a ribbed structure. The size of the sink mark, which is often only a cosmetic problem, is not only related to the material and processing conditions but also to the geometry of the part. A rib that is thick in relation to the flange thickness will result in significant sinking on the flat side of the part.

Warpage in the final product is often caused by processing conditions that cause unsymmetric residual stress distributions through the thickness of the part. Thermoplastic parts most affected by residual stresses are those that are manufactured with the injection molding process. The formation of residual stresses in injection molded parts is attributed to two major coupled factors:

³ In injection molding one can mitigate this problem by continuously pumping polymer melt into the mold cavity as the part cools until the gate freezes shut.

cooling and flow stresses. The first and most important factor is the residual stress that is formed because of the rapid cooling or quenching of the part inside the mold cavity. As will be discussed and explained later in this chapter, this dominant factor is the reason why most thermoplastic parts have residual stresses that are tensile in the central core of the part and compressive on the surface. Typical residual stress distributions are shown in Fig. 8.22 [24], which presents experimental⁴ results for PMMA and PS plates cooled at different conditions.

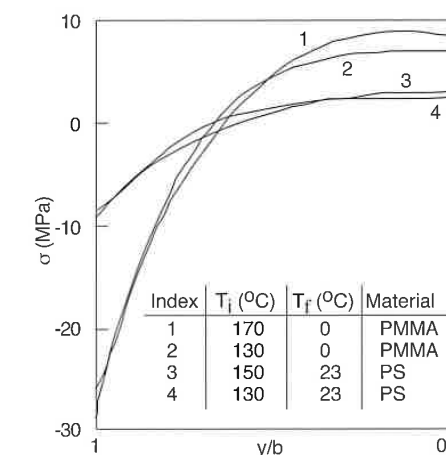


Figure 8.22 Residual stress distribution for 3 mm thick PMMA plates cooled from 170 °C and 130 °C to 0 °C, and for 2.6 mm thick PS plates cooled from 150 °C and 130 °C to 23 °C.

Residual stresses in injection molded parts are also formed by the shear and normal stresses that exist during flow of the polymer melt inside the mold cavity during the filling and packing stage. These tensile flow induced stresses are often very small compared to the stresses that build up during cooling. However, at low injection temperatures, these stresses can be significant in size, possibly leading to parts with tensile residual stresses on the surface. Figure 8.23 [25] demonstrates this concept with PS plates molded at different injection temperatures. The figure presents residual stress distributions through the thickness of the plate perpendicular and parallel to the flow direction. Isayev [24, 25] has also demonstrated that flow stresses are maximum near the gate. The resulting tensile residual stresses are of particular concern since they may lead to *stress cracking* of the polymer component.

⁴ The experimental residual stress distributions were directly computed from curvature measurements obtained by the layer removal method.

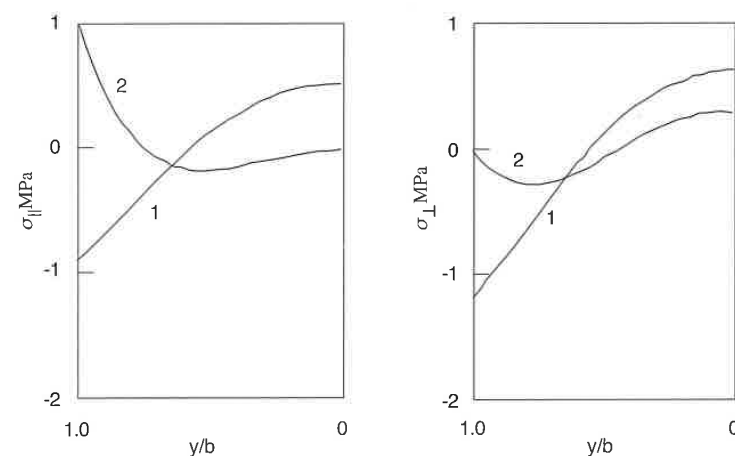


Figure 8.23 Residual stress distribution parallel and perpendicular to the flow direction for a 2.54 mm thick PS plate cooled from 244 °C (1) and 210 °C (2) to 60 °C

The development of models and simulations to predict shrinkage and warpage in the manufacturing of plastic parts is necessary to understand and control the complex thermomechanical behavior the material undergoes during processing. Shrinkage and warpage result from material inhomogeneities and anisotropy caused by mold filling, molecular or fiber orientation, curing or solidification behavior, poor thermal mold lay-out, and improper processing conditions. Shrinkage and warpage are directly related to residual stresses. Transient thermal or solidification behavior as well as material anisotropies can lead to the build-up of residual stresses during manufacturing. Such process-induced residual stresses can significantly affect the mechanical performance of a component by inducing warpage or initiating cracks and delamination in composite parts. It is hoped that an accurate prediction of the molding process and the generation of residual stresses will allow for the design of better molds with appropriate processing conditions.

This section presents basic concepts of the thermomechanical behavior during the manufacturing process of polymeric parts. The formation of residual stresses during the fabrication of plastic parts is introduced first, followed by a review of simple models used to compute residual stresses and associated warpage of plates and beams under different thermal loadings. Several models, which characterize the transient mechanical and thermomechanical behavior of thermoplastic polymers will be reviewed and discussed next. Using these existing models, residual stresses, shrinkage, and warpage of injection molded thermoplastic parts can be predicted. Furthermore, results from the literature

are presented. Since thermoset polymers behave quite differently from thermoplastic polymers during molding, other models need to be introduced to compute the thermomechanical behavior of thermoset polymers. Based on these models, results for predicting residual stresses and the resulting shrinkage and warpage for both thin and thick thermoset parts are also discussed.

8.3.1 Residual Stress Models

The formation of residual stresses is most critical during the solidification of polymer components inside injection molds. To illustrate residual stress build-up during injection molding, the plate shaped injection molding cavity shown in Fig. 8.9 is considered. As a first order approximation, it can be assumed that a hard polymer shell forms around the melt pool as the material is quenched by the cool mold surfaces. Neglecting the packing stage during the injection molding cycle, this rigid frame contains the polymer as it cools and shrinks during solidification. The shrinkage of the polymer is, in part, compensated by the deflection of the rigid surfaces, a deformation that occurs with little effort. In fact, if the packing stage is left out, it is a common experimental observation that between 85 to 90% of the polymer's volumetric changes are compensated by shrinkage through the thickness of the part [26]. To understand which material properties, boundary conditions, and processing conditions affect the residual stresses in a solidified polymer component, the cooling process of an injection molded amorphous polymer plate, as it cools inside the mold cavity, will be considered. For simplicity, in the following analysis we include only the thermal stresses which result from the solidification of an injection molded article as it is quenched from an initial temperature, T_i , to a final temperature, T_f (Fig. 8.9). However, it is important to point out again that, in injection molded parts, the solidification process starts during mold filling, and that flow continues during the post-filling or packing stage. This results in frozen-in flow stresses that are of the same order as the thermal stresses. Baaijens [27] calculated the residual stresses in injection molded parts, including the viscoelastic behavior of the polymer and the flow and thermal stresses. With his calculations, he demonstrated that the flow induced stresses are significant and that a major portion of them stems back to the post-filling stage during injection molding. This is in agreement with experimental evidence from Isayev [24] and Wimberger-Friedl [28].

In Fig. 8.9 the plate thickness, $2L$, denotes the characteristic dimension across the z -direction and is considered to be much smaller than its other dimensions. This is a common assumption for most polymer parts. It is assumed that the polymer behaves as a viscous liquid above T_g and as an elastic solid below T_g . The resulting residual stresses form because the cooling of the plate, from the outside to the inside, cause the outer layers to solidify first

without any resistance from the hot liquid core. As the inner layers solidify and cool, their shrinkage is resisted by the solidified outer surface, thus, leading to a residual stress which is tensile in the center and compressive at the surface. Hence, the residual stress build-up must depend on material and process dependent temperatures, space, thermal properties, elastic properties, and on time. This can be expressed as

$$\sigma = \sigma\{T_i - T_f, T_g - T_f, L, z, \beta, k, h, \alpha, E, \nu, t\} \quad (8.23)$$

where β is the thermal expansion coefficient, k the thermal conductivity, α the thermal diffusivity, E the elastic modulus, ν Poisson's ratio, and t time. Using the dimensional analysis and assuming that stress relaxation effects are negligible, the final residual stress can be written as

$$\frac{\sigma(1-\nu)}{E} = f(Bi, \hat{z}, \varepsilon_T) \quad (8.24)$$

where \hat{z} is a dimensionless coordinate defined by z/L and Bi is the Biot number defined by the ratio of convective heat removal to heat conduction and is calculated with

$$Bi = \frac{hL}{k} \quad (8.25)$$

A large Biot number signifies a process where the heat is removed from the surface of the part at a high rate. This is typical of fast quench processes, which result in both high temperature gradients and residual stresses. Predicted temperature distributions in a process with a large Biot number is shown in Fig. 8.24a. On the other hand, a low Biot number describes a process where the heat is removed from the part's surface at a very low rate, resulting in parts with fairly constant temperatures. Predicted temperature fields, for low Biot number processes, as shown in Fig. 8.24b, will lead to low residual stresses in the final part.

The third quantity, ε_T , found in Eq. 8.24 is the thermal strain that will lead to residual stress. It is a quantity that measures the influence of processing conditions on residual stress formation and is defined by

$$\varepsilon_T = \beta(T_g - T_f) \quad (8.26)$$

The limits of the thermal strain are described by

$$\varepsilon_T = 0 \quad (8.27)$$

if $T_f = T_g$ and

$$\varepsilon_T = \text{Maximun} \quad (8.28)$$

if $T_i = T_g$

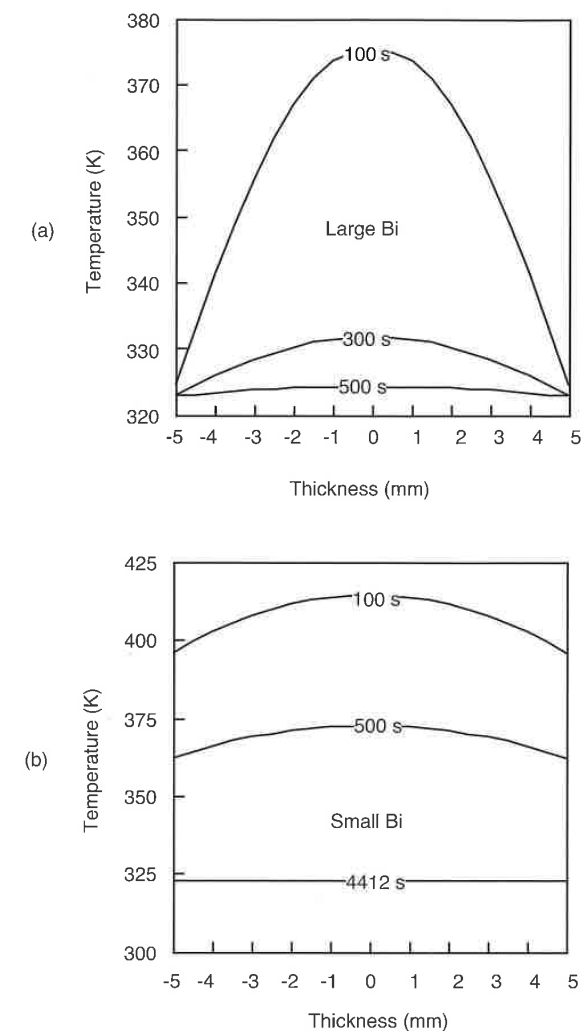


Figure 8.24 Effect of Biot number on the temperature distribution history in a cooling plate: (a) large Bi (b) small Bi.

These limits can be explained. A polymer that is only allowed to cool to T_g , where $T_f = T_m$, does not have a chance to build up any residual stresses, since these can only exist below the glass transition temperature and not in the

liquid state. On the other hand, a polymer that is initially at the glass transition temperature and cools to another temperature perceives all its strain in the solid state, hence, conceivably translating them completely into stresses.

8.3.1.1 Residual Stress Model Without Phase Change Effects

The parabolic temperature distribution which is present once the part has solidified will lead to a parabolic residual stress distribution that is compressive in the outer surfaces of the component and tensile in the inner core. Assuming no residual stress build-up during phase change, a simple function based on the parabolic temperature distribution, can be used to approximate the residual stress distribution in thin sections [28]:

$$\sigma = \frac{2}{3} \frac{E\beta}{1-\nu} (T_s - T_f) \left(\frac{6z^2}{4L^2} - \frac{1}{2} \right) \quad (8.29)$$

Here, T_s denotes the solidification temperature: the glass transition temperature for amorphous thermoplastics, or the melting temperature for semi-crystalline polymers. Equation 8.29 was derived by assuming static equilibrium (e.g., the integral of the stresses through the thickness must be zero). The full derivation is left out here, since a more general approach is presented in the next section. Figure 8.23 [29] compares the compressive stresses measured on the surface of PMMA samples to Eq. 8.29.

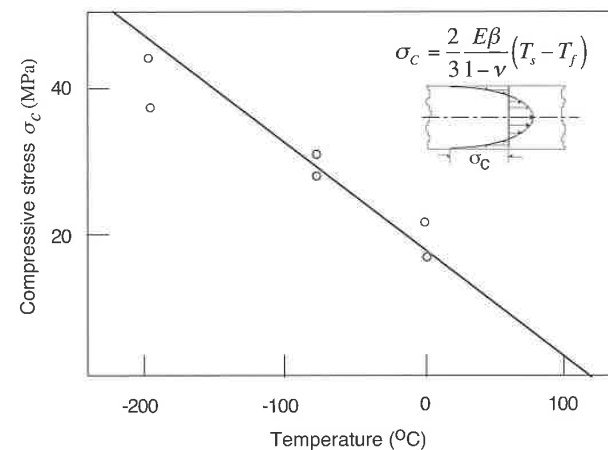


Figure 8.25 Comparison between computed, Eq. (8.29), and measured compressive stresses on the surface ($z = L$) of injection molded PMMA plates.

8.3.1.2 Model to Predict Residual Stresses with Phase Change Effects

As the plate shown in Fig. 8.9 cools, it develops a solidified layer that continues to grow until the whole plate hardens. Figure 8.11 shows a cross-section of the plate at an arbitrary point in time. At any instance of time, t , the location that has just reached T_g is defined as $Z_g(t)$. To solve for the residual stress distribution, the energy equation, Eq. 8.3, must be solved while satisfying the force balance equation within the solidified material. At the centerline, the symmetry boundary condition can be used, Eq. 8.4, and a convective boundary condition on the outer surface of the plate is needed.

$$h(T_s - T_f) = -k \frac{\partial T}{\partial z} \quad \text{at } z = L \quad (8.30)$$

The strain at any time and position is usually defined as the sum of its elastic, thermal, and viscous strain components:

$$\varepsilon(t) = \varepsilon_E + \varepsilon_{th} + \varepsilon_v \quad (8.31)$$

where ε_E is the elastic strain, ε_v the viscous strain and ε_{th} the thermal strain, which occurs only after the material is below the glass transition temperature. The thermal strain can be written as

$$\varepsilon_{th} = \beta(T(z,t) - T_g) \quad (8.32)$$

The viscous strain is the strain the layer undergoes just before solidifying, caused by thermal contraction and viscous flow. The viscous strain occurs under a negligible stress and is not felt by the layer that has just solidified. Each layer has a different viscous strain equal to the overall strain of the plate, $\varepsilon(t)$, the instant that layer has solidified, which makes the viscous strain a function of space. Solving for the elastic strain results in

$$\sigma(z,t) = \frac{E}{1-\nu} (\varepsilon(t) - \beta(T(z,t) - T_g) - \varepsilon_v(z)) \quad (8.33)$$

To solve for the total strain of the plate, the stresses must approach equilibrium and add up to zero, as

$$\int_{-L}^L \sigma(z,t) dz = 0 \quad (8.34)$$

Since the plate can be considered symmetric and the stresses are zero above the glass transition temperature, we can write

$$\int_{z_g(t)}^L \sigma(z,t) dz = 0 \quad (8.35)$$

Substituting Eq. 8.33 into Eq. 8.35 gives

$$\int_{z_g(t)}^L (\epsilon(t) - \beta(T(z,t) - T_g) - \epsilon_v(z)) dz = 0 \quad (8.36)$$

However, the plate's total strain is constant through the thickness and can be integrated out and solved for as

$$\epsilon(t) = \frac{1}{L - z_g(t)} \int_{z_g(t)}^L (\beta(T(z,t) - T_g) + \epsilon_v(z)) dz \quad (8.37)$$

The total strain $\epsilon(t)$ and its viscous component ϵ_v are unknown but equal to each other and can be found by solving both Eq. 8.37 and the energy equation, Eq. 8.3, with a convective boundary condition. The energy equation can be solved numerically by using the finite difference method. The same grid points used for the energy equation can be used for the integration of Eq. 8.37. The solution is achieved in successive time steps from the beginning of cooling until the whole plate has reached the glass transition temperature, at which point the whole viscous strain distribution is known. Now, the part needs to be cooled until its final temperature distribution of $T = T_f$ has been reached. The final residual stress distribution can be computed as

$$\sigma(z) = \frac{E}{1-\nu} (\epsilon_{tot} - \beta(T_f - T_g) - \epsilon_v(z)) \quad (8.38)$$

The total strain of the plate is unknown and can be found by solving the equilibrium equation, Eq. 8.34, using the final residual stress distribution as

$$\epsilon_{tot} = \frac{1}{L} \int_0^L (\beta(T_f - T_g) - \epsilon_v(z)) dz \quad (8.39)$$

Figures 8.24 and 8.25 show residual stress distributions for several Biot numbers and values of Θ_g , respectively. The value Θ_g is the dimensionless temperature that leads to a residual stress build-up and is defined by

$$\Theta_g = \frac{T_g - T_f}{T_i - T_f} \quad (8.40)$$

In Figure 8.25 the model described in this section is also compared to the residual stress distribution of Eq. 8.29. In this comparison, the influence of phase change effects becomes evident.

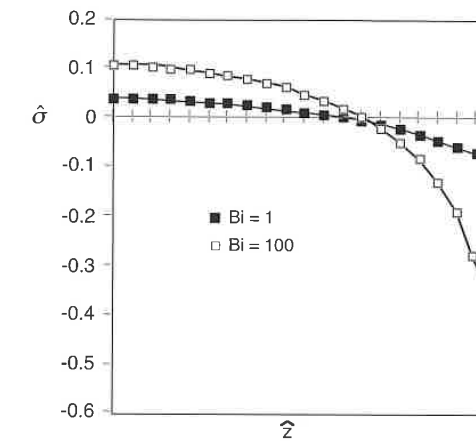


Figure 8.26 Residual stress distributions as a function of Biot number in a polystyrene plate after cooling.

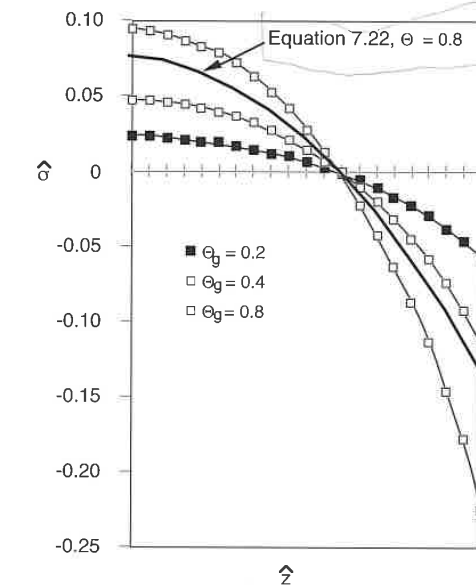


Figure 8.27 Residual stress distributions as a function of thermal boundary conditions in a polystyrene plate after cooling.

Equations 8.37–8.39 can be modified and solved together with the energy equation for thermosets, Eq. 8.20, to compute the residual distributions in thermosetting parts. Here, T_g must be replaced with the temperature of the material at the time it solidified (e.g., when its conversion was 80%).

8.3.2 Other Simple Models to Predict Residual Stresses and Warpage

In practice, the complexity of part geometry and cooling channel design in the manufacture of plastic parts can result in unsymmetric mold wall temperature variations which in turn lead to warpage of the part after it is ejected from the mold. Here, a simple model is presented to evaluate residual stress and warpage of a flat plate caused by uneven mold temperatures (Fig. 8.26a), temperature rise due to exothermic curing reaction in thermoset parts (Fig. 8.26b), and by unsymmetric stress distributions in laminated composites (Fig. 8.26c). In general, the stress distribution has to satisfy the equilibrium equation as defined in Eq. 8.33 where the stress-strain relation is defined as

$$\sigma(z) = \frac{E}{(1-\nu)} (\epsilon_{tot} - \beta \Delta T(z) - \epsilon_v(z)) \quad (8.41)$$

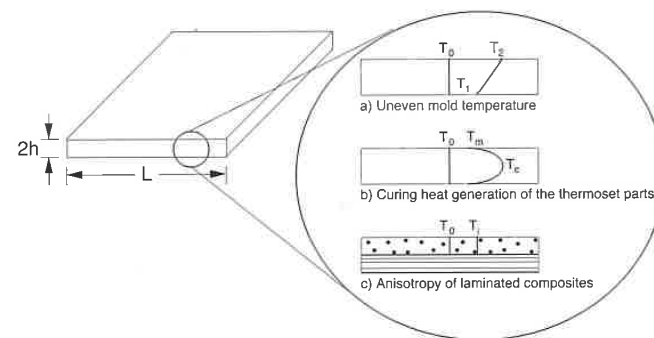


Figure 8.28 Possible causes of residual stress build-up across the thickness of a part.

Here, ϵ_{tot} is the total or actual shrinkage of the plate, ΔT the change in temperature, E Young's modulus, ν Poisson's ratio, and β the thermal expansion coefficient. For simplicity, the viscous strain is often neglected, assuming the part is thin enough that it solidifies at once. Based on classical

shell theory and using the stress distribution, one can additionally compute a thermal moment as follows:

$$M = w \int_{-L}^L \sigma(z) z dz \quad (8.42)$$

where w is the width of the plate. In the following analyses the above Eqs. 8.39–8.42 will be used to compute residual stress and warpage for various cases. If the part is fixed as it is cooled to its final temperature, the total strain, ϵ_{tot} , is zero. In such a case, residual stress is dominated by thermal strain.

8.3.2.1 Uneven Mold Temperature

During molding, the mold wall surface temperatures may vary due to improper thermal mold layout (Fig. 8.26a) with variations typically in the order of 10 °C. Furthermore, the temperatures on the mold surface may vary depending on where the heating or cooling lines are positioned. However, in the current example, we assume that this effect is negligible. The amount of warpage caused by temperature variations between the two mold halves can easily be computed using the equations of the last section. The temperature field across the thickness of a part can be described by

$$T = \left[\frac{1}{2}(T_1 + T_2) + \frac{1}{2}(T_1 - T_2) \frac{z}{L} \right] \quad (8.43)$$

After substituting Eqs. 8.34 and 8.43 into Eq. 8.41, the stress distribution throughout the thickness can be obtained:

$$\sigma = \frac{\beta E}{2(1-\nu)} \left[(T_2 - T_1) \frac{z}{L} \right] \quad (8.44)$$

Substituting Eq. 8.44 into Eq. 8.42, the thermal moment M becomes

$$M = \frac{w\beta EL^2}{3(1-\nu)} (T_2 - T_1) \quad (8.45)$$

For a part whose width, w , is much smaller than its length, ℓ , we can assume a cantilevered geometry as shown in Fig. 8.27. For this geometry the deflection, δ , that results from a moment, M , can be written as

$$\delta = \frac{M\ell^2}{2EI} \quad (8.46)$$

where the area moment of inertia, I , is written as

$$I = \frac{1}{12} w(2L)^3 \quad (8.47)$$

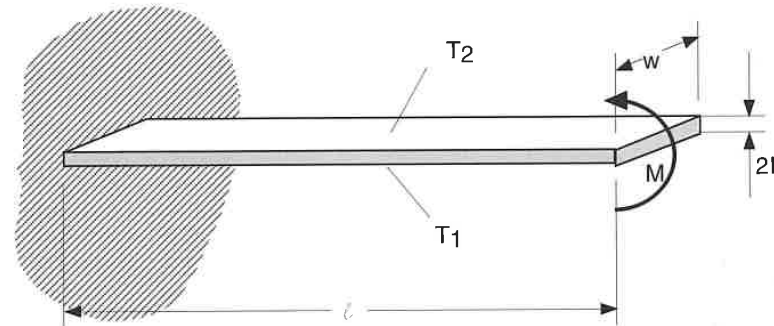


Figure 8.29 Simplified geometry of a thin slender part

Substituting Eqs. 8.45 and 8.47 into Eq. 8.46 we get

$$\delta = \frac{\beta l^2}{4L} (T_2 - T_1) \quad (8.48)$$

8.3.2.2 Residual Stress in a Thin Thermoset Part

In addition to uneven mold temperatures, the exothermic curing reaction is a known problem when manufacturing thermoset parts. Heat release during such reactions can cause the transient temperature inside the part to be higher than the mold wall temperatures. Typical temperature and curing history plots are shown in Figs. 8.17 and 8.18. Note that such a temperature distribution dominates the final residual stress distribution. Here, a simple elastic model is presented to approximate the residual stress distribution. The temperature field in the calculation can be described by a parabolic curve

$$T(z) = T_c + (T_m - T_c) \frac{z^2}{L^2} \quad (8.49)$$

where T_c and T_m are the temperature at the center of the plate and the mold surface, respectively.

We assume the part to be cooled elastically to room temperature, T_0 . Using Eq. 8.41, the stress distribution can be expressed by

$$\sigma(z) = \frac{E}{(1-\nu)} [\epsilon_{tot} - \beta(T_0 - T(z))] \quad (8.50)$$

Since the above equation has to satisfy the equilibrium equation, Eq. 8.34, the total strain can be obtained by integrating the stress field across the thickness

$$\epsilon_{tot} = \frac{\beta}{L} \left[T_0 - \frac{2}{3} T_c - \frac{1}{3} T_m \right] \quad (8.51)$$

Substituting Eq. 8.51 into Eq. 8.39, the residual stress distribution becomes

$$\sigma(z) = \frac{\beta E}{(1-\nu)} \left[\frac{1}{3} (T_c - T_m) - (T_c - T_m) \frac{z^2}{L^2} \right] \quad (8.52)$$

After defining the non-dimensional parameters, $\hat{\sigma}$ and \hat{z} , as

$$\hat{\sigma} = \frac{(1-\nu)\sigma}{E\beta(T_c - T_m)} \quad (8.53)$$

and

$$\hat{z} = \frac{z}{L} \quad (8.54)$$

Eq. 8.52 can be normalized as

$$\hat{\sigma}(\hat{z}) = \frac{1}{3} - \hat{z}^2 \quad (8.55)$$

The non-dimensional residual stress distribution across the thickness of the part is depicted in Fig. 8.27. The stresses in the outer layer are compressive while tensile stresses are found in the inner layers. A maximum compressive non-dimensional stress of $2/3$ is located on the surface and a maximum tensile stress of $1/3$ occurs at the center of the part.

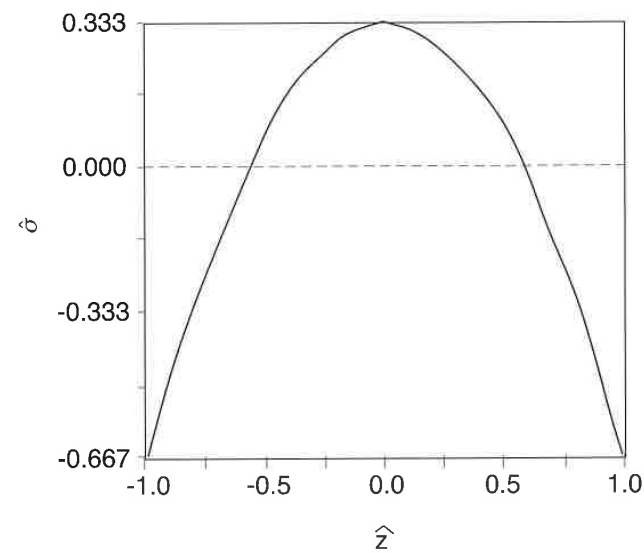


Figure 8.30 Normalized residual stress distribution in a thin thermoset part.

8.3.2.3 Anisotropy Induced Curvature Change

In the manufacturing of large and thin laminate structures or fiber reinforced composite parts with a large fiber-length/part-thickness ratio, the final part exhibits a higher thermal expansion coefficient in the thickness direction than in the surface direction. If the part is curved, it will undergo an angular distortion, as shown in Fig. 8.28, which is a consequence of the anisotropy of the composites. This phenomenon is usually called the *spring-forward* effect or *anisotropy induced curvature change* [32]. Through-thickness thermal strains, which are caused by different thermal expansion coefficients, can lead to an angle distortion of a cylindrical shell experiencing a temperature change. As demonstrated in Fig. 8.28, when a curved part undergoes a temperature change of ΔT , the curved angle, θ , will change by $\Delta\theta$. The resulting $\Delta\theta$, therefore, is dependent on the angle θ , the temperature change ΔT , and the difference of the thermal expansion coefficients in the r and θ directions [33]

$$\Delta\theta = (\beta_r - \beta_\theta)\theta\Delta T = \Delta\beta\theta\Delta T \quad (8.56)$$

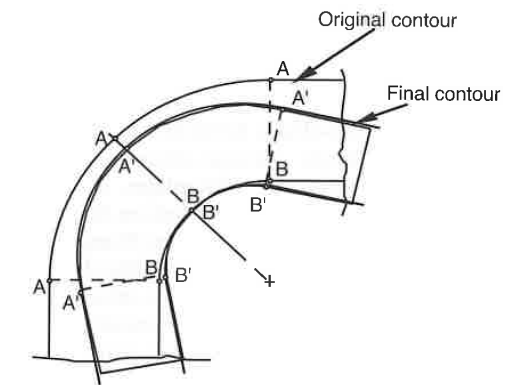


Figure 8.31 Schematic diagram of the spring-forward effect.

In plate analysis, the inclusion of anisotropies that lead to curvature changes is very involved. Hence, it is easier to introduce the curvature change by an equivalent thermal moment [34]:

$$M = \frac{E}{(1-\nu)} \frac{\Delta\beta\Delta T}{R} \frac{L^3}{12} \quad (8.57)$$

where R represents the local radius of curvature.

8.3.3 Predicting Warpage in Actual Parts

Shrinkage and warpage are directly related to residual stresses which result from locally varying strain fields that occur during the curing or solidification stage of a manufacturing process. Such strain gradients are caused by nonuniform thermomechanical properties and temperature variations inside the mold cavity. Shrinkage due to cure can also play a dominant role in the residual stress development in thermosetting polymers and becomes important for fiber reinforced thermosets when are a concern sink marks appearing in thick sections or ribbed parts.

When processing thermoplastic materials, shrinkage and warpage in a final product depend on the molecular orientation and residual stresses that form during processing. The molecular or fiber orientation and the residual stresses inside the part in turn depend on the flow and heat transfer during the mold filling, packing, and cooling stage of the injection molding process. Kabanemi

et al. [35] used a three-dimensional finite element approach to solve the thermal history and residual stress build-up in injection molded parts. To predict the residual stress in the finished part, they characterized the thermomechanical response of the polymer from melt to room temperature, or from the p-v-T behavior to stress-strain behavior. Bushko and Stokes [36, 37] used a thermorheologically simple thermo-viscoelastic material model to predict residual stresses and warpage in flat plates. With their model, they found that packing pressure had a significant effect on the shrinkage of the final part but little effect on the residual stress build-up. Wang and co-workers have developed unified simulation programs to model the filling and post-filling stages in injection molding [38-41]. In their models they perform a simultaneous analysis of heat transfer, compressible fluid flow, fiber orientation, and residual stress build-up in the material during flow and cooling using finite element/control volume approach for flow, finite difference techniques for heat transfer, and finite element methods for fiber orientation and thermomechanical analysis.

The shrinkage and warpage in thin compression molded fiber reinforced thermoset plates were predicted by various researchers [42] using fully three-dimensional finite element models and simplified finite element plate models. More recently [4, 44], the through-thickness properties, temperature, and curing variations that led to warpage have been represented with equivalent moments. By eliminating the thickness dimensions from their analysis, they significantly reduced computation costs and maintained agreement with experimental results. At the same time, they were able to use the same finite element meshes used in common commercial codes to predict the mold filling and the fiber orientation in the final part.

The governing equations used for the stress analysis of polymer components are derived using the principle of virtual work. Here, the stresses are represented as a function of local strain and residual stress $\{\sigma_0\}$.

$$\{\sigma\} = [E]\{\varepsilon\} - [E]\{\varepsilon_{int}\} + \{\sigma_0\} \quad (8.58)$$

In Eq. 8.58 the material tensor $[E]$ is anisotropic and temperature or degree of cure dependent and $\{\varepsilon_{int}\}$ is the total internal strain that occurs due to curing, cooling or heating during a time step. Two kinds of internal strains should be included when simulating the thermomechanical behavior of polymer parts. One is a thermal strain caused by temperature change and the other is a curing strain resulting from cross-linking polymerization of thermoset resins. Thus, the total internal strain can be expressed by

$$\{\varepsilon_{int}\} = \{\varepsilon_0^{th}\} + \{\varepsilon_0^c\} \quad (8.59)$$

Here, superscript *th* denotes the thermal strain and *c* the curing strain. The thermal strains can be represented in terms of temperature change and thermal expansion coefficients

$$\{\varepsilon_0^{th}\}T = \Delta T\{\alpha_{xx} \alpha_{yy} \alpha_{zz} 0 0 0\} \quad (8.60)$$

The anisotropic thermal expansion coefficient, caused by fiber orientation, is perhaps the largest cause of warpage in fiber reinforced parts. Figure 8.29 demonstrates how, for typical thermoset composite parts, the thermal shrinkage parallel to the main orientation direction is about half of that normal to the main orientation direction⁵.

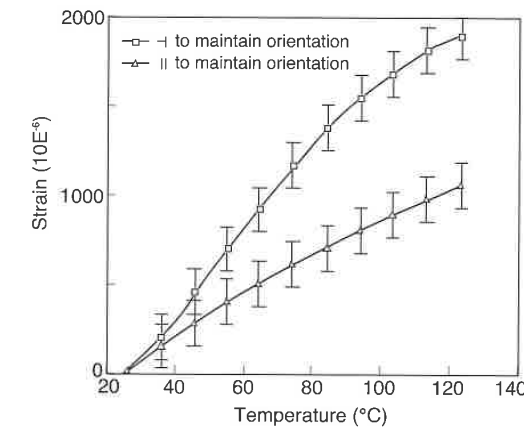


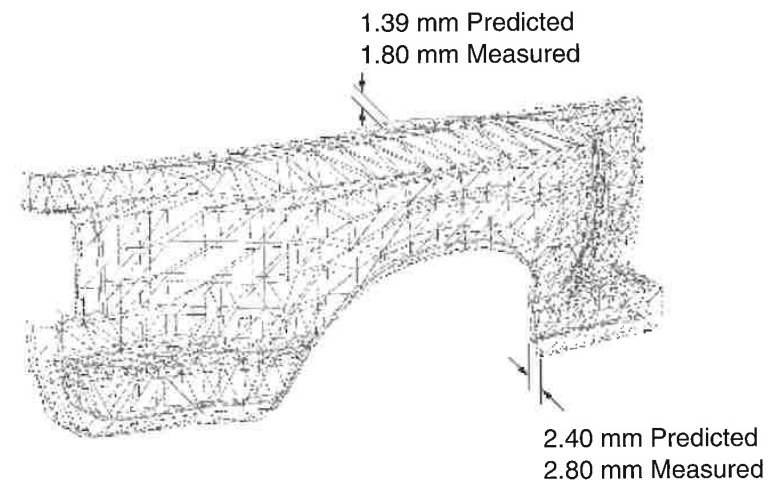
Figure 8.32 Experimentally measured thermal strains in an SMC plate with a fiber orientation distribution that resulted from a 25% initial mold coverage charge.

To calculate the residual stress development during the manufacturing process, the heat transfer equation is coupled to the stress-strain analysis through constitutive equations. Figure 8.30 compares the mold geometry with part geometry for the truck fender shown in Chapter 7, after mold removal and cooling, computed using the above model. The fiber content by volume in the part was 21% ($\phi=0.21$) and the material properties for the glass fiber and the unsaturated polyester resin are listed in Table 8.4.

⁵ The thermal shrinkage was measured from a rectangular plate molded with a charge that covered 25% of the mold surface and that was allowed to flow only in one direction.

Table 8.4 Mechanical and Thermomechanical Properties for Various Materials

	Fiberglass	Polyester	Epoxy
E (MPa)	7.3×10^4	2.75×10^3	4.1×10^3
ν	0.25	0.34	0.37
β (mm/mm/K)	5.0×10^{-6}	3.7×10^{-5}	5.76×10^{-5}

**Figure 8.33** Simulated displacements of an automotive body panel. Displacements were magnified by a factor of 20.

Minimizing warpage is one of the biggest concerns for the design engineer. One way to reduce warpage is by introducing a temperature gradient between the upper and lower mold halves. Again, this through-thickness temperature gradient will introduce a thermal moment which increases or decreases the warpage. Also, by changing the formulation of the polyester resin, the coefficient of thermal expansion of the matrix can be reduced, making it similar to the coefficient of the glass fiber. Theoretically, reduction of the coefficients for the matrix would decrease the in-plane differential shrinkage, which in turn could help reduce the final warpage. Furthermore, the fiber content also

has a great effect on the deformation of a body panel. Here, although the warpage is actually caused by the existence of fibers inside the resin, the increase of fiber content adds to the stiffness of the part which in turn reduces warpage. Further reduction in warpage can also be achieved by changing the size and location of the initial charge, a trial-and-error solution, which is still the most feasible with today's technology.

Examples

8.1 Three small samples of an epoxy resin were subjected to a temperature rise from 50 °C to 300 °C in a differential scanning calorimeter using three different heating rates: 2.78 K/min (5 F/min), 5.66 K/min (10 F/min) and 11.11 K/min (20 F/min). Table 8.5 presents the exothermal heat released during the tests. Determine the total heat of reaction using the data measured with the 2.78 K/min heating rate. Plot the degree of cure as a function of time.

In order to compute the degree of cure as a function of time we use Eq. 8.8

$$C_i^* = \frac{Q_i}{Q_T}$$

where

$$Q_i = \int_0^{t_i} \dot{Q} dt = \sum_{j=1}^i \dot{Q}_j \Delta t$$

and

$$Q_T = \int_0^{\infty} \dot{Q} dt = \sum_{j=1}^n \dot{Q}_j \Delta t$$

where n is the total number of data points and Δt is the time step. Since the data are given in terms of temperature, we must transform the temperature step to time using the heating rate 2.78 K/min using

$$\Delta t = \frac{10K}{2.78K/min}$$

The above leads to a total heat of reaction, Q_T , of 785.4 J/g or 785.4 kJ/kg. The degree of cure as a function of temperature is plotted in Fig. 8.31.

Table 8.5 DSC Data for an Epoxy Resin

T (°C)	\dot{Q} ($\frac{\text{J}}{\text{g} \cdot \text{min}}$)		
	2.78 K/min	5.66 K/min	11.11 K/min
50	0.	0.	0.
60	0.	0.	0.
70	0.01	0.	0.01
80	0.02	0.01	0.02
90	0.03	0.02	0.03
100	0.06	0.04	0.06
110	0.12	0.09	0.12
120	0.22	0.16	0.21
130	0.38	0.28	0.37
140	0.65	0.49	0.62
150	1.11	0.82	1.03
160	1.91	1.35	1.66
170	3.38	2.23	2.668
180	6.23	3.69	4.24
190	12.21	6.23	6.76
200	24.97	10.86	10.94
210	47.10	19.76	18.08
220	60.09	37.23	30.79
230	39.40	68.36	53.89
240	15.0	103.36	94.37
250	4.29	100.09	152.83
260	0.98	55.65	196.48
270	0.17	19.99	168.68
280	0.018	5.17	90.54
290	0.	0.92	31.62
300	0.	0.09	7.06

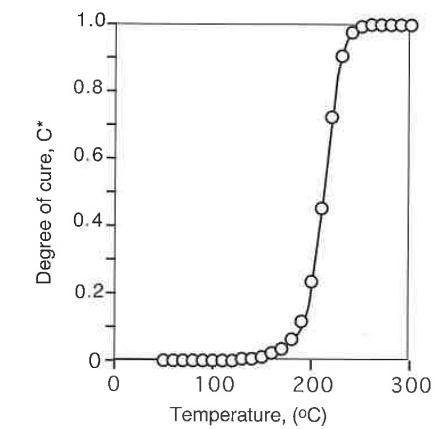


Figure 8.34 Degree of cure as function of temperature for a heating rate of 2.78 K/min.

Problems

- 8.1 Determine the constants for the curing model presented in Eq. 8.12 for the vinyl ester presented in Fig. 8.15. $\rightarrow 8.16$
- 8.2 Write a finite difference program to solve for the transient temperature distribution in a cooling amorphous polymer plate. Test the program with the data given for polystyrene in Table 8.2 for a 2 mm thick plate.
- 8.3 Using the momentum balance presented in Eq. 8.43, derive the residual stress distribution, Eq. 8.38, in a cooling polymer plate neglecting the effects of phase change.
- 8.4 A 1 mm thick polystyrene ruler is injection molded. For a resin with a glass transition temperature around 100 °C and a final ambient temperature of 20 °C, estimate the residual stress at the surface of the part shortly after demolding. Assume a Young's modulus of 3200 MPa and a thermal expansion coefficient of 7×10^{-5} mm/mm/°C. Neglect phase change effects.
- 8.5 For a standard 30 cm long, 3 cm wide, and 1 mm thick ruler, how much warpage would occur with a 5 °C temperature difference between the

mold halves? Assume a Young's modulus of 3200 MPa and a thermal expansion coefficient of 7×10^{-5} mm/mm/°C.

- 8.6 Write a finite difference program to solve for the transient temperature distribution in a cooling amorphous polymer plate. Solve Eqs. 8.31-8.39 along with the predicted temperatures to estimate the residual stress in the final plate. Compare the residual stress distribution for a 2 and a 5 mm thick polystyrene plate.
- 8.7 A long and thin unsaturated polyester - unidirectional glass fiber composite plate (1000x20x2 mm) is molded in a thermally unbalanced mold. One mold side is a 140 °C and the other at 150 °C. Assuming the temperature distribution is at steady state the instant the part solidifies, what is the residual stress distribution in the plate before it is allowed to warp. $E_{\text{composite}} = 20\text{GPa}$. Towards which direction would the plate warp, the hot side or cooler side?
- 8.8 Figure 8.31 presents a schematic of the cross-section of an SMC pick-up truck box. In the finished product, the average through the thickness thermal expansion coefficient, β_3 , is 2×10^{-5} mm/mm/K, and the average planar thermal expansion coefficient, β_1 or β_2 is 8×10^{-6} mm/mm/K. Estimate the amount and direction that the side walls will warp, if any.

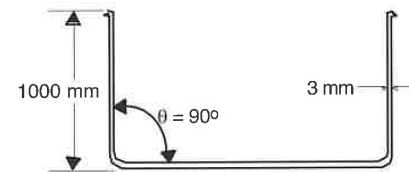


Figure 8.35 Schematic of an SMC pick-up truck cross-section.

- 8.9 Using the data given in Example 8.1, plot the degree of cure for heating rates of 5.66 K/min and 1.11 K/min. What are the characteristic curing times for all three heating rates.

References

- van Krevelen, D.W., and Hoftyzer, P.J., *Properties of Polymers*, Elsevier Scientific Publishing Company, Amsterdam, (1976).
- Wagner, H., Internal report, AEG, Kassel, Germany, (1974).
- Menges, G., and Winkel, E., *Kunststoffe*, 72, 2, 91, (1982).
- Tadmor, Z., and Gogos, C.G., *Principles of Polymer Processing*, John Wiley & Sons, New York, (1979).
- Avrami, M., *J. Chem. Phys.*, 7, 1103, (1939).
- Sharples, A., *Polymer Science, A Materials Science Handbook*, Chapter 4, A.D. Jenkins, Ed., North Holland Publishing Company, Amsterdam, (1972).
- Eder, G., and Janeschitz-Kriegl, H., *Material Science and Technology*, Vol. 18., Ed. H.E.H. Meijer, Verlag Chemie, Weinheim, (1995).
- Brandrup, J., and Immergut, E.H., *Polymer Handbook*, John Wiley & Sons, New York, (1975).
- Krobath, G., Liedauer, S., and Janeschitz-Kriegl, H., *Polymer Bulletin*, 14, 1, (1985).
- Stefan, J., *Ann. Phys. and Chem., N.F.*, 42, 269, (1891).
- Eder, G., and Janeschitz-Kriegl, H., *Polymer Bulletin*, 11, 93, (1984).
- Janeschitz-Kriegl, H., and Krobath, G., *Intern. Polym. Process.*, 3, 175, (1988).
- Randell, D.R., *Radiation Curing Polymers*, Burlington House, London, (1987).
- Palmese, G.R., Andersen, O., and Karbhari, V.M., *Advanced Composites X: Proceedings of the 10th Annual ASM/ESD Advance Composites Conference*, Dearborn, MI, ASM International, Material Park, (1994).
- Macosko, C.W., *RIM Fundamentals of Reaction Injection Molding*, Hanser Publishers, Munich, (1989).
- Enns, J.B. and Gillham, J.K., "Time-Temperature-Transformation (TTT) Cure Diagram: Modeling the Cure Behavior of Thermosets", *J. Appl. Polym. Sci.*, 28, 2567 (1983).
- Kamal, M.R., "Thermoset Characterization for Moldability Analysis", *Polym. Eng. Sci.*, 14 (3), 231 (1974).
- Rabinowitch, E., *Trans. Faraday Soc.*, 33, 1225 (1937).
- Havlicek, I and Dusek, K., in *Crosslinked Epoxies*, 417, B. Sedlacek and J. Kahovec, Eds., Walter de Gruyter, New York (1987).
- DiBenedetto, A.T., *J. Polym. Sci. Polym. Phys.*, ed., 25, 1949 (1987).
- Bogetti, T.A. and Gillespie, J.W., *45th SPI Conf. Proc.*, (1990).
- Bogetti, T.A. and Gillespie, J.W., *21st Int. SAMPE Tech. Conf.*, (1989).
- Barone, M.R. and Caulk, D.A., *Int. J. Heat Mass Transfer*, 22, 1021, (1979).
- Isayev, A.I., and Crouthamel, D.L., *Polym. Plast. Technol.*, 22, 177, (1984).
- Isayev, A.I., *Polym. Eng. Sci.*, 23, 271, (1983).
- Wübken, G., Ph.D. Thesis, IKV, RWTH-Aachen, Germany, (1974).
- Baaijens, F.P.T., *Rheol. Acta*, 30, 284, (1991).
- Wimberger-Friedl, R., *Polym. Eng. Sci.*, 30, 813, (1990).
- Ehrenstein, G.W., *Polymer-Werkstoffe*, Hanser Publishers, Munich, (1978).
- S. P. Timoshenko and Krieger, S. W., *Mechanics of Composite Materials*, McGraw-Hill, New York, (1959).

31. J. H. Faupel and Fisher, F. E., *Engineering Design*, McGraw-Hill, New York, (1981).
32. C.-C. Lee, GenCorp Research, Akron OH, Personal communication (1994).
33. O'Neill, J.M., Rogers, T.G., and Spencer, A.J.M., *Math. Eng. Ind.*, 2, 65, (1988).
34. Tseng, S.C. and Osswald, T.A., *Polymer Composites*, 15, 270, (1994).
35. Kabanemi, K.K., and Crochet, M.J., *Intern. Polym. Proc.*, 7, 60, (1992).
36. Bushko, W.C., and Stokes, V.K., *Polym. Eng. Sci.*, 35, 351, (1995).
37. Bushko, W.C., and Stokes, V.K., *Polym. Eng. Sci.*, 35, 365, (1995).
38. Chiang, H.H., Hieber, C.A., and Wang, K.K., *Polym. Eng. Sci.*, 31, 116, (1991).
39. Chiang, H.H., Hieber, C.A., and Wang, K.K., *Polym. Eng. Sci.*, 31, 125, (1991).
40. Chiang, H.H., Himasekhar, K., Santhanam, N., and Wang, K.K., *J. Eng. Mater. Tech.*, 115, 37, (1993).
41. Chiang, H.H., Santhanam, N., Himasekhar, K., and Wang, K.K., *Advances in Computer Aided Engineering (CAE) of Polymer Processing*, MD-Vol. 49, ASME, New York, (1994).
42. Osswald, T.A., *J. Thermoplast. Comp. Mater.*, 4, 173, (1991).
43. Tseng, S.C., Ph.D. Thesis, Dept. of Mech. Eng., University of Wisconsin-Madison, (1993).
44. Tseng, S.C. and Osswald, T.A., *Polymer Composites*, 15, 270, (1994).

Part III

Engineering Design Properties

Mechanical Behavior of Polymers

Polymeric materials are implemented into various designs because of their low cost, processability, and desirable material properties. Of interest to the design engineer are the short and long-term responses of a loaded component. Properties for short-term responses are usually acquired through short-term tensile tests and impact tests, whereas long-term responses depend on properties measured using techniques such as the creep and the dynamic test.

9.1 Basic Concepts of Stress and Strain

Strictly speaking, polymers cannot be modeled using linear theory of elasticity. However, the stress-strain response of a linear elastic model for the polymer component can suffice in the evaluation of a design and the prediction of the behavior of the component during loading.

For a full three-dimensional model, as shown for a small material element in Fig. 9.1, there are six components of stress and strain. The stress-strain relation for a linear elastic material is defined by the following equations:

$$\sigma_{xx} = E\epsilon_x + 2G\epsilon_{xx} \quad (9.1)$$

$$\sigma_{yy} = E\epsilon_y + 2G\epsilon_{yy} \quad (9.2)$$

$$\sigma_{zz} = E\epsilon_z + 2G\epsilon_{zz} \quad (9.3)$$

$$\tau_{xy} = G\gamma_{xy} \quad (9.4)$$

$$\tau_{yz} = G\gamma_{yz} \quad (9.5)$$

$$\tau_{zx} = G\gamma_{zx} \quad (9.6)$$

where

$$E = \frac{\nu E}{(1+\nu)(1-2\nu)} \quad (9.7)$$

and I_e is the first invariant of the strain tensor and represents the volumetric expansion of the material which is defined by

$$I_e = \epsilon_{xx} + \epsilon_{yy} + \epsilon_{zz} \quad (9.8)$$

The elastic constants E , ν and G represent the modulus of elasticity, Poisson's ratio and shear modulus, respectively. The shear modulus, or modulus of rigidity, can be written in terms of E and ν as

$$G = \frac{E}{2(1+\nu)} \quad (9.9)$$

The above equations can be simplified for different geometries and load cases. Two of the most important simplified models, the plane stress and plane strain models, are discussed below.

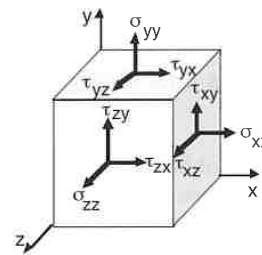


Figure 9.1 Differential material element with coordinate and stress definition.

9.1.1 Plane Stress

A common model describing the geometry and loading of many components is the plane stress model. The model reduces the problem to two dimensions by assuming that the geometry of the part can be described on the x - y plane with a relatively small thickness in the z direction. In such a case $\sigma_{zz} = \tau_{xz} = \tau_{yz} = 0$ and Eqs. 9.1-9.6 reduce to

$$\sigma_{xx} = \frac{E}{1-\nu^2} (\epsilon_{xx} + \nu \epsilon_{yy}) \quad (9.10)$$

$$\sigma_{yy} = \frac{E}{1-\nu^2} (\nu \epsilon_{xx} + \epsilon_{yy}) \quad \text{and} \quad (9.11)$$

$$\tau_{xy} = G\gamma_{xy} \quad (9.12)$$

9.1.2 Plane Strain

Another common model used to describe components is the plane strain model. Similar to the plane stress model, the geometry can be described on an x - y plane with an infinite thickness in the z direction. This problem is also two-dimensional, with negligible strain in the z direction but with a resultant σ_{zz} . For this case, Eqs. 9.1-9.8 reduce to

$$\sigma_{xx} = \frac{E(1-\nu)}{(1+\nu)(1-2\nu)} \left(\epsilon_{xx} + \frac{\nu}{1-\nu} \epsilon_{yy} \right) \quad (9.13)$$

$$\sigma_{yy} = \frac{E(1-\nu)}{(1+\nu)(1-2\nu)} \left(\frac{\nu}{1-\nu} \epsilon_{xx} + \epsilon_{yy} \right) \quad \text{and} \quad (9.14)$$

$$\tau_{xy} = G\gamma_{xy} \quad (9.15)$$

9.2 The Short-Term Tensile Test

The most commonly used mechanical test is the short-term stress-strain tensile test. Stress-strain curves for selected polymers are displayed in Fig. 9.2 [1]. For comparison, the figure also presents stress-strain curves for copper and steel. It becomes evident from Fig. 9.2 that although they have much lower tensile strengths, many engineering polymers exhibit much higher strains at break.

The next two sections discuss the short-term tensile test for elastomers and thermoplastic polymers separately. The main reason for identifying two separate topics is that the deformation of a cross-linked elastomer and an uncross-linked thermoplastic vary greatly. The deformation in a cross-linked polymer is in general reversible, whereas the deformation in typical uncross-linked polymers is associated with molecular chain relaxation, which makes the process time-dependent, and sometimes irreversible.

9.2.1 Rubber Elasticity

The main feature of elastomeric materials is that they can undergo very large and reversible deformations. This is because the curled-up polymer chains stretch during deformation but are hindered in sliding past each other by the

cross-links between the molecules. Once a load is released, most of the molecules return to their coiled shape. As an elastomeric polymer component is deformed, the slope of the stress-strain curve drops significantly as the uncurled molecules provide less resistance and entanglement, allowing them to move more freely. Eventually, at deformations of about 400%, the slope starts to increase since the polymer chains are fully stretched. This is followed by polymer chain breakage or crystallization which ends with fracture of the component. Stress-deformation curves for natural rubber (NR) [2] and a rubber compound [3] composed of 70 parts of styrene-butadiene-rubber (SBR) and 30 parts of natural rubber are presented in Fig. 9.3. Because of the large deformations, typically several hundred percent, the stress-strain data are usually expressed in terms of extension ratio, λ , defined by

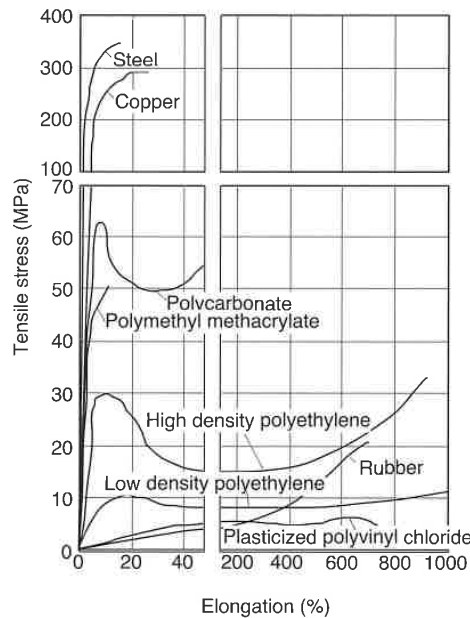


Figure 9.2 Tensile stress-strain curves for several materials.

$$\lambda = \frac{L}{L_0} \tag{9.16}$$

where L represents the instantaneous length and L_0 the initial length of the specimen.

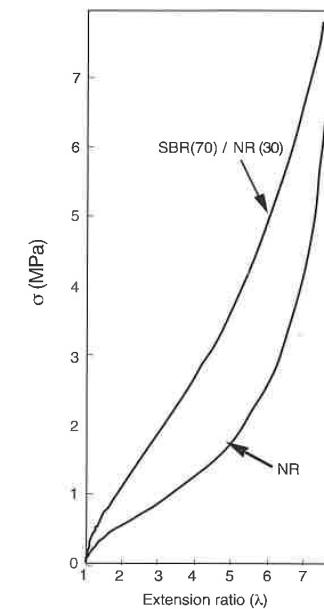


Figure 9.3 Experimental stress-extension curves for NR and a SBR/NR compound.

Based on kinetic theory of rubber elasticity [2, 4] simple expressions can be derived to predict the stress as a function of extension. For a component in uniaxial extension, or compression, the stress can be computed as¹

$$\sigma = G_0 \left(\lambda - \frac{1}{\lambda^2} \right) \tag{9.17}$$

where G_0 is the shear modulus at zero extension, which for rubbers can be approximated by

$$G_0 = \frac{E_0}{3} \tag{9.18}$$

with E_0 as the elastic tensile modulus at zero extension.

Figure 9.4 [2] compares the kinetic theory model with the experimental data for natural rubber, presented in Fig. 9.3. The agreement is good up to about 50% extension ($\lambda = 1.5$). However, Eq. 9.17 can be used to approximate the

¹ A similar equation exists for equibiaxial extension (inflation) of thin sheets. This equation is written as follows $\sigma = G_0 (\lambda^2 - 1/\lambda^4)$.

stress-strain behavior up to 600% extension ($\lambda = 7.0$). For compression, the model agrees much better with experiments, as shown for natural rubber in Fig. 9.5 [2]. Fortunately, rubber products are rarely deformed more than 25% in compression or tension, a fact which often justifies the use of Eq. 9.17.

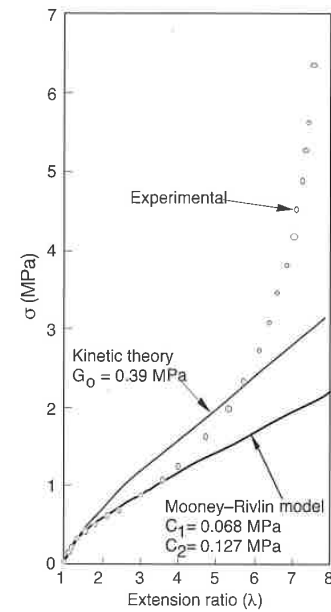


Figure 9.4 Comparison of theoretical and experimental stress-extension curves for natural rubber.

A more complex model representing the deformation behavior of elastomers in the region in which the stress-strain curve is reversible is the *Mooney-Rivlin* equation [5, 6] written as

$$\sigma = 2 \left(\lambda - \frac{1}{\lambda^2} \right) \left(C_1 + \frac{C_2}{\lambda} \right) \tag{9.19}$$

which can be rearranged to give

$$\frac{\sigma}{2 \left(\lambda - \frac{1}{\lambda^2} \right)} = C_1 + \frac{C_2}{\lambda} \tag{9.20}$$

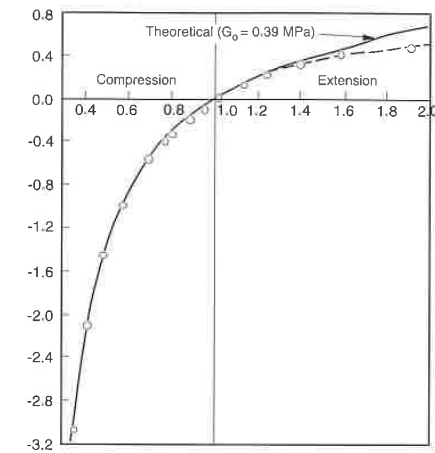


Figure 9.5 Experimental and theoretical stress-extension and compression curves for natural rubber.

A plot of $\sigma / 2(\lambda - 1/\lambda^2)$ versus $1/\lambda$ is usually referred to as a *Mooney plot* and should be linear with a slope of C_2 and an ordinate of $(C_1 + C_2)$ at $1/\lambda = 1$. A typical Mooney plot is presented in Fig. 9.6 [7] for a natural rubber with different formulations and times of vulcanization.

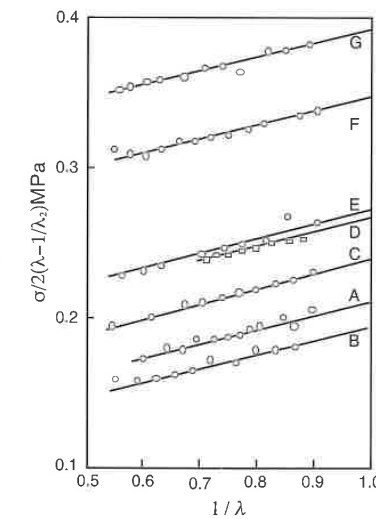


Figure 9.6 Mooney plots for rubber with various degrees of vulcanization.

The description of the various rubber formulations tested are presented in Table 9.1 [7]. It can be seen that C_2 shows little change, even with different rubber composition, and is approximately 0.1 Mpa. On the other hand, C_1 changes with degree of vulcanization and composition. A comparison between the Mooney-Rivlin model, the kinetic theory model, and experimental data for natural rubber is found in Fig. 9.4. For this material, the Mooney-Rivlin model represents the experimental data quite well up to extension ratios of 3.5.

Table 9.1 Compounding Details of the Vulcanizates Used by Gumbrell et al.^a

Mix	A	B	C	D	E	F	G
Rubber	100	100	100	100	100	100	100
Sulfur	3.0	3.0	3.0	3.0	3.25	4.0	4.0
Zinc oxide	5.0	5.0	5.0	5.0	5.0	5.0	5.0
Stearic acid	1.0	1.0	1.0	1.0	1.0	1.0	1.0
Benzthiazyl disulphide	0.5	0.5	0.5	0.75		1.0	0.5
Mercaptobenz-thiazyl-disulphide		0.5	0.5	0.25		0.3	
Zinc dimethyl dithiocarbamate				0.1		0.15	
Diphinyl guanidine					1.25		1.0
Antioxidant	1.0	1.0	1.0	1.0	1.0	1.0	1.0
Time of vulcanization at 141.5 °C (min)	45	10	30	20	60	10	12

^a Reference [7.]

Finally, it should be noted that the stiffness and strength of rubber is increased by filling with carbon black. The most common expression for describing the effect of carbon black content on the modulus of rubber was originally derived by Guth and Simha [8] for the viscosity of particle suspensions, and later used by Guth [9] to predict the modulus of filled polymers. The Guth equation can be written as

$$\frac{G_f}{G_0} = 1 + 2.5\phi + 14.1\phi^2 \quad (9.21)$$

where G_f is the shear modulus of the filled material and ϕ the volume fraction of particulate filler. The above expression is compared to experiments [10, 11] in Fig. 9.7.

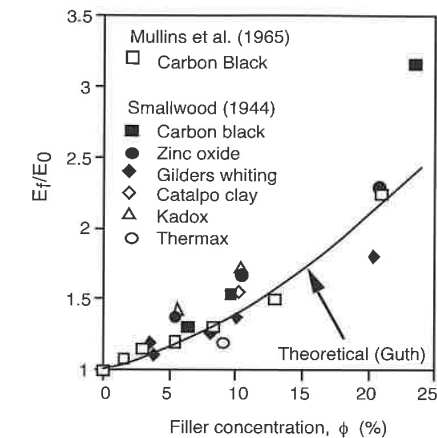


Figure 9.7 Effect of filler on modulus of natural rubber.

9.2.2 The Tensile Test and Thermoplastic Polymers

Of all the mechanical tests done on thermoplastic polymers, the tensile test is the least understood, and the results are often misinterpreted and misused. Since the test was inherited from other materials that have linear elastic stress-strain responses, it is often inappropriate for testing polymers. However, standardized tests such as DIN 53457 and ASTM D638 are available to evaluate the stress-strain behavior of polymeric materials.

The DIN 53457, for example, is performed at a constant elongational strain rate of 1% per minute, and the resulting data are used to determine the *short-term modulus*. The ASTM D638 test also uses one rate of deformation per material to measure the modulus; a slow speed for brittle materials and a fast speed for ductile ones. However, these tests do not reflect the actual rate of deformation experienced by the narrow portion of the test specimen, making it difficult to maintain a constant speed within the region of interest.

Extensive work was done by Knausenberger and Menges [12] where the rate of deformation of the test specimen is maintained constant. This is achieved by optically measuring the deformation on the specimen itself, as schematically demonstrated in Fig. 9.8 [12], and using that information as a feedback to control the elongational speed of the testing machine. The Knausenberger-Menges technique allows the testing engineer to measure the stress-strain response at various strain rates, where in each test the rate of deformation in the narrow section of the test specimen is accurately controlled. The resulting data can be used to determine the viscoelastic properties of

polymers ranging from impact to long-term responses. A typical test performed on PMMA at various strain rates at room temperature is shown in Fig. 9.9. The increased curvature in the results with slow elongational speeds suggests that stress relaxation plays a significant role during the test.

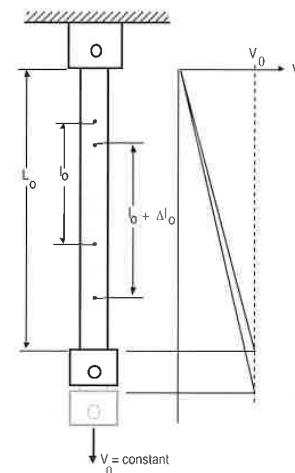


Figure 9.8 Flat tensile bar with velocity distribution.

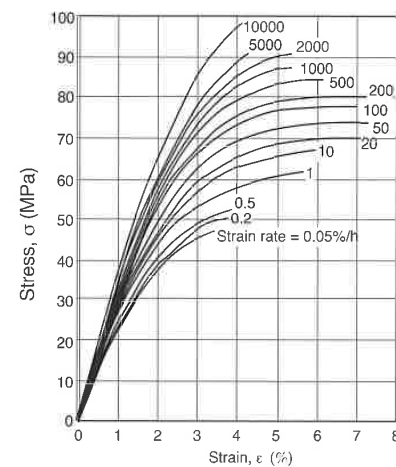


Figure 9.9 Stress-strain behavior of PMMA at various strain rates.

It can be shown that for small strains, or in linear viscoelasticity, the *secant modulus*, described by

$$E_s = \frac{\sigma}{\epsilon} \tag{9.22}$$

and the tangent modulus, defined by

$$E_t = \frac{d\sigma}{d\epsilon} \tag{9.23}$$

are independent of strain rate and are functions only of time and temperature. This is demonstrated in Fig. 9.10 [13]. The figure shows two stress-strain responses: one at a slow elongational strain rate, $\dot{\epsilon}_1$, and one at twice the speed, defined by $\dot{\epsilon}_2$. The tangent modulus at ϵ_1 in the curve with $\dot{\epsilon}_1$ is identical to the tangent modulus at ϵ_2 in the curve with $\dot{\epsilon}_2$, where ϵ_1 and ϵ_2 occurred at the same time. For small strains the tangent modulus, E_t , is identical to the relaxation modulus, E_r , measured with a stress relaxation test. This is important since the complex stress relaxation test can be replaced by the relatively simple short-term tensile test by plotting the tangent modulus versus time.

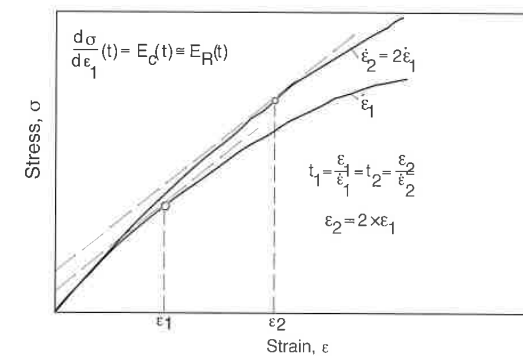


Figure 9.10 Schematic of the stress-strain behavior of a viscoelastic material at two rates of deformation.

Generic stress-strain curves and stiffness and compliance plots for amorphous and semi-crystalline thermoplastics are shown in Fig. 9.11 [14]. For amorphous thermoplastics one can usually approximate the stress-strain behavior in the curves of Fig. 9.11 by

$$\sigma(T, t) = E_0(T, t) (1 - D(T, t)\epsilon) \tag{9.24}$$

and in a short-term test a semi-crystalline polymer would behave more like

$$\sigma(T,t) = E_0(T,t) \frac{\varepsilon}{1 + D_2(T,t)\varepsilon} \quad (9.25)$$

where E_0 , D_1 and D_2 are time- and temperature-dependent material properties. However, below the glass transition temperature, the stress-strain curve of an amorphous polymer has a long and much steeper rise, with less relaxation effects, as shown in Fig. 9.10 and Eq. 9.24. In the stress-strain response of semi-crystalline polymers, on the other hand, the amorphous regions make themselves visible in long-term tensile tests. Hence, Eqs. 9.24 and 9.25 can be written in a more general form as

$$\sigma = E_0 \varepsilon \frac{1 - D_1 \varepsilon}{1 + D_2 \varepsilon} \quad (9.26)$$

The coefficients in Eq. 9.26 can be determined for various rates of deformation. For example, the curves in Fig. 9.12 [15] show the coefficient E_0 for an amorphous unplasticized PVC measured at various strain rates, $\dot{\varepsilon}$, and temperatures. The curves in the figure suggest that there is a direct relationship between temperature and strain rate or time. It can be seen that the curves, separated by equal temperature differences, are shifted from each other at equal distances, $\log(a_T)$, where

$$a_T = \frac{\dot{\varepsilon}_{ref}}{\dot{\varepsilon}} \quad (9.27)$$

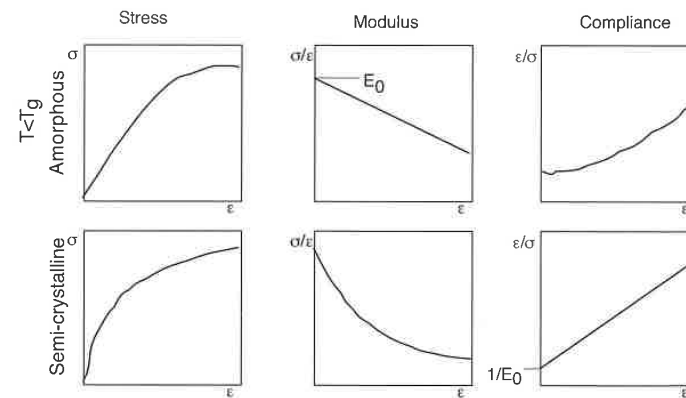


Figure 9.11 Schematic of the stress-strain response, modulus and compliance of amorphous and semi-crystalline thermoplastics at constant rates of deformation.

Since strain rate is directly related to time, one can make use of Arrhenius' relation between relaxation time, λ , and a reference relaxation time, λ_{ref} , stated by

$$\frac{\lambda}{\lambda_{ref}} = e^{-A/KT} \quad (9.28)$$

where A is the activation energy, T temperature and K a material property. The modified form of the Arrhenius equation for shifting the data can be written as

$$\log(a_T) = K \left(\frac{1}{T} - \frac{1}{T_{ref}} \right) \quad (9.29)$$

where T_{ref} is the reference temperature. The material constant K can be calculated by using data from Fig. 9.12, as shown in the sample graphical shift displayed in the figure. The coefficient K , which can be solved for by using

$$K = \frac{\log(\dot{\varepsilon}_{ref}/\dot{\varepsilon})}{1/T - 1/T_{ref}} \quad (9.30)$$

turns out to be 10,000 for the conditions shown in Fig. 9.12. This is true unless the test temperature is above the glass transition temperature, at which point the shift factor, a_T , and the coefficient K become functions of strain rate, as well as time and temperature. This is demonstrated for unplasticized PVC in Fig. 9.13 [15]. For the temperature range below T_g , displayed in Fig. 9.12, the data can easily be shifted, allowing the generation of a *master curve* at the reference temperature, T_{ref} . Figure 9.14 [15] shows such master curves for the three coefficients E_0 , D_1 and D_2 in Eq. 9.26 for the amorphous PVC shown in Figs. 9.12 and 9.13. For comparison, Fig. 9.15 [15] shows E_0 and D_2 for a high density polyethylene at 23 °C as a function of strain rate.

The values of E_0 , D_1 and D_2 can be easily calculated for each strain rate from the stress-strain diagram [16]. The modulus E_0 simply corresponds to the tangent modulus at small deformations where

$$\sigma \approx E_0 \varepsilon \quad (9.31)$$

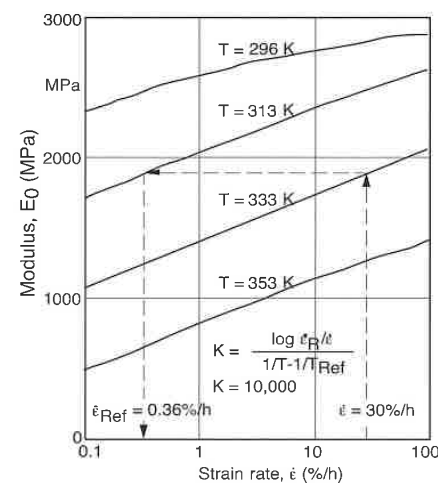


Figure 9.12 Plot of the elastic property E_0 and determining strain rate shift for an unplasticized PVC.

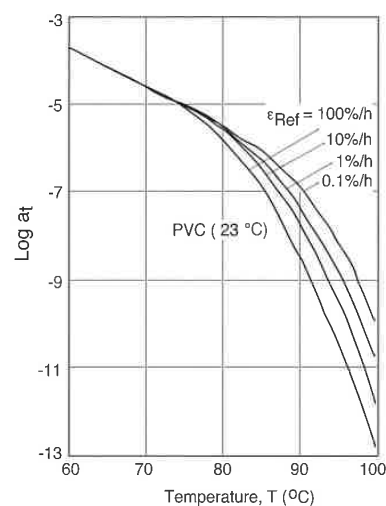


Figure 9.13 Time-temperature shift factor for an unplasticized PVC at several rates of deformation.

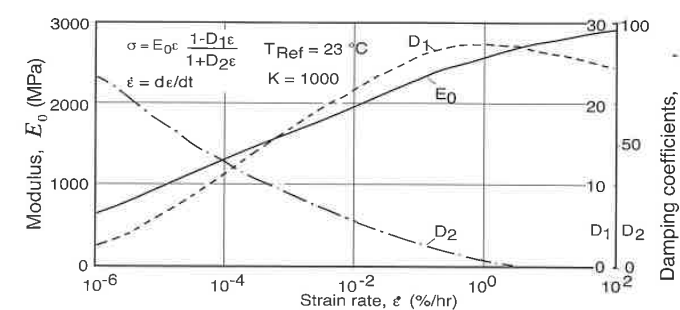


Figure 9.14 Master curves for E_0 , D_1 , and D_2 for an amorphous unplasticized PVC.

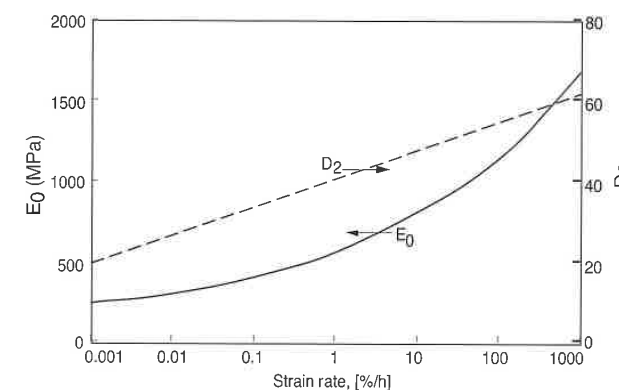


Figure 9.15 Coefficients E_0 and D_2 for a high density polyethylene at 23 °C.

Assuming that for amorphous thermoplastics $D_3 \approx 0$ when $T \ll T_g$ and for semi-crystalline thermoplastics $D_1 \approx 0$ when $T \gg T_g$ we can compute D_1 from

$$D_1 = \frac{\sigma_2 \epsilon_1 - \sigma_1 \epsilon_2}{\sigma_2 \epsilon_1^2 - \sigma_1 \epsilon_2^2} \text{ and } D_2 \text{ from } \quad (9.32)$$

$$D_2 = \frac{\sigma_1 \epsilon_2 - \sigma_2 \epsilon_1}{\epsilon_1 \epsilon_2 (\sigma_2 - \sigma_1)} \quad (9.33)$$

By introducing the values of E_0 , D_1 , and D_2 , plotted in Fig. 9.14, into Eq. 9.26 one can generate long-term behavior curves as shown in the isochronous plots

in Fig. 9.16 [15]. Here, the stress-strain behavior of unplasticized PVC is presented at constant times from 0.1 to 1000 hours of loading time. This is done by simply determining which strain rate results in a certain value of strain for a specific isochronous curve (time), then reading the values of E_0 , D_1 , and D_2 from the graphs and computing the corresponding stress using Eq. 9.26. When one uses this technique and furthermore applies the time-temperature superposition on short-term tests, one can approximate the long-term behavior of polymers which is usually measured using time consuming creep or relaxation tests.

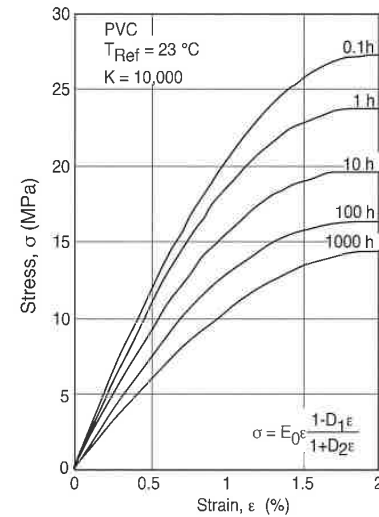


Figure 9.16 Isochronous stress-strain curves for an unplasticized PVC.

As a final note, similar to the effect of a rise in temperature, a solvent can increase the overall toughness of the material at the sacrifice of its strength and stiffness. This is shown in Fig. 9.17 [15] for a PVC plasticized with 10 and 20% dioctylphthalate (DOP). Figure 9.18 [15] shows the coefficients E_0 and D_2 for a PVC plasticized with 10 and 20% DOP. Figure 9.19 [15] demonstrates the similar effects of temperature and plasticizer.

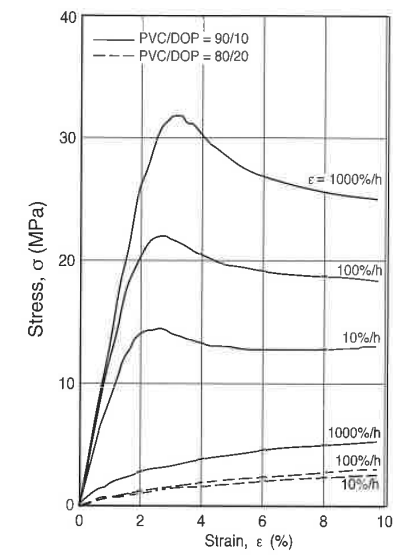


Figure 9.17 Stress-strain responses at various rates of deformation for a plasticized PVC with two plasticizer (DOP) concentrations.

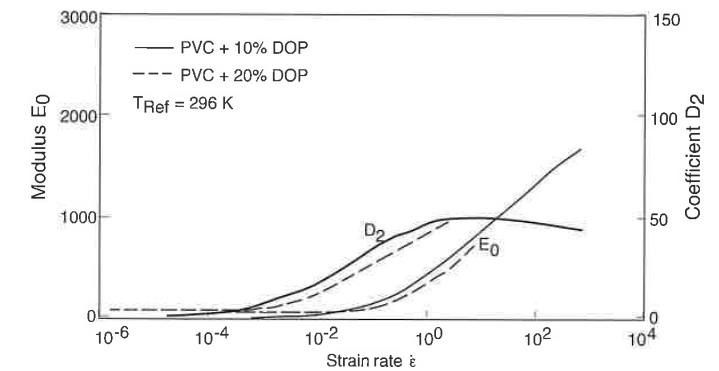


Figure 9.18 Coefficients E_0 and D_2 for polyvinyl chloride plasticized with 10% and 20% DOP.

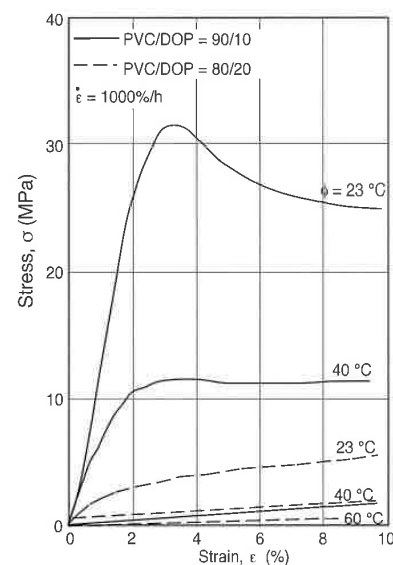


Figure 9.19 Stress-strain responses at various temperatures for a plasticized PVC with two plasticizer (DOP) concentrations.

9.3 Long-Term Tests

The stress relaxation and the creep test are well-known long-term tests. The stress relaxation test, discussed in Chapter 2, is difficult to perform and is therefore often approximated by data acquired through the more commonly used *creep test*. The stress relaxation of a polymer is often thought of as the inverse of creep.

The creep test, which can be performed either in shear, compression, or tension, measures the flow of a polymer component under a constant load. It is a common test that measures the strain, ϵ , as a function of stress, time, and temperature. Standard creep tests such as DIN 53 444 and ASTM D2990 can be used. Creep tests are performed at a constant temperature using a range of applied stress, as shown in Fig. 9.20 [17], where the creep responses of a polypropylene copolymer are presented for a range of stresses in a graph with a log scale for time. When plotting creep data in a log-log graph, in the majority of the cases, the creep curves reduce to straight lines as shown for polypropylene in Fig. 9.21 [1]. Hence, the creep behavior of most polymers can be approximated with a power-law model represented by

$$\epsilon(t) = M(\sigma, T)t^n \tag{9.34}$$

where M and n are material-dependent properties.

Similar to the stress relaxation test, the creep behavior of a polymer depends heavily on the material temperature during testing, having the highest rates of deformation around the glass transition temperature. This is demonstrated in Fig. 9.22 [18], which presents the creep compliance of plasticized PVC.

Creep data is very often presented in terms of creep modulus, E_c , defined by

$$E_c = \frac{\sigma_0}{\epsilon(t)} \tag{9.35}$$

Figure 9.23 [19] presents the creep modulus for various materials as a function of time.

Depending on the time scale of the experiment, a property that also varies considerably during testing is Poisson's ratio, ν . Figure 9.24 [14] shows Poisson's ratio for PMMA deformed at rates (%/h) between 10^{-2} (creep) and 10^3 (impact). The limits are $\nu = 0.5$ (fluid) for high temperatures or very slow deformation speeds and $\nu = 0.33$ (solid) at low temperatures or high deformation speeds.

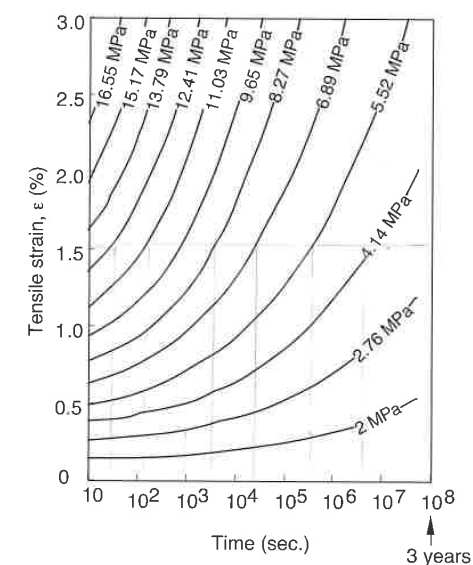


Figure 9.20 Creep response of a propylene-ethylene copolymer at 20 °C.

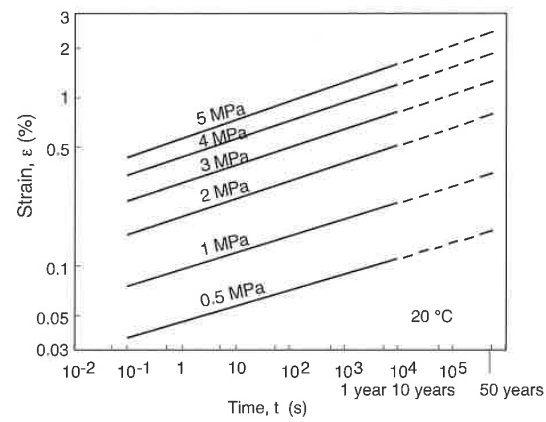


Figure 9.21 Creep response of a polypropylene plotted on a log-log scale.

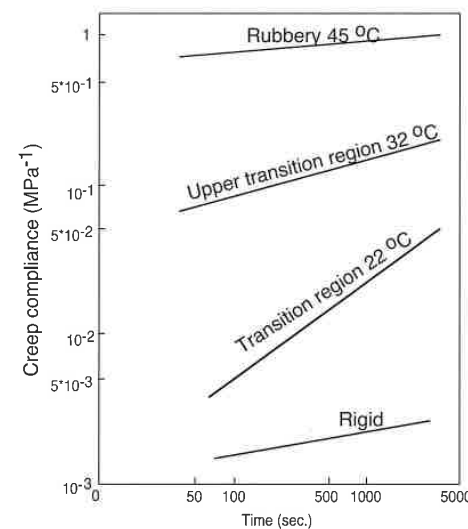


Figure 9.22 Creep compliance of a plasticized PVC at different temperatures.

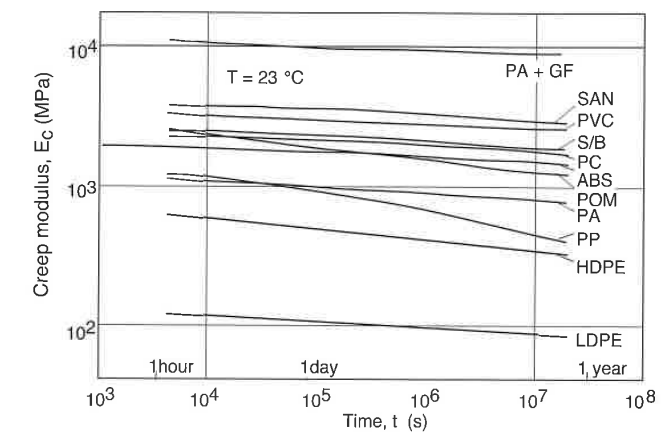


Figure 9.23 Time dependence of creep moduli for several polymer.

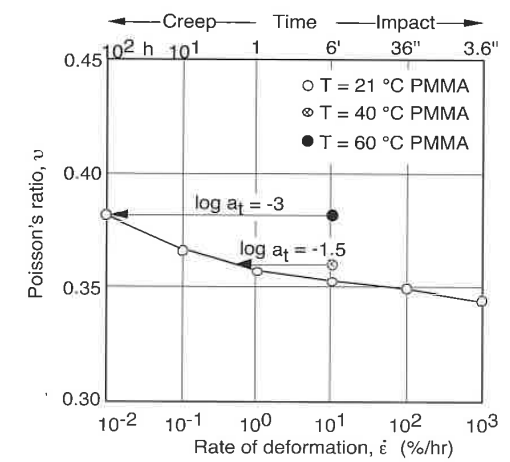


Figure 9.24 Poisson's ratio as a function of rate of deformation for PMMA at various temperatures.

9.3.1 Isochronous and Isometric Creep Plots

Typical creep test data, as shown in Fig. 9.20, can be manipulated to be displayed as short-term stress-strain tests or as stress relaxation tests. These manipulated creep-test-data curves are called *isochronous* and *isometric* graphs.

An isochronous plot of the creep data is generated by cutting sections through the creep curves at constant times and plotting the stress as a function of strain. The isochronous curves of the creep data displayed in Fig. 9.20 are presented in Fig. 9.25 [17]. Similar curves can also be generated by performing a series of *short creep tests*, where a specimen is loaded at a specific stress for a short period of time, typically around 100 s [20]. The load is then removed, and the specimen is allowed to relax for a period of 4 times greater than the time of the creep test. The specimen is then reloaded at a different stress, and the test is repeated until a sufficient number of points exists to plot an isochronous graph. This procedure is less time-consuming than the regular creep test and is often used to predict the short-term behavior of polymers. However, it should be pointed out that the short-term tests described in Section 9.2.2 are more accurate and are less time consuming and cheaper to perform.

The isometric or "equal size" plots of the creep data are generated by taking constant strain sections of the creep curves and by plotting the stress as a function of time. Isometric curves of the polypropylene creep data presented in Fig. 9.20 are shown in Fig. 9.26 [17]. This plot resembles the stress relaxation test results and is often used in the same manner. When we divide the stress axis by the strain, we can also plot the modulus versus time.

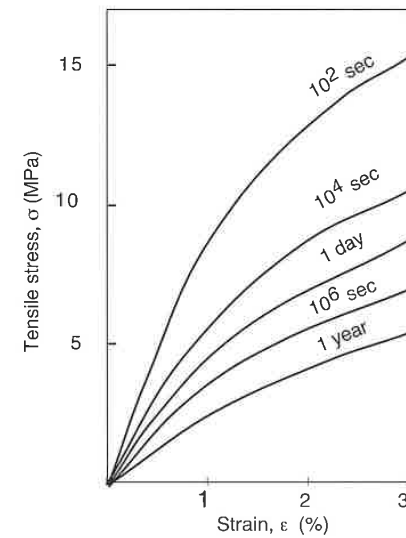


Figure 9.25 Isochronous stress-strain curves for the propylene-ethylene copolymer creep responses shown in Fig. 9.20.

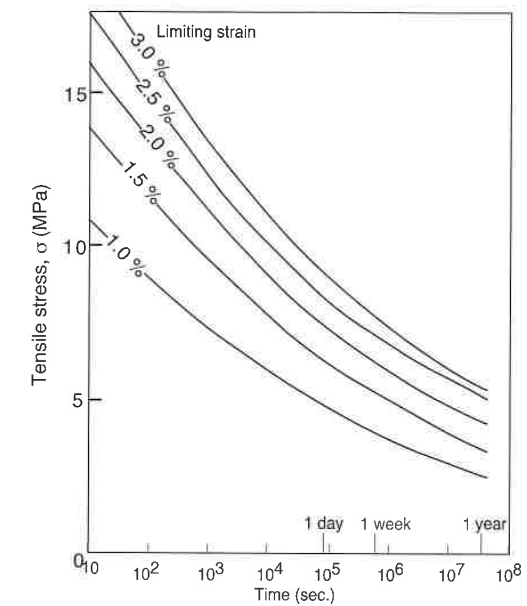


Figure 9.26 Isometric stress-time curves for the propylene-ethylene copolymer creep responses shown in Fig. 9.20.

9.4 Dynamic Mechanical Tests

9.4.1 Torsion Pendulum

The simplest dynamic mechanical test is the torsion pendulum. The standard procedure for the torsional pendulum, schematically shown in Fig. 9.27 [21], is described in DIN 53445 and ASTM D2236. The technique is applicable to virtually all plastics, through a wide range of temperatures; from the temperature of liquid nitrogen, -180°C to $50\text{--}80^{\circ}\text{C}$ above the glass transition temperature in amorphous thermoplastics and up to the melting temperature in semi-crystalline thermoplastics. With thermoset polymers one can apply torsional tests up to the degradation temperatures of the material.

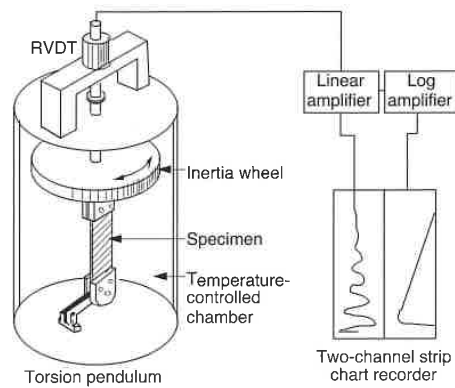


Figure 9.27 Schematic diagram of the torsion pendulum test equipment.

The torsion pendulum apparatus is made up of an inertia wheel, grips, and the specimen contained in a temperature-controlled chamber. The rectangular test specimen can be cut from a polymer sheet or part, or it can be made by injection molding. To execute the test the inertia wheel is deflected, then released and allowed to oscillate freely. The angular displacement or twist of the specimen is recorded over time. The frequency of the oscillations is directly related to the elastic shear modulus of the specimen, G' , and the decay of the amplitude is related to the damping or logarithmic decrement, Δ , of the material. The elastic shear modulus (Pascals) can be computed using the relation²

$$G' = \frac{6.4\pi^3 I L f^2}{\mu b t^3} \quad (9.36)$$

where I is the polar moment of inertia (g/cm^2), L the specimen length (cm), f the frequency (Hz), b the width of the specimen, t the thickness of the specimen, and μ a shape factor which depends on the width-to-thickness ratio. Typical values of μ are listed in Table 9.2 [18]. The logarithmic decrement can be computed using

$$\Delta = \ln \left(\frac{A_n}{A_{n+1}} \right) \quad (9.37)$$

where A_n represents the amplitude of the n th oscillation.³ Although the elastic shear modulus, G' , and the logarithmic decrement, Δ , are sufficient to characterize a material, one can also compute the loss modulus G'' by using

² For more detail, please consult ASTM D2236.

³ When $\Delta > 1$, a correction factor must be used to compute G' . See ASTM D2236.

$$G'' = \left(\frac{G' \Delta}{\pi} \right) \quad (9.38)$$

Table 9.2 Shape Factor μ for Various Rectangular Cross-Sections

Ratio of specimen width to thickness	μ
1.0	2.249
1.2	2.658
1.4	2.990
1.6	3.250
1.8	3.479
2.0	3.659
2.5	3.990
3.0	4.213
4.0	4.493
5.0	4.662
10.0	4.997
50.0	5.266
∞	5.333

The logarithmic decrement can also be written in terms of loss tangent, $\tan \delta$, where δ is the out-of-phase angle between the strain and stress responses. The loss tangent is defined as

$$\tan \delta = \frac{G''}{G'} = \frac{\Delta}{\pi} \quad (9.39)$$

Figures 9.28 [1] and 9.29 [1] show the elastic shear modulus and the loss tangent for high impact polystyrene, and various polypropylene grades, respectively. In the graph for high impact polystyrene, the glass transition temperatures for polystyrene at 120 °C and for butadiene at -50 °C, are visible. For the polypropylene grades, the glass transition temperatures and the melting temperatures can be seen. The vertical scale in plots such as Figs. 9.28 and 9.29 is usually a logarithmic scale. However, a linear scale better describes the mechanical behavior of polymers in design aspects. Figure 9.30 [1] presents the elastic shear modulus on a linear scale for several thermoplastic polymers as a function of temperature.

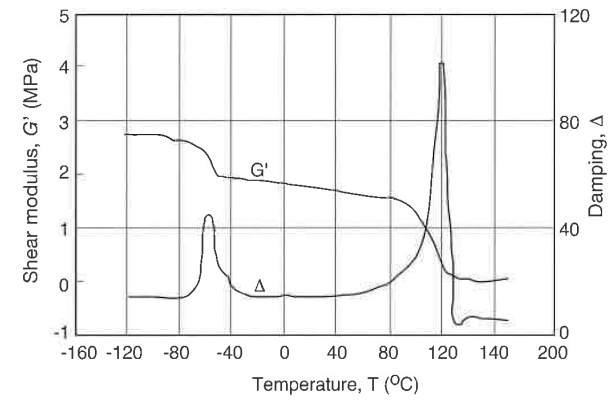


Figure 9.28 Elastic shear modulus and loss tangent for HIPS.

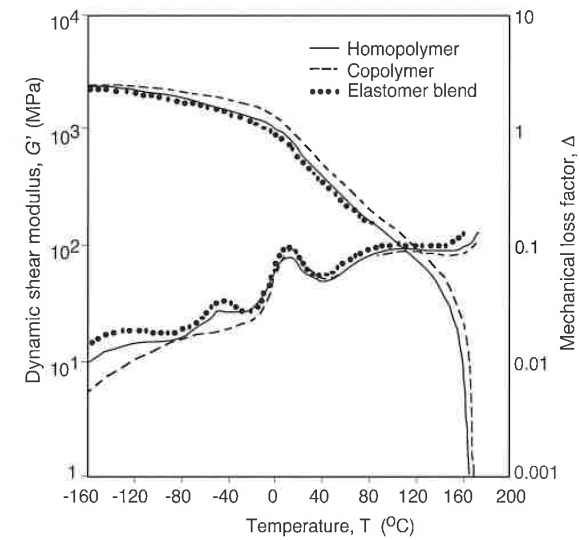


Figure 9.29 Elastic shear modulus and loss tangent for various polypropylene grades.

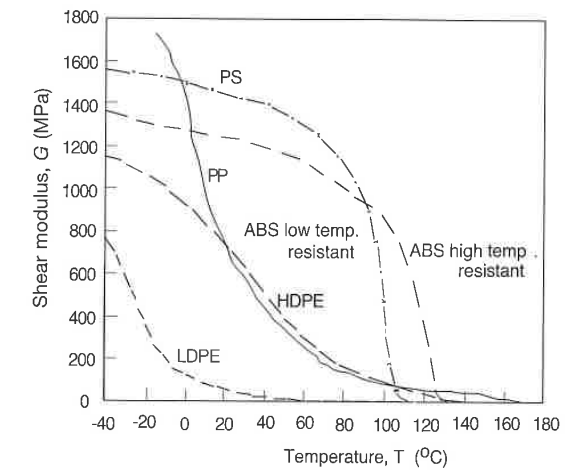


Figure 9.30 Elastic shear modulus for several thermoplastics.

9.4.2 Sinusoidal Oscillatory Test

In the sinusoidal oscillatory test, a specimen is excited with a low frequency stress input which is recorded along with the strain response. The shapes of the test specimen and the testing procedure vary significantly from test to test. The various tests and their corresponding specimens are described by ASTM D4065 and the terminology, such as the one already used in Eqs. 9.36–9.39, is described by ASTM D4092.

If the test specimen in a sinusoidal oscillatory test is perfectly elastic, the stress input and strain response would be as follows:

$$\tau(t) = \tau_0 \cos \omega t \quad (9.40)$$

$$\gamma(t) = \gamma_0 \cos \omega t \quad (9.41)$$

For an ideally viscous test specimen, the strain response would lag $\pi/2$ radians behind the stress input:

$$\tau(t) = \tau_0 \cos \omega t \quad (9.42)$$

$$\gamma(t) = \gamma_0 \cos \left(\omega t - \frac{\pi}{2} \right) \quad (9.43)$$

Polymers behave somewhere in between the perfectly elastic and the perfectly viscous materials and their response is described by

$$\tau(t) = \tau_0 \cos \omega t \quad \text{and} \quad (9.44)$$

$$\gamma(t) = \gamma_0 \cos(\omega t - \delta) \quad (9.45)$$

The shear modulus takes a complex form of

$$G^* = \frac{\tau(t)}{\gamma(t)} = \frac{\tau_0 e^{i\delta}}{\gamma_0} = \frac{\tau_0}{\gamma_0} (\cos \delta + i \sin \delta) = G' + G'' \quad (9.46)$$

which is graphically represented in Fig. 9.31. G' is usually referred to as *storage modulus* and G'' as *loss modulus*. The ratio of loss modulus to storage modulus is referred to as *loss tangent*:

$$\tan \delta = \frac{G''}{G'} \quad (9.47)$$

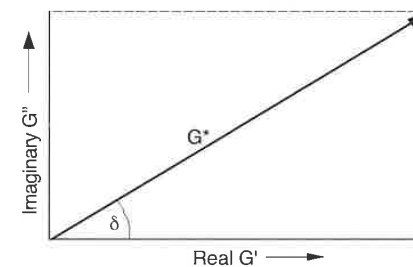


Figure 9.31 Vector representation of the complex shear modulus.

9.5 Viscoelastic Behavior of Polymers

Linear viscoelastic models were already introduced in Chapter 2. The main assumptions made in linear viscoelasticity is that the deformations must be small and that various loadings at different times are simply superimposed on one another as stated by *Boltzmann's superposition principle*. Several models exist to simulate the linear viscoelastic behavior of polymers. These physical models are generally composed of one or several elements such as dashpots, springs, or friction elements that represent viscous, elastic, or yielding properties,

respectively. All models must satisfy the momentum balance and continuity or deformation equation, along with the appropriate constitutive laws. The most commonly used constitutive equations are the viscous or *Newtonian model*, which is written as

$$\sigma = \eta \dot{\epsilon} \quad (9.48)$$

and the linear elastic or *Hookean model*, which is represented by

$$\sigma = E \epsilon \quad (9.49)$$

where η and E are the viscosity and Young's modulus, respectively.

9.5.1 Kelvin Model

The Kelvin model, sometimes also called the Kelvin-Voigt model, is shown in Fig. 9.32. It is the simplest model that can be used to represent the behavior of a solid polymer component at the beginning of loading.

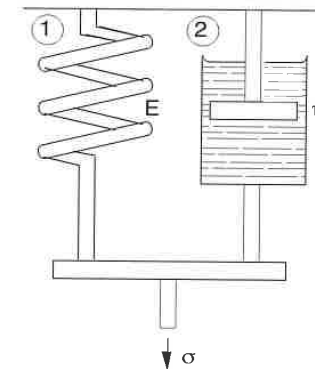


Figure 9.32 Schematic diagram of the Kelvin model.

The momentum balance for the Kelvin model is stated as

$$\sigma = \sigma_1 + \sigma_2 \quad (9.50)$$

and the continuity equation is represented by

$$\epsilon = \epsilon_1 = \epsilon_2 \quad (9.51)$$

Using Eq. 9.51 with the constitutive relations in Eqs. 9.48 and 9.49, the governing equation, Eq. 9.50, can be rewritten as

$$\sigma = E\varepsilon + \eta\dot{\varepsilon} \quad (9.52)$$

9.5.1.1 Kelvin Model Creep Response

Using Eq. 9.52, the strain in a creep test in the Kelvin model can be solved for as

$$\varepsilon(t) = \frac{\sigma_0}{E} (1 - e^{-t/\lambda}) \quad (9.53)$$

where λ , (E/η) , is the relaxation time. The creep modulus is defined as

$$E_c(t) = \frac{E}{(1 - e^{-t/\lambda})} \quad (9.54)$$

The creep response of the Kelvin model is shown in Fig. 9.33.

9.5.1.2 Kelvin Model Stress Relaxation

In the Kelvin model the stress does not relax and remains constant at

$$\sigma = E\varepsilon_0 \quad (9.55)$$

This is shown in Fig. 9.33.

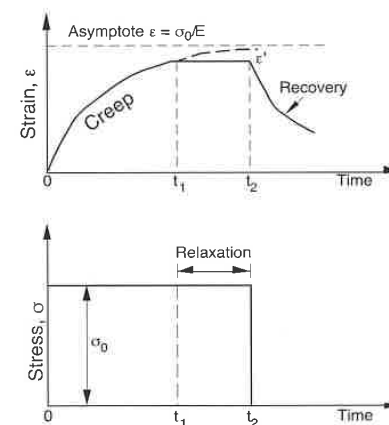


Figure 9.33 Creep, relaxation, and recovery response of the Kelvin model.

9.5.1.3 Kelvin Model Strain Recovery

Since the stresses do not relax in a Kelvin model, the full shape of the original component or specimen can be recovered. The strain recovery response can be written as

$$\varepsilon(t) = \varepsilon_0 e^{-t/\lambda} \quad (9.56)$$

and is represented in Fig. 9.33.

9.5.1.4 Kelvin Model Dynamic Response

We can also consider the response of a Kelvin model subjected to a sinusoidal strain given by

$$\varepsilon(t) = \varepsilon_0 \sin(\omega t) \quad (9.57)$$

where ε_0 is the strain amplitude and ω is the frequency. Differentiating Eq. 9.57 and substituting into Eq. 9.52 results in

$$\sigma(t) = E\varepsilon_0 \sin(\omega t) + \eta\omega\varepsilon_0 \cos(\omega t) \quad (9.58)$$

Dividing Eq. 9.58 by the strain amplitude results in the *complex modulus*, which is formed by the *storage modulus* defined by

$$E' = E \quad (9.59)$$

and the loss modulus given by

$$E'' = \eta\omega \quad (9.60)$$

9.5.2 Jeffrey Model

As shown in Fig. 9.34, the Jeffrey model is a Kelvin model with a dashpot. This extra feature adds the missing long-term creep to the Kelvin model.

The momentum balance of the Jeffrey model is represented by two equations as

$$\sigma = \sigma_3 \quad \text{and} \quad (9.61)$$

$$\sigma = \sigma_1 + \sigma_2 \quad (9.62)$$

as is the continuity equation by

$$\epsilon_1 = \epsilon_2 \quad \text{and} \quad (9.63)$$

$$\epsilon = \epsilon_2 + \epsilon_3 \quad (9.64)$$

Combining Eq. 9.61-9.64 and applying the constitutive equations gives

$$\sigma + \left(\frac{\eta_1 + \eta_3}{E_2} \right) \dot{\sigma} = \eta_3 \dot{\epsilon} + \left(\frac{\eta_3 \eta_1}{E_2} \right) \ddot{\epsilon} \quad (9.65)$$

which is sometimes written as

$$\sigma + \lambda_1 \dot{\sigma} = \eta_0 (\dot{\epsilon} + \lambda_2 \ddot{\epsilon}) \quad (9.66)$$

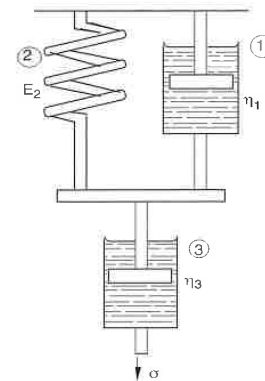


Figure 9.34 Schematic diagram of the Jeffrey model.

9.5.2.1 Jeffrey Model Creep Response

Using Eq. 9.66, the strain in a creep test in the Jeffrey model can be solved for as

$$\epsilon(t) = \frac{\sigma_0}{E} (1 - e^{-t/\lambda_2}) + \frac{\sigma_0}{\eta_0} t \quad (9.67)$$

and is depicted in Fig. 9.35. The creep modulus of the Jeffrey model is written as

$$E_c(t) = \left(\frac{(1 - e^{-t/\lambda_2})}{E} + \frac{t}{\eta_3} \right)^{-1} \quad (9.68)$$

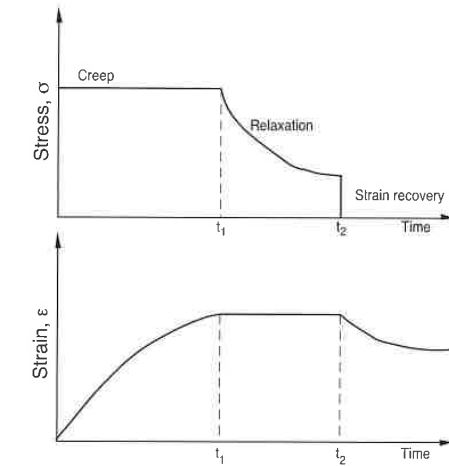


Figure 9.35 Creep, relaxation and recovery response of the Jeffrey model.

9.5.2.2 Jeffrey Model Stress Relaxation

The stress relaxation of the Jeffrey model is derived from the governing equation, Eq. 9.66 as

$$\sigma = \sigma_0 e^{-t/\lambda_1} \quad (9.69)$$

and is also represented in Fig. 9.35.

9.5.2.3 Jeffrey Model Strain Recovery

The unrelaxed stress is recovered in the same way as in the Kelvin model

$$\epsilon(t) = \epsilon_0 e^{-t/\lambda} \quad (9.70)$$

9.5.3 Standard Linear Solid Model

The standard linear solid model, shown in Fig. 9.36, is a commonly used model to simulate the short-term behavior of solid polymer components. The momentum balance of the standard linear solid model is expressed with two equations as

$$\sigma = \sigma_1 + \sigma_2 \quad (9.71)$$

and

$$\sigma_1 = \sigma_3 \tag{9.72}$$

Continuity or deformation is represented with

$$\varepsilon = \varepsilon_1 + \varepsilon_3 \tag{9.73}$$

and

$$\varepsilon = \varepsilon_2 \tag{9.74}$$

When we combine Eqs. 9.71-9.74 and use the constitutive equations for the spring and dashpot elements, we get the governing equation for the standard linear solid model:

$$\eta \dot{\sigma} + E_1 \sigma = \eta(E_1 + E_2) \dot{\varepsilon} + E_1 E_2 \varepsilon \tag{9.75}$$

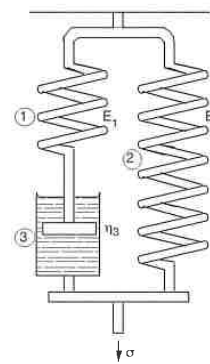


Figure 9.36 Schematic diagram of the standard linear solid model.

9.5.3.1 Standard Linear Solid Model Creep Response

Using Eq. 9.75, the strain in a creep test in the standard linear solid model can be solved for as

$$\varepsilon = \frac{\sigma_0}{E_2} + \left(\frac{\sigma_0}{E_1 + E_2} - \frac{\sigma_0}{E_2} \right) e^{-E_1 E_2 / \eta (E_1 + E_2) t} \tag{9.76}$$

and is plotted in Fig. 9.37.

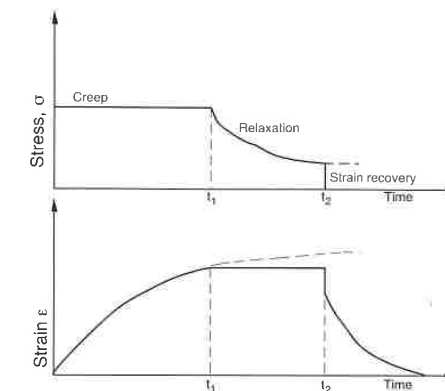


Figure 9.37 Creep, relaxation, and recovery response of the standard linear solid model.

9.5.3.2 Standard Linear Solid Model Stress Relaxation

The stress relaxation of the standard linear solid model can be derived by integrating Eq. 9.75 and is represented by

$$\sigma = \varepsilon_0 (E_2 + E_1) e^{-(E_1 / \eta) t} \tag{9.77}$$

9.5.4 Maxwell-Wiechert Model

The Maxwell-Wiechert model, shown in Fig. 9.38, is a generalized model which consists of an arbitrary number of Maxwell models connected in parallel.

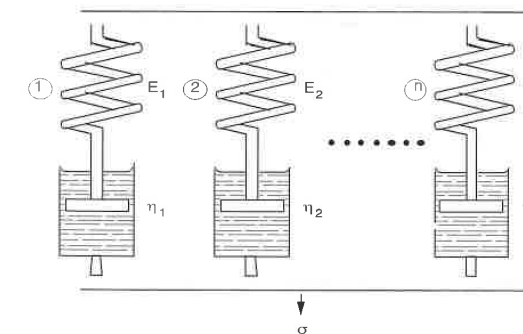


Figure 9.38 Schematic diagram of the Maxwell-Wiechert model.

The momentum balance in the i th Maxwell element of the Maxwell-Wiechert model is expressed as

$$\sigma_i = \sigma_{i1} + \sigma_{i2} \quad (9.78)$$

and the full momentum balance for a model with n elements is written as

$$\sigma = \sum_{i=1}^n \sigma_i \quad (9.79)$$

Continuity or deformation for the i th Maxwell element is expressed as

$$\varepsilon_i = \varepsilon_{i1} + \varepsilon_{i2} \quad (9.80)$$

and for the full model

$$\varepsilon = \varepsilon_1 = \varepsilon_2 = \varepsilon_i \dots \quad (9.81)$$

The governing equation for the Maxwell-Wiechert model is written as

$$\dot{\varepsilon} = \frac{\dot{\sigma}_i}{E_i} + \frac{\sigma_i}{\eta_i} \quad (9.82)$$

9.5.4.1 Maxwell-Wiechert Model Stress Relaxation

The stress relaxation of the Maxwell-Wiechert model can be derived by integrating Eq. 9.82 and substituting the resulting stress into Eq. 9.79. Dividing by the applied strain ε_0 results in an expression for the relaxation model which is written as

$$E(t) = \sum_{i=1}^n E_i e^{-(t/\lambda_i)} \quad (9.83)$$

which represents a model with n relaxation times and where $\lambda_i = \eta_i/E_i$. As an example, we can approximate the relaxation behavior of the polyisobutylene shown in Fig. 2.29 by using a Maxwell-Wiechert model having two Maxwell elements with $\lambda_1 = 10^{-8}$ h and $\lambda_2 = 100$ h, and $E_1 = 3 \times 10^9$ Pa and $E_2 = 10^6$ Pa. Figure 9.39 compares the experimental relaxation modulus with the model. One can see that although there are big differences between the two curves, the model, with its two relaxation times, does at least qualitatively represent the experimental values.

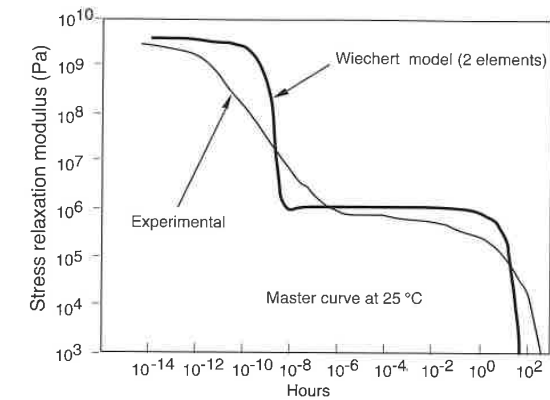


Figure 9.39 Comparison of the experimental stress relaxation for polyisobutylene to a two-component Maxwell-Wiechert model response.

9.5.4.2 Maxwell-Wiechert Model Dynamic Response

We can also consider the response of a Maxwell-Wiechert model subjected to a sinusoidal strain given by Eq. 9.57. In a similar analysis to that presented for the Kelvin model and for the Maxwell model in Chapter 2, the *storage modulus* is given by

$$E' = \sum_{i=1}^n \left(\frac{E_i (\omega \lambda_i)^2}{1 + (\omega \lambda_i)^2} \right) \quad (9.84)$$

and the viscous term or the *loss modulus*, is given by

$$E'' = \sum_{i=1}^n \left(\frac{E_i \omega \lambda_i}{1 + (\omega \lambda_i)^2} \right) \quad (9.85)$$

9.6 Effects of Structure and Composition on Mechanical Properties

The shear modulus versus temperature diagram is a very useful description of the mechanical behavior of certain materials. It is possible to generate a general shear modulus versus temperature diagram for all polymers by using a reduced temperature described by

$$T_{red} = \frac{293K}{T_g} \quad (9.86)$$

Fig. 9.40 [22] shows this diagram with the shear modulus of several polymers. The upper left side of the curve represents the stiff and brittle cross-linked materials, and the upper right side represents the semi-crystalline thermoplastics whose glass transition temperature is below room temperature. The lower right side of the curve represents elastomers, positioned accordingly on the curve depending on their degree of cross-linkage.

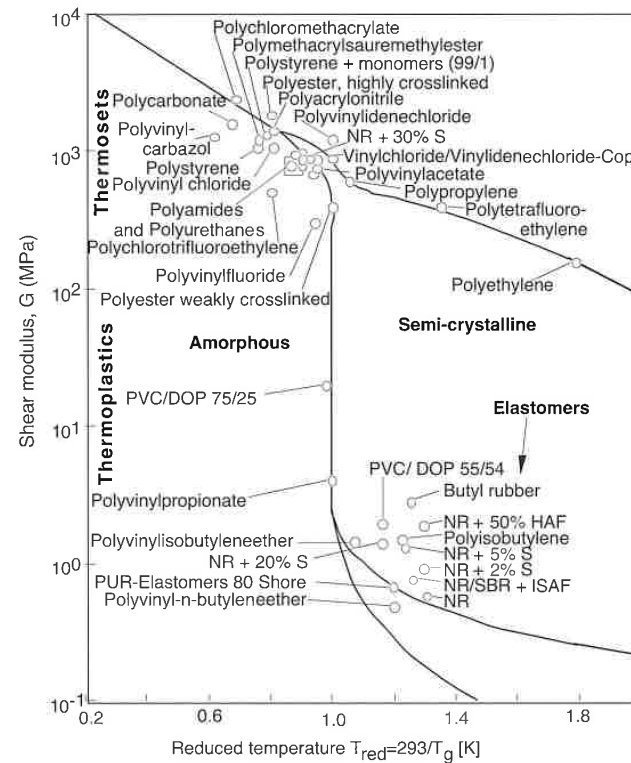


Figure 9.40 Shear modulus of several polymers as a function of reduced glass transition temperature.

9.6.1 Amorphous Thermoplastics

Amorphous thermoplastics exhibit "useful" behavior below their glass transition temperature. Figure 9.41 shows the shear modulus of an unplasticized PVC with respect to temperature. In this figure we observe that the material solidifies at the glass transition temperature, between 80 and 90 °C. We note that one cannot exactly pinpoint T_g but only a range within which it will occur. In fact, already at 60 °C the stiffness dramatically drops as the U-PVC starts to soften. Below -10 °C, the U-PVC becomes very stiff and brittle, making it useful only between -10 °C and 60 °C for most applications. As mentioned before, the properties of thermoplastics can be modified by adding plasticizing agents. This is shown for PVC in Fig. 9.42 where the shear modulus drops at much lower temperatures when a plasticizing agent is added.

Often the tensile stress and strain at failure are plotted as a function of temperature. Figure 9.43 shows this for a typical amorphous thermoplastic. The figure shows how the material is brittle below the glass transition temperature and, therefore, fails at low strains. As the temperature increases, the strength of the amorphous thermoplastic decreases, since it becomes leathery in texture and is able to withstand larger deformations. Above T_g , the strength decreases significantly, as the maximum strain continues to increase, until the flow properties have been reached at which point the mechanical strength is negligible. This occurs around the "flow temperature" marked as T_f in the diagram. If the temperature is further increased, the material will eventually thermally degrade at the degradation temperature, T_d .

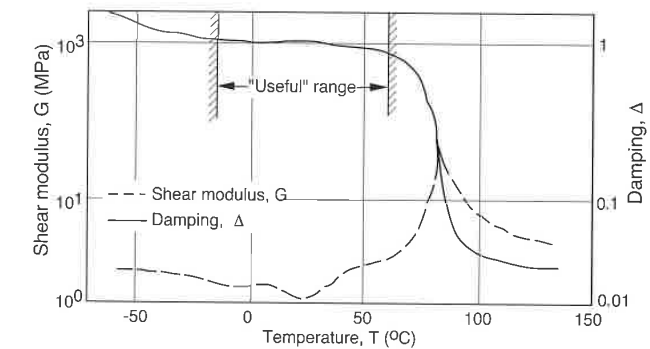


Figure 9.41 Shear modulus and mechanical damping for an unplasticized PVC.

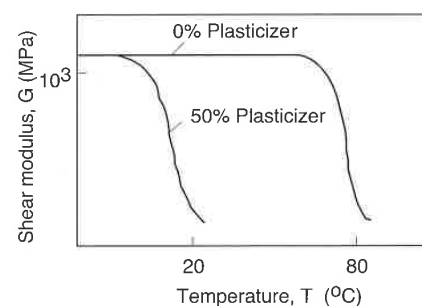


Figure 9.42 Shear modulus as a function of temperature for a PVC with and without a plasticizing agent.

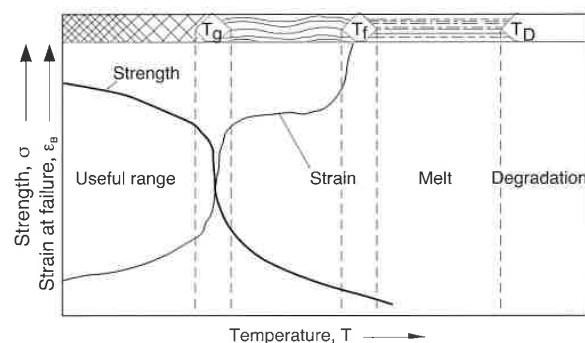


Figure 9.43 Tensile strength and strain at failure as a function of temperature for an amorphous thermoplastic.

Some amorphous thermoplastics can be made high impact resistant (less brittle) through copolymerization. The most common example is acrylonitrile-butadiene-styrene, also known as ABS. Since butadiene chains vitrify at temperatures below -50 °C, ABS is very tough at room temperature in contrast to polystyrene and acrylics by themselves. Due to the different glass transition temperatures present in the materials which form the blend, ABS shows two general transition regions, one around -50 °C and the other at 110 °C, visible in both the logarithmic decrement and the shear modulus.

9.6.2 Semi-Crystalline Thermoplastics

The properties of semi-crystalline thermoplastics can also be analyzed by plotting mechanical properties with respect to temperature. An interesting

example is shown in Fig. 9.44, which presents plots of shear modulus versus temperature of a polystyrene with different molecular structures after having gone through different stereo-specific polymerization techniques: low molecular weight PS (A), a high molecular weight PS (B), a semi-crystalline PS (C), and a cross-linked PS (D). In Fig. 9.44 we can see that the low molecular weight material flows before the high molecular weight one, simply due to the fact that the shorter chains can slide past each other more easily—reflected in the lower viscosity of the low molecular weight polymer. The semi-crystalline polystyrene is still brittle at room temperature, it is not very useful to the polymer industry. Figure 9.44 also demonstrates that a cross-linked polystyrene will not melt.

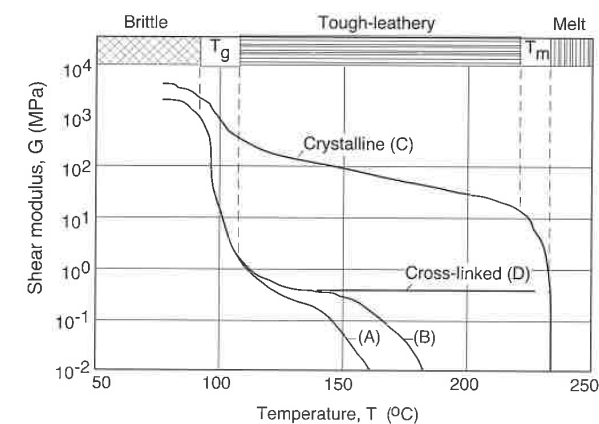


Figure 9.44 Shear modulus curves for amorphous, semi-crystalline and cross-linked polystyrene. (A) low molecular weight amorphous, (B) high molecular weight amorphous, (C) semi-crystalline, (D) cross-linked.

Semi-crystalline thermoplastics are leathery and tough at room temperature since their atactic and amorphous regions vitrify at much lower temperatures. Figure 9.45 shows the shear modulus plotted versus temperature for polypropylene at various degrees of crystallinity. In each case the amorphous regions “solidify” at around 0 °C, whereas the melting temperature goes up significantly with increasing degree of crystallinity. The brittle behavior of polypropylene at 0 °C can sometimes pose a problem in design. This problem can be mitigated through copolymerization— in this case PP copolymerized with ethylene or in elastomers such as ethylene-propylene-diene terpolymer (EPDM).

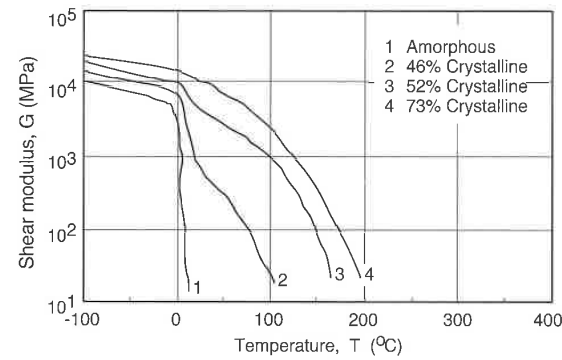


Figure 9.45 Shear modulus for polypropylene with various degrees of crystallinity.

The tensile stress and the strain at failure for a common semi-crystalline thermoplastic is shown in Fig. 9.46. The figure shows an increase in toughness between the glass transition temperature and the melting temperature. The range between T_g and T_m applies to most semi-crystalline thermoplastics.

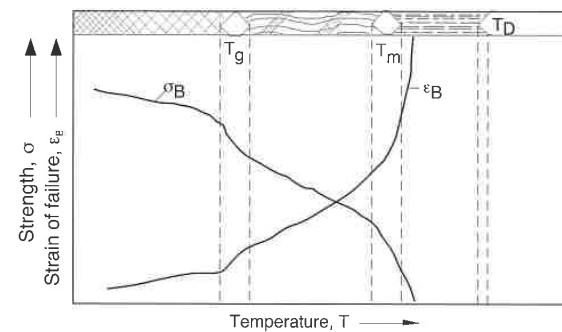


Figure 9.46 Tensile strength and strain at failure as a function of temperature for a semi-crystalline thermoplastic.

9.6.3 Oriented Thermoplastics

If a thermoplastic is deformed at a temperature high enough so that the polymer chains can slide past each other but low enough such that the relaxation time is much longer than the time it takes to stretch the material, then the orientation generated during stretching is retained within the polymer

component. We note that the amount of stretching, L/L_0 , is not always proportional to the degree of orientation within the component; for example, if the temperature is too high during stretching, the molecules may have a chance to fully relax, resulting in a component with little or no orientation. Any degree of orientation results in property variations within thermoplastic polymers. Figure 9.47 [23] shows the influence stretching has on various properties of common amorphous thermoplastics. The stretching will lead to decreased strength and stiffness properties perpendicular to the orientation and increased properties parallel to the direction of deformation. In addition, highly oriented materials tend to split along the orientation direction under small loads.

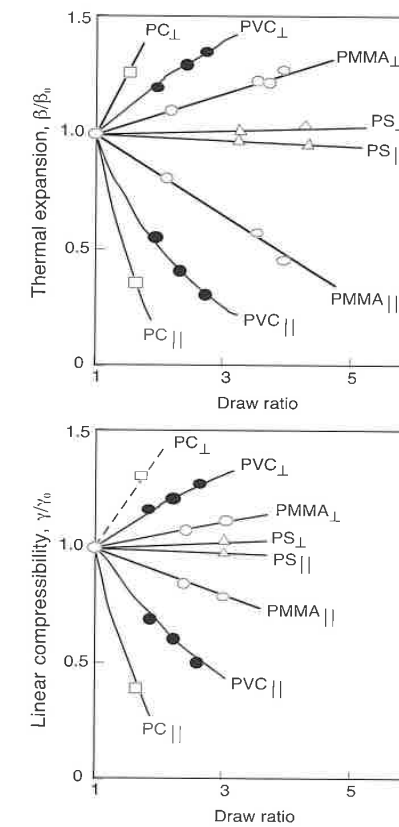


Figure 9.47 Influence of stretch on different properties of amorphous thermoplastics: (top) Thermal expansion, (bottom) Linear compressibility (continued).

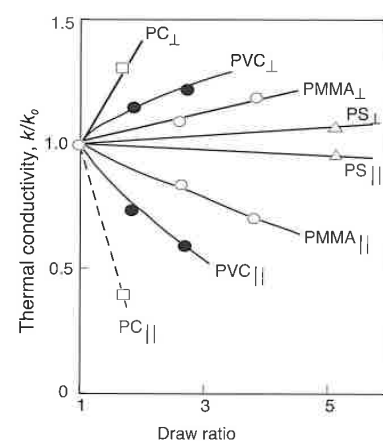


Figure 9.47 Influence of stretch on different properties of amorphous thermoplastics (continued): Thermal conductivity.

In amorphous thermoplastics the stretching that leads to permanent property changes occurs between 20 and 40 °C above the glass transition temperature, T_g , whereas with semi-crystalline thermoplastics they occur between 10 and 20 °C below the melting temperature, T_m . After having stretched a semi-crystalline polymer, one must anneal it at temperatures high enough that the amorphous regions relax. During stretching the spherulites break up as whole blocks of lamellae slide out, shown schematically in Fig. 9.48 [24]. Whole lamellae can also rotate such that by sufficiently high stretching, all molecules are oriented in the same direction. The lamellae blocks are now interconnected by what is generally called *tie molecules*. If this material is annealed in a fixed position, a very regular, oriented structure can be generated. This highly oriented material becomes dimensionally stable at elevated temperatures, including temperatures slightly below the annealing or fixing temperature. However, if the component is not fixed during the annealing process, the structure before stretching would be recovered. Figure 9.49 has stress-strain plots for polyethylene with various morphological structures. If the material is stretched such that a needle-like or fibrilic morphological structure results, the resulting stiffness of the material is very high. Obviously, a more realistic structure that would result from stretching would lead to a stacked platelike structure with lower stiffness and ultimate strength. An unstretched morphological structure would be composed of spherulites and exhibit much lower stiffness and ultimate strength. The strength of fibrilic structures is taken advantage of when making synthetic fibers. Figure 9.50 shows theoretical and achievable elastic moduli of various synthetic fiber materials.

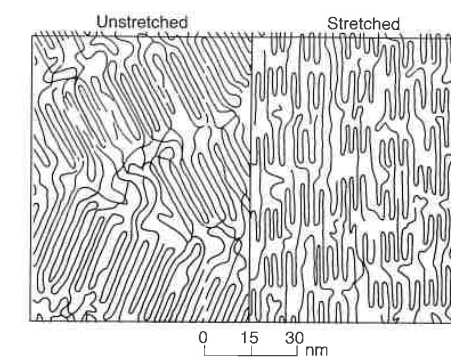


Figure 9.48 Schematic of the sliding and re-orientation of crystalline blocks in semi-crystalline thermoplastics.

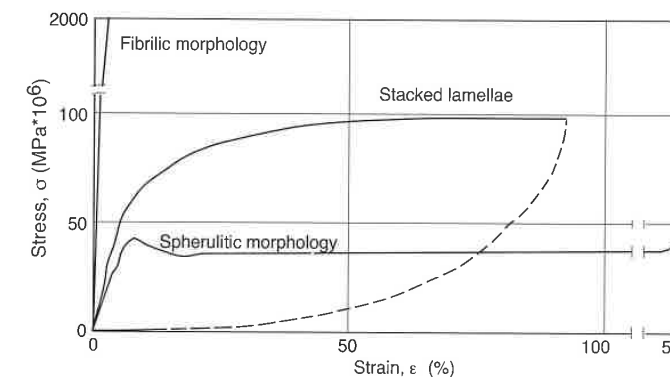


Figure 9.49 Stress-strain behavior of polyethylene with various morphologies.

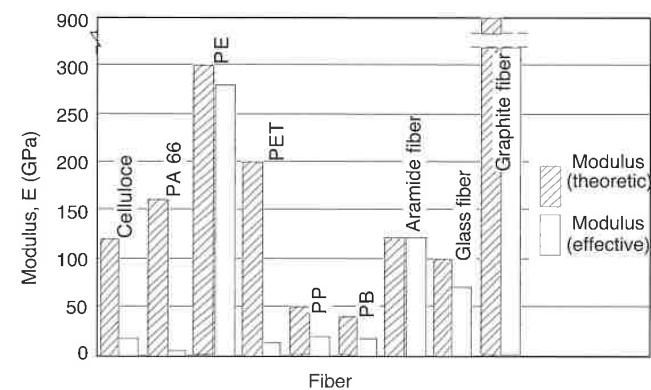


Figure 9.50 Tensile modulus for various fibers.

High-stiffness and high-strength synthetic fibers are becoming increasingly important for lightweight high-strength applications. Extended-chain ultra-high molecular weight polyethylene fibers have only been available commercially since the mid 1980s. The fibers are manufactured by drawing or extending fibers of small diameters at temperatures below the melting point. The modulus and strength of the fiber increase with the drawing ratio or stretch. Due to intermolecular entanglement, the natural draw ratio of high molecular weight high-density polyethylene is only 5⁴. To increase the draw ratio by a factor of 10 or 100, polyethylene must be processed in a solvent such as paraffin oil or paraffin wax.

Figure 9.51 [25] presents the tensile modulus of super-drawn ultra-high molecular weight high-density polyethylene fibers as a function of draw ratio. It can be seen that at draw ratios of 250, a maximum modulus of 200 GPa is reached. In addition to amorphous and semi-crystalline thermoplastics, there is a whole family of thermoplastic materials whose molecules do not relax and, thus, retain their orientation even in the melt state. This class of thermoplastics is the *liquid crystalline polymers*. One such material is the aramid fiber, most commonly known by its tradename, Kevlar®, which has been available in the market for several years. To demonstrate the structure of liquid crystalline polymers, successive enlargement of an aramid pellet is shown in Fig. 9.52 [26]. For comparison, Table 9.3 presents mechanical properties of aramid and polyethylene fibers and other materials.

⁴ It is interesting that a semi-crystalline thermoplastic stretches more at low molecular weights than at high molecular weights. This contradicts what we expect from theory that longer molecules allow the component to stretch following the relation $\lambda_{max} = M^{0.5}$. An explanation for this may be the *trapped entanglements* found in high molecular weight, semi-crystalline polymers that act as semi-permanent cross-links which rip at smaller deformations.

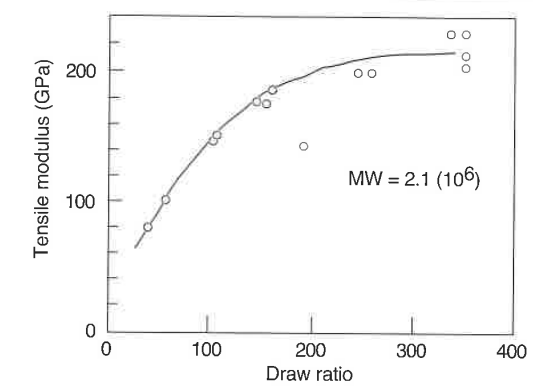


Figure 9.51 Tensile modulus as a function of draw ratio for a UHMWPE ($M_w \sim 2.1 \times 10^6$).

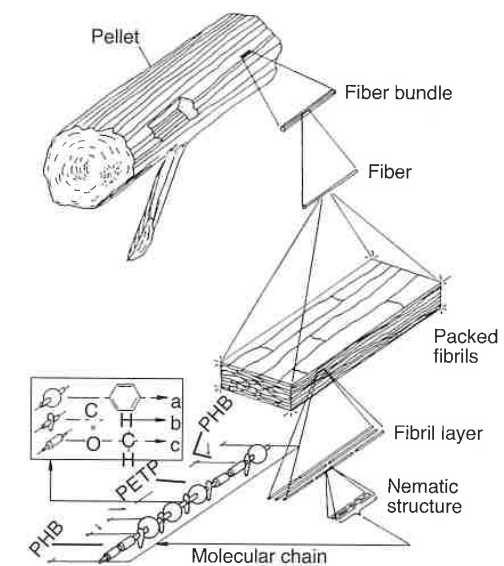


Figure 9.52 Schematic of the structure of a LC-PET.

Table 9.3 Mechanical Properties of Selected Fibers

Fiber	Tensile strength (MPa)	Tensile modulus (GPa)	Elongation to break (%)	Specific gravity
Polyethylene	3000	172	2.7	0.97
Aramid	2760	124	2.5	1.44
Graphite	2410	379	0.6	1.81
S-glass	4585	90	2.75	2.50

The anisotropy of the oriented material can be approximated by assuming that there are covalent bonds joining the molecular chains along the orientation direction, whereas only van der Waals forces act in the two directions perpendicular to the main orientation. With this so called 1:2 rule, we can write

$$a_{||} + 2a_{\perp} = 3a_0 \quad \text{and} \quad (9.87)$$

$$a_1 + 2a_2 = 3a_0 \quad (9.88)$$

where a_0 is the property for the isotropic material, $a_{||}$ and a_{\perp} are the values for the fully oriented material, and a_1 and a_2 are the values that correspond to the parallel and perpendicular directions with respect to the main orientation. The actual degree of orientation in the above analysis is unknown. The 1:2 rule can be applied to strength properties such as elastic modulus and Poisson's ratio as well as to thermal expansion coefficient and thermal diffusivity. For the elastic modulus, we can write

$$\frac{1}{E_{||}} + \frac{2}{E_{\perp}} = \frac{3}{E_0} \quad (9.89)$$

This rule can be used to approximate mechanical properties of synthetic fibers. For example, a polypropylene fiber will have a tensile elastic modulus of 700 MPa compared to an elastic modulus of 30 MPa for the isotropic material.

9.6.4 Cross-Linked Polymers

Cross-linked polymers, such as thermosets and elastomers, behave completely differently than their counterparts, thermoplastic polymers. In cross-linked systems, the mechanical behavior is also best reflected by the plot of the shear modulus versus temperature. Figure 9.53 compares the shear modulus between highly cross-linked, cross-linked, and uncross-linked polymers. The coarse cross-linked system, typical of elastomers, has a low modulus above the glass transition temperature. The glass transition temperature of these materials is

usually below -50°C , so they are soft and flexible at room temperature. On the other hand, highly cross-linked systems, typical in thermosets, show a smaller decrease in stiffness as the material is raised above the glass transition temperature; the decrease in properties becomes smaller as the degree of cross-linking increases. Figure 9.54 shows ultimate tensile strength and strain curves plotted versus temperature. It is clear that the strength remains fairly constant up to the thermal degradation temperature of the material.

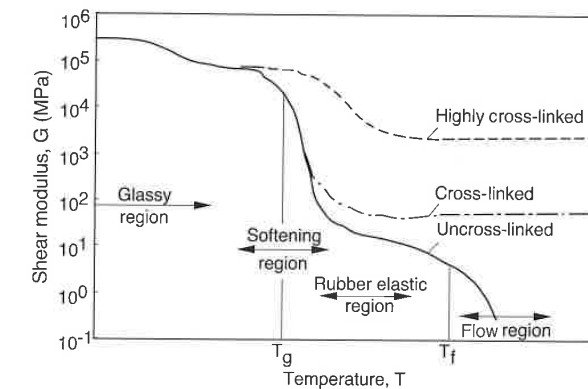


Figure 9.53 Shear modulus and behavior of cross-linked and uncross-linked polymers.

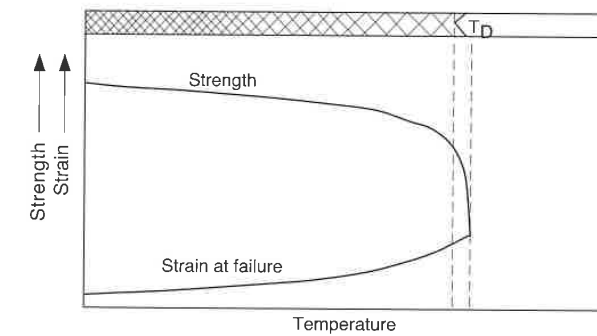


Figure 9.54 Tensile strength and strain at failure as a function of temperature for typical thermosets.

9.7 Mechanical Behavior of Filled and Reinforced Polymers

When we talk about fillers, we refer to materials that are intentionally placed in polymers to make them stronger, lighter, electrically conductive, or cheaper. Any filler will affect the mechanical behavior of a polymeric material. For example, long fibers will make it stiffer but usually denser, whereas foaming will make it more compliant but much lighter. On the other hand, a filler such as calcium carbonate will decrease the polymer's toughness while making it considerably cheaper. Figure 9.55 [27] shows a schematic plot of the change in stiffness as a function of volume fraction for several types of filler materials.

Figure 9.56 shows the increase in dynamic shear modulus for polybutylene terephthalate with 10 and 30% glass fiber content. However, fillers often decrease the strength properties of polymers— this is discussed in more detail in the next chapter.

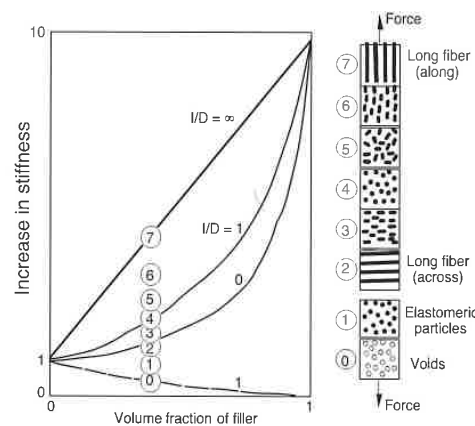


Figure 9.55 Relation between stiffness and filler type and orientation in polymeric materials.

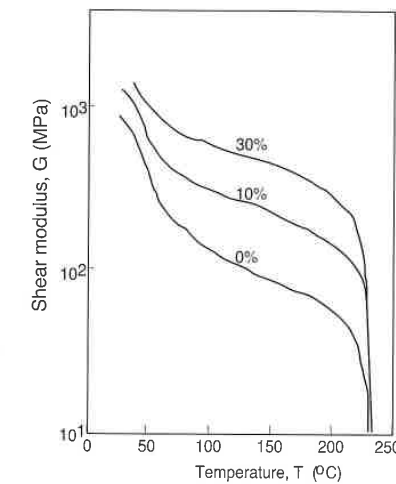


Figure 9.56 Shear modulus for a polybutylene terephthalate with various degrees of glass fiber content by weight.

However, when we refer to reinforced plastics, we talk about polymers (matrix) whose properties have been enhanced by introducing a reinforcement (fibers) of higher stiffness and strength. Such a material is usually called a *fiber reinforced polymer* (FRP) or a *fiber reinforced composite* (FRC). The purpose of introducing a fiber into a matrix is to transfer the load from the weaker material to the stronger one. This load transfer occurs over the length of the fiber as schematically represented in Fig. 9.57. The length it takes to complete the load transfer from the matrix to the fiber, without fiber or matrix fracture, is usually referred to as critical length, L_c . For the specific case where there is perfect adhesion between fiber and matrix, the critical length can be computed as

$$L_c = D \frac{\sigma_{ff}}{2\tau_{um}} \tag{9.90}$$

where D is the fiber diameter, σ_{ff} is the tensile strength of the fiber and τ_{um} is the shear strength of the matrix. Although Eq. 9.90 predicts L/D as low as 10, experimental evidence suggests that aspect ratios of 100 or higher are required to achieve maximum strength [28]. If composites have fibers that are shorter than their critical length they are referred to as *short fiber composites*, and if the fibers are longer they are referred to as *long fiber composites* [29].

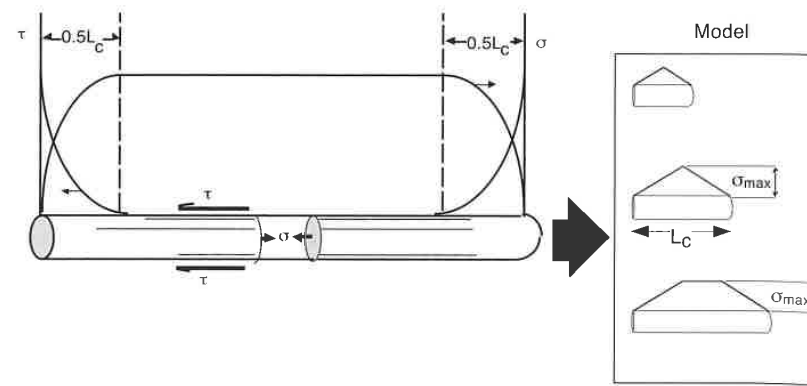


Figure 9.57 Schematic diagram of load transfer from matrix to fiber in a composite.

9.7.1 Anisotropic Strain-Stress Relation

As discussed in Chapter 6, filled polymers are often anisotropic, and the relations presented in Eqs. 9.1-9.15 are not valid. The three-dimensional anisotropic strain-stress relation where, for simplicity, x , y , and z have been replaced by 1, 2, and 3, respectively, is often written as

$$\epsilon_{11} = \frac{1}{E_{11}}\sigma_{11} - \frac{\nu_{21}}{E_{22}}\sigma_{22} - \frac{\nu_{31}}{E_{33}}\sigma_{33} \tag{9.91}$$

$$\epsilon_{22} = -\frac{\nu_{12}}{E_{11}}\sigma_{11} + \frac{1}{E_{22}}\sigma_{22} - \frac{\nu_{32}}{E_{33}}\sigma_{33} \tag{9.92}$$

$$\epsilon_{33} = -\frac{\nu_{13}}{E_{11}}\sigma_{11} - \frac{\nu_{23}}{E_{22}}\sigma_{22} + \frac{1}{E_{33}}\sigma_{33} \tag{9.93}$$

$$\gamma_{12} = \frac{1}{G_{12}}\tau_{12} \tag{9.94}$$

$$\gamma_{23} = \frac{1}{G_{23}}\tau_{23} \tag{9.95}$$

$$\gamma_{31} = \frac{1}{G_{31}}\tau_{31} \tag{9.96}$$

and in matrix form for the more general case:

$$\begin{Bmatrix} \epsilon_{11} \\ \epsilon_{22} \\ \epsilon_{33} \\ \gamma_{12} \\ \gamma_{23} \\ \gamma_{31} \end{Bmatrix} = \begin{bmatrix} S_{11} & S_{12} & S_{13} & S_{14} & S_{15} & S_{16} \\ S_{21} & S_{22} & S_{23} & S_{24} & S_{25} & S_{26} \\ S_{31} & S_{32} & S_{33} & S_{34} & S_{35} & S_{36} \\ S_{41} & S_{42} & S_{43} & S_{44} & S_{45} & S_{46} \\ S_{51} & S_{52} & S_{53} & S_{54} & S_{55} & S_{56} \\ S_{61} & S_{62} & S_{63} & S_{64} & S_{65} & S_{66} \end{bmatrix} \begin{Bmatrix} \sigma_{11} \\ \sigma_{22} \\ \sigma_{33} \\ \tau_{12} \\ \tau_{23} \\ \tau_{31} \end{Bmatrix} \tag{9.97}$$

where coupling between the shear terms and the elongational terms can be introduced.

9.7.2 Aligned Fiber Reinforced Composite Laminates

The most often applied form of the above equations is the two-dimensional model used to analyze the behavior of aligned fiber reinforced laminates, such as that shown schematically in Fig. 9.58. For this simplified case, Eqs. 9.91-9.96 reduce to

$$\epsilon_L = \frac{1}{E_L}\sigma_L - \frac{\nu_{TL}}{E_T}\sigma_T \tag{9.98}$$

$$\epsilon_T = -\frac{\nu_{LT}}{E_L}\sigma_L + \frac{1}{E_T}\sigma_T \tag{9.99}$$

$$\gamma_{LT} = \frac{1}{G_{LT}}\tau_{LT} \tag{9.100}$$

which can also be written as

$$\{\epsilon_{LT}\} = [S_{LT}]\{\sigma_{LT}\} \tag{9.101}$$

where the subscripts L and T define the longitudinal and transverse directions, respectively, as described in Fig. 9.58, and $[S_{LT}]$ is referred to as the compliance matrix.

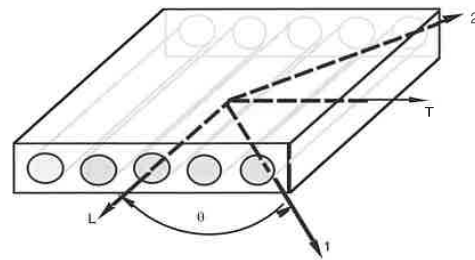


Figure 9.58 Schematic diagram of unidirectional continuous fiber reinforced laminated structure.

The longitudinal and transverse properties can be calculated using the widely used Halpin-Tsai model [30] as

$$E_L = E_m \left(\frac{1 + \xi \eta \phi}{1 - \eta \phi} \right) \quad (9.102)$$

$$E_T = E_m \left(\frac{1 + \eta \phi}{1 - \eta \phi} \right) \quad (9.103)$$

$$G_{LT} = G_m \left(\frac{1 + \lambda \phi}{1 - \lambda \phi} \right) = G_m \frac{v_{LT}}{v_m} \quad (9.104)$$

where

$$\eta = \frac{\left(\frac{E_f}{E_m} - 1 \right)}{\left(\frac{E_f}{E_m} + \xi \right)} \quad (9.105)$$

$$\lambda = \frac{\left(\frac{G_f}{G_m} - 1 \right)}{\left(\frac{G_f}{G_m} + 1 \right)} \quad (9.106)$$

$$\xi = 2 \left(\frac{L}{D} \right) \quad (9.107)$$

Here, the subscripts *t* and *m* represent the fiber and matrix, respectively; *L* the fiber length; *D* the fiber diameter; ϕ the volume fiber fraction which can be expressed in terms of weight fraction, ψ , as

$$\phi = \frac{\psi}{\psi + (1 + \psi)(\rho_f / \rho_m)} \quad (9.108)$$

It should be pointed out that, in addition to the Halpin-Tsai model, there are several other models in use today to predict the elastic properties of aligned fiber reinforced laminates [31, 33]. Most models predict the longitudinal modulus quite accurately as shown in Fig. 9.59 [31], which compares measured values to computed values using the *mixing rule*. This comes as no surprise, since experimental evidence clearly shows that longitudinal modulus is directly proportional to the fiber content for composites with unidirectional reinforcement. However, differences do exist between the models when predicting the transverse modulus, as shown in Fig. 9.60 [31].

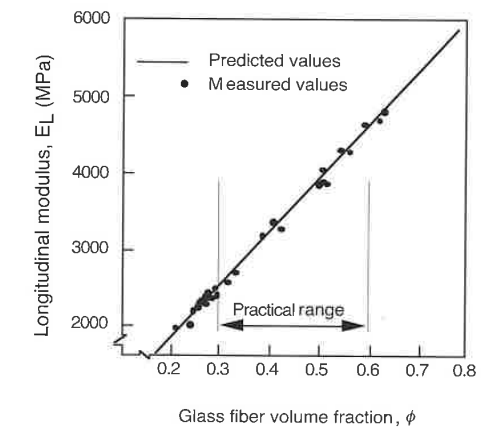


Figure 9.59 Measured and predicted longitudinal modulus for an unsaturated polyester/aligned glass fiber composite laminate as a function of volume fraction of glass content.

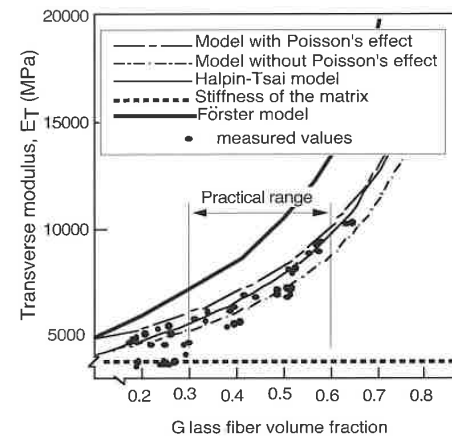


Figure 9.60 Measured and predicted transverse modulus for an unsaturated polyester/aligned glass fiber composite laminate as a function of volume fraction of glass content.

9.7.3 Transformation of Fiber Reinforced Composite Laminate Properties

The loading in a laminated structure is not always aligned with the transverse and longitudinal directions of the reinforcement. Hence, it is often necessary to rotate the laminate and its properties by an angle θ . Figure 9.58 depicts the laminate's material coordinate system L-T and a rotated arbitrary coordinate system 1-2. If we rotate the axes from the 1-2 system to the L-T system, we can transform the stress components using

$$\begin{Bmatrix} \sigma_L \\ \sigma_T \\ \tau_{LT} \end{Bmatrix} = \begin{bmatrix} c^2 & s^2 & 2sc \\ s^2 & c^2 & -2sc \\ -sc & sc & (c^2 - s^2) \end{bmatrix} \begin{Bmatrix} \sigma_{11} \\ \sigma_{22} \\ \tau_{12} \end{Bmatrix} \quad \text{or} \quad (9.109)$$

$$\{\sigma_{LT}\} = [T_\sigma] \{\sigma_{12}\} \quad (9.110)$$

The transformation of the strain components carry an extra 1/2 term for the shear strains and is written as

$$\begin{Bmatrix} \epsilon_L \\ \epsilon_T \\ \gamma_{LT} \end{Bmatrix} = \begin{bmatrix} c^2 & s^2 & sc \\ s^2 & c^2 & -sc \\ -2sc & 2sc & (c^2 - s^2) \end{bmatrix} \begin{Bmatrix} \epsilon_{11} \\ \epsilon_{22} \\ \gamma_{12} \end{Bmatrix} \quad \text{or} \quad (9.111)$$

$$\{\epsilon_{LT}\} = [T_\epsilon] \{\epsilon_{12}\} \quad (9.112)$$

Combining Eq. 9.101 with the above transformations, we can write

$$[T_\epsilon] \{\epsilon_{12}\} = [S_{LT}] [T_\sigma] \{\sigma_{12}\} \quad (9.113)$$

or

$$\{\epsilon_{12}\} = [T_\epsilon]^{-1} [S_{LT}] [T_\sigma] \{\sigma_{12}\} \quad (9.114)$$

The compliance matrix in the L-T coordinate system has four independent components and the 1-2 system has six. The inverse of $[T_\epsilon]$ is equivalent to rotating the coordinates back by $-\theta$. This leads to

$$\begin{Bmatrix} S_{11} \\ S_{22} \\ S_{12} \\ S_{44} \\ S_{14} \\ S_{24} \end{Bmatrix} = \begin{bmatrix} c^4 & s^4 & 2c^2s^2 & c^2s^2 \\ s^4 & c^4 & 2s^2c^2 & c^2s^2 \\ c^2s^2 & c^2s^2 & (c^4 + s^4) & -c^2s^2 \\ 4c^2s^2 & 4c^2s^2 & -8c^2s^2 & (c^2 - s^2)^2 \\ 2c^3s & -2cs^3 & 2(cs^3 - c^3s) & (cs^3 - c^3s) \\ 2cs^3 & -2c^3s & 2(c^3s - cs^3) & (c^3s - cs^3) \end{bmatrix} \begin{Bmatrix} S_{LL} \\ S_{TT} \\ S_{LT} \\ S_{SS} \end{Bmatrix} \quad (9.115)$$

or

$$\{S_{12}\} = [R(\theta)] \{S_{LT}\} \quad (9.116)$$

The engineering elastic constants in the 1-2 system can easily be computed:

$$E_{11} = \frac{1}{S_{11}} \quad (9.117)$$

$$E_{22} = \frac{1}{S_{22}} \quad (9.118)$$

$$G_{12} = \frac{1}{S_{44}} \quad (9.119)$$

$$\nu_{12} = -\frac{S_{12}}{S_{11}} \quad (9.120)$$

$$\nu_{21} = -\frac{S_{12}}{S_{22}} \quad (9.121)$$

$$\eta_{14} = \frac{S_{14}}{S_{11}} \quad (9.122)$$

$$\eta_{24} = \frac{S_{24}}{S_{22}} \quad (9.123)$$

$$\eta_{41} = \frac{S_{41}}{S_{44}} \quad (9.124)$$

$$\eta_{42} = \frac{S_{42}}{S_{44}} \quad (9.125)$$

Figure 9.61 [33] shows how the stiffness decreases as one rotates away from the longitudinal axis for an aligned fiber reinforced composite with different volume fraction fiber content. From the figure it is evident that for high volume fraction fiber contents only a slight misalignment of the fibers from the loading direction results in a drastic reduction of the properties. Along with the predicted stiffness properties, the figure also presents the stiffness for a composite with 0.56 volume fraction of fibers measured at various angles from the longitudinal axis of the composite. The measured and the predicted values agree quite well.

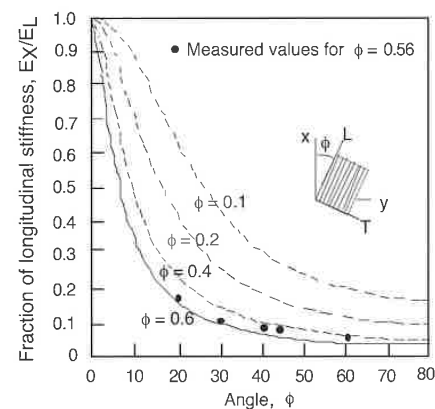


Figure 9.61 Measured and predicted elastic modulus in a unidirectional fiber reinforced laminate as a function of angle between loading and fiber direction.

9.7.4 Reinforced Composite Laminates with a Fiber Orientation Distribution Function

The above transformation can be used to compute the properties of planar systems with a fiber orientation distribution function. This is done by superposing aligned fiber laminates rotated away from the principal 1-2 coordinate system by an angle θ and with a volume fiber fraction given by $\psi(\theta)$. The transformation is written as

$$\{S_{12}\} = \int_{-\pi/2}^{\pi/2} \{R(\theta)\} \{S_{LT}\} \psi(\theta) d\theta \quad (9.126)$$

which can be written in discrete terms to be used with fiber orientation distribution function attained from computer simulation:

$$\{S_{12}\} = \sum_{i=1}^N \{R(\theta_i)\} \{S_{LT}\} \psi(\theta_i) \Delta\theta \quad (9.127)$$

Using Eq. 9.126, one can easily predict the stiffness properties of a part with randomly oriented fibers, where $\psi(\theta) = 1/\pi$, using⁵

$$\frac{1}{E_{11}} = \frac{1}{E_{22}} = \frac{1}{E_{\text{random}}} = \frac{3}{8} \frac{1}{E_L} + \frac{3}{8} \frac{1}{E_T} - \frac{2}{8} \frac{v_{LT}}{E_L} + \frac{1}{8} \frac{1}{G_{LT}} \quad (9.128)$$

9.8 Strength Stability Under Heat

As mentioned earlier, polymers soften and eventually flow as they are heated. It is, therefore, important to know what the limiting temperatures are at which a polymer component can still be loaded with moderate deformations. Three tests are commonly performed on polymer specimens to determine this limiting temperature for that material. They are the *Vicat temperature test* (DIN 53460), shown in Fig. 9.62, the *Martens temperature test* (DIN 53458 or 53462), and the *heat-distortion temperature (HDT) test* (ASTM D 648-72) shown in Fig. 9.63⁶.

⁵ The incorrect expression $E_{\text{random}} = 3/8 E_L + 5/8 E_T$ is often successfully used, for low fiber content, to approximate the stiffness of the composite with randomly oriented fibers. However, using this equation for composites with large differences between E_L and E_T , the stiffness can be overestimated by 50%.

⁶ Courtesy of BASF.

In the Vicat temperature test, a needle loaded with weights is pushed against a plastic specimen inside a glycol bath. This is shown schematically in Fig. 9.62. The uniformly heated glycol bath rises in temperature during the test. The *Vicat number* or Vicat temperature is measured when the needle has penetrated the polymer by 1 mm. The advantage of this test method is that the test results are not influenced by the part geometry or manufacturing technique. The practical limit for thermoplastics, such that the finished part does not deform under its own weight, lies around 15 K below the Vicat temperature.

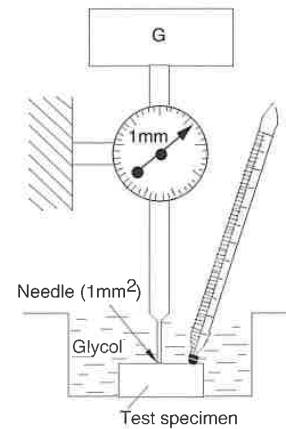


Figure 9.62 Apparatus to determine a material's shape stability under heat [BASF] using the Vicat temperature test.

To determine the heat distortion temperature, the standard specimen lies in a fluid bath on two knife edges separated by a 10 cm distance. A bending force is applied on the center of the specimen. Similar to the Vicat temperature test, the bath's temperature is increased during the test. The HDT is the temperature at which the rod has bent 0.2 mm to 0.3 mm (see Fig. 9.63). The Vicat temperature is relatively independent of the shape and type of part, whereas the heat-distortion-data are influenced by the shaping and pretreatment of the test sample. Table 9.4 shows the heat distortion temperature for selected thermoplastics measured using ASTM D648.

In the Martens temperature test, the temperature at which a cantilevered beam has bent 6 mm is recorded. The test sample is placed in a convection oven with a constantly rising temperature. In Europe, the HDT test has replaced the *Martens temperature test*.

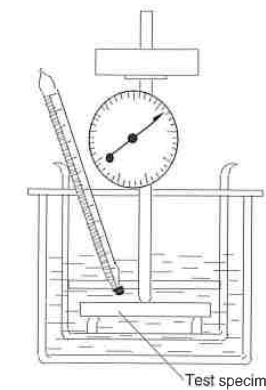


Figure 9.63 Apparatus to determine a material's shape stability under heat using the heat-distortion-temperature test (HDT).

It is important to point out that these test methods do not give enough information to determine the allowable operating temperature of molded plastic components subjected to a stress. Heat distortion data is excellent when comparing the performance of different materials and should only be used as a reference not as a direct design criterion.

Table 9.4 Heat Distorsion Temperature for Selected Thermoplastics

Material	HDT (°C) 1.86 MPa	0.45 MPa
HDPE	50	50
PP	45	120
uPVC	60	82
PMMA	60	100
PA66	105	200
PC	130	145

Examples

- 9.1 A loaded high-density polyethylene component is not to exceed 4% strain after 60 days of loading at room temperature. Using the short term data presented in Fig. 9.64 estimate the maximum allowable stress within the component.

Figure 9.64 presents constants E_0 and D_2 as a function of rate of the deformation $\dot{\epsilon}$. The time given in this design is 60 days (1440 h) and the strain is 4%. Therefore the average rate of deformation is $4\%/1440\text{h} = 0.0028\%/h$. At that rate, we read $E_0 = 250\text{MPa}$ and $D_2 = 28$. We can now use Eq. 9.25 to compute the allowable stress

$$\sigma = \frac{E_0 \epsilon}{1 + D_2 \epsilon} = \frac{250\text{MPa}(0.04)}{1 + 28(0.04)} = 4.72\text{MPa}$$

It should be noted that the prescribed strain of 4% is quite high. As a rule of thumb, a component that is subjected to a long term load should not have strains larger than 2%, to avoid creep rupture. Hence, if we reduce our allowable strain to 2%, the rate of deformation during the 60 days should be $\dot{\epsilon} = 2\%/1440\text{h} = 0.0014\%/h$. At the new rate we read $E_0 = 245\text{MPa}$ and $D_2 = 26$ from Fig. 9.64. Using the new constants, the maximum allowable stress for a 2% strain in 60 days is 3.22 MPa.

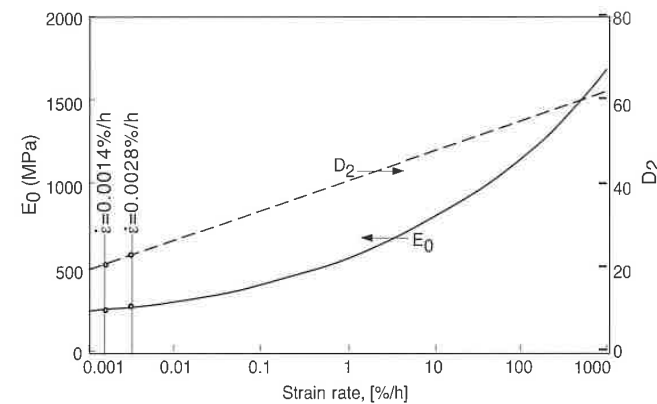


Figure 9.64 Coefficients for PE-HD short term data

9.2 In a special laboratory experiment, a PMMA pipe is used to cap a tank that is pressurized at 2 MPa, as shown in Fig. 9.65. The 3 mm thick pipe has a 50 mm internal diameter and is 300 mm long. Estimate the diameter change of the pipe after one year of testing? Use the creep data given below [34].

To solve this problem we can use the thin pressure vessel approximation, working with an average diameter, $\bar{D} = 53\text{mm}$. This is a

case of biaxial stress, composed of a hoop stress, σ_H , and an axial stress, σ_A , defined by

$$\sigma_H = \frac{p\bar{D}}{2h} = 17.67\text{ MPa} \text{ and } \sigma_A = \frac{p\bar{D}}{4h} = 8.83\text{ MPa}$$

where, p is the pressure and h is the thickness. These stresses are constant and will cause the pipe to creep. Using the PMMA creep data we can generate a 1 year isochronous curve, which is presented in Fig.9.67. The strains that correspond to stresses of 17.67 MPa and 8.83 MPa are $\epsilon_H = 1.32\%$ and $\epsilon_A = 0.6\%$, respectively. Since this is a biaxial case we must correct the hoop strain using Poisson's effect, before computing the diameter change. For this we use

$$\epsilon'_H = \epsilon_H - \nu\epsilon_A$$

However, since we were not given Poisson's ration, ν , we assume a value of $1/3$. Thus,

$$\epsilon'_H = 1.32 - (1/3)0.6 = 1.12\%$$

To compute the diameter change we use

$$\epsilon'_H = \Delta D / D$$

Hence,

$$\Delta D = (53\text{mm})(0.0112) = 0.594\text{mm}$$

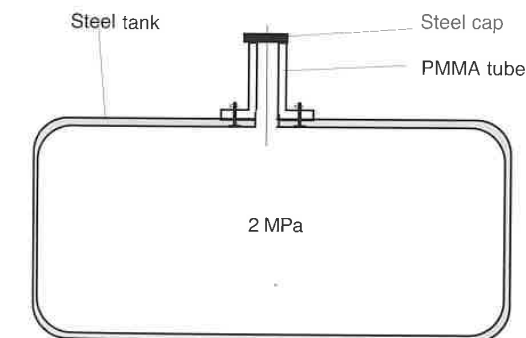


Figure 9.65 Schematic of the apparatus described in Example 9.2.

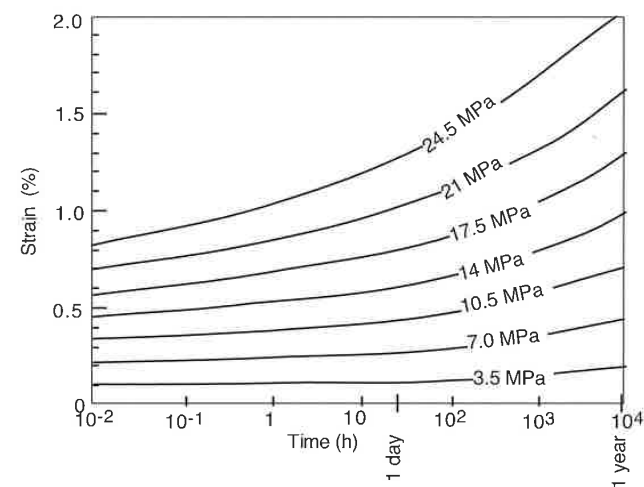


Figure 9.66 PMMA creep data.

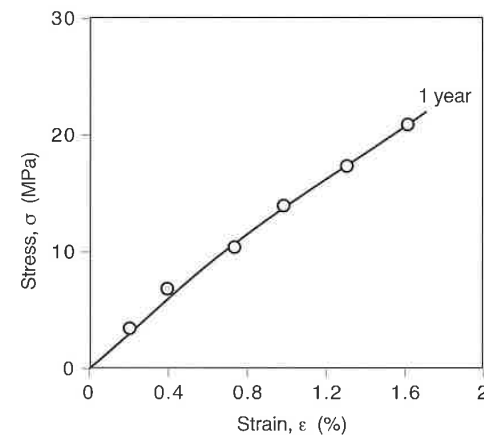


Figure 9.67 A 1 year isochronous curve for PMMA.

9.3 In the assembly shown in Fig. 9.68, a tubular polypropylene feature is pressed on a 15 mm long metal stud. The inner diameter of the 1 mm thick PP tubular element is 10 mm. The metal stud is slightly oversized with a diameter of 10.15 mm. With a coefficient of friction $\mu=0.3$ estimate the force required to disassemble the parts shortly after assembly, and after one year. Use the creep data given in Fig. 9.69.

This is a classic constant strain, ϵ_0 , stress relaxation problem. The initial hoop stress that holds the assembly together can be quite high. However, as time passes the hoop stress relaxes and it becomes easier to disassemble the two components. The strain in the system after assembly is computed using

$$\epsilon_0 = \frac{\Delta D}{D} = \frac{0.16 \text{ mm}}{11 \text{ mm}} = 0.0145 \rightarrow 1.45\%$$

In order to follow the hoop stress history after assembly we generate a 1.45% isometric curve, which is shown below (Fig. 9.70).

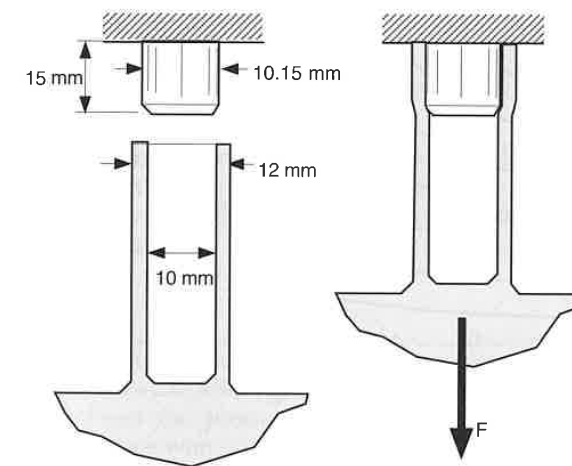


Figure 9.68 Assembly for Example 9.3.

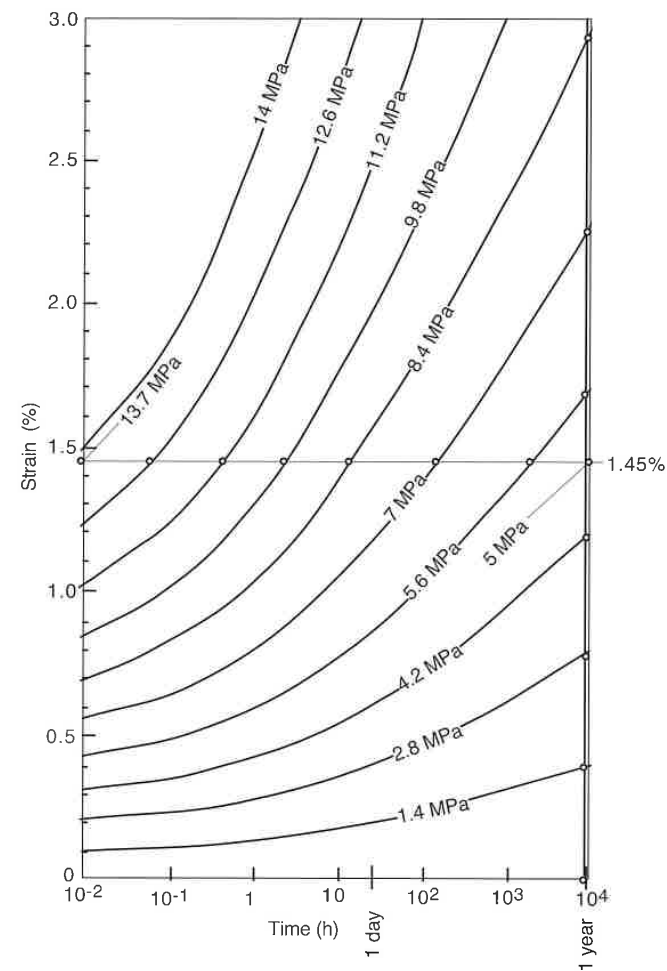


Figure 9.69 PP creep data.

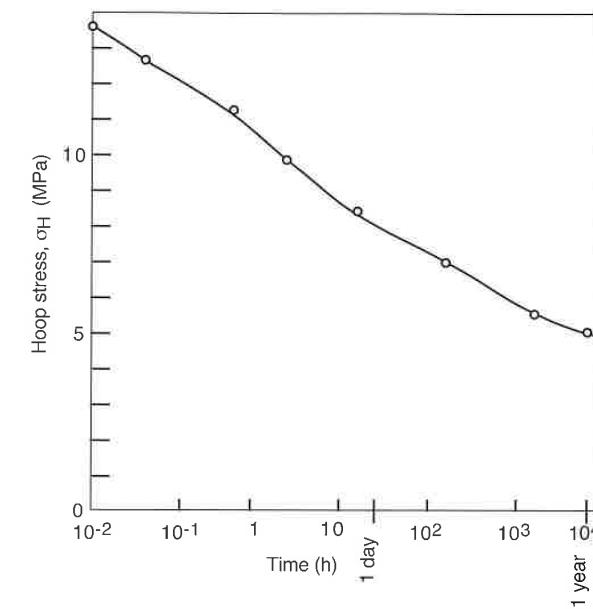


Figure 9.70 Isochronous curve for PP at 1.45% strain.

From the isochronous curve we can deduce that the hoop stress, σ_H , is 13.7 MPa shortly after assembly and about 5 MPa one year after assembly. The pressure acting on the metal stud, due to the hoop stress, can be computed using

$$p = \frac{2h\sigma_H}{D}$$

which gives $p = 2.49$ MPa right after assembly and $p = 0.91$ MPa after one year. From the pressure and the friction we can calculate the disassembly force with

$$F = \mu p(\pi D, L)$$

where $L = 15$ mm is the length of the stud. Using the above equation, the computed force necessary to pull the two components apart is 358 N (80 lb) after assembly and 130 N (29 lb) after one year.

9.4 You are asked to design a polypropylene bracket of circular cross-section, as depicted in Fig. 9.71, to hold a 10 N load for a one year period. The maximum strain you would like the bracket to feel is 2%. Calculate the diameter of the bracket using the PP creep data given in Example 9.3.

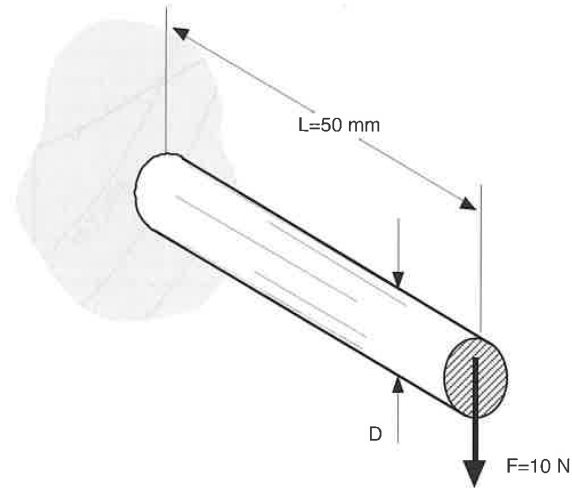


Figure 9.71 Cantilevered bracket of circular cross-section.

In this design, the instant the bracket is loaded it will begin to creep. Since the life of the system is designed to be one year, with a maximum strain of 2%, we will work with a 1 year isochronous curve (Fig. 9.72), generated using Fig. 9.69.

From the isochronous curve we find that 6.5 MPa is the stress that corresponds to a 2% strain. In a cantilevered beam the maximum stresses occur in the upper (tensile) and lower (compressive) points where the bracket joins the wall. For a cantilevered system we use

$$\sigma = \frac{Mc}{I}, \text{ where } \begin{cases} c = D/2 \\ M = FL \\ I = \frac{\pi D^4}{64} \end{cases}$$

Hence, we can solve for D using

$$D = \sqrt[3]{\frac{32FL}{\pi\sigma}} = \sqrt[3]{\frac{32(10\text{N})(0.05\text{m})}{\pi(6.5 \times 10^6\text{Pa})}} = 9.2\text{mm}$$

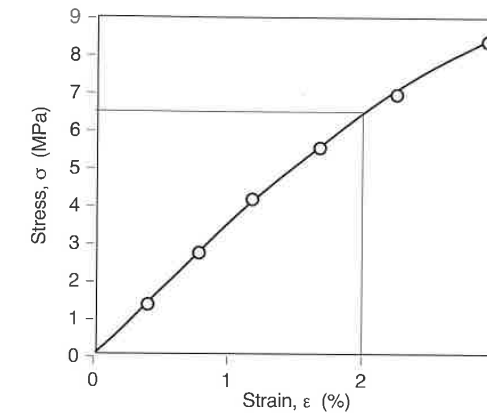


Figure 9.72 A 1 year isochronous curve for PP.

At this point it is important to mention that this design has many flaws. First a solid cross-section such as this will result in a long cycle time during manufacturing due to the slow cooling. In addition, thick cross-sections result in large amounts of shrinkage, especially with a semi-crystalline material such as polypropylene. Finally, the bending strength of a solid circular cross-section is only a fraction (lower than 20%) of the bending strength that an I-beam could deliver. This means that by changing the cross-sectional geometry of the beam, we would only need 20% or less of the material required for the present design.

Problems

9.1 Using the coefficients E_0 and D_2 for the high-density polyethylene presented in Fig. 9.73 compute the stress for 0%, 2%, 4%, and 6% strain and reconstruct the stress-strain curve for a specimen tested at 23 °C with a 100%/h deformation rate.

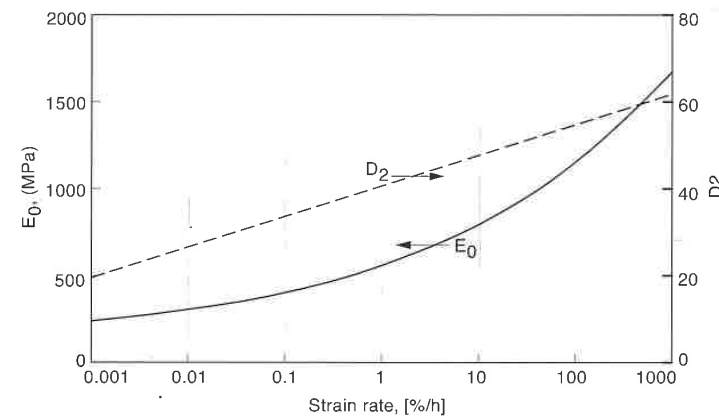


Figure 9.73 Coefficients E_0 and D_2 for a high density polyethylene at 23 °C.

9.2 For the above material calculate the 1% strain secant modulus for 6 min, 1 h, 10 h, and 100 h. Plot the data and comment on your results.

9.3 Using the time-temperature superposition principle described below, plot the stress-strain curve of Problem 9.1 for $T = 40$ °C.

$$\text{Log}(\dot{\epsilon}_{ref} / \dot{\epsilon}) = k(1/T - 1/T_{ref}), \text{ with } k = 10400\text{K}$$

9.4 Generate a 2 year isochronous curve for the polypropylene curve presented in Fig. 9.21. Using this curve estimate the thickness of a 50 mm diameter polypropylene pipe whose maximum allowable strain in a 2 year period should be 2%, while subjected to a 200 kPa internal pressure. Note: neglect effect of biaxial state of stress.

9.5 After a continuous 1 year operation, what is the diameter change of a cast acrylic tube which is part of a fluids experimental set-up that transports

air at a pressure of 10 bar. Use the following

- Tube inside diameter = 50 mm,
- Tube thickness = 3 mm,
- Tube length = 300 mm.

Use the 20 °C creep curves given below.

9.6 You are to re-design the 50 mm long solid polypropylene circular bracket described in Example 9.4 using a hollow circular cross-section with a 2 mm thickness. How much material are you saving?

9.7 A cast iron pump housing has a polypropylene cover. The cover is tightened with steel bolts causing a compressive strain of 1.5% on the edge of the plate. When will the pump start leaking if it generates internal pressures of up to 4 MPa. Use the creep data given in Fig. 9.20.

9.8 Rework Example 9.3 using polyacetal data given in Fig. 9.74.

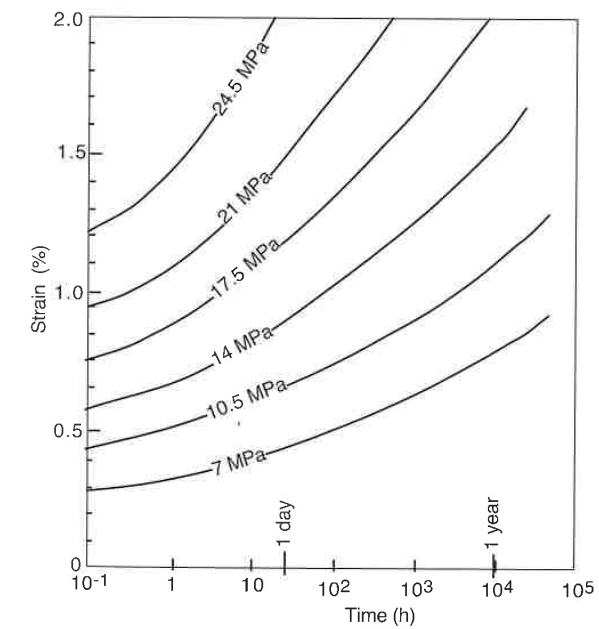


Figure 9.74 Creep data for polyacetal.

- 9.9 Two metal pipes are to be connected using a polypropylene fitting as shown in Fig. 9.75. The tubes are inserted onto the fitting causing a 1% hoop strain.

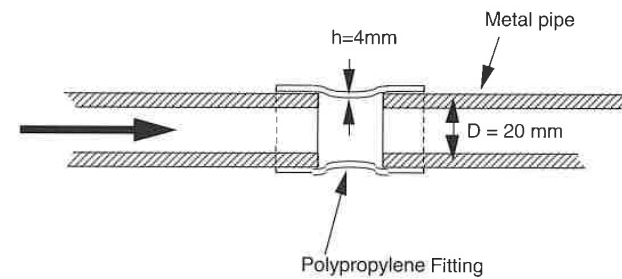


Figure 9.75 Polypropylene snap-fit assembly.

Using the creep curves given in Fig. 9.69, estimate the initial hoop stress in the polypropylene fitting.

The pressure of the water inside the tubes is 5 MPa. Estimate how long will this design be water-proof?

What initial hoop strain do you recommend to make the design water proof for 1 year?

Draw a 1 day isochronous stress-strain curve.

- 9.10 Derive the equation given for Young's modulus, E_{random} , for a plate with randomly oriented fibers. Assume that the fiber length is much larger than the thickness of the plate.
- 9.11 Similar to the Halpin-Tsai model, the mixing rule is another common technique to compute the properties of a unidirectional fiber reinforced composite part. The mixing rule for the longitudinal modulus is written as

$$E_L = \phi E_f + (1 - \phi) E_m$$

Plot E_L as a function of ϕ for $E_f/E_m = 2, 10$ and 20 .

- 9.12 You are to design two long fiber reinforced cylindrical structural components. Component A is to be loaded axially. Component B is to be loaded in torsion.
- What is the ideal orientation of the fibers for each component?
 - If you were to choose between pultrusion, filament winding, and injection molding, which process would you choose to manufacture your components. Why?
- 9.13 You are asked to design a polyacetal snap-fit as depicted in Fig. 9.76. Find the maximum force between the two components shortly after assembly, and after one year. Use the creep data presented in Fig. 9.74 [20].

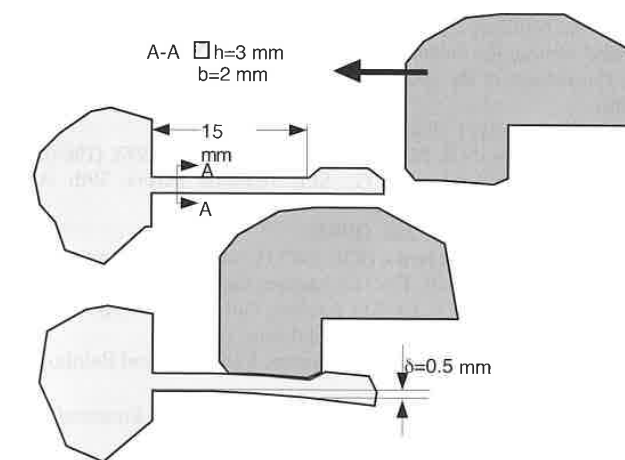


Figure 9.76 Polyacetal snap-fit assembly.

- 9.14 In a certain design, in which creep plays a significant role, you need to decide between a polyacetal and a polypropylene component. Your maximum allowable strain is 2% after one year. Which one would you choose if cost plays a major role in your design decision. To help you solve this problem, use the creep data presented in Figs. 9.76 and 9.69, for POM and PP, respectively, and the cost data presented in Chapter 1.

- 9.15 In Problem 9.13, how would your decision be if weight played a higher role than cost?

References

1. Dominghaus, H., *Plastics for Engineers*, Hanser Publishers, Munich, (1993).
2. Treloar, L.R.G., *The Physics of Rubber Elasticity*, 3rd. Ed., Clarendon Press, Oxford, (1975).
3. Courtesy ICIPC, Medellin, Colombia.
4. Ward, I.M., and Hadley, D.W., *An Introduction to Mechanical Properties of Solid Polymers*, John Wiley & Sons, Chichester, (1993).
5. Mooney, M., *J. Appl. Phys.*, 11, 582, (1940).
6. Rivlin, R.S., and Saunders, D.W., *Phil. Trans. Roy. Soc.*, A243, 251, (1951).
7. Gumbrell, S.M., Mullins, L., and Rivlin, R.S., *Trans. Faraday Soc.*, 49, 1495, (1953).
8. Guth, E., and Simha, R., *Kolloid-Zeitschrift*, 74, 266, (1936).
9. Guth, E., *Proceedings of the American Physical Society*, (1937): *Physical Review*, 53, 321, (1938).
10. Smallwood, H.M., *J. Appl. Phys.*, 15, 758, (1944).
11. Mullins, L., and Tobin, N.R. N.R., *J. Appl. Polym. Sci.*, 9, 2993, (1965).
12. Knausenberger, R., and Menges, G., *SPE Technical Papers*, 39th ANTEC, 240, (1981).
13. Retting, W., *Rheologica Acta*, 8, 258, (1969).
14. Schmachtenberg, E., Ph.D. Thesis, IKV, RWTH-Aachen, Germany, (1985).
15. Krämer, S., Ph.D. Thesis, IKV, RWTH-Aachen, Germany, (1987).
16. Weng, M., Ph.D. Thesis, IKV, RWTH-Aachen, Germany, (1988).
17. ASTM, *Plastics (II)*, 08.02, ASTM, Philadelphia, (1994).
18. Nielsen, L.E., *Mechanical Properties of Polymers*, Van Nostrand Reinhold, New York, (1962).
19. Menges, G., (after Retting, W. and Lörtsch), *Werkstoffkunde Kunststoffe*, 3rd. Ed., Hanser Publishers, Munich, (1989).
20. Crawford, R.J., *Plastics Engineering*, 2nd ed., 47, Pergamon Press, Oxford, (1987).
21. O'Toole, J.L., *Modern Plastics Encyclopedia*, McGraw Hill, New York, (1983).
22. Thimm, Th., *Plastomere, Elastomere, Duromere, Kautschuk und Gummi*, 14, 8, 233, (1961).
23. Henning, F., *Kunststoffe*, 65, 401, (1975).
24. Hosemann, R., *Kristall und Technik*, 11, 1139, (1976).
25. Zachariades, A.E., and Kanamoto, T., *High Modulus Polymers*, A.E. Zachariades, and R.S. Porter, Eds., Marcel Dekker, Inc., New York, (1988).
26. Becker, H., Diploma Thesis, IKV, RWTH-Aachen, Germany, (1986).
27. Wende, A., *Glasfaserverstärkte Plaste*, VEB Deutscher Verlag für die Grundstoff-Industrie, Leipzig, (1969).
28. Nielsen, L.E., and Landel, R.F., *Mechanical Properties of Polymers and Composites*, 2nd Ed., Marcel Dekker, Inc., New York, (1994).
29. Krishnamachari, S.I., *Applied Stress Analysis of Plastics*, Van Nostrand Reinhold, New York, (1993).
30. Tsai, S.W., Halpin, J.C., and Pagano, N.J., *Composite Materials Workshop*, Technomic Publishing Co., Stamford, (1968).
31. Brintrup, H., Ph.D. Thesis, IKV, RWTH-Aachen, Germany (1974).
32. Ehrenstein, G.W., *Faserverbundkunststoffe*, Hanser Verlag, München, (1992).
33. Menges, G., and Bintrup, H., Chapter 4 in *Polymere Werkstoffe*, Georg Thieme Verlag Stuttgart, (1984).
34. Powell, P.C., "Engineering with Polymers," Chapman and Hall, London, (1983).

Failure and Damage of Polymers

Failure of a component is a designer and engineer's biggest headache. The field of study that analyzes failed products or predicts failure is very large and complex. With polymers, failure is caused by mechanical, thermal, chemical, or other environmental influences. This chapter begins with a small overview of fracture mechanics. Here, simple models are presented that can be used to quantify the strength of polymers. The subsequent sections cover short term behavior, impact strength, creep rupture, fatigue, wear, and environmental effects.

10.1 Fracture Mechanics

A common and relatively simple approach to analyzing failure of polymer components is derived from linear elastic fracture mechanics (LEFM). The main assumption when using LEFM is that the material under consideration behaves like a linear elastic solid. The technique has been found to work well even for those materials for which the region near the crack tip behaves inelastically but everywhere the material shows elastic behavior. When a polymer component is loaded at relatively high speeds, its behavior can be considered elastic, justifying the usage of linear elastic fracture mechanics to analyze its failure. In fact, polymer components made of a ductile material will often undergo a brittle failure when subjected to impact.

However, LEFM is not appropriate to model the fracture behavior in viscoelastic media or where extensive plasticity is present during deformation. For these cases the *J-integrals* can be used to determine energy change during fracture. LEFM does not apply to long-term tests such as creep rupture since the mechanical properties of the component or test specimen are viscoelastic. If the time scale of the loaded component is carried to the extreme, say on the order of a few months or years, the material behavior is viscous.

The next sections will discuss linear elastic as well as linear viscoelastic fracture mechanics, applying them to quantitatively analyze strength properties of cracked polymer components or parts with sharp notches or stress concentrators.

10.1.1 Fracture Predictions Based on the Stress Intensity Factor

From the basic three crack growth modes of failure, shown in Fig. 10.1, mode I most resembles an internal crack growing under a tensile load. For the analysis, consider the cracked body displayed in Fig. 10.2 with a crack length of $2a$ and an applied stress σ . Near but not at the crack tip, the stress in the direction of loading can be approximated by

$$\sigma_y = \frac{K_{Ic}}{\sqrt{2\pi r}} \tag{10.1}$$

where r is the distance from the crack tip and K_{Ic} is the *critical stress intensity factor* needed for mode I crack growth and failure, defined by

$$K_{Ic} = \sigma\sqrt{\pi a} \tag{10.2}$$

This stress intensity factor depends on crack size relative to component size, crack shape, boundary conditions, etc. Hence, a more general form of Eq. 10.2 is given by

$$K_{Ic} = Y\sigma\sqrt{\pi a} \tag{10.3}$$

where Y is a dimensionless correction factor tabulated for various geometries in Table 10.1. In a linear elastic solid, fracture occurs instantaneously at a combination of stress and crack size that results in a critical stress intensity factor, K_{Ic} . The critical stress intensity factor is a material property that depends on the temperature, grade of polymer, orientation, etc., where a large value implies a tough material. Table 10.2 [1, 2] shows stress intensity factors, also called *fracture toughness*, for common polymers.

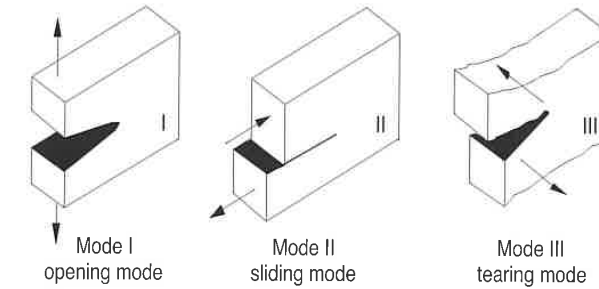


Figure 10.1 Three modes of crack loadings.

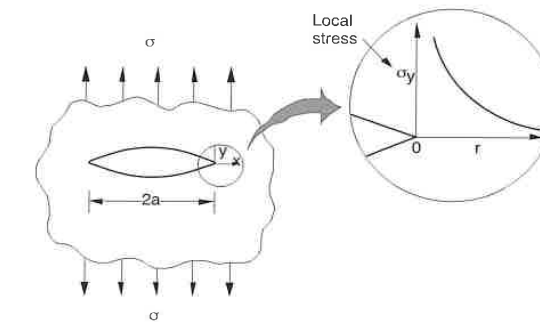


Figure 10.2 Stress near a crack tip in an infinite plate.

Table 10.1 Values for Geometry Factor Y For Various Crack Configurations

Central crack	$Y = \sqrt{\frac{W}{\pi a} \tan\left(\frac{\pi a}{W}\right)}$
Double edge crack	$Y = \sqrt{\frac{W}{\pi a} \tan\left(\frac{\pi a}{W}\right) + \frac{0.2W}{\pi a} \sin\left(\frac{\pi a}{W}\right)}$
Single edge crack	$Y = 1.12 - 0.23\left(\frac{a}{w}\right) + 10.6\left(\frac{a}{w}\right)^2 - 21.7\left(\frac{a}{w}\right)^3 + 30.4\left(\frac{a}{w}\right)^4$

Table 10.2 Values of Plane Stress Intensity Factor and Strain Toughness for Various Materials

Material	$K_{Ic}(MN/m^{3/2})$	$G_{Ic}(kJ/m^2)$
ABS	2-4	5
Acetal	4	1.2-2
Epoxy	0.3-0.5	0.1-0.3
LDPE	1	6.5
MDPE-HDPE	0.5-5	3.5-6.5
Polyamide 66	3	0.25-4
Polycarbonate	1-2.6	5
Polyester-glass reinforced	5-7	5-7
Polypropylene copolymer	3-4.5	8
Polystyrene	0.7-1.1	0.3-0.8
PMMA	1.1	1.3
uPVC	1-4	1.3-1.4
Aluminum-alloy	37	20
Glass	0.75	0.01-0.02
Steel-mild	50	12
Steel-alloy	150	107
Wood	0.5	0.12

10.1.2 Fracture Predictions Based on an Energy Balance

To analyze a mode I crack growth case using an energy balance and LEFM, consider the cracked body used in the previous analysis, where the actual forces are used instead of stresses, as displayed in Fig. 10.3. The crack width is also $2a$, and the body is subjected to a load F . The load-displacement behavior of the cracked body is described by the solid line in Fig. 10.4. The elastic energy stored in the loaded component is given by the area under the curve:

$$U_c = \frac{1}{2}FX \tag{10.4}$$

As the crack grows by an amount Δa , the stiffness of the component decreases as shown by the dashed line in Fig. 10.4, and the elastic energy changes to

$$U'_c = \frac{1}{2}(F + \Delta F)(X + \Delta X) \tag{10.5}$$

The change in stored elastic energy for the body with the growing crack is described by

$$\Delta U = U_c - U'_c \tag{10.6}$$

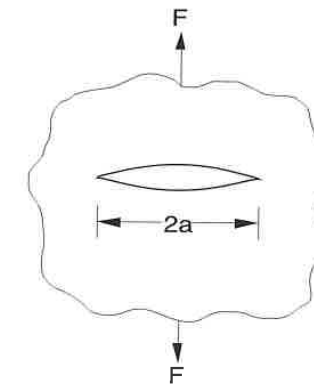


Figure 10.3 Load applied on a cracked specimen.

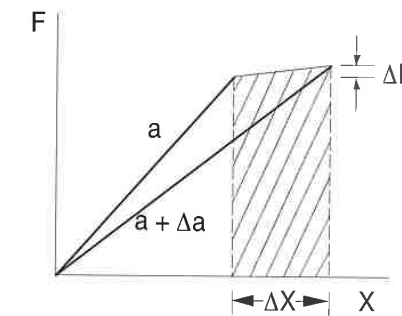


Figure 10.4 Linear elastic behavior of a cracked specimen.

The external work done as the crack grows the distance Δa is defined by the shaded area in Fig. 10.4 and can be written as

$$\Delta U_c = \left(F + \frac{\Delta F}{2} \right) \Delta X \tag{10.7}$$

By subtracting Eq. 10.6 from Eq. 10.7 we can compute the energy required to generate new surfaces during fracture:

$$\Delta U_c - \Delta U = \frac{1}{2}(F\Delta X - X\Delta F) \quad (10.8)$$

Griffith's hypothesis [3], commonly used as a fracture criterion, states that for a crack to increase in size, the rate of stored elastic energy decrease must be larger or equal to the rate at which surface energy is created during crack growth. Griffith's hypothesis can be related to the expression in Eqs. 10.6 and 10.7 as

$$\frac{1}{t} \frac{\partial(U_c - U)}{\partial a} \geq G_{lc} \quad (10.9)$$

where G_{lc} defines the energy required to increase a crack by a unit length in a component of unit width and is usually referred to as the *elastic energy release rate*, the *toughness* or the *critical energy release rate*. Equations 10.6, 10.7, and 10.9 can be combined to give

$$G_{lc} = \frac{1}{2} \left(F \frac{\partial X}{\partial a} - X \frac{\partial F}{\partial a} \right) \quad (10.10)$$

Making use of the compliance defined by

$$J = \frac{X}{F} \quad (10.11)$$

and defining the force at the onset of crack propagation by F_c , we can rewrite Eq. 10.10 as

$$G_{lc} = \frac{F_c^2}{2t} \frac{\partial J}{\partial a} \quad (10.12)$$

This equation describes the fundamental material property, G_{lc} , as a function of applied force at fracture and the rate at which compliance changes with respect to crack size. Equation 10.12 is more useful if it is written in terms of stress as

$$G_{lc} = \frac{\pi \sigma_c^2 a}{E} \quad (10.13)$$

This equation only applies for plane stress and must be redefined for the plane strain case as

$$G_{lc} = \frac{\pi \sigma_c^2 a}{E} (1 - \nu^2) \quad (10.14)$$

Table 10.2 also displays typical values of toughness for common materials.

By substituting Eq. 10.3 into Eqs. 10.13 and 10.14, we can relate the stress intensity factor K_{lc} and the toughness G_{lc} with

$$G_{lc} = \frac{K_{lc}^2}{Y^2 E} \quad (10.15)$$

for the plane stress case and

$$G_{lc} = \frac{K_{lc}^2}{Y^2 E} (1 - \nu^2) \quad (10.16)$$

for the plane strain case.

10.1.3 Linear Viscoelastic Fracture Predictions Based on J-Integrals

Because of the presence of viscous components and the relatively large crack-tip plastic zone during deformation, the elastic energy release rate, G_{lc} , is not an appropriate measure of the energy release or toughness during fracture of many thermoplastic polymers. The J-integral concept was developed by Rice [4] to describe the strain energy transfer into the crack tip region and, using the notation in Fig. 10.5, is defined by

$$J_{lc} = \int_{\Gamma} W dy - \int_{\Gamma} \mathbf{T} \frac{\partial \mathbf{u}}{\partial \mathbf{x}} ds \quad (10.17)$$

where W represents the strain energy density, \mathbf{T} the traction vector, and \mathbf{u} the displacement vector. As with G_{lc} , J_{lc} is a measure of the energy release rate, thus, analogous to Fig. 10.4. We can consider Fig. 10.6 to determine the energy release in a viscoelastic material with a growing crack. Again, the shaded area in the curve represents the energy release rate which, apart from second order effects, is the same for constant load and constant deformation and for a specimen of thickness t can be computed by

$$\Delta U = J_{lc} t \Delta a \quad (10.18)$$

which gives

$$J_{lc} = -\frac{1}{t} \left(\frac{\partial U}{\partial a} \right) \quad (10.19)$$

10.2.1 Brittle Failure

Brittle failure usually occurs with thermoplastics below their glass transition temperature, T_g , and with highly cross-linked polymers. However, as discussed later in this chapter, brittle failure also occurs in creep rupture and fatigue tests performed at temperatures above the glass transition temperature of the polymer. Typically, it occurs at very small strains—perhaps 1% or less—and it is generally associated with amorphous thermoplastics below their glass transition temperature. Figure 10.8 shows the stress-strain curve for the injection molded polystyrene ASTM D638M type I test specimen shown in Fig. 10.9. The stress strain curve has a constant slope until the point where small microcracks form just before failure. These small microcracks form in the plane perpendicular to the maximum principal stress and are nucleated at points of high stress concentrations such as scratches, dust particles in the material and material inhomogeneities. These cracks, which are more commonly known as crazes, impair clarity and reflect light, which makes them particularly obvious in transparent materials.

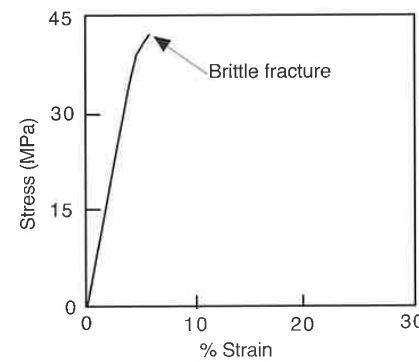


Figure 10.8 Stress-strain curve for a polystyrene at room temperature.

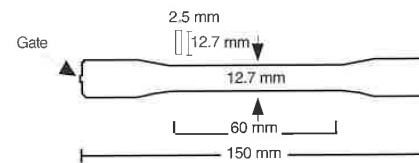


Figure 10.9 ASTM Type I test specimen.

Figure 10.10 [6] shows electron micrographs of the center and edge of a craze in a polystyrene specimen. As can be seen in the micrograph, the craze boundaries are connected with load bearing fibrils which make them less dangerous than actual cracks. Crazing is directly related to the speed at which the component or test specimen is being deformed. At high deformation speeds, the crazes are small and form shortly before failure, which makes them difficult to detect. At slow rates of deformation, crazes tend to be large and occur early on during loading. A typical craze is about $0.5 \mu\text{m}$ wide at the center and $200 \mu\text{m}$ long.² However, the length and width of a craze is material-dependent.

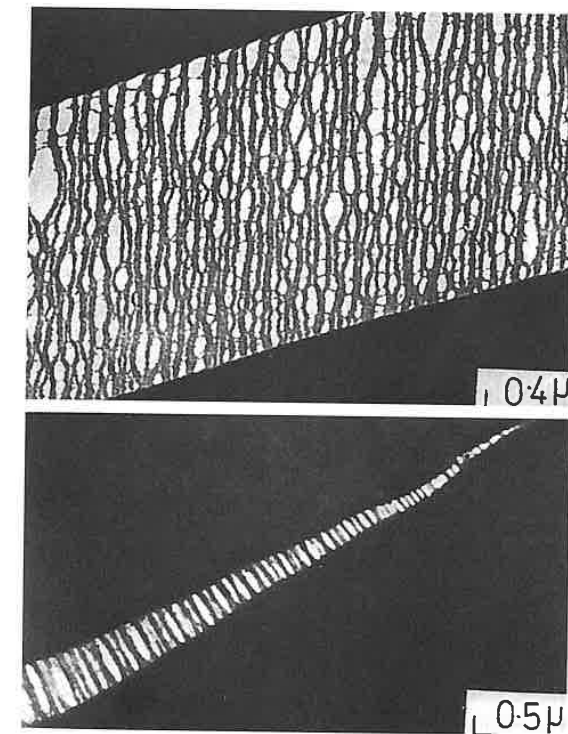


Figure 10.10 Electron micrographs of the center and edge of a craze in a polystyrene specimen.

² The length of a craze will vary between $10 \mu\text{m}$ and $1000 \mu\text{m}$.

Figure 10.11 [7] shows the relation between stress, strain, craze size formation and failure. By extrapolating the craze formation line, one can see that at high stress crazes form at the same time as failure. When crazes form under static loading, they do not pose immediate danger to the polymer component. However, crazes are irreversible, and they imply a permanent damage within the material. It should also be noted that once crazes and microcracks have formed, the material no longer obeys the laws of linear viscoelasticity. The limit strain at which microcracks will form is sometimes depicted by $\epsilon_{F\infty}$. Complex models exist, beyond the scope of this book, which relate the critical strain to the surface energy within a craze [8].

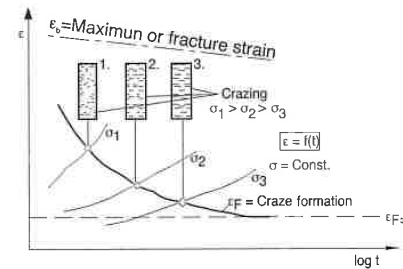


Figure 10.11 Relation between stress, strain, time and craze formation.

Figure 10.12 [7] shows the relationship between strain, time, and damage for PMMA. The bottom of the figure shows the time-temperature superposition. For example, the damage that occurs at 10 hours for 23 °C will occur at 10⁵ hours for a component at 60 °C. It is interesting to see how the critical strain, $\epsilon_{F\infty}$, is delayed as the temperature of the polymer component rises.

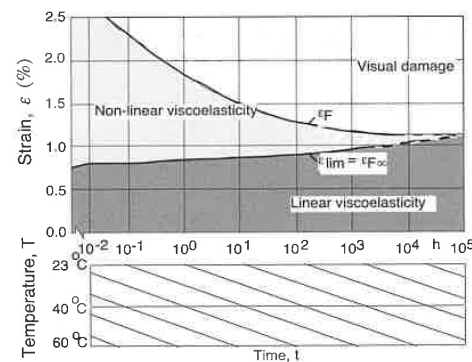


Figure 10.12 Strain limits for linear viscoelasticity.

Figure 10.13 [7] shows a plot of critical strain versus temperature for an impact resistant polystyrene and compares the damage behavior curve to the shear modulus. The two curves are almost a mirror images of each other and demonstrate that the formation of microcracks is inversely proportional to the stiffness of the material. The figure also demonstrates the influence of orientation on the onset of microcracks. As expected, in a component loaded perpendicular to the orientation, or across the polymer chains, the microcracks form earlier than in one loaded parallel to the orientation direction.

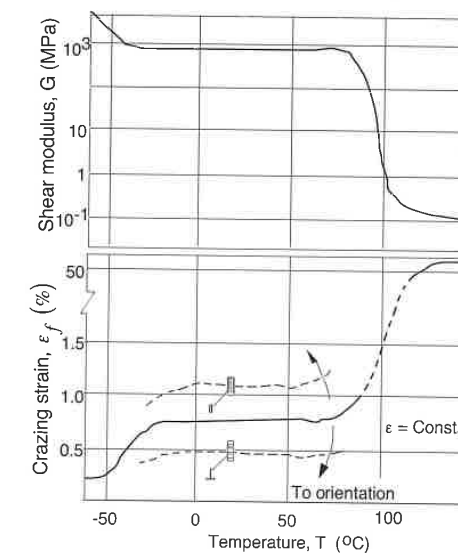


Figure 10.13 Shear modulus and crazing strain as a function of temperature for a high impact polystyrene.

10.2.2 Ductile Failure

A ductile failure takes place with semi-crystalline thermoplastics at temperatures between the glass transition temperature, T_g , and the melting temperature, T_m . A ductile failure is a succession of several events, as is clearly shown in the stress-strain diagram for polypropylene, shown in Fig. 10.14 and explained in the following paragraphs.

At first, the semi-crystalline polymer behaves like an elastic solid whose deformation is reversible. For the polypropylene sample test results shown in Fig. 10.14, this linear elastic behavior holds for deformations of up to 0.5%. This

behavior takes place when the component's load is applied and released fairly quickly, without causing a permanent damage to the material and allowing the component to return to its original shape. This is graphically depicted in Fig. 10.15 [7].

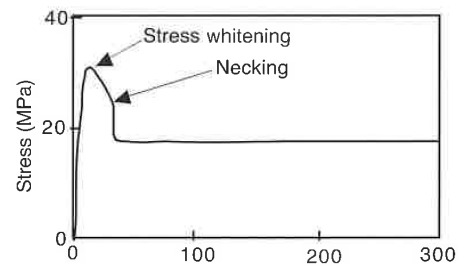


Figure 10.14 Stress-strain curve for a polypropylene at room temperature.

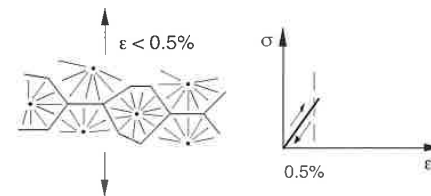


Figure 10.15 Elastic deformation within a spherulitic structure.

If the load is increased or the process is slowed, the stress-strain curve becomes non-linear, reflected by the reduction of rate of stress increase. At this point, microcracks form in the interface between neighboring spherulites, as shown in the photograph of Fig. 10.16 [9] and schematically in Fig. 10.17 [7].



Figure 10.16 Micrograph of crack formation at inter-spherulitic boundaries (polypropylene).

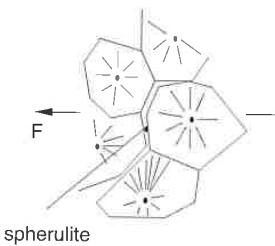


Figure 10.17 Schematic of crack formation at inter-spherulitic boundaries.

The formation of such microcracks, also called *stress whitening*, is an irreversible process, causing a permanent deformation in the polymer component. Other than the white coloration that makes itself noticeable in the stressed component, the cracks are not visible to the naked eye. These microcracks are fairly constant in length, about the size of the spherulites. Their formation and growth, and their relation to the stress-strain behavior of a semi-crystalline polymer, are depicted in Fig. 10.18 [7].

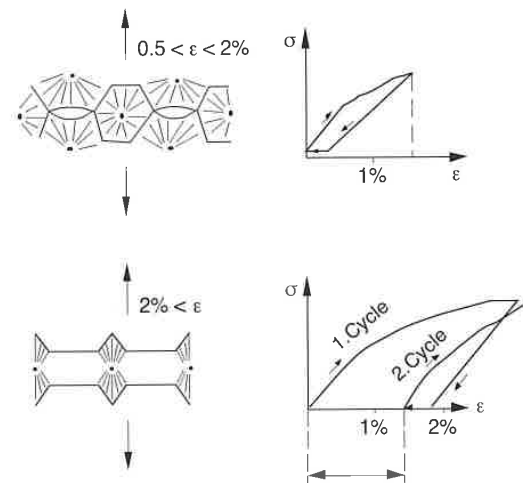


Figure 10.18 Relation between microcrack formation and the stress-strain behavior of a semi-crystalline polymer.

Figure 10.14 shows that by further deforming the specimen, the stress-strain curve reaches a maxima called the *yield point* or *yield strength*. Beyond the yield point the stress drops, an event that is followed by *necking*, a localized reduction in cross-sectional area. Once necking has occurred, the specimen or component continues a long cold drawing process where the spherulitic structure is first deformed and then broken up, creating highly oriented regions within the polymer component. Figure 10.19 shows the progression of the necked region during tensile tests of polypropylene samples. This mode of failure is common in semi-crystalline components, such as the one shown in Fig. 10.20 for a polyethylene automotive fan blade.

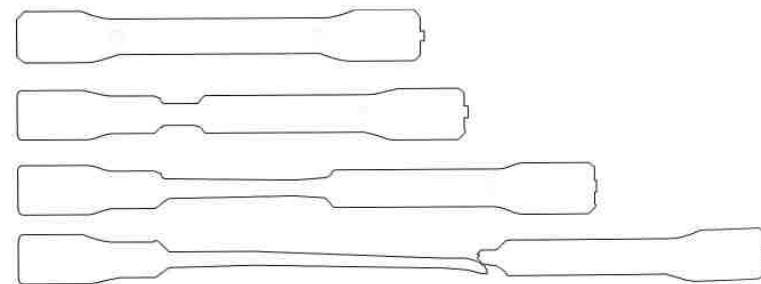


Figure 10.19 Necking progression of a polypropylene specimen during a tensile test.

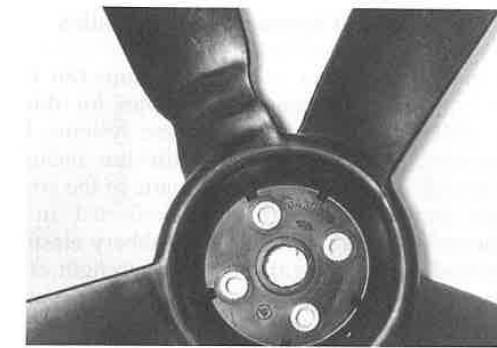


Figure 10.20 Necking of a polyethylene automotive fan blade [11].

Necking and cold drawing can be explained with the molecular model [10] shown in Fig. 10.21. Once the amorphous ties between lamellae have been completely extended, a slip-tilting of the lamellae is induced. As deformation continues, lamellae fragments get aligned in the direction of draw, forming fibrils of alternating crystal blocks and stretched amorphous regions.

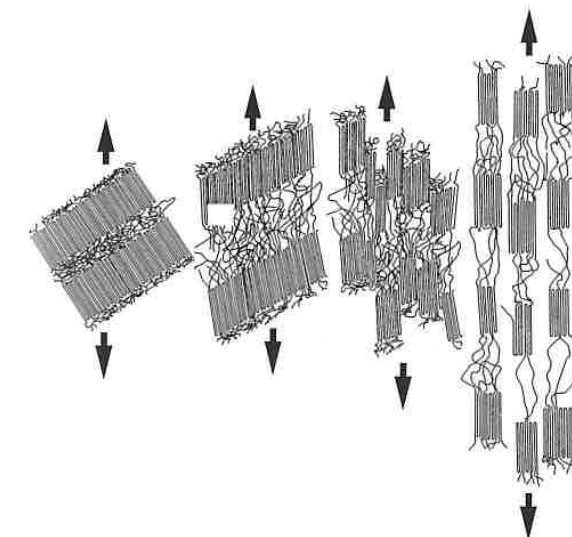


Figure 10.21 Molecular model used to represent necking and drawing during a tensile test.

10.2.3 Failure of Highly Filled Systems or Composites

A polymer that usually fails under a brittle fracture can be toughened by adding filler particles. The most common examples for this effect are high impact polystyrene (HIPS) and ABS. In both these systems, brittle polymers, acrylic, and polystyrene, were toughened with the inclusion of rubbery particles into the material as shown in the schematic of the structure of HIPS in Fig. 10.22 [12]. This increase in toughness is reflected in the stress-strain behavior of HIPS shown in Fig. 10.23, where the rubbery elastic behavior of the rubber particles lowered the stiffness and ultimate strength of the material but increased its toughness. The rubber particles halt the propagation of a growing craze. Characteristic lengths of crazes that form in such systems are only as large as the characteristic gap between filler particles. This creates a system that has a large number of small crazes instead of the small number of large crazes present in the unfilled polymer. Table 10.3 [2] presents the effect of volume fraction of rubber particles on the mechanical and fracture properties of rubber-modified polystyrene. The impact strength and the fracture strain are maximized at a rubber particle volume fraction of about 20%.

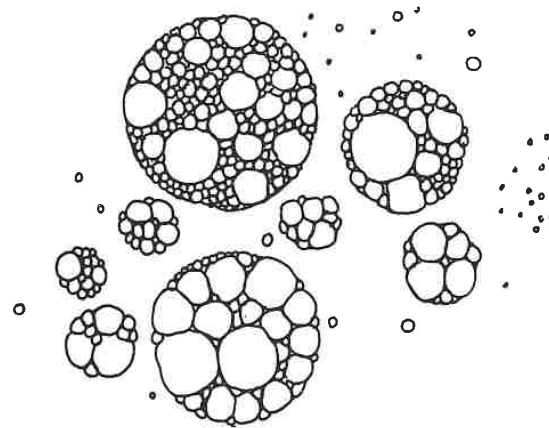


Figure 10.22 Schematic of the structure of a high impact polystyrene.

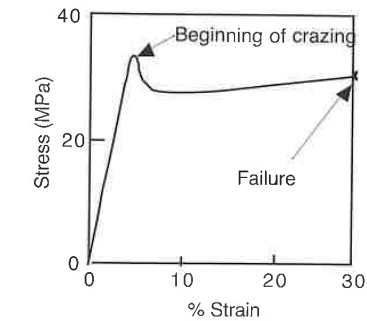


Figure 10.23 Stress-strain curve of a high impact polystyrene.

Table 10.3 Effect of Rubber Particle Volume Fraction, ϕ , on the Properties of Rubber Modified Polystyrene

Volume fraction ϕ	Tensile modulus GPa	Impact strength MJ/m ³	Fracture strain %
0.06	2.8	0.42	3
0.12	2.4	1.90	20
0.22	1.9	11.6	45
0.30	1.0	5.6	34
0.78	0.55	1.2	8

This increase in toughness can be observed even if the filler material is also brittle. Electron micrographs of such systems have shown that cracks propagate until they hit a filler particle, which often stops the propagation [2]. In thermosetting polymers, this effect is commonly referred to as *crack pinning*. Figure 10.24 compares plots of impact-absorbed energy as a function of specimen size for unfilled epoxy and epoxies filled with irregular-shaped silica with weight percents of 55% and 64%.

The failure of a fiber-filled material begins at the interface between filler or reinforcement and the matrix, as shown in the electron micrograph presented in Fig. 10.25 [13]. The micrograph was taken when a glass fiber filled polyester specimen was placed under loading and shows the breakage of the adhesion between imbedded glass fibers and their matrix. This breakage is generally referred to as *debonding*. This initial microcrack formation is reflected in a stress-strain curve by the deviation from the linear range of the elastic constants. In fact, the failure is analogous to the microcracks that form between spherulites when a semi-crystalline polymer is deformed.

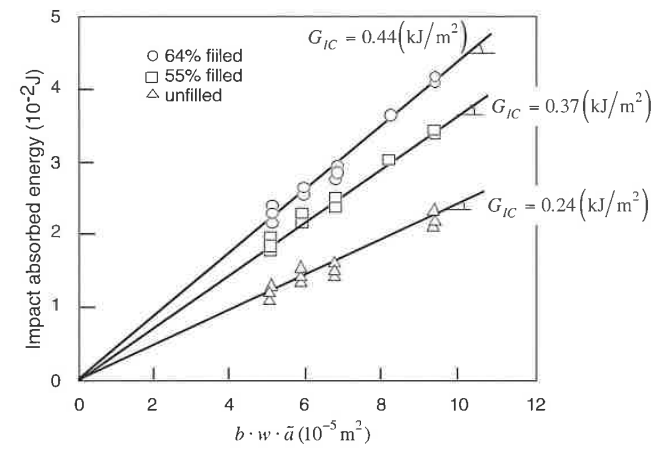


Figure 10.24 Impact absorbed energy as a function of specimen size for unfilled epoxy and epoxies filled with irregular-shaped silica with weight percents of 55% and 64%.

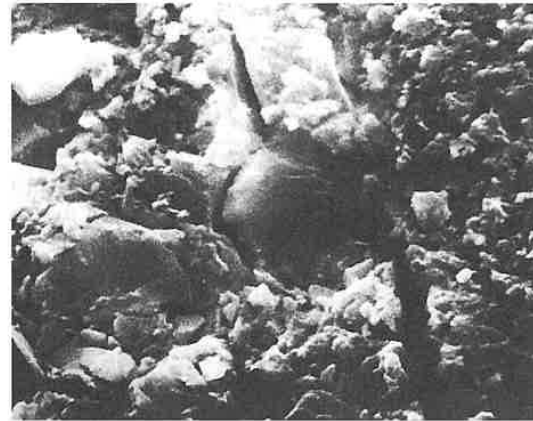


Figure 10.25 Electron micrograph of crack formation between polyester matrix and a glass fiber.

10.3 Impact Strength³

In practice, nearly all polymer components are subjected to impact loads. Since many polymers are tough and ductile, they are often well suited for this type of loading. However, under specific conditions even the most ductile materials, such as polypropylene, can fail in a brittle manner at very low strains. These types of failure are prone to occur at low temperatures and at very high deformation rates.

According to several researchers [14, 15] a significantly high rate of deformation leads to complete embrittlement of polymers which results in a lower threshold of elongation at break. Menges and Boden designed a special high-speed elongational testing device that was used to measure the minimum work required to break the specimens. The minimum strain, ϵ_{min} , which can be measured with such a device, is a safe value to use in calculations for design purposes. One should always assume that if this minimum strain value is exceeded at any point in the component, initial fracture has already occurred. Table 10.4 [16, 17] presents minimum elongation at break values for selected thermoplastics on impact loading.

On the other hand, the stiffness and the stress at break of the material under consideration increase with the rate of deformation. Table 10.5 [16] presents data for the stress at break, σ_{min} , for selected thermoplastics on impact loading. This stress corresponds to the point where the minimum elongation at break has just been reached.

Table 10.4 Minimum Elongation at Break on Impact Loading

Polymer	ϵ_{min} (%)
HMW-PMMA	2.2
PA6 + 25% SFR	1.8
PP	1.8
uPVC	2.0
POM	4.0
PC + 20% SFR	4.0
PC	6.0

³ The term "impact strength" is widely misused, since one is actually referring to energy absorbed before failure.

Table 10.5 Minimum Stress at Break on Impact Loading

Polymer	σ_{min} (MPa)
HMW-PMMA	135
PA6 + 25% SFR	175
uPVC	125
POM	>130
PC + 20% SFR	>110
PC	>70

Figure 10.26 summarizes the stress-strain and fracture behavior of a HMW-PMMA tested at various rates of deformation. The area under the stress-strain curves represents the *volume-specific energy to fracture* (w). For impact, the elongation at break of 2.2% and the stress at break of 135 MPa represent a minimum of volume-specific energy because the stress increases with higher rates of deformation, but the elongation at break remains constant. Hence, if we assume a linear behavior, the *minimum volume-specific energy absorption* up to fracture can be calculated using

$$w_{min} = 0.5\sigma_{max}\epsilon_{min} \quad (10.21)$$

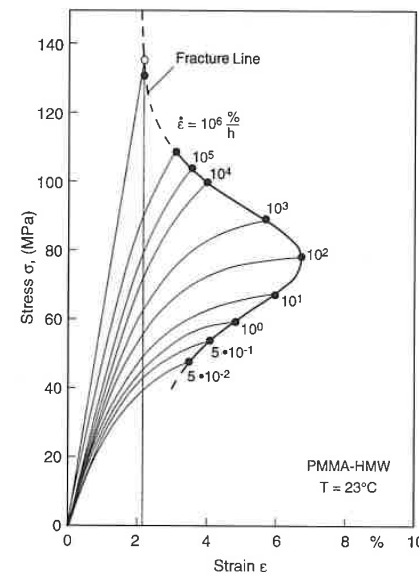


Figure 10.26 Stress-strain behavior of HMW-PMMA at various rates of deformation.

If the stress-strain distribution in the polymer component is known, one can estimate the minimum energy absorption capacity using w_{min} . It can be assumed that failure occurs if w_{min} is exceeded in any part of the loaded component. This minimum volume-specific energy absorption, w_{min} , can be used as a design parameter. It was also used by Rest [18] for fiber-reinforced polymeric materials.

Glass fiber reinforced thermoplastics generally undergo brittle failure. Figure 10.27 [16] shows how the impact resistance of a polyamide 6 material was dramatically reduced with the addition of a glass reinforcement. Interesting to note is that the impact resistance of polyamide 6 with 6% and 30% glass reinforcement is essentially the same when compared to the unfilled material. However, a specimen with a sharp notch that resembles a crack will have a higher impact resistance if it is glass reinforced. Figure 10.28 [16] illustrates this by showing a plot of izod test data for polyamide 6 specimens and polyamide 6 specimens filled with 30% glass reinforcement as a function of notch radius. Here, the data for a small notch radius reflect the energy it takes to propagate the crack through the specimen. The data for a large notch radius approach the energy it takes to both, initiate and propagate a crack. In a filled polymer, a filler can sometimes increase the impact resistance of the component. For example, the volume fraction of crazes in a rubber particle filled polystyrene increases with increasing particle content. Figure 10.29 shows the volume fraction of craze voids as a function of rubber particle content in a high impact polystyrene. The figure also schematically depicts the relation between rubber particle content and craze geometry.

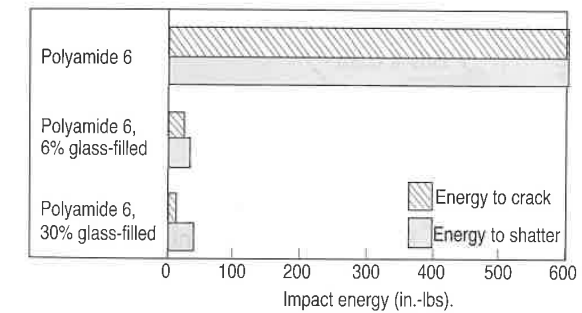


Figure 10.27 Effect of glass fiber content on energy to crack and shatter for polyamide 6.

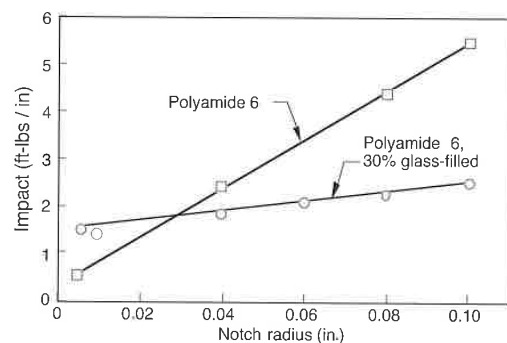


Figure 10.28 Impact strength as a function of notch tip radius for a filled and unfilled polyamide 6.

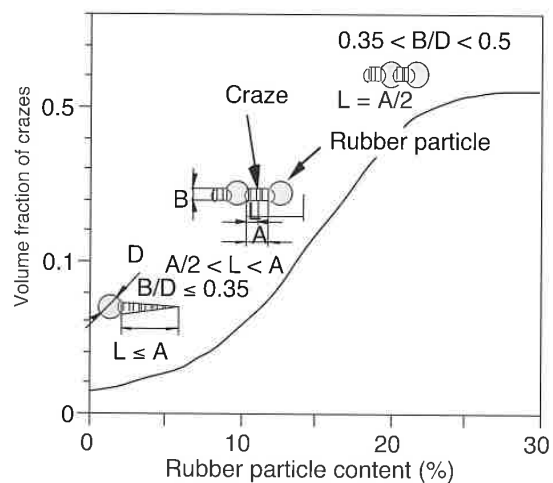


Figure 10.29 Volume fraction of craze voids as a function of rubber particle content in a high impact polystyrene.

The impact strength of a copolymer and polymer blend of the same materials can be quite different, as shown in Fig. 10.30. From the figure it is clear that the propylene-ethylene copolymer, which is an elastomer, has a much higher impact resistance than the basic polypropylene-polyethylene blend. It should be pointed out here that elastomers usually fail by ripping. The ripping

or tear strength of elastomers can be tested using the ASTM D1004, ASTM D1938, or DIN 53507 test methods. The latter two methods make use of rectangular test specimens with clean slits cut along the center. A typical tear propagation test for an elastomer composed of 75 parts of natural rubber (NR) and 25 parts of styrene butadiene rubber (SBR) is presented in Fig. 10.31.⁴ The tear strength of elastomers can be increased by introducing certain types of particulate fillers. For example, a well dispersed carbon black filler can double the ripping strength of a typical elastomer. Figure 10.32 [7] shows the effect that different types of fillers have on the ripping strength of a polychloroprene elastomer.

In general, one can say if the filler particles are well dispersed and have diameters between 20 nm and 80 nm, they will reinforce the matrix. Larger particles will act as microscopic stress concentrators and will lower the strength of the polymer component. A case where the filler adversely affects the polymer matrix is presented in Fig. 10.33 [7], where the strength of PVC is lowered with the addition of a calcium carbonate powder.

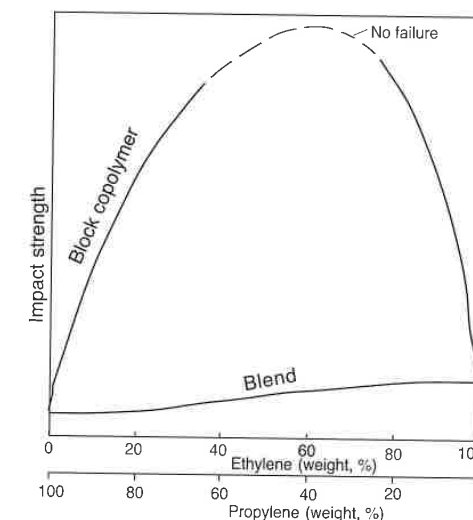


Figure 10.30 Impact strength of a propylene-ethylene copolymer and a polypropylene-polyethylene polymer blend.

⁴ Courtesy of ICIPC, Medellín, Colombia.

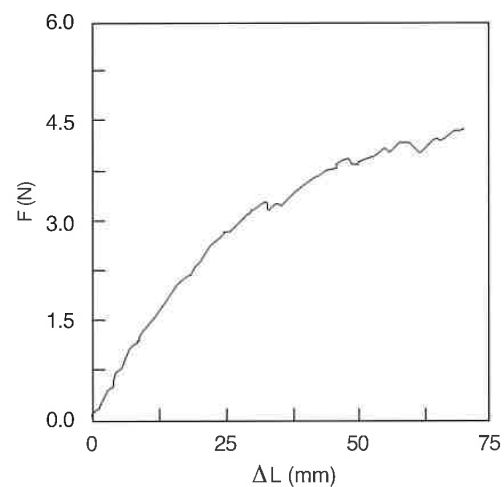


Figure 10.31 Tear propagation test for an elastomer composed of 75 parts of natural rubber (NR) and 25 parts of styrene butadiene rubber (SBR).

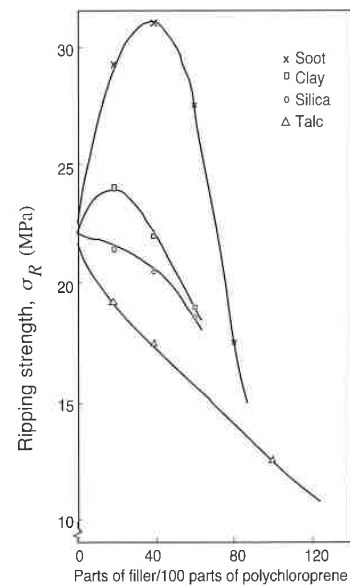


Figure 10.32 Ripping strength of a polychloroprene elastomer as a function of filler content for different types of fillers.

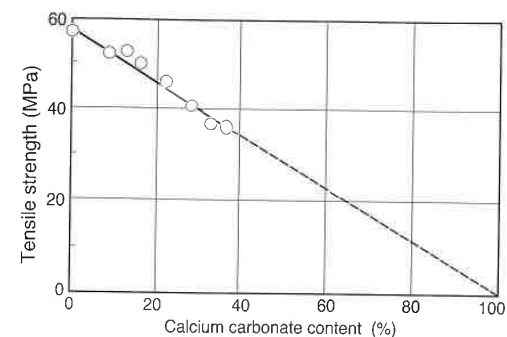


Figure 10.33 Tensile strength of PVC as a function of calcium carbonate content.

10.3.1 Impact Test Methods

Impact tests are widely used to evaluate a material's capability to withstand high velocity impact loadings. The most common impact tests are the *Izod* and the *Charpy* tests. The *Izod* test evaluates the impact resistance of a cantilevered notched bending specimen as it is struck by a swinging hammer. Figure 10.34 [19] shows a typical *Izod*-type impact machine, and Fig. 10.35 [19] shows a detailed view of the specimen, the clamp, and the striking hammer. The pendulum or hammer is released from a predetermined height and after striking the specimen, travels to a recorded height. The energy absorbed by the breaking specimen is computed from the difference between the two heights. The standard test method that describes the *Izod* impact test is the ASTM-D 256 test. There are several variations of the *Izod* test. These variations include positioning the test specimen such that the stresses in the notch are tensile or compressive by having the notch face away or toward the swinging pendulum, respectively. In addition, the clamping force exerted on the test specimen can have a great effect on the test results. The *Charpy* test evaluates the bending impact strength of a small notched or unnotched simply supported specimen that is struck by a hammer similar to the *Izod* impact tester [19]. The notched *Charpy* test is done such that the notch faces away from the swinging hammer creating tensile stresses within the notch, see Fig. 10.36. Both, the standard ASTM D256 and DIN 53453 tests describe the *Charpy* impact test.

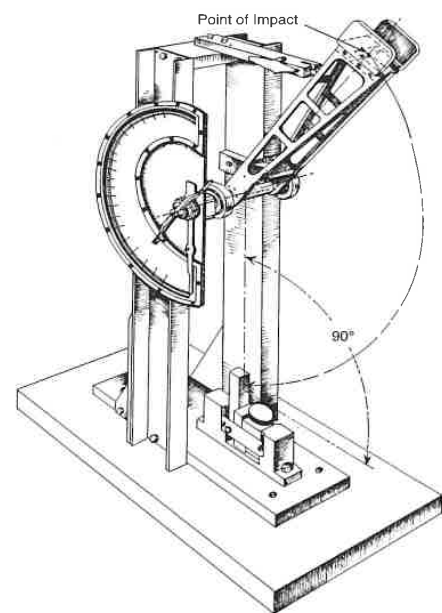


Figure 10.34 Cantilever beam Izod impact machine.

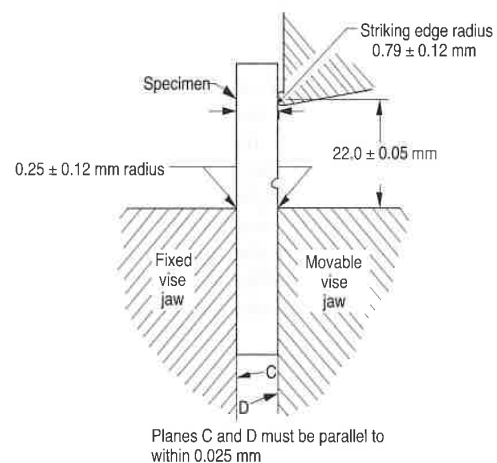


Figure 10.35 Schematic of the clamp, specimen and striking hammer in an izod impact test.
Planes C and D must be parallel to within 0.025 mm

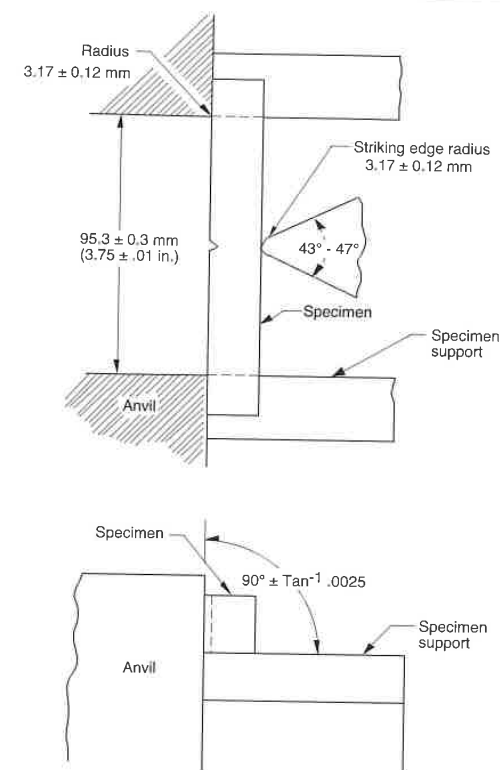


Figure 10.36 Schematic of the clamp, specimen, and striking hammer in a Charpy impact test.

A variable of both tests is the notch tip radius. Depending on the type of material, the notch tip radius may significantly influence the impact resistance of the specimen. Figure 10.37 [2] presents impact strength for various thermoplastics as a function of notch tip radius. As expected, impact strength is significantly reduced with decreasing notch radius. Another factor that influences the impact resistance of polymeric materials is the temperature. This is clearly demonstrated in Fig. 10.38 [2], in which PVC specimens with several notch radii are tested at various temperatures. In addition, the impact test sometimes brings out brittle failure in materials that undergo a ductile breakage in a short-term tensile test. The brittle behavior is sometimes developed by lowering the temperature of the specimen or by decreasing the notch tip radius. Figure 10.39 [1] shows the brittle to ductile behavior regimes as a function of temperature for several thermoplastic polymers.

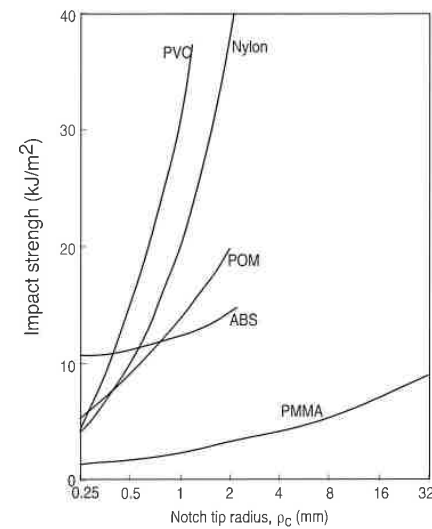


Figure 10.37 Impact strength as a function of notch tip radius for various polymers.

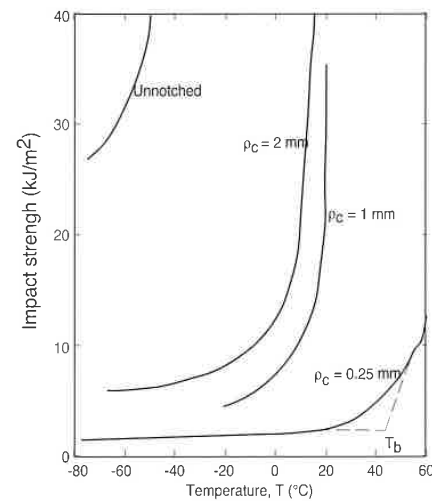


Figure 10.38 Impact strength of PVC as a function of temperature for various notch tip radii.

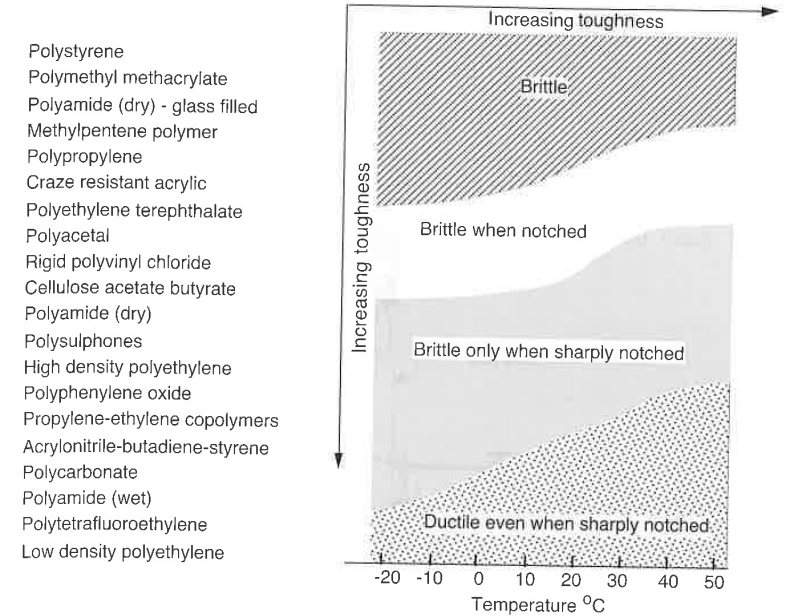


Figure 10.39 Brittle to ductile behavior regimes as a function of temperature for several thermoplastic polymers.

Another impact test worth mentioning is the *falling dart* test. This test is well suited for specimens that are too thin or flexible to be tested using the Charpy and Izod tests. This test, which is described by the ASTM 3029 and DIN 53 453 standard methods, also works well when the fracture toughness of a finished product with large surfaces is sought. Figure 10.40 shows a schematic of a typical falling dart test set-up [19]. The test consists of dropping a *tup*, with a spherical tip and otherwise variable shape and weight on a usually circular test specimen that is clamped around the periphery. The weight of the tup and the height from which it is dropped are the test variables. The energy needed to fracture the test specimen is directly computed from the potential energy of the tup before it is released; written as

$$U_p = mgh \tag{10.22}$$

where m is the mass of the tup, h the height from which it is dropped, and g gravity. It is assumed that the potential energy is fully transformed into kinetic energy and, in turn, into fracture energy. The test itself is much simpler than the Charpy and Izod tests, since Eq. 10.22 can be used to interpret the results

directly. However, a large number of tests are required to determine the energy required for fracture.

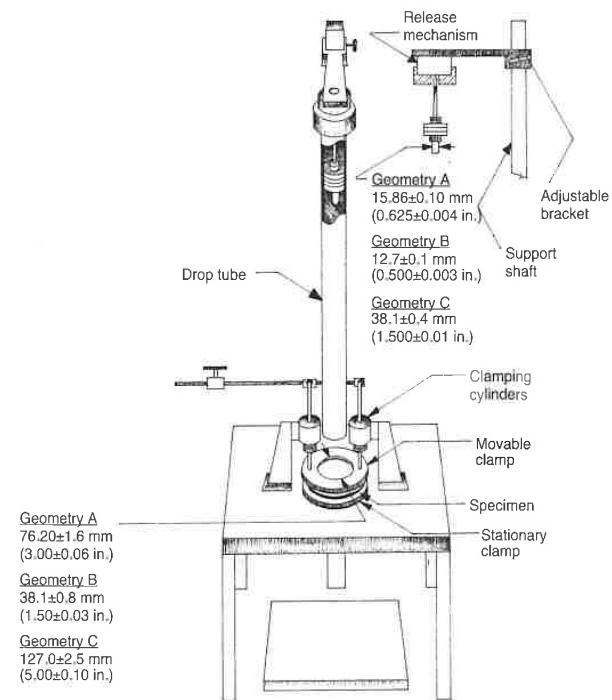


Figure 10.40 Schematic of a drop weight impact tester.

10.3.2 Fracture Mechanics Analysis of Impact Failure

Although the most common interpretation of impact tests is qualitative, it is possible to use linear elastic fracture mechanics to quantitatively evaluate impact test results. Using LEFM, it is common to compute the material's fracture toughness G_{Ic} from impact test results. Obviously, LEFM is only valid if the Izod or Charpy test specimen is assumed to follow linear elastic behavior and contains a sharp notch. At the onset of crack propagation, Eq. 10.4, which gives the elastic energy stored in the loaded test specimen, can be rewritten in terms of compliance, J , as

$$U_c = \frac{1}{2} F_c^2 J \quad (10.23)$$

Solving for F_c in Eq. 10.12 and substituting into Eq. 10.23 results in

$$U_c = G_{Ic} t \left(\frac{J}{\partial J / \partial a} \right) \quad (10.24)$$

Introducing the test specimen's width, w , and a geometrical crack factor, \bar{a} , given by

$$\bar{a} = \left(\frac{1}{J} \frac{\partial J}{\partial a} \right)^{-1} \quad (10.25)$$

we can write Eq. 10.24 as

$$U_c = G_{Ic} w t \bar{a} \quad (10.26)$$

The parameter \bar{a} is found in Table 10.6 [20] for various Charpy impact test specimens and in Table 10.7 [20] for various Izod impact test specimens. The elastic energy absorbed by the test specimen during fracture, U_c , can also be represented with energy lost by the pendulum, U_L . This allows the test engineer to relate impact test results with the fracture toughness G_{Ic} of a material. When plotting U_c versus $tw\bar{a}$, the kinetic effects lead to a positive intercept on the U_c axis. This can be corrected by subtracting the kinetic effects, U_k , from U_c . The kinetic effects can be computed using [20]

$$U_k = (1 + e) \left(1 + \frac{1}{2} \frac{m}{M} (1 - e) \right) m \left(\frac{M}{m + M} \right) V^2 \quad (10.27)$$

where m is the mass of the specimen, M the mass of the tup, V the velocity, and e the coefficient of restitution.

Figure 10.41 contains both Charpy and Izod test result data for a medium density polyethylene [20] as plots of U_c versus $tw\bar{a}$ with kinetic energy corrections. We can now calculate G_{Ic} from the slope of the curve (Eq. 10.26).

However, as mentioned earlier for polymers that undergo significant plastic deformation before failure, Eq. 10.26 does not apply and the J-integral must be used. Here, by taking the Charpy or Izod specimen and assuming full yield, having a plastic hinge, we can calculate the energy by using

$$U_c = \frac{\delta}{2} \sigma_y t (w - a) \quad (10.28)$$

Table 10.6 Charpy Impact Test Geometric Crack Factors \bar{a}

a/D	$2L/D=4$	$2L/D=6$	$2L/D=8$	$2L/D=10$	$2L/D=12$
0.04	1.681	2.456	3.197	3.904	4.580
0.06	1.183	1.715	2.220	2.700	3.155
0.08	0.933	1.340	1.725	2.089	2.432
0.10	0.781	1.112	1.423	1.716	1.990
0.12	0.680	0.957	1.217	1.461	1.688
0.14	0.605	0.844	1.067	1.274	1.467
0.16	0.550	0.757	0.950	1.130	1.297
0.18	0.505	0.688	0.858	1.015	1.161
0.20	0.468	0.631	0.781	0.921	1.050
0.22	0.438	0.584	0.718	0.842	0.956
0.24	0.413	0.543	0.664	0.775	0.877
0.26	0.391	0.508	0.616	0.716	0.808
0.28	0.371	0.477	0.575	0.665	0.748
0.30	0.354	0.450	0.538	0.619	0.694
0.32	0.339	0.425	0.505	0.578	0.647
0.34	0.324	0.403	0.475	0.542	0.603
0.36	0.311	0.382	0.447	0.508	0.564
0.38	0.299	0.363	0.422	0.477	0.527
0.42	0.276	0.328	0.376	0.421	0.462
0.44	0.265	0.311	0.355	0.395	0.433
0.46	0.254	0.296	0.335	0.371	0.405
0.48	0.244	0.281	0.316	0.349	0.379
0.50	0.233	0.267	0.298	0.327	0.355
0.52	0.224	0.253	0.281	0.307	0.332
0.54	0.214	0.240	0.265	0.288	0.310
0.56	0.205	0.228	0.249	0.270	0.290
0.58	0.196	0.216	0.235	0.253	0.271
0.60	0.187	0.205	0.222	0.238	0.253

Table 10.7 Izod Impact Test Geometric Crack Factors \bar{a}

a/D	$2L/D=4$	$2L/D=6$	$2L/D=8$	$2L/D=10$	$2L/D=12$
0.06	1.540	1.744	1.850	2.040	—
0.08	1.273	1.400	1.485	1.675	1.906
0.10	1.060	1.165	1.230	1.360	1.570
0.12	0.911	1.008	1.056	1.153	1.294
0.14	0.795	0.890	0.932	1.010	1.114
0.16	0.708	0.788	0.830	0.900	0.990
0.18	0.650	0.706	0.741	0.809	0.890
0.20	0.600	0.642	0.670	0.730	0.810
0.22	0.560	0.595	0.614	0.669	0.750
0.24	0.529	0.555	0.572	0.617	0.697
0.26	0.500	0.525	0.538	0.577	0.656
0.28	0.473	0.500	0.510	0.545	0.618
0.30	0.452	0.480	0.489	0.519	0.587
0.32	0.434	0.463	0.470	0.500	0.561
0.34	0.420	0.446	0.454	0.481	0.538
0.36	0.410	0.432	0.440	0.468	0.514
0.38	0.397	0.420	0.430	0.454	0.494
0.40	0.387	0.410	0.420	0.441	0.478
0.42	0.380	0.400	0.411	0.431	0.460
0.44	0.375	0.396	0.402	0.423	0.454
0.46	0.369	0.390	0.395	0.415	0.434
0.48	0.364	0.385	0.390	0.408	0.422
0.50	0.360	0.379	0.385	0.399	0.411

Using the relation in Eq. 10.20 with Eq. 10.28 we can write

$$J_{Ic} = \frac{2U_c}{A} \quad (10.29)$$

where $t(w-a)$ was replaced by A or the cross-sectional area of the specimen where fracture occurs. Figure 10.42 gives results for U_c as a function of A for high-impact polystyrene. The results show close agreement between the Charpy and Izod test methods and a linear correlation exists, as predicted with Eq. 10.29.

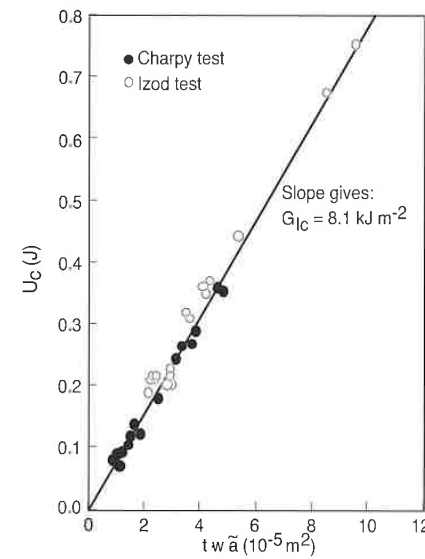


Figure 10.41 Elastic energy absorbed at impact fracture as a function of test specimen cross-sectional geometry for a medium-density polyethylene.

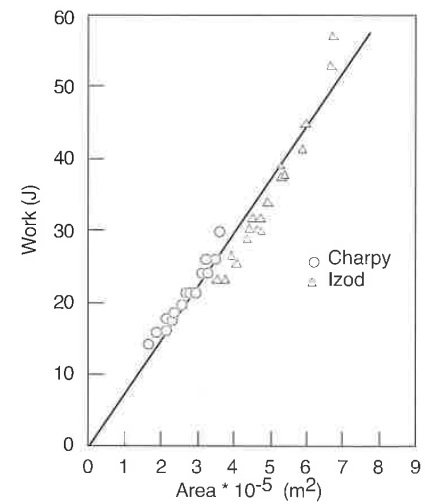


Figure 10.42 Elastic energy absorbed as a function of cross-sectional area for a high impact polystyrene test specimen.

10.4 Creep Rupture

During creep, a loaded polymer component will gradually increase in length until fracture or failure occurs. This phenomenon is usually referred to as *creep rupture* or, sometimes, as *static fatigue*. During creep, a component is loaded under a constant stress, constantly straining until the material cannot withstand further deformation, causing it to rupture. At high stresses, the rupture occurs sooner than at lower stresses. However, at low enough stresses, failure may never occur. The time it takes for a component or test specimen to fail depends on temperature, load, manufacturing process, environment, etc. It is important to point out that damage is often present and visible before creep rupture occurs. This is clearly demonstrated in Fig. 10.43 [7], which presents isochronous creep curves for polymethyl methacrylate at three different temperatures. The regions of linear and non-linear viscoelasticity and of visual damage are highlighted in the figure.

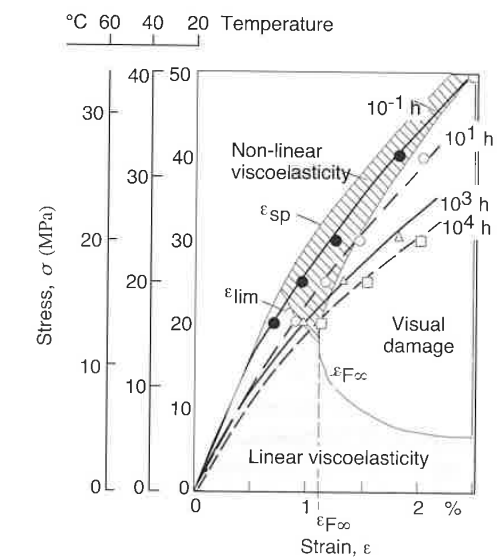


Figure 10.43 Isochronous creep curves for PMMA at three different temperatures.

10.4.1 Creep Rupture Tests

The standard test to measure creep rupture is the same as the creep test discussed in the previous chapter. Results from creep rupture tests are usually presented in graphs of applied stress versus the logarithm of time to rupture. A sample of creep rupture behavior for several thermoplastics is presented in Fig. 10.44 [21]. As the scale in the figure suggests, the tests were carried out with loadings that cause the material to fail within a few weeks. An example of a creep rupture test that ran for 10 years is shown in Fig. 10.45 [22, 23]. Here, the creep rupture of high density polyethylene pipes under internal pressures was tested at different temperatures. Two general regions with different slopes become obvious in the plots. The points to the left of the knee represent pipes that underwent a ductile failure, whereas those points to the right represent the pipes that had a brittle failure. As pointed out, generating a graph such as the one presented in Fig. 10.45, is an extremely involved and lengthy task, that takes several years of testing.⁵ Usually, these types of tests are carried out to 1,000 h (6 weeks) or 10,000 h (60 weeks) as shown in Fig. 10.46⁶ for a polyamide 6 with 30% glass fibers tested at different temperatures. Once the steeper slope, which is typical of the brittle fracture has been reached, the line can be extrapolated with some degree of confidence to estimate values of creep rupture at future times.

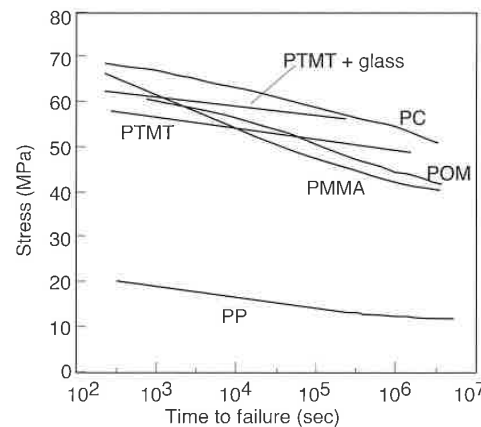


Figure 10.44 Creep rupture behavior for various thermoplastics.

⁵ These tests were done between 1958 and 1968 at Hoechst AG, Germany.

⁶ Courtesy: Bayer AG.

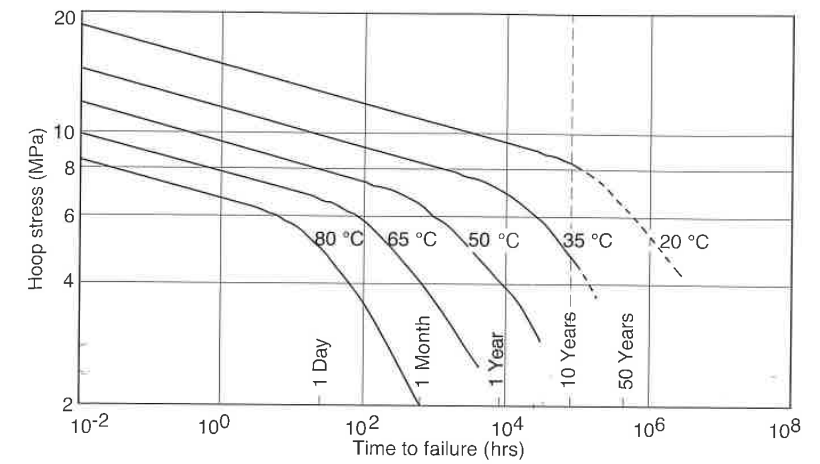


Figure 10.45 Creep rupture behavior as a function of temperature for a high density polyethylene.

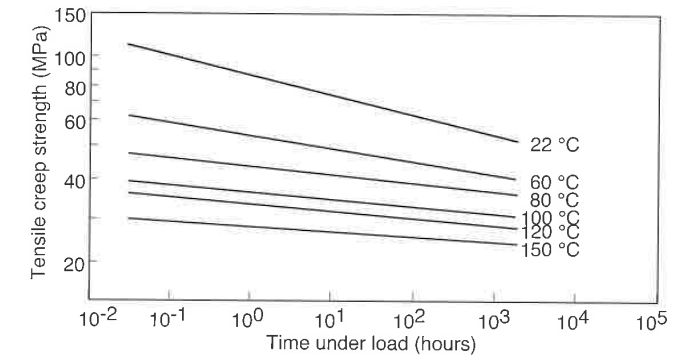


Figure 10.46 Creep rupture behavior as a function of temperature for a polyamide 6 with 30% glass fibers (Durethan BKV 30).

Although the creep test is considered a long term test, in principle it is difficult to actually distinguish it from monotonic stress strain tests or even impact tests. In fact, one can plot the full behavior of the material, from impact to creep, on the same graph as shown for PMMA under tensile loads at room temperature in Fig. 10.47 [7].

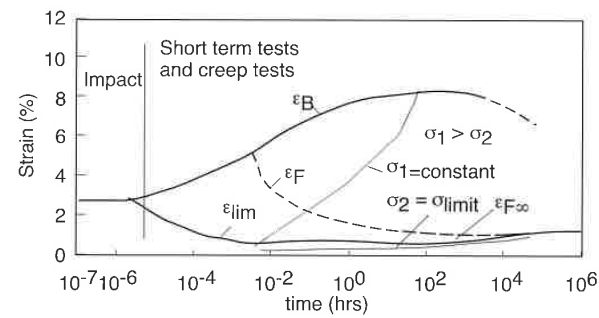


Figure 10.47 Plot of material behavior at room temperature, from impact to creep, for a PMMA under tensile loads.

The figure represents strain as a function of the logarithm of time. The strain line that represents rupture is denoted by ϵ_B . This line represents the maximum attainable strain before failure as a function of time. Obviously, a material tested under an impact tensile loading will strain much less than the same material tested in a creep test. Of interest in Fig. 10.47 are the two constant stress lines denoted by σ_1 and σ_2 . The following example will help the reader interpret Fig. 10.47. It can be seen that a PMMA specimen loaded to a hypothetical stress of σ_1 will behave as a linear viscoelastic material up to a strain of 1%, at which point the first microcracks start forming or the craze nucleation begins. The crazing appears a little later after the specimen's deformation is slightly over 2%. The test specimen continues to strain for the next 100 h until it ruptures at a strain of about 8%. From the figure it can be deduced that the first signs of crazing can occur days and perhaps months or years before the material actually fractures. The stress line denoted by σ_2 , where $\sigma_1 > \sigma_2$, is a limiting stress under which the component will not craze. Figure 10.47 also demonstrates that a component loaded at high speeds (i.e., impact) will craze and fail at the same strain. A limiting strain of 2.2% is shown.

Since these tests take a long time to perform, it is often useful to test the material at higher temperatures, where a similar behavior occurs in a shorter period of time. Figure 10.48 [7] shows tests performed on PMMA samples at five different temperatures. When comparing the results in Fig. 10.48 to the curve presented in Fig. 10.47, a clear time-temperature superposition becomes visible. In the applied stress versus logarithm of time to rupture curves, such as the one shown in Fig. 10.45, the time-temperature superposition is also evident.

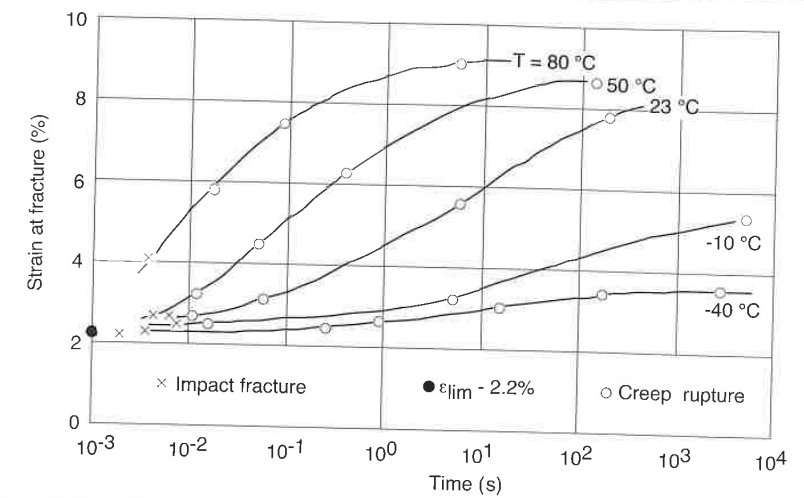


Figure 10.48 Strain at fracture for a PMMA in creep tests at various temperatures.

10.4.2 Fracture Mechanics Analysis of Creep Rupture

Crack growth rates during static tests have been found to have a power law relation with the stress intensity factor K_{Ic} , as

$$\frac{da}{dt} = AK_{Ic}^m \quad (10.30)$$

where A and m are material properties and K_{Ic} can be computed using Eq. 10.3 which results in

$$\frac{da}{dt} = A(Y\sigma)^m (\pi a)^{m/2} \quad (10.31)$$

By ignoring the time it takes for crack initiation, this equation may be used to predict a conservative time for creep rupture of a polymer component. If we integrate Eq. 10.31, we can predict the time it takes for a crack to grow from a length a_1 to a length a_2 by using

$$t = \frac{2(a_1^{1-m/2} - a_2^{1-m/2})}{[(m-2)C_1(Y\sigma\sqrt{\pi})^m]} \quad (10.32)$$

Experimental evidence shows that for slow crack growth, the value of m is large, and ranges between 7 and 25. Hence, the time it takes for a crack to grow between a_1 and a_2 is dominated by the initial crack length, because a small crack will grow much slower than a large one.

10.5 Fatigue

Dynamic loading of any material that leads to failure after a certain number of cycles is called *fatigue* or *dynamic fatigue*. Dynamic fatigue is of extreme importance since a cyclic or fluctuating load will cause a component to fail at much lower stresses than it does under monotonic loads.

10.5.1 Fatigue Test Methods

The standard fatigue tests for polymeric materials are the ASTM-D 671 test and the DIN 50100 test. In the ASTM test, a cantilever beam, shown in Fig. 10.49 [19], is held in a vise and bent at the other end by a yoke which is attached to a rotating variably eccentric shaft. A constant stress throughout the test region in the specimen is achieved by its triangular shape.

Fatigue testing results are plotted as stress amplitude versus number of cycles to failure. These graphs are usually called *S-N curves*, a term inherited from metal fatigue testing [24]. Figure 10.50 [25] presents S-N curves for several thermoplastic and thermoset polymers tested at a 30-Hz frequency and about a zero mean stress, σ_m .

We must point out here, that most fatigue data presented in the literature and in resin supplier data sheets does not present the frequency, specimen geometry or environmental conditions at which the tests were performed. Hence, such data is not suitable for use in design. The data we present in this section is only intended to illustrate the various problems that arise when measuring fatigue life of a polymer. The information should also serve to reflect trends and as a comparison between various materials and conditions.

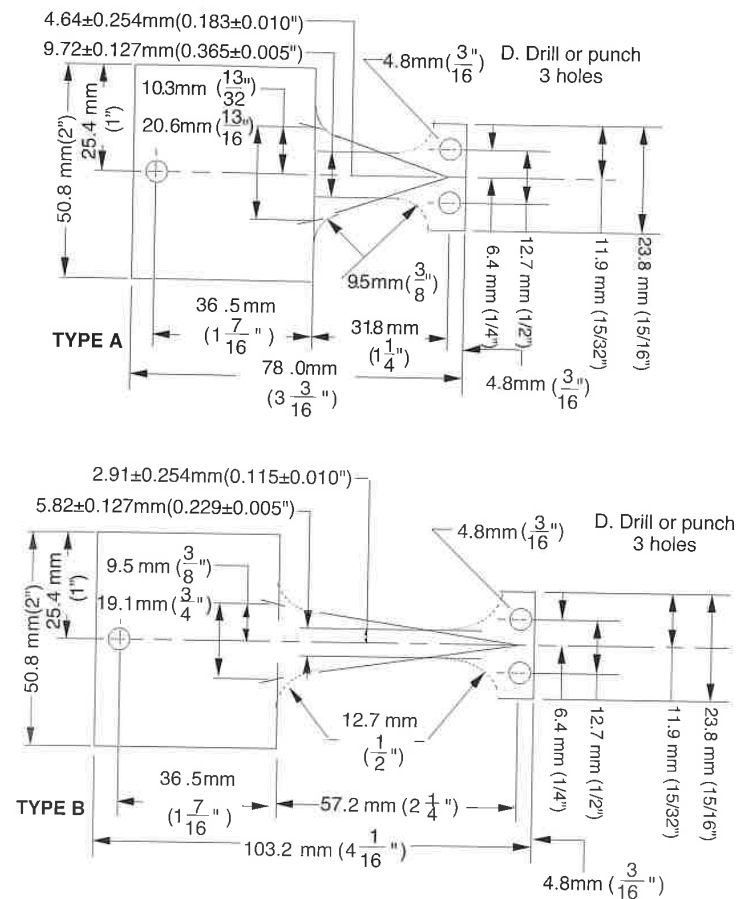


Figure 10.49 ASTM constant force fatigue test specimens.

Fatigue in plastics is strongly dependent on the environment, the temperature, the frequency of loading, the surface, etc. For example, due to surface irregularities and scratches, crack initiation at the surface is more likely in a polymer component that has been machined than in one that was injection molded. As mentioned in Chapter 5, an injection molded article is formed by several layers of different orientation. In such parts the outer layers act as a protective skin that inhibits crack initiation. In an injection molded article, cracks are more likely to initiate inside the component by defects such as weld

lines and filler particles. The gate region is also a prime initiator of fatigue cracks. Corrosive environments also accelerate crack initiation and failure via fatigue. Corrosive environments and weathering will be discussed in more detail later in this chapter.

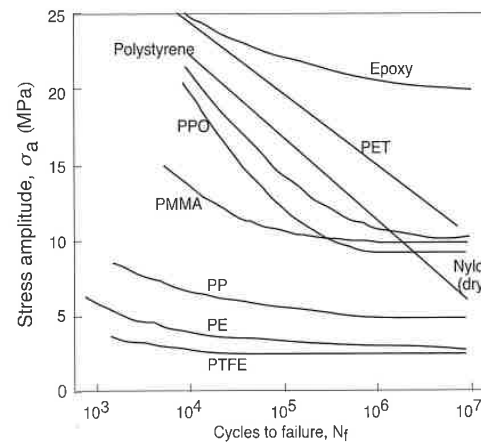


Figure 10.50 Stress-life (S-N) curves for several thermoplastic and thermoset polymers tested at a 30-Hz frequency about a zero mean stress.

It is interesting to point out in Fig. 10.50 that thermoset polymers show a higher fatigue strength than thermoplastics. An obvious cause for this is their greater rigidity. However, more important is the lower internal damping or friction, which reduces temperature rise during testing. Temperature rise during testing is one of the main factors that lead to failure when experimentally testing thermoplastic polymers under cyclic loads. The heat generation during testing is caused by the combination of internal frictional or hysteretic heating and low thermal conductivity. At a low frequency and low stress level, the temperature inside the polymer specimen will rise and eventually reach thermal equilibrium when the heat generated by hysteretic heating equals the heat removed from the specimen by conduction. As the frequency is increased, viscous heat is generated faster, causing the temperature to rise even further. This phenomenon is shown in Fig. 10.51 [21] in which the temperature rise during uniaxial cyclic testing of polyacetal is plotted. After thermal equilibrium has been reached, a specimen eventually fails by conventional brittle fatigue, assuming the stress is above the endurance limit.

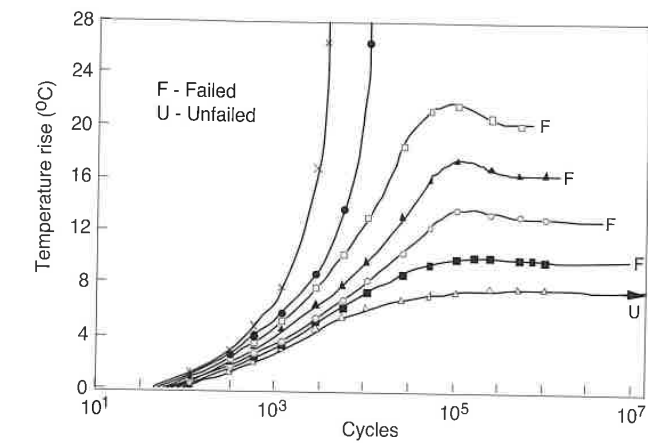


Figure 10.51 Temperature rise during uniaxial cycling under various stresses at 5-Hz.

However, if the frequency or stress level is increased even further, the temperature will rise to the point at which the test specimen softens and ruptures before reaching thermal equilibrium. This mode of failure is usually referred to as *thermal fatigue*. This effect is clearly demonstrated in Fig. 10.52 [21]. The points marked T denote those specimens that failed due to thermal fatigue. The other points represent the specimens that failed by conventional mechanical fatigue. A better picture of how frequency plays a significant role in fatigue testing of polymeric materials is generated by plotting results such as those shown in Fig. 10.52 [21] for several frequencies (Fig. 10.53 [21]). The temperature rise in the component depends on the geometry and size of test specimen. For example, thicker specimens will cool slower and are less likely to reach thermal equilibrium. Similarly, material around a stress concentrator will be subjected to higher stresses which will result in temperatures that are higher than the rest of the specimen leading to crack initiation caused by localized thermal fatigue. To neglect the effect of thermal fatigue, cyclic tests with polymers must be performed at very low frequencies that make them much lengthier than those performed with metals and other materials which have high thermal conductivity.

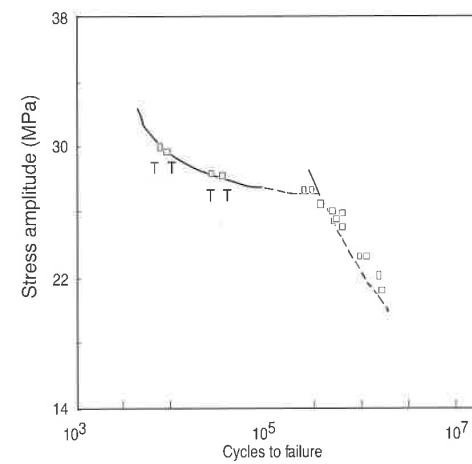


Figure 10.52 Fatigue and thermal failures in acetal tested at 1.67 Hz.

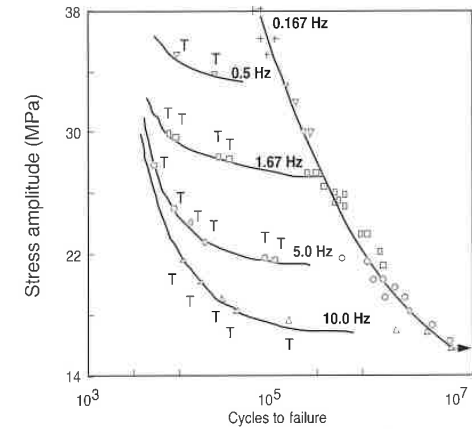


Figure 10.53 Fatigue and thermal failures in acetal tested at various frequencies.

As mentioned earlier, stress concentrations have a great impact on the fatigue life of a component. Figures 10.54⁷ and 10.55⁶ compare S-N curves for uPVC and polyamide 66, respectively, for specimens with and without a 3 mm

⁷ All courtesy of Bayer AG, Germany.

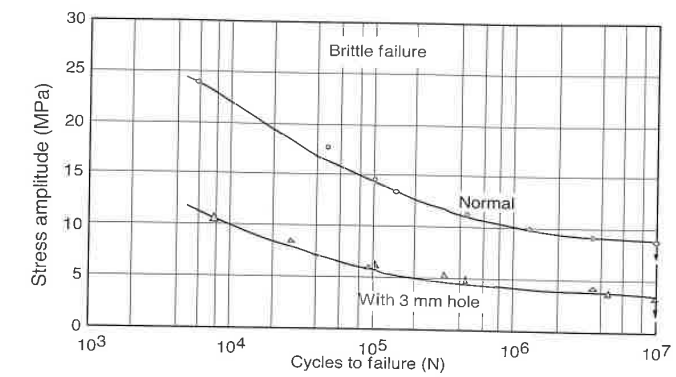


Figure 10.54 Fatigue curves for an uPVC using specimens with and without 3 mm hole stress concentrators tested at 23 °C and 7-Hz with a zero mean stress.

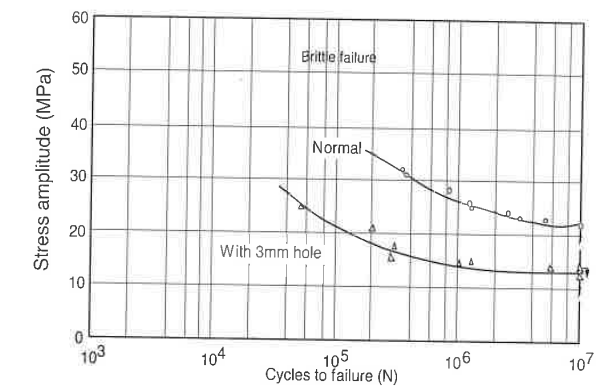


Figure 10.55 Fatigue curves for polyamide 66 (Durethan A30S) using specimens with and without 3 mm hole stress concentrators tested at 23 °C and 7-Hz with a zero mean stress.

circular hole acting as a stress concentrator. Material irregularities caused by filler particles or by weld lines also affect the fatigue of a component. Figures 10.56⁶ and 10.57⁶ compare S-N curves for regular PC and ABS test specimens to fatigue behavior of specimens with a weld line and specimens with a 3-mm circular hole.

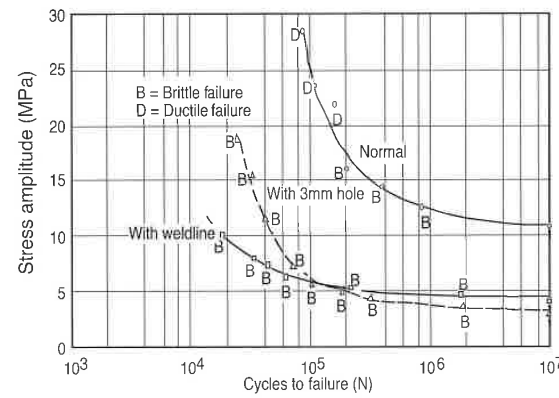


Figure 10.56 Fatigue curves for polycarbonate (Makrolon 2800) using regular specimens and specimens with 3 mm hole stress concentrators and weldlines tested at 23 °C and 7-Hz with a zero mean stress.

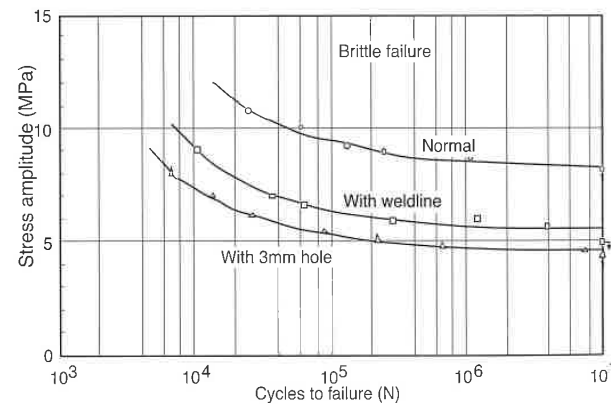


Figure 10.57 Fatigue curves for ABS (Novodur PH/AT) using regular specimens and specimens with 3 mm hole stress concentrators and weldlines tested at 23 °C and 7-Hz with a zero mean stress.

Up to this point, we assumed a zero mean stress, σ_m . However, many polymer components that are subjected to cyclic loading have other loads and stresses applied to them, leading to non-zero mean stress values. This superposition of two types of loading will lead to a combination of creep, caused by the mean stress, and fatigue, caused by the cyclic stress, σ_a . Test results from experiments with cyclic loading and non-zero mean stresses are complicated by the fact that some specimens fail due to creep and others due to conventional brittle fatigue. Figure 10.58 illustrates this phenomenon for both cases with and without thermal fatigue, comparing them to experiments in which a simple static loading is applied. For cases with two or more dynamic loadings with different stress or strain amplitudes, a similar strain deformation progression is observed. Figure 10.59 [26] presents the strain progression in polyacetal specimens in which two stress amplitudes, one above and one below the linear viscoelastic range of the material, are applied. The strain progression, $\Delta\epsilon$, is the added creep per cycle caused by different loadings, similar to ratcheting effects in metal components where different loadings are combined.

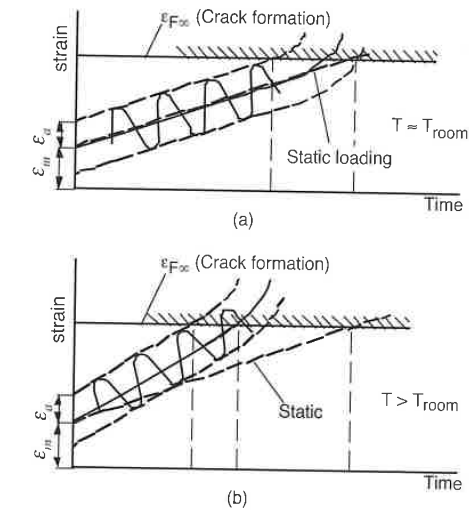


Figure 10.58 Creep and thermal fatigue effects during cyclic loading.

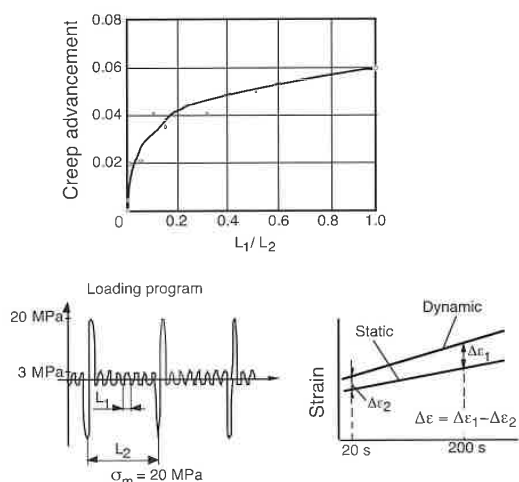


Figure 10.59 Strain progression in polyacetal specimens during fatigue tests with two stress amplitudes.

Fiber-reinforced composite polymers are stiffer and less susceptible to fatigue failure. Reinforced plastics have also been found to have lower hysteretic heating effects, making them less likely to fail by thermal fatigue. Figure 10.60 [27] presents the flexural fatigue behavior for glass fiber filled and unfilled polyamide 66 tested at 20 °C and a 0.5 Hz frequency with a zero mean stress. Parallel to the fiber orientation, the fatigue life was greater than the life of the specimens tested perpendicular to the orientation direction and the unfilled material specimens. The fatigue life of the unfilled specimen and the behavior perpendicular to the orientation direction were similar. However, the unfilled material failed by thermal fatigue at high stresses, whereas both the specimens tested perpendicular and parallel to the orientation direction failed by conventional fatigue at high stress levels. Fiber reinforced systems generally follow a sequence of events during failure consisting of debonding, cracking, and separation [28]. Figure 10.61 [29] clearly demonstrates this sequence of events with a glass-filled polyester mat tested at 20 °C and a frequency of 1.67 Hz. In most composites, debonding occurs after just a few cycles. It should be pointed out that often reinforced polymer composites do not exhibit an endurance limit, making it necessary to use factors of safety between 3 and 4. The fracture by fatigue is generally preceded by cracking of the matrix material, which gives a visual warning of imminent failure. It is important to mention that the fatigue life of thermoset composites is also affected by temperature. Figure 10.62 [30] shows the tensile strength versus

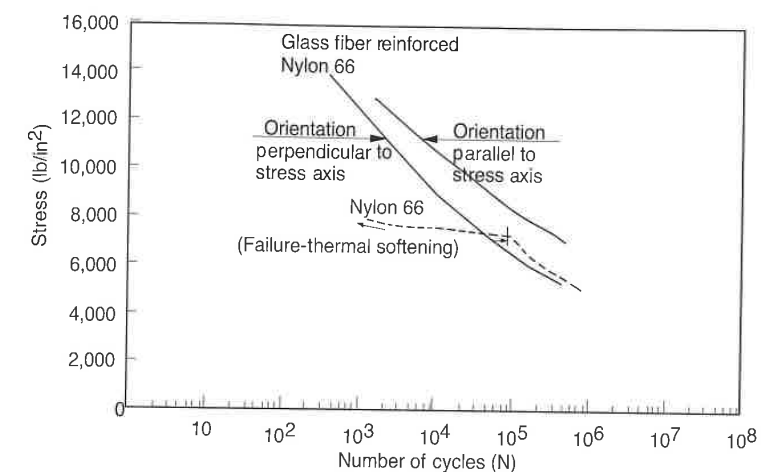


Figure 10.60 Flexural fatigue curves for a polyamide 66 and a glass fiber filled polyamide 66 tested at 20 °C and 0.5 Hz with a zero mean stress.

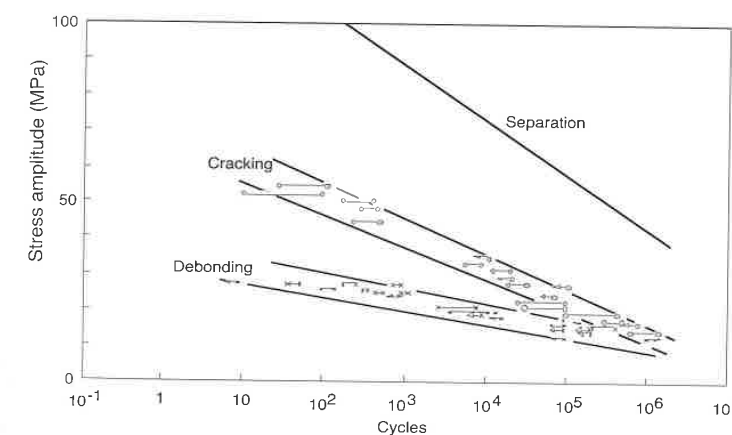


Figure 10.61 Fatigue curves for a glass filled polyester mat tested at 20 °C and a frequency of 1.67 Hz.

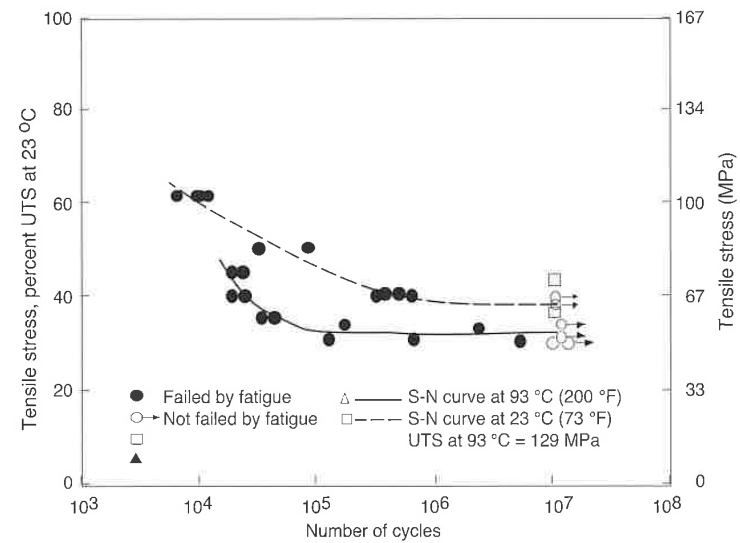


Figure 10.62 Fatigue curves for a 50% by weight glass fiber reinforced polyester resin sheet molding compound tested at 23 °C and 93 °C and 10 Hz.

number of cycles to failure for a 50% glass fiber filled unsaturated polyester tested at 23 °C and 93 °C. At ambient temperature, the material exhibits an endurance limit of about 65 MPa, which is reduced to 52 MPa at 93 °C.

10.5.2 Fracture Mechanics Analysis of Fatigue Failure

Crack growth rates during cyclic fatigue tests are related to the stress intensity factor difference, ΔK_{Ic} ,

$$\frac{da}{dt} = B(\Delta K_{Ic})^n \tag{10.33}$$

where B and n are material properties and $\Delta K_{Ic} = K_{Ic,max} - K_{Ic,min}$ can be computed using Eq. 10.3 with the maximum and minimum alternating stresses. Crack growth behavior for several polymers is shown in Fig. 10.63 [29, 31]. Hertzberg and Manson [29] also show that for some materials, the crack growth rate is reduced somewhat with increasing test frequency.

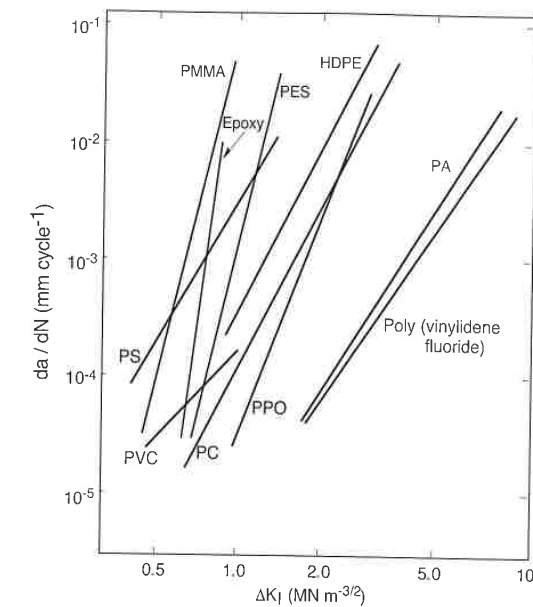


Figure 10.63 Crack growth rate during fatigue for various polymers.

10.6 Friction and Wear

Friction is the resistance that two surfaces experience as they slide or try to slide past each other. Friction can be dry (i.e., direct surface-surface interaction) or lubricated, where the surfaces are separated by a thin film of a lubricating fluid.

The force that arises in a dry friction environment can be computed using Coulomb's law of friction as

$$F = \mu N \tag{10.34}$$

where F is the force in surface or sliding direction, N the normal force, and μ the coefficient of friction. Coefficients of friction between several polymers and different surfaces are listed in Table 10.8 [7]. However, when dealing with polymers, the process of two surfaces sliding past each other is complicated by the fact that enormous amounts of frictional heat can be generated and stored near the surface due to the low thermal conductivity of the material. The

analysis of friction between polymer surfaces is complicated further by environmental effects such as relative humidity and by the likeliness of a polymer surface to deform when stressed, such as shown in Fig. 10.64 [7]. The top two figures illustrate metal-metal friction, whereas the bottom figures illustrate metal-polymer friction.

Table 10.8 Coefficient of Friction for Various Polymers

Specimen	Partner	Velocity (mm/s)					
		0.03	0.1	0.4	0.8	3.0	10.6
<i>Dry friction</i>							
PP ⁱ	PP ^s	0.54	0.65	0.71	0.77	0.77	0.71
PA ⁱ	PA ⁱ	0.63	-	0.69	0.70	0.70	0.65
PP ^s	PP ^s	0.26	0.29	0.22	0.21	0.31	0.27
PA ^m	PA ^m	0.42	-	0.44	0.46	0.46	0.47
Steel	PP ^s	0.24	0.26	0.27	0.29	0.30	0.31
Steel	PA ^m	0.33	-	0.33	0.33	0.30	0.30
PP ^s	Steel	0.33	0.34	0.37	0.37	0.38	0.38
PA ^m	Steel	0.39	-	0.41	0.41	0.40	0.40
<i>Water lubricated</i>							
PP ^s	PP ^s	0.25	0.26	0.29	0.30	0.28	0.31
PA ^m	PA ^m	0.27	-	0.24	0.22	0.21	0.19
Steel	PP ^s	0.23	0.25	0.26	0.26	0.26	0.22
PP ^s	Steel	0.25	0.25	0.26	0.26	0.25	0.25
PA ^m	Steel	0.20	-	0.23	0.23	0.22	0.18
<i>Oil lubricated</i>							
PP ^s	PP ^s	0.29	0.26	0.24	0.25	0.22	0.21
PA ^m	PA ^m	0.22	-	0.15	0.13	0.11	0.08
Steel	PP ^s	0.17	0.17	0.16	0.16	0.14	0.14
Steel	PA ^m	0.16	-	0.11	0.09	0.08	0.08
PP ^s	Steel	0.31	0.30	0.30	0.29	0.27	0.25
PA ^m	Steel	0.26	-	0.15	0.12	0.07	0.04

Note ⁱ = injection molded, ^s = sandblasted, ^m = machined.

Temperature plays a significant role on the coefficient of friction μ as clearly demonstrated in Fig. 10.65 for polyamide 66 and polyethylene. In the case of polyethylene, the friction first decreases with temperature. At 100 °C the friction increases because the polymer surface becomes tacky. The friction coefficient starts to drop as the melt temperature is approached. A similar behavior is encountered with the polyamide curve.

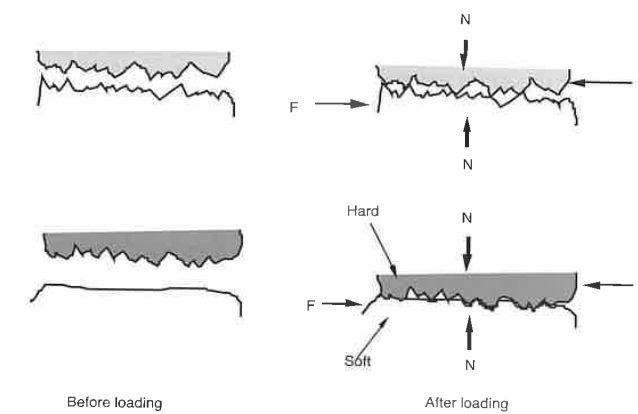


Figure 10.64 Effect of surface finish and hardness on frictional force build-up.

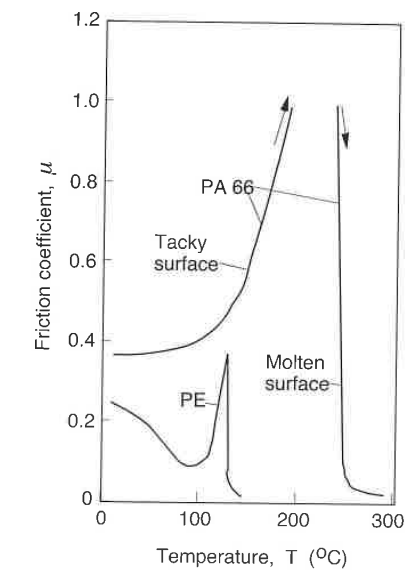


Figure 10.65 Temperature effect on coefficient of friction for a polyamide 66 and a high density polyethylene.

As mentioned earlier, temperature increases can be caused by the energy released by the frictional forces. A temperature increase in time, due to friction between surfaces of the same material, can be estimated using

$$\Delta T = \frac{2\dot{Q}\sqrt{t}}{\sqrt{\pi}\sqrt{k\rho C_p}} \quad (10.35)$$

where k is the thermal conductivity of the polymer, ρ the density, C_p the specific heat and the rate of energy created by the frictional forces which can be computed using

$$\dot{Q} = Fv \quad (10.36)$$

where v is speed between the sliding surfaces.

Wear is also affected by the temperature of the environment. Figure 10.66 shows how wear rates increase dramatically as the surface temperature of the polymer increases, causing it to become tacky.

Table 10.9 [32] presents relative volumetric wear values for selected polymers and beechwood using the volumetric wear of steel St 37 as a reference.

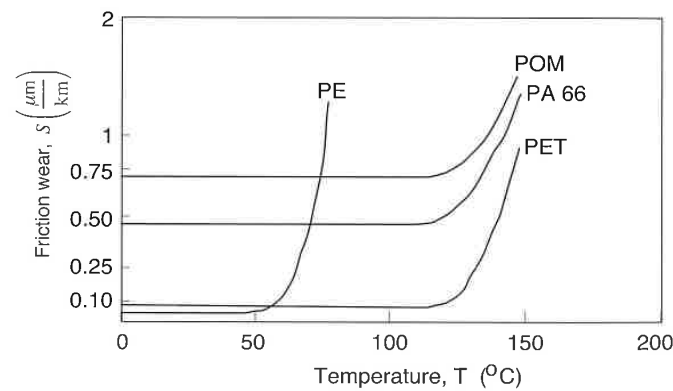


Figure 10.66 Wear as a function of temperature for various thermoplastics.

8 Courtesy of BASF.

Table 10.9 Relative Volumetric Wear

Polymer	Density (g/cm ³)	Wear/Wear _{steel}
Steel	7.45	1.0
Beechwood	0.83	17.9
PMMA	1.31	11.2
PVC-U	1.33	5.8
HDPE	0.92	3.8
PP	0.90	2.8
HDPE	0.95	2.1
PA 66	1.13	1.0
UHMW-HDPE	0.94	0.6

10.7 Stability of Polymer Structures

The failure of certain structures is often determined by the stiffness of the structural element and not by the strength of the material. Such a failure is commonly referred to as *buckling*. The common example of buckling is the failure of a slender column under compressive loads. Slender columns with hinged ends have a critical load, F_{crit} , defined by

$$F_{crit} = \frac{\pi^2 EI}{L^2} \quad (10.37)$$

where E is the modulus, I the area moment of inertia and L the length of the column. If we use the relation $I = Ar^2$, where A is the cross-sectional area of the column and r is the radius of gyration, we can rewrite Eq. 10.37 as

$$\frac{F_{crit}}{A} = \frac{\pi^2 EI}{(L/r)^2} = \frac{\pi^2 EI}{\lambda^2} \quad (10.38)$$

where F_{crit}/A is often referred to as critical unit load and λ the slenderness ratio. For a square cross-section of dimensions $a \times a$ the slenderness ratio is defined by

$$\lambda = \frac{L}{a} \sqrt{12} \quad (10.39)$$

Menges and Dolfen performed a series of compression tests on glass fiber reinforced unsaturated polyester specimens of square cross-section. Figure 10.67 [33] presents the unit loads and compressive strains at failure of the composite columns as a function of slenderness ratio. Their experiments demonstrated that at slenderness ratios smaller than 20 the columns failed by a shear delamination mode, while columns with slenderness ratios larger than 20 failed by buckling. Similarly, Gaube and Menges [34] performed experiments with various shell structures. Figure 10.68 presents the critical strain as a function of slenderness ratio. We can see here that in all cases buckling of polymer structures occurred below the value predicted by classical stability theory.

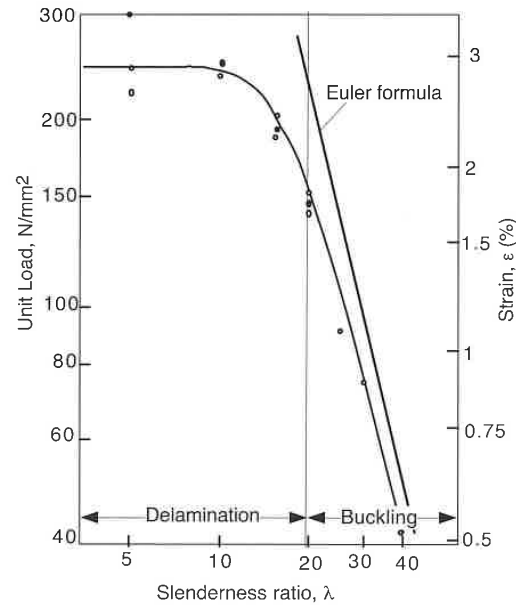


Figure 10.67 Delamination and buckling of glass reinforced UPE columns.

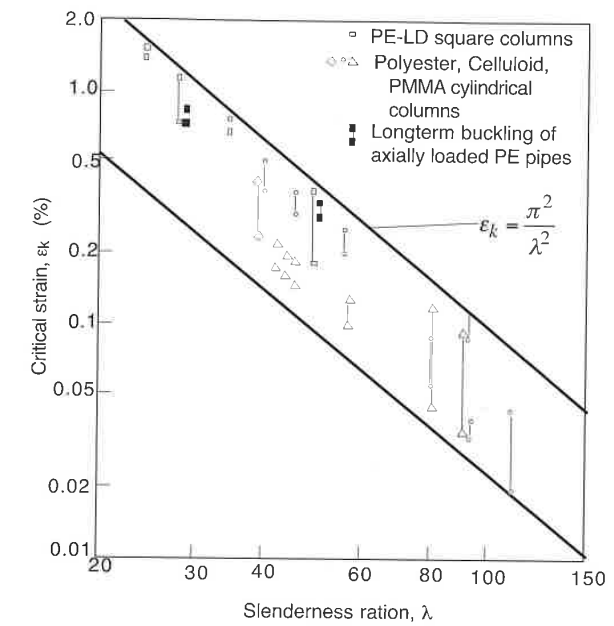


Figure 10.68 Buckling of columns and tubes.

10.8 Environmental Effects on Polymer Failure

The environment or the media in contact with a loaded or unloaded component plays a significant role on its properties, life span, and mode of failure. The environment can be a natural one, such as rain, hail, solar ultra-violet radiation, extreme temperatures, etc., or an artificially created one, such as solvents, oils, detergents, high temperature environments, etc. Damage in a polymer component due to natural environmental influences is usually referred to as *weathering*.

10.8.1 Weathering

When exposed to the elements, polymeric materials begin to exhibit environmental cracks, which lead to early failure at stress levels significantly

lower than those in the absence of these environments. Figure 10.69 [35] shows an electron micrograph of the surface of a high-density polyethylene beer crate after nine years of use and exposure to weathering. The surface of the HDPE exhibits brittle cracks, which resulted from ultra violet rays, moisture, and extremes in temperature.



Figure 10.69 Electron micrograph of the surface of a high density polyethylene beer crate after nine years of use and exposure to weathering.

Standard tests such as the DIN 53486 test are available to evaluate effects of weathering on properties of polymeric materials. It is often unclear which weathering aspects or what combination of them influence material decay the most. Hence, laboratory tests are often done to isolate individual weathering factors such as ultra-violet radiation. For example, Fig. 10.70 shows the surface of a polyoxymethylene specimen irradiated with ultra violet light for 100 h in a laboratory environment. The DIN 53487 xenotest is a standard test to expose polymer test specimens to UV radiation in a controlled environment. Figure 10.71 is a plot of impact strength of notched PMMA specimens as a function of hours of UV radiation exposure in a controlled DIN 53487 test and years of weathering under standard DIN 53486 conditions. The correlation between the two tests is clear. The ASTM-D 4674 test evaluates the color stability of polymer specimens exposed to ultra violet radiation. Standard tests also exist to test materials for specific applications such as the ASTM-D 2561 test, which evaluates the environmental stress cracking resistance of blow molded polyethylene containers.

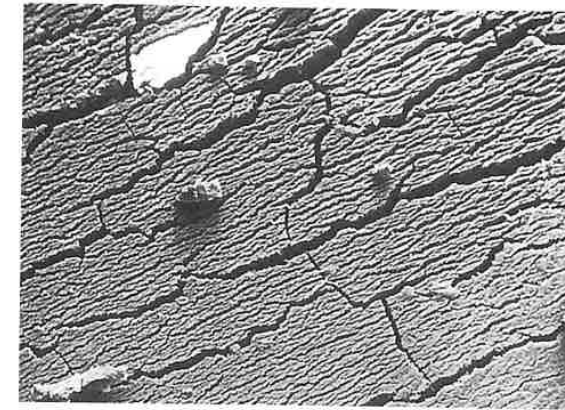


Figure 10.70 Surface of a polyoxymethylene specimen irradiated with ultra violet light for 100 h in a laboratory environment.

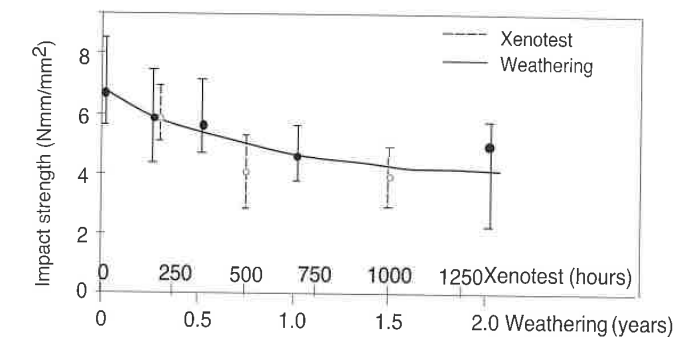


Figure 10.71 Impact strength of notched PMMA specimens as a function of hours of UV radiation exposure in a controlled test and weathering exposure time.

As can be seen, the effect of ultra violet radiation, moisture, and extreme temperature is detrimental to the mechanical properties of plastic parts. One example in which weathering completely destroys the strength properties of a material is shown for PVC in Fig. 10.72. The figure presents the decay of the impact strength of PVC pipes exposed to weathering in the United Kingdom [36]. As can be seen, the impact strength rapidly decreases in the first six months and is only 11% of its original value after only two years. The location and climate of a region can play a significant role on the weathering of polymer components. Figure 10.73 [36] shows the decrease in impact strength

of rigid PVC as a function of time at five different sites. After five years of weathering, the PVC exposed in Germany still has 95% of its original impact strength, whereas the samples exposed in Singapore have less than 5% of their initial strength. The degradation in PVC samples is also accompanied by discoloration as presented in Fig. 10.74 [36]. The figure shows discoloration of white PVC as a function of time at various locations. The samples exposed in Arizona showed significantly higher discoloration than those exposed in Pennsylvania and Florida.

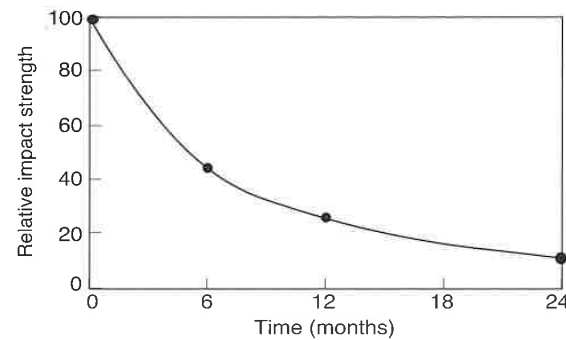


Figure 10.72 Impact strength of PVC pipe as a function weathering exposure time in the United Kingdom.

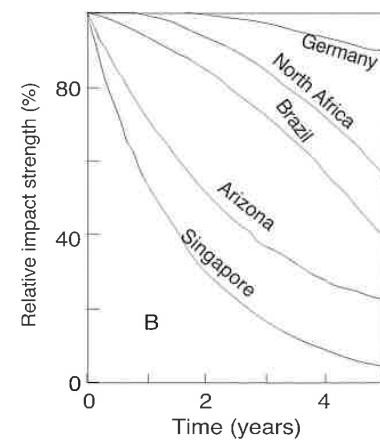


Figure 10.73 Impact strength as a function of weathering time of uPVC exposed in different geographic locations.

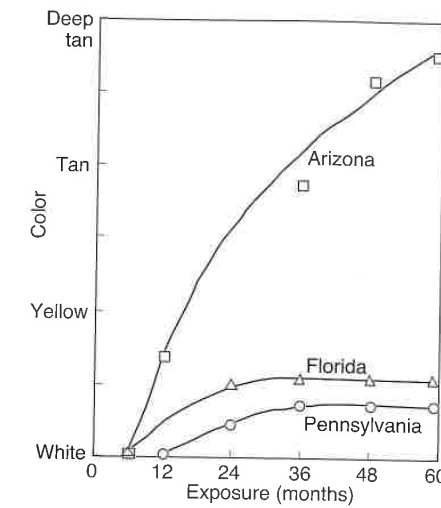


Figure 10.74 Discoloration as a function of weathering time of white PVC exposed in different geographic locations.

The strength losses and discoloration in a weathering process are mainly attributed to the ultra-violet rays received from sunshine. This can be demonstrated by plotting properties as a function of actual sunshine received instead of time exposed. Figure 10.75 [37] is a plot of percent of initial impact strength for an ABS as a function of total hours of exposure to sun light in three different locations: Florida, Arizona, and West Virginia. The curve reveals the fact that by "normalizing" the curves with respect to exposure to actual sunshine, the three different sites with three completely different weather conditions⁹ lead to the same relation between impact strength and total sunshine.

⁹ Florida has a subtropical coastal climate with a yearly rainfall of 952 mm and sunshine of 2750 hours. Arizona has a hot dry climate with 116 mm of rainfall and 3850 hours of sunshine. West Virginia has a milder climate with 992 mm of rainfall and 2150 hours of sunshine [28].

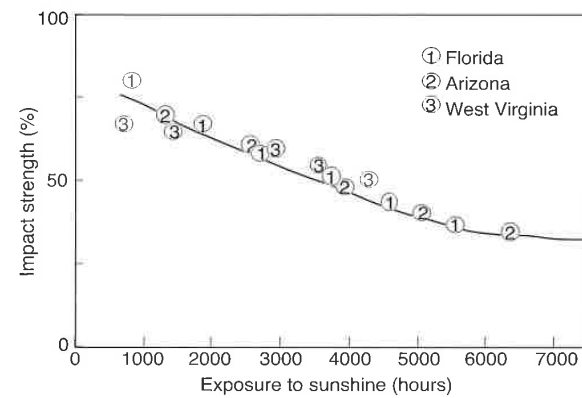


Figure 10.75 Impact strength of an ABS as a function of hours to actual sunshine exposure.

The effect of weathering can often be mitigated with the use of pigments, such as TiO_2 or soot, which absorb ultra violet radiation, making it more difficult to penetrate the surface of a polymer component. The most important one is soot. For example, ABS with white and black pigments exhibit a noticeable improvement in properties after exposure to ultra violet radiation. Figure 10.76 [37] shows the reduction of impact strength in ABS samples as a function of exposure time to sunshine for four pigment concentrations: 0.5%, 0.7%, 1%, and 2%. It is clear that the optimal pigment concentration is around 1%. Beyond 1% of pigmentation there is little improvement in the properties.

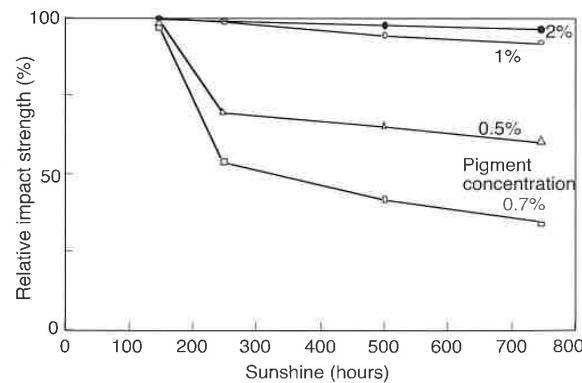


Figure 10.76 Influence of pigment concentration on the impact strength reduction of ABS specimens exposed to weathering.

10.8.2 Chemical Degradation

Liquid environments can have positive and negative effects on the properties of polymeric materials. Some chemicals or solvents can have detrimental effects on a polymer component. Figure 10.77 [25] shows results of creep rupture tests done on PVC tubes as a function of the hoop stress. It can be seen that the life span of the tubes in contact with the iso-octane and isopropanol has been significantly reduced as compared to the tubes in contact with water. The measured data for the pipes that contained iso-octane clearly show a slope reduction with a visible endurance limit, making it possible to do long-life predictions. On the other hand, the isopropanol samples do not exhibit such a slope reduction, suggesting that isopropanol is a harmful environment which acts as a solvating agent and leads to gradual degradation of the PVC surface.

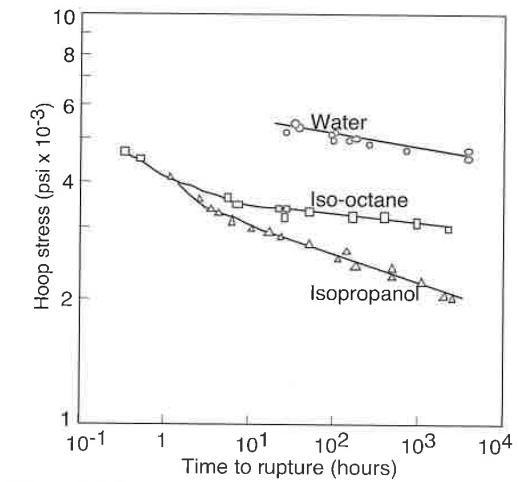


Figure 10.77 Effect of different environments on the stress rupture life of PVC pipe at 23 °C.

The question, of whether a chemical is harmful to a specific polymeric material is one that needs to be addressed if the polymer component is to be placed in a possibly threatening environment. Similar to polymer solutions, a chemical reaction between a polymer and another substance is governed by the Gibbs free energy equation, as discussed in Chapter 5. If the change in enthalpy, ΔH , is negative then a chemical reaction will occur between the polymer and the solvent.

The effect of the solubility parameter of several solvents on the fatigue response of polystyrene samples is presented in Fig. 10.78 [31]. Here, the relation in Eq. 6.24 becomes evident; as the absolute difference between the solubility parameter of polystyrene, which is $9.1 \text{ (cal/cm}^3)^{1/2}$, and the solubility parameter of the solvent decreases, the fatigue life drops significantly.

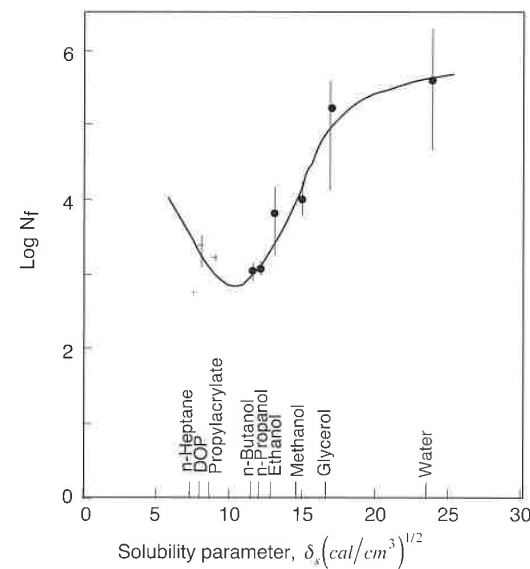


Figure 10.78 Effect of solubility parameter of the surrounding media on the fatigue life of polystyrene specimens.

It should be pointed out again that some substances are more likely to be absorbed by the polymer than others¹⁰. A polymer that is in a soluble environment is more likely to generate stress cracks and fail. This is illustrated in Fig. 10.79 [38], which shows the strain for crack formation in polyphenylene oxide samples as a function of solubility parameter¹¹ of various solutions. The specimens in solutions that were $\pm 1 \text{ (cal/cm}^3)^{1/2}$ away from the solubility parameter of the polymer generated cracks at fairly low strains, whereas those specimens in solutions with a solubility parameter further away from the solubility of the polymer formed crazes at much higher strains.

¹⁰ Please refer to Chapter 13.

¹¹ Please refer to Chapter 6.

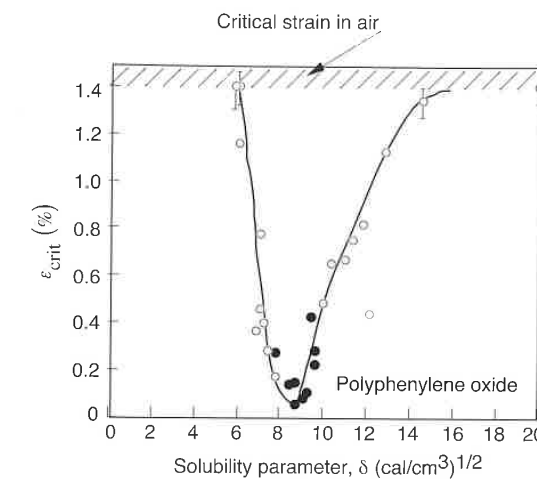


Figure 10.79 Strains at failure as a function of solubility parameter for polyphenylene oxide specimens: (•) cracking, (O) crazing.

Environmental stress cracking or stress corrosion in a polymer component only occurs if crazes or microcracks exist. Hence, stress corrosion in a hostile environment can be avoided if the strain within the component is below the critical strain, ϵ_{fc} .

10.8.3 Thermal Degradation of Polymers

Because plastics are organic materials, they are threatened by chain breaking, splitting off of substituents, and oxidation. This degradation generally follows a reaction which can be described by the Arrhenius principle. The period of dwell or residence time permitted before thermal degradation occurs is given by

$$t_{\text{permitted}} \sim \exp\left(\frac{\Delta}{RT}\right) \quad (10.40)$$

where Δ is the activation energy of the polymer, R the gas constant and T the absolute temperature.

A material that is especially sensitive to thermal degradation is PVC; furthermore, the hydrogen chloride that results during degradation attacks metal parts. Ferrous metals act as a catalyzer and accelerate degradation.

An easy method for determining the flash point of molding batches is by burning the hydrocarbons which are released at certain temperatures. This is shown schematically in Fig. 10.80¹². For PVC one should use a vial with soda lye, instead of a flame, to determine the conversion of chlorine.

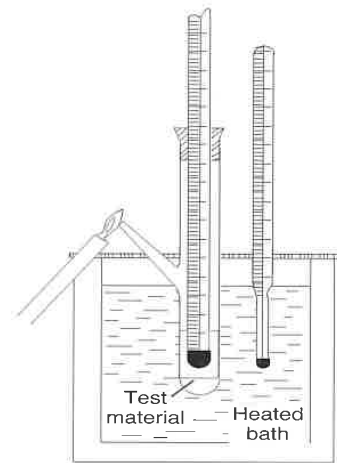


Figure 10.80 Test procedure to determine flash point of polymers.

Thermogravimetry (TGA) is another widely used method to determine the resistance to decomposition or degradation of polymers at high temperatures. For this purpose, the test sample is warmed up in air or in a protective gas while placed on a highly sensitive scale. The change in weight of the test sample is then observed and recorded (see Chapter 3). It is also very useful to observe color changes in a sample while they are heated inside an oven. For example, to analyze the effect of processing additives, polymers are kneaded for different amounts of time, pressed onto a plate, and placed inside a heated oven. The time when a color change occurs is recorded to signify when degradation occurs.

¹² Courtesy of BASF.

Examples

10.1 Charpy Impact tests were performed on PVC samples with crack lengths of 1, 2, 3, 4, and 5 mm. The energy absorbed by the specimen during impact was 0.1, 0.062, 0.046, 0.037 and 0.031 J. The specimen's cross-section was 10 mm x 10 mm, and its length 40 mm. For a PVC modulus of 2 GPa what is the material's fracture toughness?

We must first compute a/D and read \bar{a} from Table 10.6, where $D=10$ mm and $L=40$ mm. Next we can calculate $Dw\bar{a}$ ($Dw\bar{a}$ for the notation used in Table 10.6), where $w=10$ mm. Table 10.10 tabulates all the data.

We can now plot U versus $Dw\bar{a}$ and estimate the fracture toughness from the slope, as shown in Fig. 10.82.

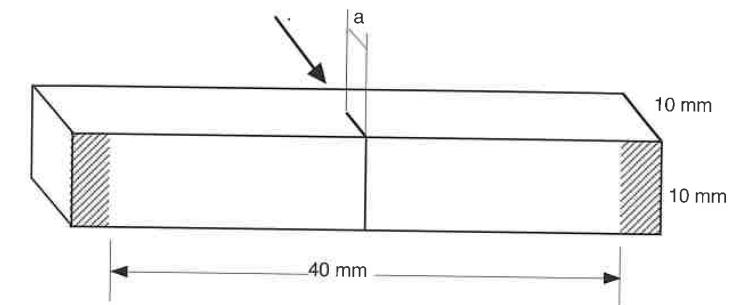


Figure 10.81 Sample geometry for Example 10.1.

Table 10.10 Tabulated data for Example 10.1

a (mm)	a/D	\bar{a}	$Dw\bar{a}$ (m ²)	U (J)
1	0.1	0.781	78.1×10^{-6}	0.1
2	0.2	0.468	46.8×10^{-6}	0.062
3	0.3	0.354	35.4×10^{-6}	0.0465
4	0.4	0.287	28.7×10^{-6}	0.037
5	0.5	0.233	23.3×10^{-6}	0.031

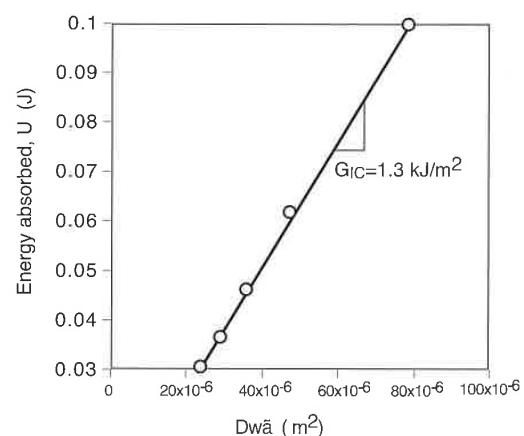


Figure 10.82 Fracture toughness plot for Example 10.1.

We can also compute the critical stress intensity factor K_{IC} using

$$K_{IC} = \sqrt{EG_{IC}} = 1.61 \text{ MNm}^{-3/2}$$

10.2 You are asked to design a cylindrical 200 mm diameter, 5 mm thick polycarbonate pressure vessel, as depicted in Fig. 10.83. To attach a fixture, the pressure vessel has a series of 0.5 mm deep grooves along its length. During its life, the pressure vessel will experience occasional pressure surges. Using the data given below, estimate the critical pressure inside the vessel that will result in fracture.

$$G_{IC} = 5 \text{ kJ/m}^2, \quad E = 2.1 \text{ GPa}, \quad \nu = 0.33$$

This problem can be solved using Eq. 10.14

$$G_{IC} = \frac{\pi \sigma_c^2 a}{E} (1 - \nu^2)$$

where, σ_c is the hoop stress given by

$$\sigma_c = \frac{pD}{2h}$$

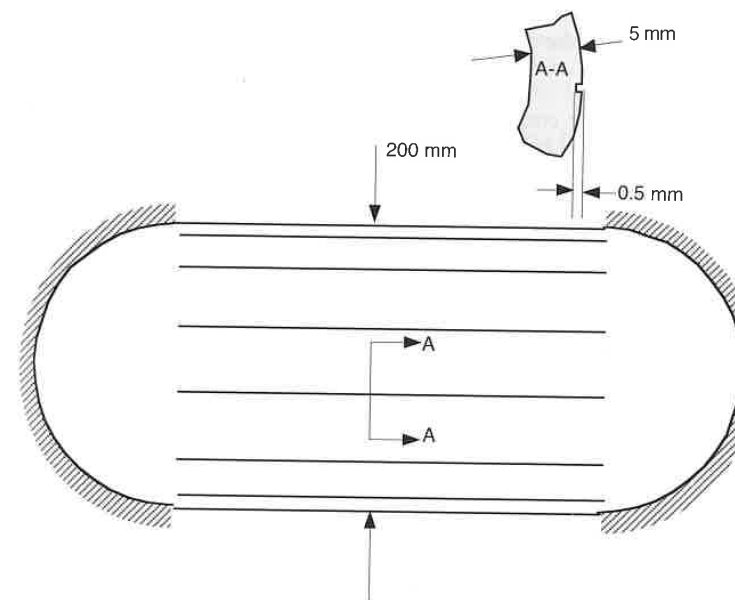


Figure 10.83 Pressure vessel geometry for Example 10.2.

Note that since the vessel is axially restricted, the axial stress can be neglected. We can now solve for the pressure that will lead to failure using

$$p = \left[\frac{G_{IC}}{\pi a} \frac{4Eh^2}{(1-\nu^2)D^2} \right]^{1/2} = \left[\frac{5 \text{ kJ/m}^2}{\pi(0.5 \text{ mm})} \frac{4(2.1 \text{ GPa})(5 \text{ mm})^2}{(1-0.33^2)(197.5 \text{ mm})^2} \right]^{1/2} = 4.39 \text{ MPa (645 psi)}$$

Problems

- 10.1 Is polystyrene an appropriate material to use for safety goggles? Why?
- 10.2 A high impact strength polycarbonate has a stress intensity factor, K_{IC} , of $2.6 \text{ MN/m}^{3/2}$, and a strain toughness, G_{IC} of 5.0 kJ/m^2 . The polycarbonate will be used to assemble a hockey face guard. The face guard will fit onto the helmet using several snap-fits located on the helmet. This requires

- 1.5 mm deep grooves on the polycarbonate face guard. What maximum stresses will you be able to subject the face guard in the region of the grooves.
- 10.3 Someone in your company designed high-density polyethylene water pipes to transport cold and hot water at pressures of 1.5 bar. The hot water will be at 50 °C, and you can assume the cold water to be at room temperature. The pipe's inner diameter is 50 mm with a wall thickness of 1 mm. Would you approve this product with a 5 year warranty for the above specifications? Why?
- 10.4 A PS-HI test specimen with a 20 mm x 1 mm cross-section and 2 mm long central crack is carrying a 100 N load. Plot the stress distribution near, but not at the crack tip.
- 10.5 A PS component with 0.5 mm long crazes is being stressed between -5 MPa and +5MPa. At what rate is the length of the crazes growing? Estimate the number of cycles to failure.
- 10.6 A creeping PS component loaded to a stress of 2 MPa is showing the formation of small crazes that measure approximately 200 μm. Estimate the time it takes for the crazes to grow to a length of 500 μm. Use $m = 7$ and $m = 25$.

References

1. Crawford, R.J., *Plastics Engineering*, 2nd, Ed., Pergamon Press, (1987).
2. Kinloch, A.J., Young, R.J., *Fracture Behavior of Polymers*, Applied Science Publishers, London, (1983).
3. Griffith, A.A., *Phil. Trans. Roy. Soc.*, A221, 163, (1920).
4. Rice, J.R., *J. Appl. Mech.*, 35, 379, (1965).
5. Vincent, P.I., *Plastics*, 29, 79 (1964).
6. Beahan, P., Bevis, M., and Hull, D., *Phil. Mag.*, 24, 1267, (1971).
7. Menges, G., *Werkstoffkunde der Kunststoffe*, 2nd Ed., Hanser Publishers, Munich, (1984).
8. Nicolay, Ph.D. Thesis, IKV, RWTH-Aachen, (1976).
9. Menges, G., and Alf, E., *Kunststoffe*, 62, 259, (1972).
10. Schultz, J.M., *Polymer Materials Science*, Prentice-Hall, Englewood Cliffs, N.J., (1974).
11. Ehrenstein, G.W., *Polymeric Materials*, Hanser Publishers, Munich, (2001).
12. Engel, L., Klingele, H., Ehrenstein, G.W., and Schaper, H., *An Atlas of Polymer Damage*, Hanser Publishers, Munich, (1978).
13. Roskothen, H.J., Ph.D. Thesis, IKV, RWTH-Aachen, (1974).
14. Boyer, R.F., *Polymer Eng. Sci.*, 8, 161, (1968).
15. Boden, H.E., Ph.D. Thesis, IKV, RWTH-Aachen, Germany, (1983).
16. Menges, G., and Boden, H.-E., *Failure of Plastics*, Chapter 9, Eds. W. Brostow, and R.D. Corneliussen, Hanser Publishers, Munich, (1986).
17. Andrews, E.H., *Fracture in Polymers*, Oliver and Body, London, (1968).
18. Rest, H., Ph.D. Thesis, IKV-Aachen, (1984).
19. ASTM, Vol .08.01, *Plastics (I): C 177-D 1600, ASTM-D 256*, 58-74, (1991).
20. Plati, E. and Williams, J.G., *Polym. Eng. Sci.*, 15, 470, (1975).
21. Crawford, R.J., and Benham, P.P., *Polymer*, 16, 908, (1975).
22. Richard, K., Gaube, E., and Diedrich, G., *Kunststoffe*, 49, 516, (1959).
23. Gaube, E. and Kausch, H.H., *Kunststoffe*, 63, 391, (1973).
24. Bannantine, J.A., Comer, J.J., and Handrock, J.L., *Fundamentals of Metal Fatigue Analysis*, Prentice Hall, Englewood Cliffs, (1990).
25. Riddell, M.N., *Plast. Eng.*, 40, 4, 71, (1974).
26. Kleinemeier, B., Ph.D. Thesis, IKW-Aachen, Germany, (1979).
27. Bucknall, C.B., Gotham, K.V., and Vincent, P.I., *Polymer Science. A Materials Handbook*, Ed. A.D. Jenkins, Vol. 1, Chapter 10, American Elsevier, New York, (1972).
28. Owen, M.J., Smith, T.R., and Dukes, R., *Plast. Polym.*, 37, 227, (1969).
29. Hertzberg, R.W., and Manson, J.A., *Fatigue of Engineering Plastics*, Academic Press, New York, (1980).
30. Denton, D.L., *The Mechanical Properties of an SMC-R50 Composite*, Owens-Corning Fiberglas Corp., (1979).
31. Hertzberg, R.W., Manson, J.A., and Skibo, M.D., *Polym. Eng. Sci.*, 15, 252, (1975).
32. Domininghaus, H., *Plastics for Engineers*, Hanser Publishers, Munich, (1993).
33. Dolfen, E., Ph.D. Thesis, IKV, RWTH-Aachen, (1978).
34. Menges, G., *Werkstoffkunde Kunststoffe*, Hanser Publishers, Munich, (1990).
35. Engel, L., Klingele, H., Ehrenstein, G.W., and Schaper, H., *An Atlas of Polymer Damage*, Hanser Publishers, Munich, (1978).
36. Davis, A. and Sims, D., *Weathering of Polymers*, Applied Science Publishers, London, (1983).
37. Ruhnke, G.M. and Biritz, L.F., *Kunststoffe*, 62, 250, (1972).
38. Bernier, G.A., and Kambour, R.P., *Macromolecules*, 1, 393, (1968).

Electrical Properties of Polymers

In contrast to metals, common polymers are poor electron conductors. Similar to mechanical properties, their electric properties depend to a great extent on the flexibility of the polymer's molecular blocks. The intent of this chapter is to familiarize the reader with electrical properties of polymers by discussing the dielectric, conductive, and magnetic properties.

11.1 Dielectric Behavior¹

11.1.1 Dielectric Coefficient

The most commonly used electrical property is the dielectric coefficient, ϵ_r . Let us begin the discussion on dielectricity by looking at a disk condenser charged by the circuit shown in Fig 11.1. The accumulated charge, Q , is proportional to the consumed voltage, U :

$$Q = CU \quad (11.1)$$

where the proportionality constant, C , is called *capacitance*. The capacitance for the disk condenser in a vacuum, also valid for air, is defined by

$$C_0 = \epsilon_0 \frac{A}{d} \quad (11.2)$$

where ϵ_0 is the vacuum's dielectric coefficient, A the disk's area and d the separation between the plates. Hence, the condenser's charge is given by

$$Q_0 = C_0 U \quad (11.3)$$

¹ Parts of this chapter are based on the lecture notes of Prof. H. Hersping at the RWTH-Aachen, Germany, (1972).

If we replace the vacuum or air between the disks of the condenser by a real dielectric, the charge increases, for the same voltage U , by the factor ϵ_r , represented by

$$Q = \epsilon_r Q_0 \tag{11.4}$$

and the capacity changes to

$$C = \epsilon_r C_0 = \epsilon_r \epsilon_0 \frac{A}{d} \tag{11.5}$$

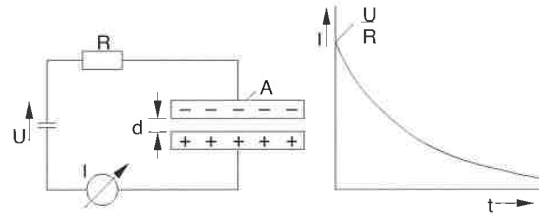


Figure 11.1 Condenser circuit used to measure capacitance properties.

The constant ϵ_r is often called the *relative dielectric coefficient*. It is dimensionless, and it is dependent on the material, temperature, and frequency. However, the charge changes when a dielectric material is inserted between the plates. This change in charge is due to the influence of the electric field developing polarization charges in the dielectric. This is more clearly represented in Fig. 11.2. The new charges that develop between the condenser's metal disks are called Q_p . Hence, the total charge becomes

$$Q = Q_0 + Q_p \tag{11.6}$$

In general terms, the charge is expressed per unit area as

$$\frac{Q}{A} = \frac{Q_0}{A} + \frac{Q_p}{A} = D \tag{11.7}$$

where D is the total charge per unit area. Introducing the *electric field intensity*, E , Eq. 11.2 can be rewritten as

$$E = \frac{U}{d} = \frac{1}{\epsilon_0} \frac{Q_0}{A} = \frac{1}{\epsilon_0 \epsilon_r} \frac{Q}{A} \tag{11.8}$$

which results in

$$\frac{Q_0}{A} = \epsilon_0 E \tag{11.9}$$

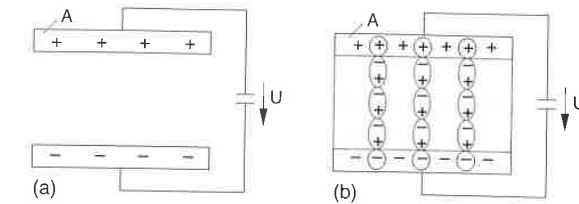


Figure 11.2 Polarization charges a) without a dielectric, b) with a dielectric.

If the charged condenser is separated from the voltage source beforehand, the voltage of the condenser will decrease with insertion of a dielectric. Thus, the inserted dielectric also increases the capacity of the condenser. Let us define the charge density of the polarization surface as

$$P = \frac{Q_p}{A} \tag{11.10}$$

This causes the total charge per unit area to become

$$D = \epsilon_0 E + P \tag{11.11}$$

which can be rewritten as

$$P = D - \epsilon_0 E \tag{11.12}$$

No field can develop within metallic condenser plates because of the high electric conductivity. Therefore, using the dielectric charge density per unit area, Eqs. 11.7 and 11.8 can be combined to give

$$D = \epsilon_0 \epsilon_r E \tag{11.13}$$

Substituting this result into Eq. 11.12, we get

$$P = \epsilon_0 \epsilon_r E - \epsilon_0 E \tag{11.14}$$

or

$$P = \epsilon_0 [\epsilon_r - 1] E = \epsilon_0 \chi E \tag{11.15}$$

The factor χ is generally referred to as *dielectric susceptibility*. It is a measurement of the ability of a material to be a polarizer.

Table 11.1 lists the relative dielectric coefficients of important polymers. The measurements were conducted using the standard test DIN 53 483 in condensers of different geometries which, in turn depended on the sample type. The ASTM standard test is described by ASTM D150. Figures 11.3 [1] and 11.4 [1]

present the dielectric coefficient for selected polymers as a function of temperature and frequency, respectively.

Table 11.1 Relative Dielectric Coefficient, ϵ_r , of Various Polymers [Hersping]

Polymer	Relative dielectric coefficient, ϵ_r	
	800 Hz	10^6 Hz
Expanded polystyrene	1.05	1.05
Polytetrafluoroethylene	2.05	2.05
Polyethylene (density dependent)	2.3-2.4	2.3-2.4
Polystyrene	2.5	2.5
Polypropylene	2.3	2.3
Polyphenyleneether	2.7	2.7
Polycarbonate	3.0	3.0
Polyethyleneterephthalate	3.0-4.0	3.0-4.0
ABS	4.6	3.4
Celluloseacetate, type 433	5.3	4.6
Polyamide 6 (moisture content dependent)	3.7-7.0	
Polyamide 66 (moisture content dependent)	3.6-5.0	
Epoxy resin (unfilled)		2.5-5.4
Phenolic type 31.5	6.0-9.0	6.0
Phenol type 74	6.0-10.0	4.0-7.0
Urea type 131.5	6.0-7.0	6.0-8.0
Melamine type 154	5.0	10.0

11.1.2 Mechanisms of Dielectrical Polarization

The two most important molecular types for the polarization of a dielectric in an electric field are *displacement polarization* and *orientation polarization*.

Under the influence of an electric field, the charges deform in field direction by aligning with the atomic nucleus (electron polarization) or with the ions (ionic polarization). This is usually called *displacement polarization* and is clearly demonstrated in Fig. 11.5.

Because of their structure, some molecules possess a dipole moment in the spaces that are free of an electric field. Hence, when these molecules enter an electric field, they will orient according to the strength of the field. This is generally referred to as *orientation polarization* and is schematically shown in Fig. 11.5.

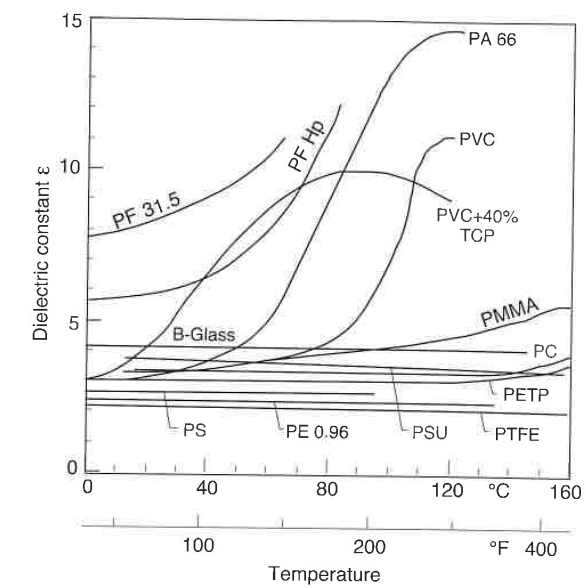


Figure 11.3 Dielectric constant as a function of temperature for various polymers.

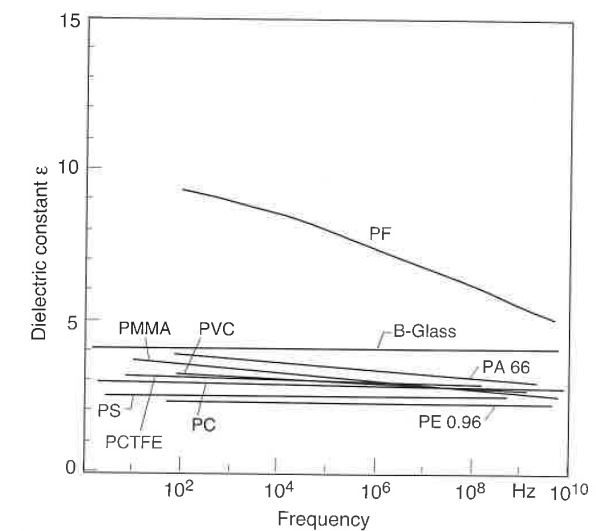


Figure 11.4 Dielectric constant as a function of frequency for various polymers.

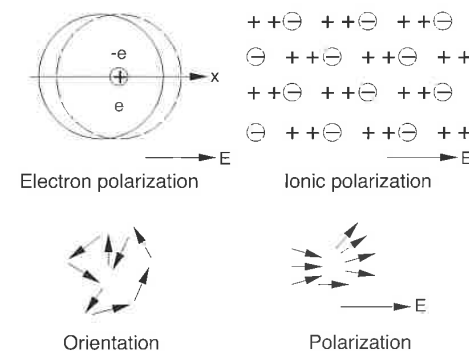


Figure 11.5 Polarization processes.

It takes some time to displace or deform the molecular dipoles in the field direction and even longer time for the orientation polarization. The more viscous the surrounding medium is, the longer it takes. In alternating fields of high frequency, the dipole movement can lag behind at certain frequencies. This is called dielectric relaxation, which leads to dielectric losses that appear as dielectric heating of the polar molecules.

In contrast to this, the changes in the displacement polarization happen so quickly that it can even follow a lightwave. Hence, the refractive index, n , of light is determined by the displacement contribution, ϵ_v , of the dielectric constant². The relation between n and ϵ_v is given by

$$n = \sqrt{\epsilon_v} \quad (11.16)$$

Hence, we have a way of measuring polarization properties since the polarization of electrons determines the refractive index of polymers. It should be noted that ion or molecular segments of polymers are mainly stimulated in the middle of the infrared spectrum.

A number of polymers have permanent dipoles. The best known polar polymer is polyvinyl chloride, and C=O groups also represent a permanent dipole. Therefore, polymers with that kind of building block suffer dielectric losses in alternating fields of certain frequencies. For example, Fig. 11.6 shows the frequency dependence of susceptibility.

² For a more in-depth coverage of optical properties the reader is referred to Chapter 11 of this book.

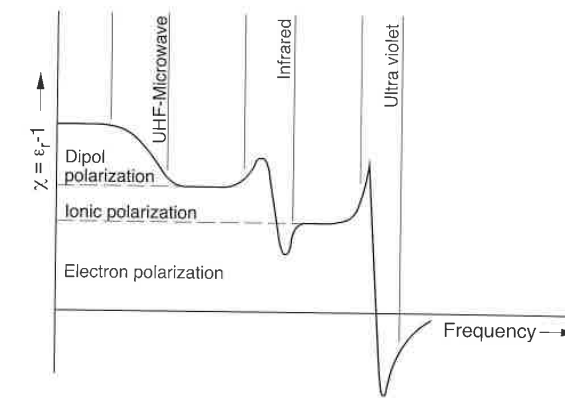


Figure 11.6 Frequency dependence of different polarization cases.

In addition, the influence of fillers on the relative dielectric coefficient is of considerable practical interest. The rule of mixtures can be used to calculate the effective dielectric coefficient of a matrix with assumingly spherically shaped fillers as

$$\epsilon_{\text{eff}} = \epsilon_{\text{matrix}} \left(1 - 3\phi \frac{\epsilon_{\text{matrix}} - \epsilon_{\text{filler}}}{2\epsilon_{\text{matrix}} + \epsilon_{\text{filler}}} \right) \quad (11.17)$$

Materials with air entrapments such as foams, have a filler dielectric coefficient of $\epsilon_{\text{air}} = 1$; thus, the effective dielectric coefficient of the material reduces to

$$\epsilon_{\text{foam}} = \epsilon_{\text{matrix}} \left(1 - 3\phi \frac{\epsilon_{\text{matrix}} - 1}{2\epsilon_{\text{matrix}} + 1} \right) \quad (11.18)$$

and, for metal fillers where $\epsilon_{\text{metal}} = \infty$, it can be written as

$$\epsilon_{\text{eff}} = \epsilon_{\text{matrix}} (1 + 3\phi) \quad (11.19)$$

Whether a molecule is stimulated to its resonant frequency in alternating fields or not depends on its relaxation time. The relaxation time, in turn, depends on viscosity, η , temperature, T , and radius, r , of the molecule. The following relationship can be used:

$$\lambda_m \sim \frac{\eta r^3}{T} \quad (11.20)$$

The parameter λ_m is the time a molecule needs to move back to its original shape after a small deformation. Hence, the resonance frequency, f_m , can be computed using

$$f_m = \frac{\omega_m}{2\pi} = \frac{1}{2\pi\lambda_m} \quad (11.21)$$

11.1.3 Dielectric Dissipation Factor

The movement of molecules, for example, during dipole polarization or ion polarization in an alternating electric field, leads to internal friction and, therefore, to the heating of the dielectric. The equivalent circuit shown in Fig. 11.7 is used here to explain this phenomenon. Assume an alternating current is passing through this circuit, with the effective value of U volts and an angular frequency ω defined by

$$\omega = 2\pi f \quad (11.22)$$

where f is the frequency in Hz. Through such a system, a complex current I^* will flow, composed of a resistive or loss component, I_r , and of a capacitive component, I_c . The vector diagram in Fig. 11.8 shows that with

$$I_r = U/R \quad (11.23)$$

and

$$I_c = \omega CU \quad (11.24)$$

we can write

$$I^* = U/R + i\omega CU \quad (11.25)$$

Here, i represents an imaginary component oriented in the imaginary axis of the vector diagram in Fig. 11.8. An alternating current applied to a condenser free of any current loss components would result in

$$\frac{I_r}{I_c} = \tan \delta \rightarrow 0 \quad (11.26)$$

In such a case, the condenser current is purely capacitive, which leads to no losses at all. This results in a voltage that is lagging the current by 90° , as demonstrated in Fig. 11.9. Accordingly, capacitance also consists of a real component and an imaginary component.

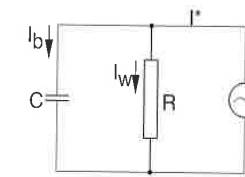


Figure 11.7 Equivalent circuit diagram for the losses in a dielectric.

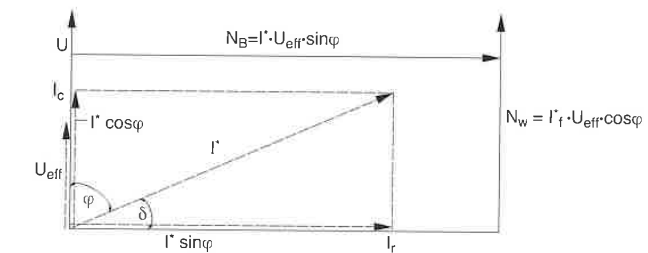


Figure 11.8 Current-voltage diagram or power-indicator diagram of electric alternating currents.

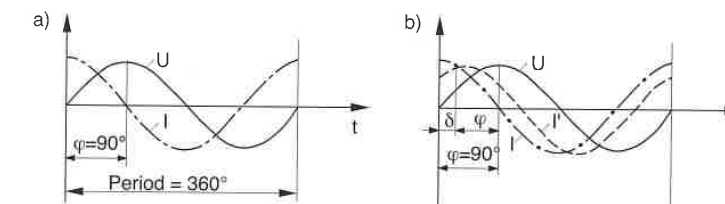


Figure 11.9 Current and voltage in a condenser. $I \equiv$ current, $U \equiv$ voltage, $t \equiv$ time
a) Without dielectric losses (ideal condition), current and voltage are displaced by the phase angle $\varphi = 90^\circ$ or $\pi/2$; b) With dielectric loss, the current curve I' is delayed by the loss angle δ .

If the condenser has losses, when $\tan \delta > 0$, a resistive current I_r is formed which leads to a heating energy rate in the dielectric of

$$E_h = \frac{1}{2} U I_{eff} \tan \delta \quad (11.27)$$

where I_{eff} represents the total current or the magnitude of the vector in Fig. 11.8. Using Eq. 11.25 for capacitance leads to

$$C^* = C' - \frac{1}{R\omega} = C' - iC'' \quad (11.28)$$

where C^* is the complex capacitance, with C' as the real component defined by

$$C' = \epsilon_0 \epsilon_r' \frac{A}{d} \quad (11.29)$$

and C'' as the imaginary component described by

$$C'' = \frac{1}{R\omega} = \epsilon_0 \epsilon_r'' \frac{A}{d} \quad (11.30)$$

Using the relationship in Eq. 11.5 we can write

$$C^* = C_0(\epsilon_r' - i\epsilon_r'') = C_0 \epsilon_r^* \quad (11.31)$$

where ϵ_r^* is called the *complex dielectric coefficient*. According to Eqs. 11.25 and 11.31, the phase angle difference or *dielectric dissipation factor* can be defined by

$$\tan \delta = \frac{I_c}{I_e} = \frac{\epsilon_r''}{\epsilon_r'} \quad (11.32)$$

If we furthermore consider that electric conductivity is determined by

$$\sigma = \frac{1}{R} \frac{d}{A} \quad (11.33)$$

then the imaginary component of the complex dielectric coefficient can be rewritten as

$$\epsilon_r'' = \frac{\sigma}{\omega \epsilon_0} = \epsilon_r' \tan \delta \quad (11.34)$$

Typical ranges for the dielectric dissipation factor of various polymer groups are shown in Table 11.2. Figures 11.10 [1] and 11.11 [1] present the dissipation factor $\tan \delta$ as a function of temperature and frequency, respectively.

Table 11.2 Dielectric Dissipation Factor ($\tan \delta$) for Various Polymers

Material	$\tan \delta$
Non-polar polymers (PS, PE, PTFE)	< 0.0005
Polar polymers (PVC and others)	0.001-0.02
Thermoset resins filled with glass, paper, cellulose	0.02-0.5

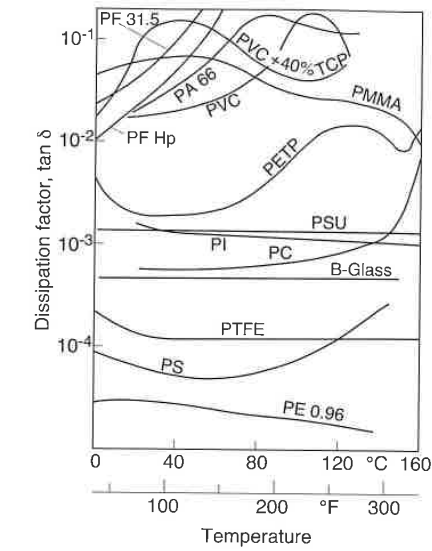


Figure 11.10 Dielectric dissipation factor as a function of temperature for various polymers.

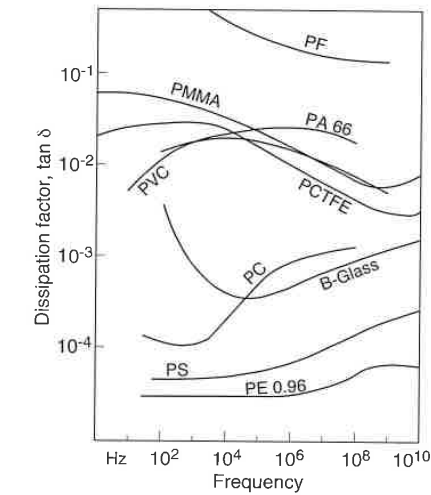


Figure 11.11 Dielectric dissipation factor as a function of frequency for various polymers.

11.1.4 Implications of Electrical and Thermal Loss in a Dielectric

The electric losses through wire insulation running high frequency currents must be kept as small as possible. Insulators are encountered in transmission lines or in high-frequency fields such as the housings of radar antennas. Hence, we would select materials which have low electrical losses for these types of applications.

On the other hand, in some cases we want to generate heat at high frequencies. Heat sealing of polar polymers at high frequencies is an important technique used in the manufacturing of soft PVC sheets such as the ones encountered in automobile vinyl seat covers.

To assess whether a material is suitable for either application, one must know the loss properties of the material and calculate the actual electrical loss. To do this, we can rewrite Eq. 11.27 as

$$E_h = U^2 \omega C \tan \delta \quad (11.35)$$

or as

$$E_h = 2\pi f U^2 d^2 \epsilon_0 \epsilon' \tan \delta C_0 \quad (11.36)$$

The factor that is dependent on the material and indicates the loss is the *loss factor* $\epsilon' \tan \delta$, called ϵ'' in Eq. 11.34. As a rule, the following should be used:

$\epsilon' \tan \delta < 10^{-3}$ for high-frequency insulation applications, and

$\epsilon' \tan \delta > 10^{-2}$ for heating applications.

In fact, polyethylene and polystyrene are perfectly suitable as insulators in high-frequency applications. To measure the necessary properties of the dielectric, the standard DIN 53 483 and ASTM D 150 tests are recommended.

11.2 Electric Conductivity

11.2.1 Electric Resistance

The current flow resistance, R , in a plate-shaped sample in a direct voltage field is defined by Ohm's law as

$$R = \frac{U}{I} \quad (11.37)$$

or by

$$R = \frac{1}{\sigma} \frac{d}{A} \quad (11.38)$$

where σ is known as the conductivity and d and A are the sample's thickness and surface area, respectively. The resistance is often described as the inverse of the conductance, G ,

$$R = \frac{1}{G} \quad (11.39)$$

and the conductivity as the inverse of the specific resistance, ρ ,

$$\sigma = \frac{1}{\rho} \quad (11.40)$$

The simple relationship found in Eq. 11.37-39 is seldom encountered since the voltage, U , is rarely steady and usually varies in cyclic fashion between 10^{-1} to 10^{11} Hz [2].

Current flow resistance is called *volume conductivity* and is measured one minute after direct voltage has been applied using the DIN 53 482 standard test. The time definition is necessary, because the resistance decreases with polarization. For some polymers we still do not know the final values of resistance. However, this has no practical impact, since we only need relative values for comparison. Figure 11.12 compares the specific resistance, ρ , of various polymers and shows its dependence on temperature. Here, we can see that similar to other polymer properties, such as the relaxation modulus, the specific resistance not only decreases with time but also with temperature.

The surface of polymer parts often shows different electric direct-current resistance values than their volume. The main cause is from surface contamination (e.g., dust and moisture). We therefore have to measure the surface resistance using a different technique. One common test is DIN 53 482, which uses a contacting sample. Another test often used to measure surface resistance is DIN 53 480. With this technique, the surface resistance is tested between electrodes placed on the surface. During the test, a saline solution is dripped on the electrodes causing the surface to become conductive, thus heating up the surface and causing the water to evaporate. This leads not only to an increased artificial contamination but also to the decomposition of the polymer surface. If during this process conductive derivatives such as carbon form, the conductivity quickly increases to eventually create a short circuit. Polymers that develop only small traces of conductive derivatives are considered resistant. Such polymers are polyethylene, fluoropolymers, and melamines.

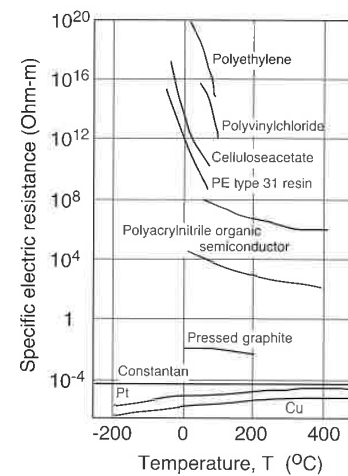


Figure 11.12 Specific electric resistance of polymers and metals as a function of temperature.

11.2.2 Physical Causes of Volume Conductivity

Polymers with a homopolar atomic bond, which leads to pairing of electrons, do not have free electrons and are not considered to be conductive. Conductive polymers—still in the state of development—in contrast, allow for movement of electrons along the molecular cluster, since they are polymer salts. The classification of these polymers with different materials is given in Fig. 11.13.

Potential uses of electric conductive polymers in electrical engineering include flexible electric conductors of low density, strip heaters, anti-static equipment, high-frequency shields, and housings. In semi-conductor engineering, some applications include semi-conductor devices (Schottky-Barriers) and solar cells. In electrochemistry, applications include batteries with high energy and power density, electrodes for electrochemical processes, and electrochromic instruments.

Because of their structure, polymers cannot be expected to conduct ions. Yet the extremely weak electric conductivity of polymers at room temperature and the fast decrease of conductivity with increasing temperatures is an indication that ions do move. They move because engineering polymers always contain a certain amount of added low-molecular constituents which act as moveable charge carriers. This is a diffusion process which acts in field direction and across the field. The ions “jump” from potential hole to potential hole as activated by higher temperatures (Fig. 11.12). At the same time, the lower

density speeds up this diffusion process. The strong decrease of specific resistance with the absorption of moisture is caused by ion conductivity.

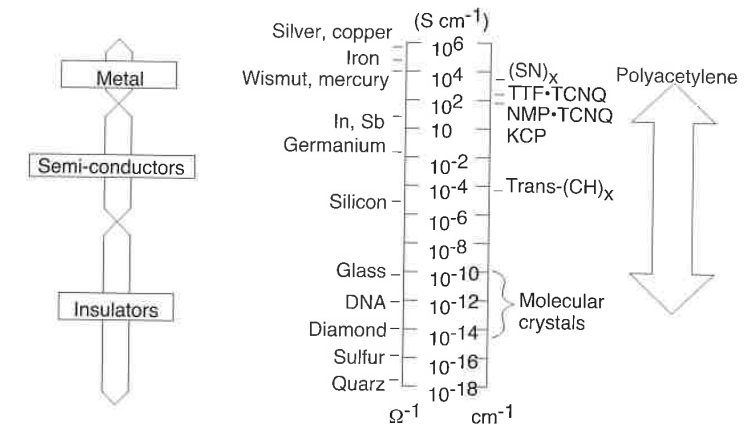


Figure 11.13 Electric conductivity of polyacetylene (*trans*-(CH)_x) in comparison to other materials.

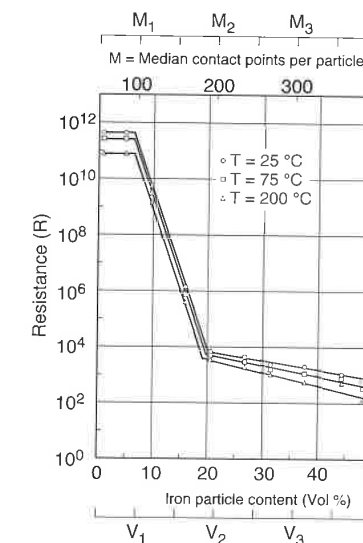


Figure 11.14 Resistance R of a polymer filled with metal powder (iron).

Conducting polymers are useful for certain purposes. When we insulate high-energy cables, for example, as a first transition layer we use a polyethylene filled with conductive filler particles such as soot. Figure 11.14 demonstrates the relationship between filler content and resistance. When contact tracks develop, resistance drops spontaneously. The number of inter-particle contacts, M , determines the resistance of a composite. At M_1 or $M=1$ there is one contact per particle. At this point, the resistance starts dropping. When two contacts per particle exist, practically all particles participate in setting up contact and the resistance levels off. The sudden drop in the resistance curve indicates why it is difficult to obtain a medium specific resistance by filling a polymer.

Figure 11.15 [3] presents the resistance in metal flakes or powder filled epoxy resins. The figure shows how the *critical volume concentration* for the epoxy systems filled with copper or nickel flakes is about 7% concentration of filler, and the critical volume concentration for the epoxy filled with steel powder is around 15%.

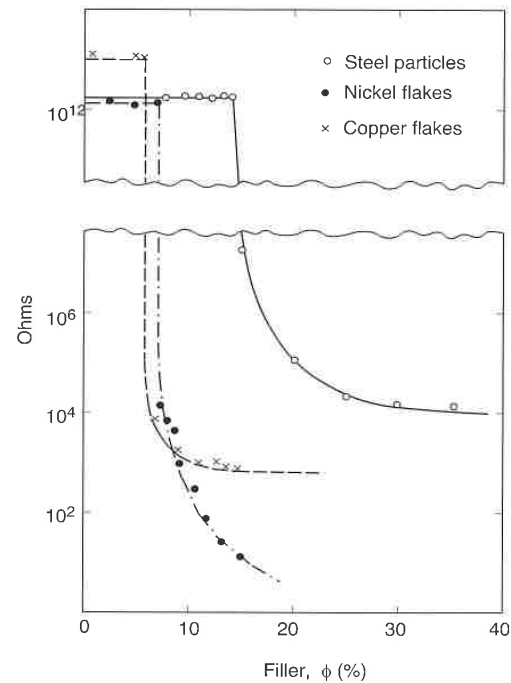


Figure 11.15 Resistance in metal flakes and powder filled epoxy resins.

11.3 Application Problems

11.3.1 Electric Breakdown

Since the electric breakdown of insulation may lead to failure of an electric component or may endanger people handling the component, it must be prevented. Hence, we have to know the critical load of the insulating material to design the insulation for long continuous use and with a great degree of confidence. One of the standard tests used to generate this important material property data for plate or block-shaped specimens is DIN 53 481. This test neglects the effect of material structure and of processing conditions. From the properties already described, we know that the *electric breakdown resistance* or *dielectric strength* must depend on time, temperature, material condition, load application rate, and frequency. It is furthermore dependent on electrode shape and sample thickness. In practice, however, it is very important that the upper limits measured on the experimental specimens in the laboratory are never reached. The rule of thumb is to use long-term load values of only 10% of the short-term laboratory data. Experimental evidence shows that the *dielectric strength* decreases as soon as crazes form in a specimen under strain and continues to decrease with increasing strain. This is demonstrated in Fig 11.16 [4].

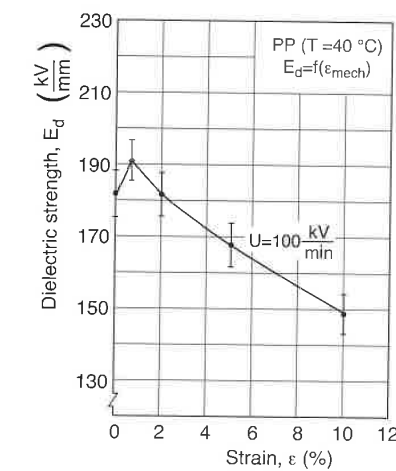


Figure 11.16 Drop of the dielectric strength of PP films with increasing strain.

On the other hand, Fig. 11.17 [4] demonstrates how the *dielectric dissipation factor*, $\tan \delta$, rises with strain. Hence, one can easily determine the beginning of the viscoelastic region (begin of crazing) by noting the starting point of the change in $\tan \delta$. It is also known that amorphous polymers act more favorably to electric breakdown resistance than partly crystalline polymers. Semi-crystalline polymers are more susceptible to electric breakdown as a result of breakdown along inter-spherulitic boundaries as shown in Fig. 11.18 [5]. Long-term breakdown of semi-crystalline polymers is either linked to "treeing," as shown in Fig. 11.19, or occurs as a heat breakdown, burning a hole into the insulation, such as the one in Fig. 11.18. In general, with rising temperature and frequency, the dielectric strength continuously drops.

Insulation materials— mostly LDPE— are especially pure and contain voltage stabilizers. These stabilizers are low-molecular cyclic aromatic hydrocarbons. Presumably, they diffuse into small imperfections or failures, fill the empty space and thereby protect them from breakdown.

Table 11.3 [6] gives dielectric strength and resistivity for selected polymeric materials.

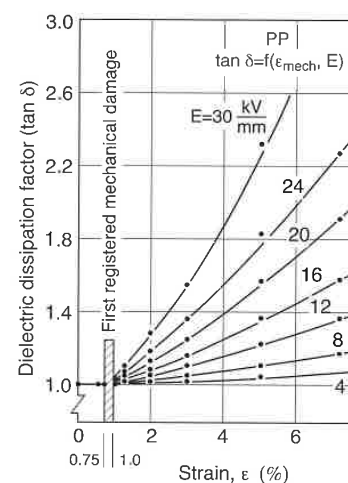


Figure 11.17 Increase of dielectric dissipation with increased strain in PP foils.

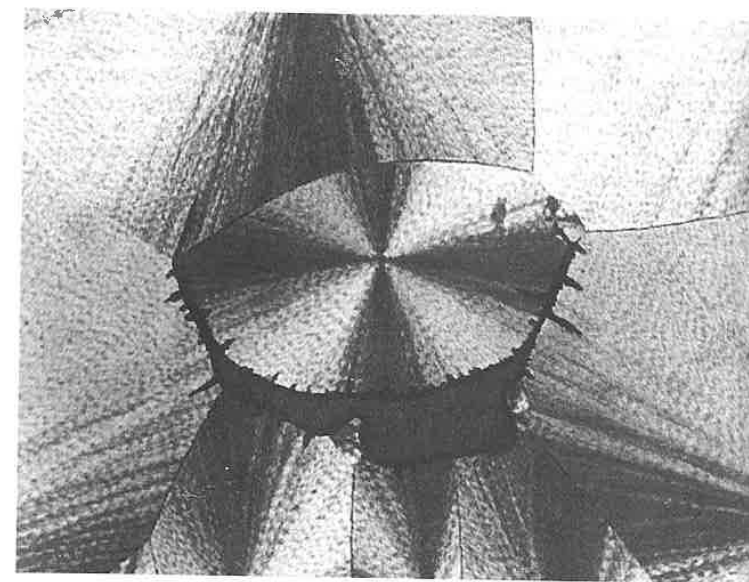


Figure 11.18 Breakdown channel around a polypropylene spherulitic boundary.

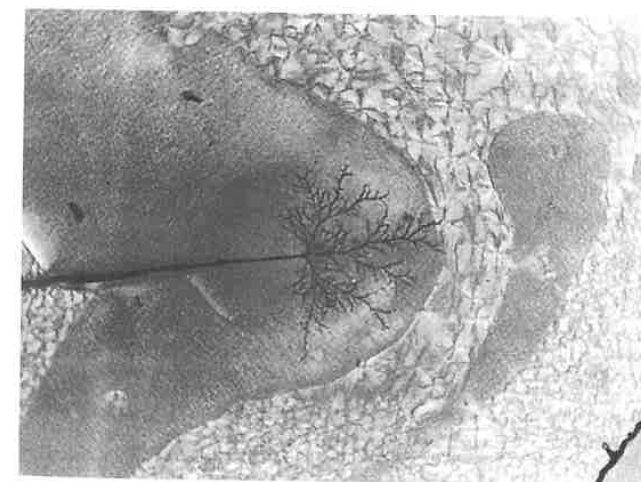


Figure 11.19 Breakdown channel in structureless finely crystalline zone of polypropylene.

Table 11.3 Dielectric Strength and Resistivity for Selected Polymers

Polymer	Dielectric strength MV/m	Resistivity Ohm-m
ABS	25	10^{14}
Acetal (homopolymer)	20	10^{13}
Acetal (copolymer) acrylic	20	10^{13}
Acrylic	11	10^{13}
Cellulose acetate	11	10^9
CAB	10	10^9
Epoxy	16	10^{13}
Modified PPO	22	10^{15}
Nylon 66	8	10^{13}
Nylon 66 + 30% GF	15	10^{12}
PEEK	19	10^{14}
PET	17	10^{13}
PET + 36% GF	50	10^{14}
Phenolic (mineral filled)	12	10^9
Polycarbonate	23	10^{15}
Polypropylene	28	10^{15}
Polystyrene	20	10^{14}
LDPE	27	10^{14}
HDPE	22	10^{15}
PTFE	45	10^{16}
uPVC	14	10^{12}
pPVC	30	10^{11}
SAN	25	10^{14}

11.3.2 Electrostatic Charge

An electrostatic charge is often a result of the excellent insulation properties of polymers— the very high surface resistance and current-flow resistance. Since polymers are bad conductors, the charge displacement of rubbing bodies, which develops with mechanical friction, cannot equalize. This charge displacement results from a surplus of electrons on one surface and a lack of electrons on the other. Electrons are charged positively or negatively up to hundreds of volts. They release their surface charge only when they touch another conductive body or a body which is inversely charged. Often the discharge occurs without contact, as the charge arches through the air to the close-by conductive or inversely charged body, as demonstrated in Fig. 11.20.

The currents of these breakdowns are low. For example, there is no danger when a person suffers an electric shock caused by a charge from friction of synthetic carpets or vinyls. There is danger of explosion, though, when the sparks ignite flammable liquids or gases.

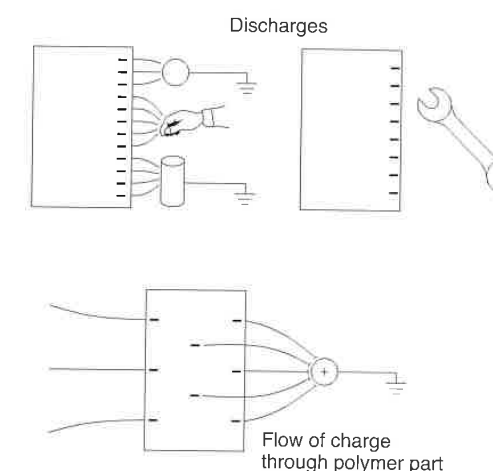


Figure 11.20 Electrostatic charges in polymers.

As the current-flow resistance of air is generally about $10^9 \Omega\text{cm}$, charges and flashovers only occur if the polymer has a current-flow resistance of $>10^9$ to $10^{10} \Omega\text{cm}$. Another effect of electrostatic charges is that they attract dust particles on polymer surfaces.

Electrostatic charges can be reduced or prevented by the following means:

- Reduce current-flow resistance to values of $<10^9 \Omega\text{cm}$, for example, by using conductive fillers such as graphite.
- Make the surfaces conductive by using hygroscopic fillers that are incompatible with the polymer and surface. It can also be achieved by mixing-in hygroscopic materials such as strong soap solutions. In both cases, the water absorbed from the air acts as a conductive layer. It should be pointed out that this treatment loses its effect over time. Especially, the rubbing in of hygroscopic materials has to be repeated over time.
- Reduce air resistance by ionization through discharge or radioactive radiation.

11.3.3 Electrets

An electret is a solid dielectric body that exhibits permanent dielectric polarization. One can manufacture electrets out of some polymers when they are solidified under the influence of an electric field, when bombarded by electrons, or sometimes through mechanical forming processes.

Applications include films for condensers (polyester, polycarbonate, or fluoropolymers).

11.3.4 Electromagnetic Interference Shielding (EMI Shielding)

Electric fields surge through polymers as shown schematically in Fig. 11.20. Since we always have to deal with the influence of interference fields, signal-sensitive equipment such as computers cannot operate in polymer housings. Such housings must therefore have the function of Faraday shields. Preferably, a multilayered structure is used—the simplest solution is to use one metallic layer. Figure 11.21 classifies several materials on a scale of resistances. We need at least $10^2 \Omega\text{cm}$ for a material to fulfill the shielding purpose. With carbon fibers or nitrate coated carbon fibers used as a filler, one achieves the best protective properties. The shielding properties are determined using the standard ASTM ES 7-83 test.

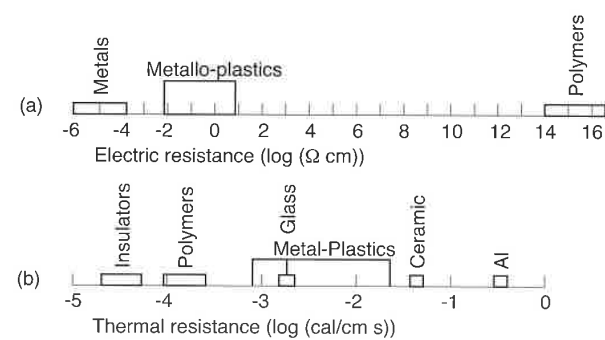


Figure 11.21 Comparison of conductive polymers with other materials: a) Electric resistance ρ of metal-plastics compared to resistance of metals and polymers b) Thermal resistance λ of metal-plastics compared to other materials

11.4 Magnetic Properties

External magnetic fields have an impact on substances which are subordinate to them because the external field interacts with the internal fields of electrons and atomic nuclei.

11.4.1 Magnetizability

Pure polymers are diamagnetic; that is, the external magnetic field induces magnetic moments. However, permanent magnetic moments, which are induced on ferromagnetic or paramagnetic substances, do not exist in polymers. This magnetizability M of a substance in a magnetic field with a field intensity H is computed with the magnetic susceptibility, χ as

$$M = \chi H \quad (11.41)$$

The susceptibility of pure polymers as *diamagnetic substances* has a very small and negative value. However, in some cases, we make use of the fact that fillers can alter the magnetic character of a polymer completely. The magnetic properties of polymers are often changed using magnetic fillers. Well-known applications are injection molded or extruded magnets or magnetic profiles, and all forms of electronic storage such as recording tape, floppy or magnetic disks.

11.4.2 Magnetic Resonance

Magnetic resonance occurs when a substance, in a permanent magnetic field, absorbs energy from an oscillating magnetic field. This absorption develops as a result of small paramagnetic molecular particles stimulated to vibration. We use this phenomenon to a great extent to clarify structures in physical chemistry. Methods to achieve this include *electron spinning resonance* (ESR) and, above all, *nuclear magnetic resonance* (NMR) spectroscopy.

Electron spinning resonance becomes noticeable when the field intensity of a static magnetic field is altered and the microwaves in a high frequency alternating field are absorbed. Since we can only detect unpaired electrons using this method, we use it to determine radical molecule groups.

When atoms have an odd number of nuclei, protons and neutrons, the magnetic fields which are caused by self-motivated spin cannot equalize. The alignment of nuclear spins in an external magnetic field leads to a magnetization vector which can be measured macroscopically as is

schematically demonstrated in Fig. 11.22 [7]. This method is of great importance for the polymer physicist to learn more about molecular structures.

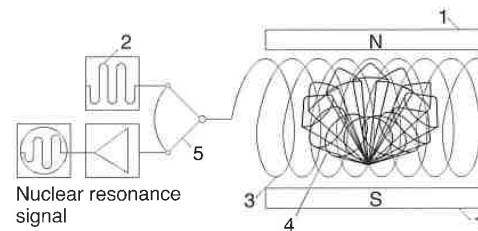


Figure 11.22 Schematic of the operating method of a nuclear spin tomograph: 1) magnet which produces a high steady magnetic field 2) radio wave generator 3) high-frequency field, produced by 2, when switch 5 is in upper position 4) processing nucleus, simulated by high frequency field 5) switch; in this position the decrease of relaxation of the nucleus' vibrations is measured.

References

1. Dominghaus, H., *Plastics for Engineers*, Hanser Publishers, Munich, (1993).
2. Baer, E., *Engineering Design for Plastics*, Robert E. Krieger Publishing Company, (1975).
3. Reboul, J.-P., *Thermoplastic Polymer Additives*, Chapter 6, J.T. Lutz, Jr., Ed., Marcel Dekker, Inc., New York, (1989).
4. Berg, H., Ph.D Thesis, IKV, RWTH-Aachen, Germany, (1976).
5. Wagner, H., Internal report, AEG, Kassel, Germany, (1974).
6. Crawford, R.J., *Plastics Engineering*, 2nd Ed., Pergamon Press, (1987).
7. From *Bild der Wissenschaft*.

Optical Properties of Polymers

Since some polymers have excellent optical properties and are easy to mold and form into any shape, they are often used to replace transparent materials such as inorganic glass. Polymers have been introduced into a variety of applications such as automotive headlights, signal light covers, optical fibers, imitation jewelry, chandeliers, toys, and home appliances. Organic materials such as polymers are also an excellent choice for high-impact applications where inorganic materials such as glass would easily shatter. However, due to the difficulties encountered in maintaining dimensional stability, they are not apt for precision optical applications. Other drawbacks include lower scratch resistance, when compared to inorganic glasses, making them still impractical for applications such as automotive windshields.

In this section, we will discuss basic optical properties which include the index of refraction, birefringence, transparency, transmittance, gloss, color, and behavior of polymers in the infrared spectrum.

12.1 Index of Refraction

As rays of light pass through one material into another, the rays are bent due to the change in the speed of light from one media to the other. The fundamental material property that controls the bending of the light rays is the *index of refraction*, N . The index of refraction for a specific material is defined as the ratio between the speed of light in a vacuum to the speed of light through the material under consideration

$$N = \frac{c}{v} \quad (12.1)$$

where c and v are the speeds of light through a vacuum and transparent media, respectively. In more practical terms, the refractive index can also be computed

as a function of the angle of incidence, θ_i , and the angle of refraction, θ_r , as follows:

$$N = \frac{\sin \theta_i}{\sin \theta_r} \tag{12.2}$$

where θ_i and θ_r are defined in Fig. 12.1.

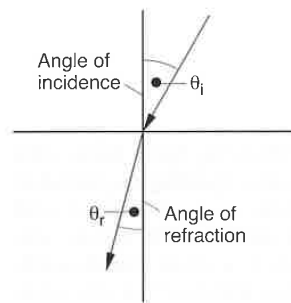


Figure 12.1 Schematic of light refraction.

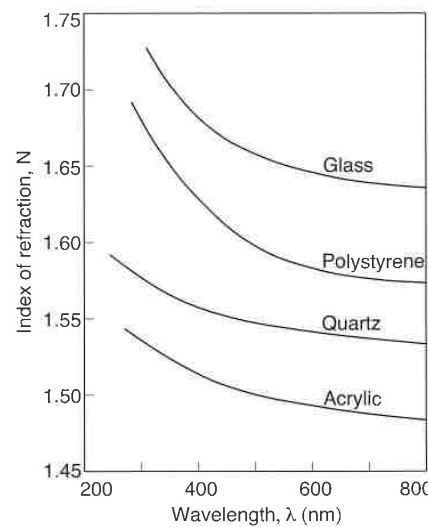


Figure 12.2 Index of refraction as a function of wavelength for various materials.

The index of refraction for organic plastic materials can be measured using the standard ASTM D 542 test. It is important to mention that the index of refraction is dependent on the wavelength of the light under which it is being measured. Figure 12.2 shows plots of the refractive index for various organic and inorganic materials as a function of wavelength. One of the significant points of this plot is that acrylic materials and polystyrene have similar refractive properties as inorganic glasses.

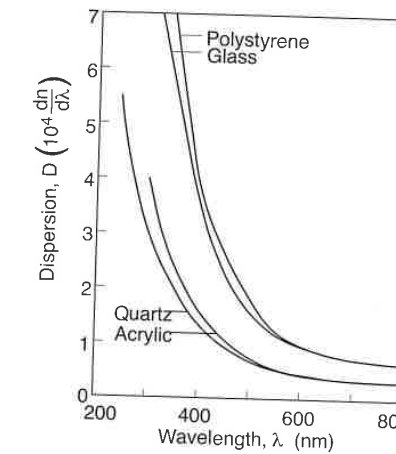


Figure 12.3 Dispersion as a function of wavelength for various materials.

An important quantity that can be deduced from the light's wavelength dependence on the refractive index is the dispersion, D , which is defined by

$$D = \frac{dN}{d\lambda} \tag{12.3}$$

Figure 12.3 shows plots of dispersion as a function of wavelength for the same materials shown in Fig. 12.2. The plots show that polystyrene and glass have a high dispersion in the ultra-violet light domain.

It is also important to mention that since the index of refraction is a function of density, it is indirectly affected by temperature. Figure 12.4 shows how the refractive index of PMMA changes with temperature. A closer look at the plot reveals the glass transition temperature.

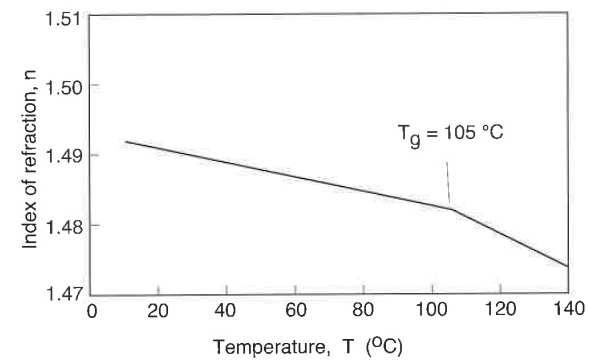


Figure 12.4 Index of refraction as a function of temperature for PMMA ($\lambda = 589.3$ nm).

12.2 Photoelasticity and Birefringence

Photoelasticity and flow birefringence are applications of the optical anisotropy of transparent media. When a transparent material is subjected to a strain field or a molecular orientation, the index of refraction becomes directional; the principal strains ϵ_1 and ϵ_2 are associated with principal indices of refraction N_1 and N_2 in a two-dimensional system. The difference between the two principal indices of refraction (*birefringence*) can be related to the difference of the principal strains using the *strain-optical coefficient*, k , as

$$N_1 - N_2 = k(\epsilon_1 - \epsilon_2) \quad (12.4)$$

or, in terms of principal stress, and

$$N_1 - N_2 = C(\sigma_1 - \sigma_2) \quad (12.5)$$

where C is the stress-optical coefficient.

Double refractance in a material is caused when a beam of light travels through a transparent media in a direction perpendicular to the plane that contains the principal directions of strain or refraction index, as shown schematically in Fig. 12.5 [1]. The incoming light waves split into two waves that oscillate along the two principal directions. These two waves are out of phase by a distance δ , defined by

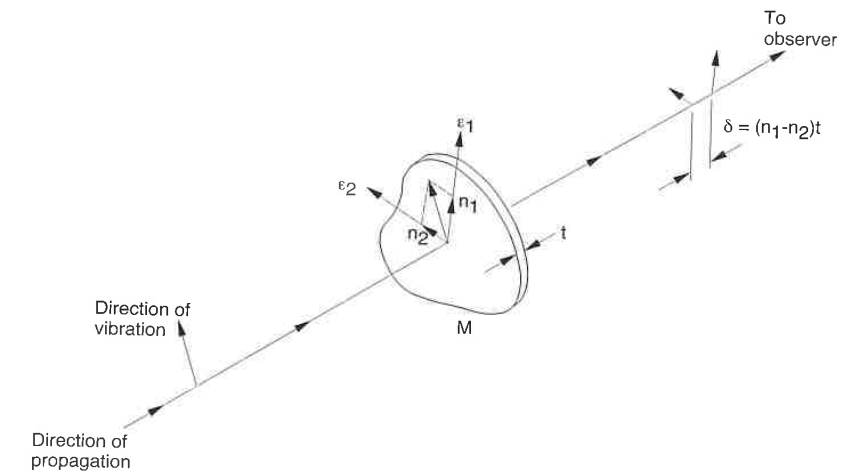


Figure 12.5 Propagation of light in a strained transparent media.

$$\delta = (N_1 - N_2)d \quad (12.6)$$

where d is the thickness of the transparent body. The out-of-phase distance, δ , between the oscillating light waves is usually referred to as the *retardation*.

In photoelastic analysis, one measures the direction of the principal stresses or strains and the retardation to determine the magnitude of the stresses. The technique and apparatus used to perform such measurements is described in the ASTM D 4093 test. Figure 12.6 shows a schematic of such a set-up, composed of a narrow wavelength band light source, two polarizers, two quarterwave plates, a compensator, and a monochromatic filter. The polarizers and quarterwave plates must be perpendicular to each other (90°). The compensator is used for measuring retardation, and the monochromatic filter is needed when white light is not sufficient to perform the photoelastic measurement. The set-up presented in Fig. 12.6 is generally called a *polariscope*.

The parameter used to quantify the strain field in a specimen observed through a polariscope is the color. The retardation in a strained specimen is associated to a specific color. The sequence of colors and their respective retardation values and fringe order are shown in Table 12.1 [1]. The retardation and color can also be associated to a *fringe order* using

$$\text{fringe order} = \frac{\delta}{\lambda} \quad (12.7)$$

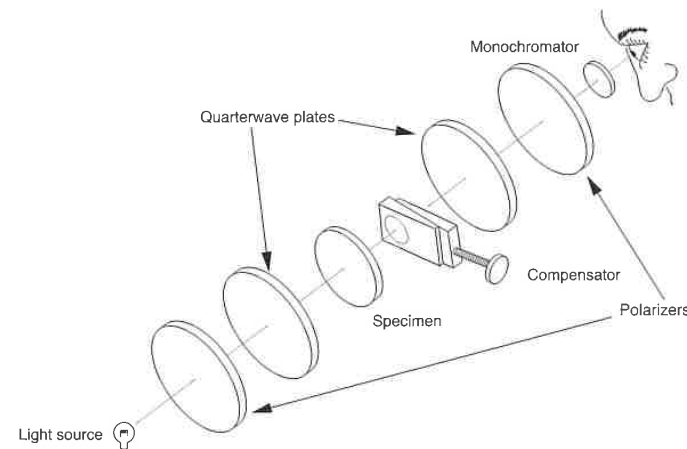


Figure 12.6 Schematic diagram of a polariscope.

Table 12.1 Retardation and Fringe Order Produced in a Polariscope

Color	Retardation (nm)	Fringe order
Black	0	0
Gray	160	0.28
White	260	0.45
Yellow	350	0.60
Orange	460	0.79
Red	520	0.90
Tint of passage	577	1.00
Blue	620	1.06
Blue-green	700	1.20
Green-yellow	800	1.38
Orange	940	1.62
Red	1050	1.81
Tint of passage	1150	2.00
Green	1350	2.33
Green-yellow	1450	2.50
Pink	1550	2.67
Tint of passage	1730	3.00
Green	1800	3.10
Pink	2100	3.60
Tint of passage	2300	4.00
Green	2400	4.13

A black body (fringe order zero) represents a strain free body, and closely spaced color bands represent a component with high strain gradients. The color bands are generally called the *isochromatics*. Figure 12.7 shows the isochromatic fringe pattern in a stressed notched bar. The fringe pattern can also be a result of molecular orientation and residual stresses in a molded transparent polymer component. Figure 12.8 shows the orientation induced fringe pattern in a molded part. The residual stress-induced birefringence is usually smaller than the orientation-induced pattern, making them more difficult to measure.

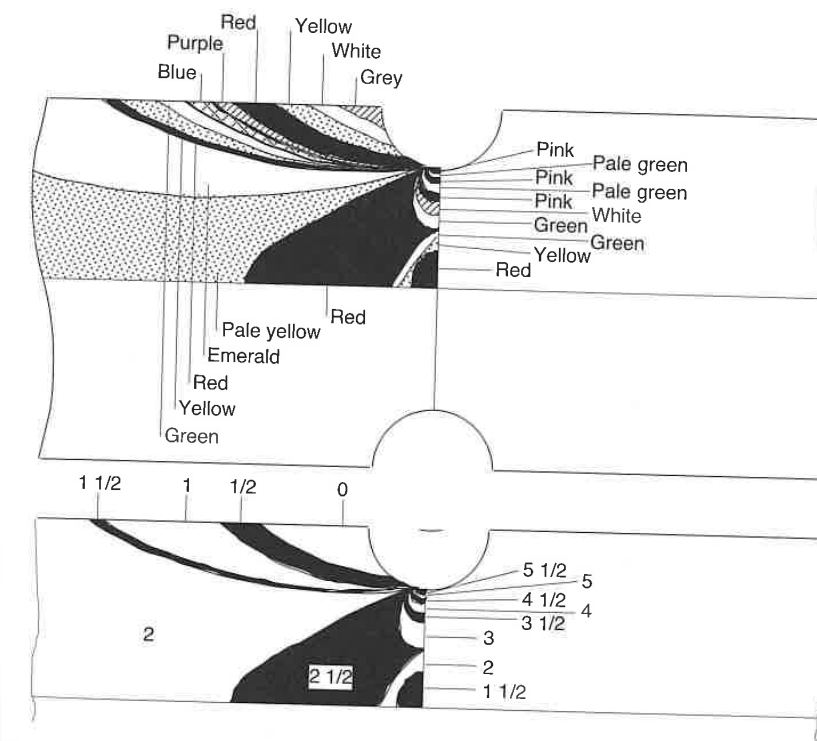


Figure 12.7 Fringe pattern on a notched bar under tension.

Flow induced birefringence is an area explored by several researchers [2-4]. Likewise, the flow induced principal stresses can be related to the principal refraction indices. For example, in a simple shear flow this relation can be written as [5]

$$(N_1 - N_2) = \frac{2C}{\sin 2x} \tau_{12} = \frac{2C}{\sin 2x} \eta \dot{\gamma} \quad (12.8)$$

where x is the orientation of the principal axes in a simple shear flow.

Figure 12.9 [6] shows the birefringence pattern for the flow of linear low-density polyethylene in a rectangular die.

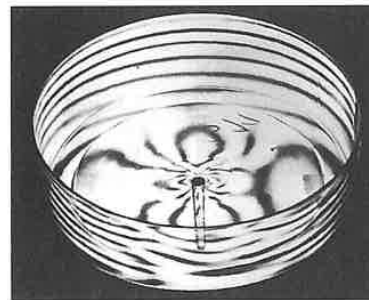


Figure 12.8 Transparent injection molded part viewed through a polariscope.

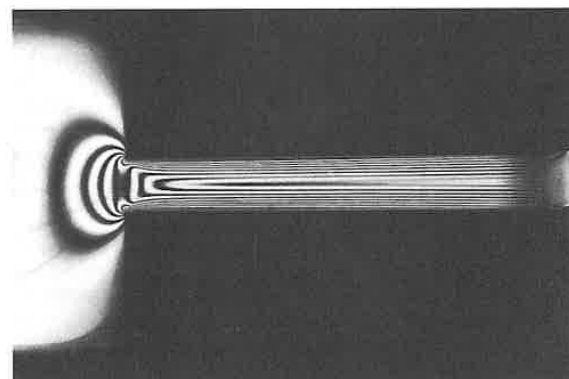


Figure 12.9 Birefringence pattern for flow of LLDPE in a rectangular die.

12.3 Transparency, Reflection, Absorption, and Transmittance

As rays of light pass through one media into another of a different refractive index, light will be scattered if the interface between the two materials shows discontinuities larger than the wavelength of visible light¹. Hence, the transparency in semi-crystalline polymers is directly related to the crystallinity of the polymer. Since the characteristic size of the crystalline domains are larger than the wavelengths of visible light, and since the refractive index of the denser crystalline domains is higher compared to the amorphous regions, semi-crystalline polymers are not transparent; they are opaque or translucent. Similarly, high impact polystyrene— which is actually formed by two amorphous components, polybutadiene rubber particles² and polystyrene — appears white and translucent due to the different indices of refraction of the two materials. However, filled polymers can be made transparent if the filler size is smaller than the wavelength of visible light. Figure 12.10 shows various types of high impact polystyrene. The two types of HIPS shown in the lower part of the figure have polybutadiene particles that are smaller than the wavelength of visible light, making them transparent.

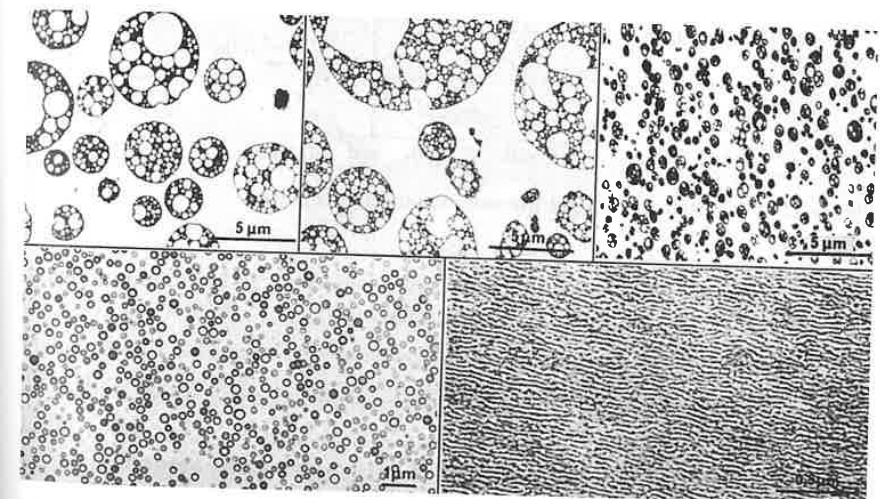


Figure 12.10 Morphology of polybutadiene particles in a polystyrene matrix for different types of high impact polystyrene.

- 1 The wavelength of visible light runs between 400 and 700 nm (0.4 and 0.7 μm).
- 2 The characteristic size of a rubber particle in high impact polystyrene is 1-10 μm .

The concept of absorption and transmittance can be illustrated using the schematic and notation shown in Fig. 12.11. The figure plots the intensity of a light ray as it strikes and travels through an infinite plate of thickness d . For simplicity, the angle of incidence, θ_i , is 0° . The initial intensity of the incoming light beam, I , drops to I_0 as a fraction ρ_0 of the incident beam is reflected out. The reflected light beam can be computed using

$$I_r = \rho_0 I \quad (12.9)$$

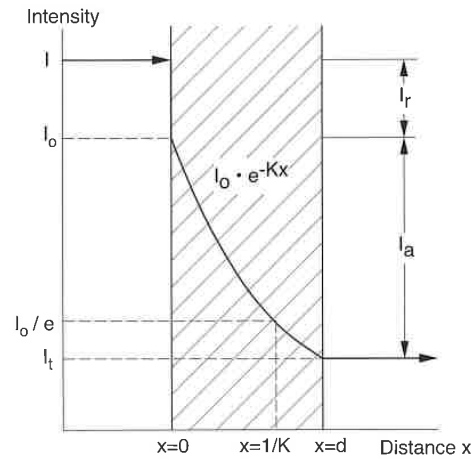


Figure 12.11 Schematic of light transmission through a plate.

The fraction of the incident beam which is reflected can be computed using Beer's law:

$$\rho_0 = \frac{(N-1)^2 + \chi^2}{(N+1)^2 + \chi^2} \quad (12.10)$$

Here, χ is the absorption index described by

$$\chi = \frac{K\lambda}{4\pi} \quad (12.11)$$

where λ is the wavelength of the incident light beam and K the coefficient of absorption.

The fraction of the beam that does penetrate into the material continues to drop due to absorption as it travels through the plate. The intensity fraction of the incident beam as it is transmitted through the material can be computed using *Bourger's law*,

$$T(x) = I_0 e^{-Kx} \quad (12.12)$$

where K is the coefficient of absorption. The intensity fraction of the incident beam transmitted to the rear surface of the plate can now be computed using

$$\tau = (1 - \rho_0) e^{-Kd} \quad (12.13)$$

However, as illustrated in Fig. 12.12, part of the beam is reflected back by the rear surface of the plate and is subsequently reflected and absorbed several times as it travels

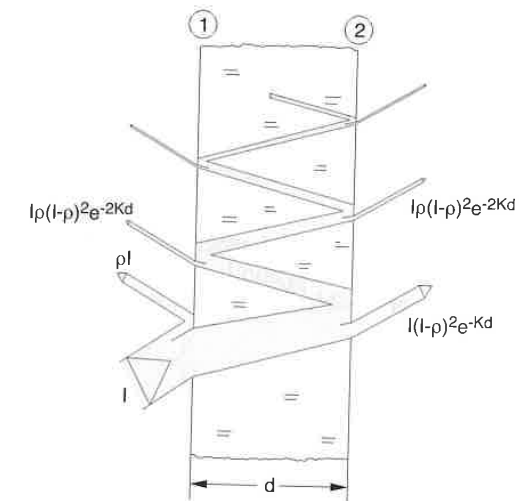


Figure 12.12 Schematic of light reflectance, absorption and transmission through a plate.

between the front and back surfaces of the plate. The infinite sum of transmitted rays can be approximated by

$$\tau = \frac{(1 - \rho_0)^2 e^{-Kd}}{1 - \rho_0^2 e^{-2Kd}} \quad (12.14)$$

and the total reflected rays can be approximated with

$$\rho = \rho_0(1 + \tau e^{-Kd}) \tag{12.15}$$

The fraction of incident beam absorbed by the material and transformed into heat inside the material is calculated using

$$\alpha = 1 - \tau - \rho \tag{12.16}$$

Figure 12.3 shows this relationship as a function of dimensionless thickness Kd .

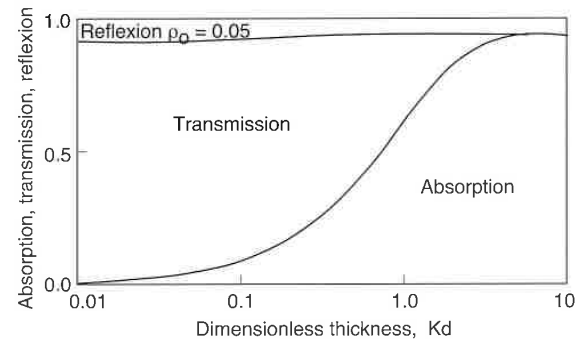


Figure 12.13 Reflection, transmission and absorption as a function of thickness.

The above analysis is complicated further for the case where the incident angle is no longer 0° . For such a case, and for materials with low coefficient of absorption, the amount of visible light reflected can be computed using Fresnel's equation [7],

$$I_r = \frac{1}{2} \left(\frac{\sin^2(\theta_i - \theta_r)}{\sin^2(\theta_i + \theta_r)} + \frac{\tan^2(\theta_i - \theta_r)}{\tan^2(\theta_i + \theta_r)} \right) I_0 \tag{12.17}$$

which can be written as

$$I_r = \rho I_0 \tag{12.18}$$

Plots of ρ as a function of incidence angle are shown in Fig. 12.14 for various refraction indices.

For the case with $\theta_i = 0^\circ$ the equation can be rewritten in terms of transmittance, T , as

$$T = \left(1 - \frac{(N-1)^2}{N^2+1} \right) \tag{12.19}$$

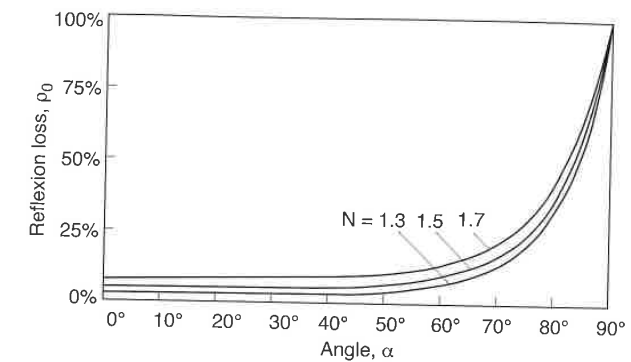


Figure 12.14 Influence of incidence angle on reflection losses.

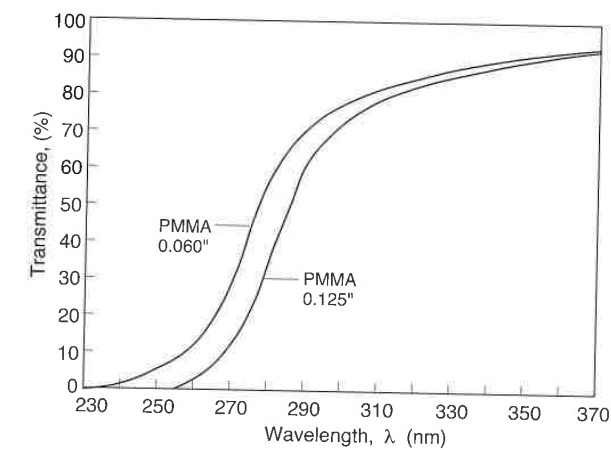


Figure 12.15 Ultraviolet light transmission through PMMA.

which is the fraction of the incident light that is transmitted through the material. For example, a PMMA with a refractive index of 1.49 would at best have a transmittance of 0.92 or 92%. The transmittance becomes less as the wavelength of the incident light decreases, as shown for PMMA in Fig. 12.15. The figure also demonstrates the higher absorption of the thicker sheet.

The transmissivity of polymers can be improved by altering their chemical composition. For example, the transmissivity of PMMA can be improved by substituting hydrogen atoms by fluorine atoms. The improvement is clearly

demonstrated in Fig. 12.16³. Such modifications bring polymers a step closer to materials appropriate for usage in fiber optic applications⁴. Nucleating agents can also be used to improve the transmissivity of semi-crystalline polymers. A large number of nuclei will reduce the average spherulite size to values below the wavelength of visible light.

The haziness or luminous transmittance of a transparent polymer is measured using the standard ASTM D 1003 test, and the transparency of a thin polymer film is measured using the ASTM D 1746 test. The haze measurement (ASTM D 1003) is the most popular measurement for film and sheet quality control and specification purposes.

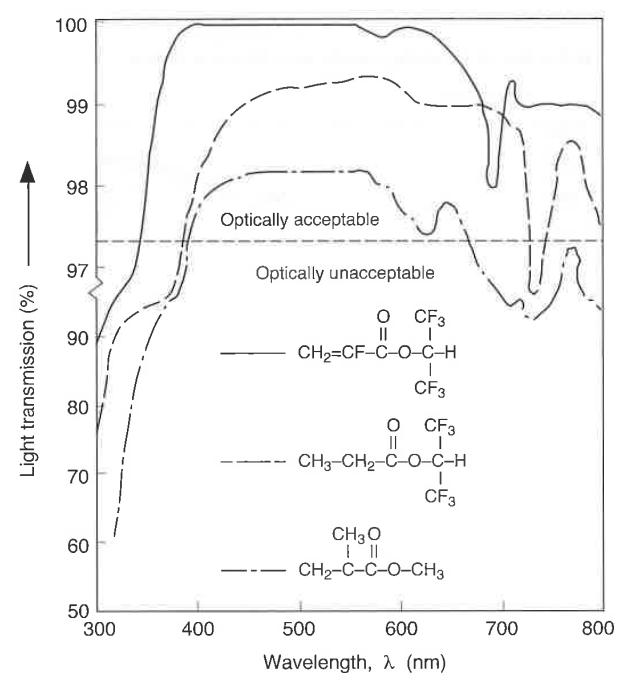


Figure 12.16 Effect of fluorine modification on the transmissivity of light through PMMA.

³ Courtesy of Hoechst, Germany.

⁴ Their ability to withstand shock and vibration and cost savings during manufacturing make some amorphous polymers important materials for fiber optics applications. However, in unmodified polymer fibers, the initial light intensity drops to 50% after only 100 m, whereas when using glass fibers the intensity drops to 50% after 3000 m.

12.4 Gloss

Strictly speaking, all of the above theory is valid only if the surface of the material is perfectly smooth. However, the reflectivity of a polymer component is greatly influenced by the quality of the surface of the mold or die used to make the part.

Specular gloss can be measured using the ASTM D 2457 standard technique which describes a part by the quality of its surface. A glossmeter or lustrometer is usually composed of a light source and a photometer as shown in schematic diagram in Fig. 12.17 [8]. These types of glossmeters are called *goniophotometers*. As shown in the figure, the specimen is illuminated with a light source from an angle α , and the photometer reads the light intensity from the specimen from a variable angle β . The angle α should be chosen according to the glossiness of the surface. For example, for transparent films values for α range from 20° for high gloss, 45° for intermediate and 60° low gloss. For opaque specimens ASTM test E 97 should be used. Figure 12.18 presents plots of reflective intensity as a function of photometer orientation for several surfaces with various degrees of gloss illuminated by a light source oriented at a 45° angle from the surface. The figure shows how the intensity distribution is narrow and sharp at 45° for a glossy surface, and the distribution becomes wider as the surface becomes matte. The color of the surface also plays a significant role on the intensity distribution read by the photometer as it sweeps through various angular positions. Figure 12.19 shows plots for a black and a white surface with the same degree of glossiness. The specular gloss is used as a measurement of the glossy appearance of films. However, gloss values of opaque and transparent films should not be compared with each other.

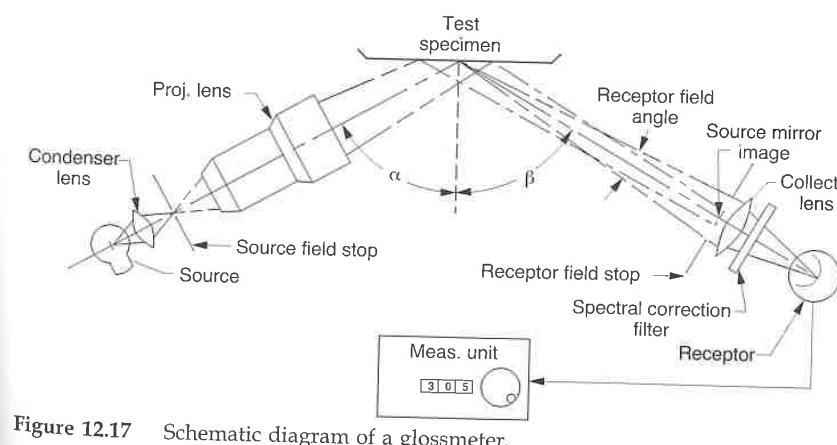


Figure 12.17 Schematic diagram of a glossmeter.

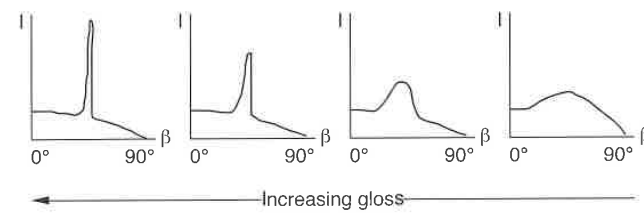


Figure 12.18 Reflective intensity as a function of photometer orientation for specimens with various degrees of surface gloss.

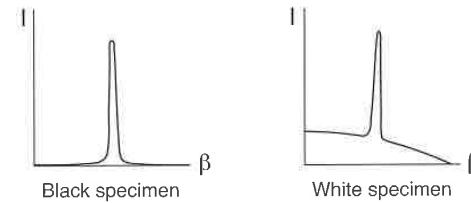


Figure 12.19 Reflective intensity as a function of photometer orientation for black and white specimens with equal surface gloss.

12.5 Color

The surface quality of a part is not only determined by how smooth or glossy it is but also by its color. Color is often one of the most important specifications for a part. In the following discussion it will be assumed that the color is homogeneous throughout the surface. This assumption is linked to processing, where efficient mixing must take place to disperse and distribute the pigments that will give the part color.

Color can always be described by combinations of basic red, green, and blue⁵. Hence, to quantitatively evaluate or measure a color, one must filter the intensity of the three basic colors. A schematic diagram of a color measurement device is shown in Fig. 12.20. Here, a specimen is lit in a diffuse manner using a photometric sphere, and the light reflected from the specimen is passed through red, green, and blue filters. The intensity coming from the three filters are allocated the variables X , Y , and Z for red, green, and blue, respectively. The variables X , Y , and Z are usually referred to as *tristimulus values*.

⁵ Most color measurement techniques are based on the CIE system. CIE is the *Commission Internationale de l'Eclairage*, or International Commission on Illumination.

Another form

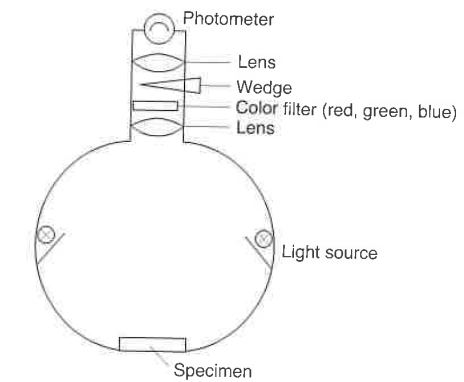


Figure 12.20 Schematic diagram of a colorimeter.

of measuring color is to have an observer compare two surfaces. One surface is the sample under consideration illuminated with a white light. The other surface is a white screen illuminated by light coming from three basic red, green, and blue sources. By varying the intensity of the three light sources, the color of the two surfaces are matched. This is shown schematically in Fig. 12.21 [9]. Here too, the intensities of red, green, and blue are represented with X , Y , and Z , respectively.

The resulting data is better analyzed by normalizing the individual intensities as

$$x = \frac{X}{X + Y + Z} \tag{12.20}$$

$$y = \frac{Y}{X + Y + Z} \tag{12.21}$$

$$z = \frac{Z}{X + Y + Z} \tag{12.22}$$

The parameters X , Y , and Z , usually termed *trichromatic coefficients*, are plotted on a three-dimensional graph that contains the whole spectrum of

visible light, as shown in Fig. 12.22. This graph is usually referred to as a *chromaticity diagram*. The standard techniques that make use of the chromaticity diagram are ASTM E 308-90 and DIN 5033. Three points in the diagram have been standardized:

- Radiation from a black body at 2848 K corresponding to a tungsten filament light and denoted by A in the diagram;
- Sunlight, denoted by B; and
- North sky light, denoted by C.

It is important to note that colors plotted on the chromaticity diagram are only described by their *hue* and *saturation*. The *luminance* factor is plotted in the z direction of the diagram. Hence, all neutral colors such as black, gray, and white lie on point C of the diagram.

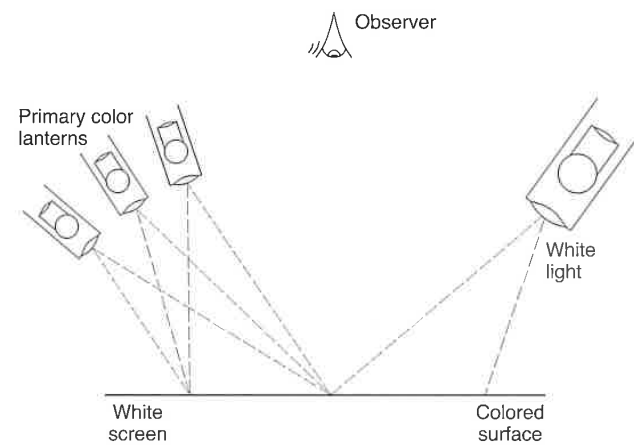


Figure 12.21 Schematic diagram of a visual colorimeter.

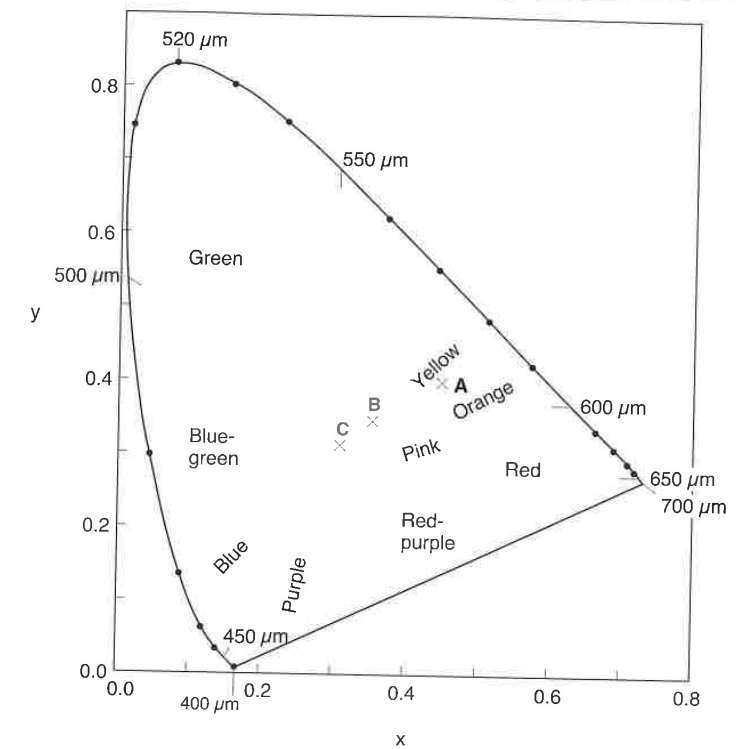


Figure 12.22 Chromaticity diagram with approximate color locations.

12.6 Infrared Spectroscopy

Infrared spectroscopy has developed into one of the most important techniques used to identify polymeric materials. It is based on the interaction between matter and electromagnetic radiation of wavelengths between 1 and 50 μm . The atoms in a molecule vibrate in a characteristic mode, which is usually called a fundamental frequency. Thus, each molecule has a set group of characteristic frequencies which can be used as a diagnostics tool to detect the presence of distinct groups. Table 12.2 [10] presents the absorption wavelength for several chemical groups. The range for most commercially available infrared spectrometers is between 2 and 25 μm . Hence, the spectrum taken between 2 and 25 μm serves as a fingerprint for that specific polymer, such as shown in Fig. 12.23 for polycarbonate.

An *infrared spectrometer* to measure the absorption spectrum of a material is schematically represented in Fig.12.24. It consists of an infrared light source that can sweep through a certain wavelength range, and that is split in two beams: one that serves as a reference and the other that is passed through the test specimen. The comparison of the two gives the absorption spectrum, such as shown in Fig. 12.23.

Using infrared spectroscopy, also helps in quantitatively evaluating the effects of weathering (e.g., by measuring the increase of the absorption band of the COOH group, or by monitoring the water intake over time). One can also use the technique to follow reaction kinetics during polymerization.

Table 12.2 Absorption Wavelengths for Various Groups

Group	Wavelength region (μm)
O-H	2.74
N-H	3.00
C-H	3.36
C-O	9.67
C-C	11.49
C=O	5.80
C=N	5.94
C=C	6.07
C=S	6.57

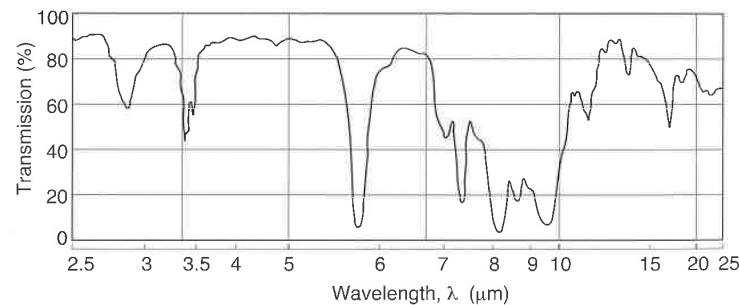


Figure 12.23 Infrared spectrum of a polycarbonate film.

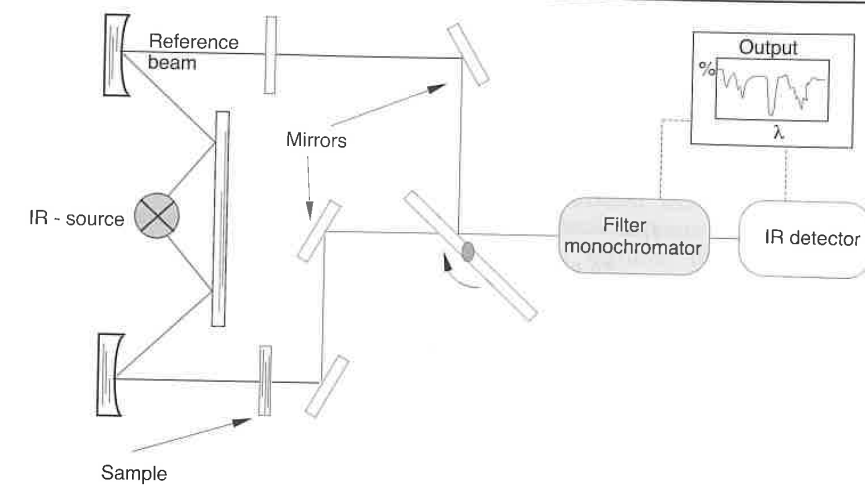


Figure 12.24 Schematic diagram of an infrared spectrometer.

12.7 Infrared Pyrometry

Today it is possible to measure the temperature at the surface of a polymer melt or component using an infrared probe. Infrared pyrometry is based on Planck's law, which describes the spectral distribution of blackbody radiation by

$$I_{\lambda} = \frac{c_1}{\pi \lambda^5 \left[\exp\left(\frac{c_2}{\lambda T_{\lambda}}\right) - 1 \right]} \quad (12.23)$$

where λ is the mean effective wavelength utilized by an IR pyrometer, I_{λ} is the amount of spectral radiance emitted by a blackbody with a spectral radiance temperature of T_{λ} (K), and $c_1 (= 3.742 \times 10^8 \text{ W}\mu\text{m}^4/\text{m}^2)$ and $c_2 (= 1.439 \times 10^4 \mu\text{m}^0\text{K})$ are Planck's first and second radiation constants, respectively. Within the range of typical polymer processing temperatures, Planck's law can be further simplified as Wien's law, i.e., $\exp(c_2/\lambda T) \gg 1$ which is given by

$$I_{\lambda} = \frac{c_1}{\pi \lambda^5 \exp\left(\frac{c_2}{\lambda T_{\lambda}}\right)} \quad (12.24)$$

Equations 12.23 or 12.24 can be used to convert the measured radiance from an IR pyrometer, I_λ , into a temperature, T_λ , for a blackbody with an emissivity of 1.0. However, when measuring the temperature of a non-blackbody whose emissivity is ϵ_λ ($\neq 1.0$), the true surface temperature of the non-blackbody, T_s , and the spectral radiance temperature, T_λ , can be related to each other using Eq. 12.24 by the following equation

$$I_\lambda = \frac{c_1}{\pi \lambda^5 \exp\left(\frac{c_2}{\lambda T_\lambda}\right)} = \frac{\epsilon_\lambda c_1}{\pi \lambda^5 \exp\left(\frac{c_2}{\lambda T_s}\right)} \quad (12.25)$$

The true surface temperature of a polymer melt or component can then be calculated from rearranging Eq. 12.25 to,

$$\frac{1}{T_s} = \frac{1}{T_\lambda} + \frac{\lambda}{c_2} \ln(\epsilon_\lambda) \quad (12.26)$$

The spectral surface emissivity of a material can be obtained by either direct measurement [11] or by calculation using both Kirchhoff's law and the radiation energy balance equation (i.e., Eq. 12.16). Kirchhoff's law basically states that the emissivity and the absorptivity of the material are equal (i.e., $\epsilon_\lambda = \alpha_\lambda$). Therefore, if the reflectivity and transmissivity of a semi-transparent polymer are known, then the emissivity of a polymer can be computed from Eq. 12.16 as

$$\epsilon_\lambda = 1 - \tau_\lambda - \rho_\lambda \quad (12.27)$$

However, if the polymer specimen is thick enough, we can eliminate transmissivity from Eq. 12.27, taking the measurements at a wavelength at which polymers absorb strongly; that is, at a wavelength which has a strong dip in its spectrum. To do this we select proper narrow-band filters to control the bandwidth and mean effective wavelength of the pyrometer. This concept is clearly demonstrated in Fig. 12.25 [12], which shows the transmissivity spectrum of polyethylene and polytetrafluoroethylene. It is easy to spot the bands of low transmissivity such as the one around $6.8 \mu\text{m}$ (CH_3 band) in the PE spectrum. For most polymer films one can assume a reflectivity value, ρ , of 0.05 [13].

As indicated from the preceding description, if the mean effective wavelength of an IR pyrometer is controlled at a bandwidth where the target polymer has a low transmissivity, then the IR pyrometer can measure the surface temperature of the target polymer. More recently, attempts have been made to measure the subsurface temperature in a polymer melt stream in a non-invasive manner using IR probes [14, 15]. For such measurements, the mean effective wavelength of an IR pyrometer is controlled at a bandwidth

where the transmissivity of the polymer is relatively high (i.e., the polymer has a low radiation absorbing behavior), then the IR pyrometer is able to capture subsurface radiation and provide bulk temperature information of the polymer. Since the captured bulk temperatures contain detailed thermal information about the volume of the polymer, it is possible to retrieve the detailed temperature profile from the captured bulk temperatures using an inverse radiation technique [16]. The inverse radiation technique basically deciphers a set of bulk radiation measured at several different mean effective wavelengths utilized by an IR pyrometer, to retrieve the temperature distribution within the polymer. The theoretical background of the inverse radiation technique provides the foundation of a new generation IR pyrometer which will be very useful for process monitoring during polymer processing.

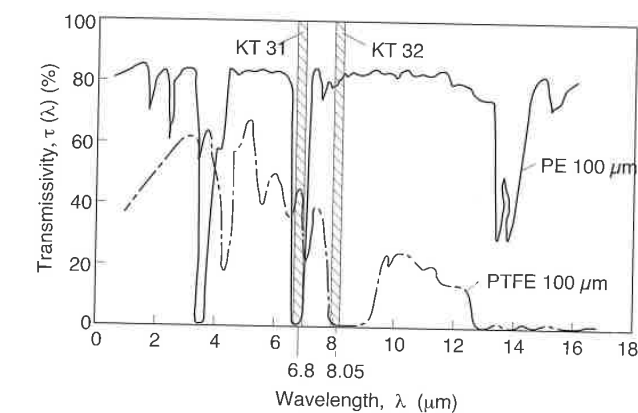


Figure 12.25 Transmissivity of a polyethylene and a polytetrafluoroethylene.

12.8 Heating with Infrared Radiation

Although the heating of polymer sheets for thermoforming or other membrane stretching processes belongs to the field of radiative heat transfer, it is largely an optical problem. In such processes, an infrared heater is used to radiate infrared rays onto the surface of the sheet under consideration. Much of the process that takes place can be analyzed using the theory of absorption and transmittance discussed in Section 12.3. For example, the absorption properties largely depend on pigments or spherulite size. Figure 12.26 [17] shows a plot of

the inverse of the absorption coefficient (penetration depth) of polypropylene with two different spherulite sizes as a function of the wavelength. Figure 12.27 [15] presents a similar graph for polystyrene without pigmentation, translucent polystyrene with a blue pigment, and opaque polystyrene with a white pigment. The absorption of polymers also varies according to the temperature of the radiative heater. Figure 12.28 [15] shows this dependence for various polymer sheets of 1 mm thickness and variable pigment. It is interesting to note that all polymers observe a similar absorption at a heater temperature of 1200 K.

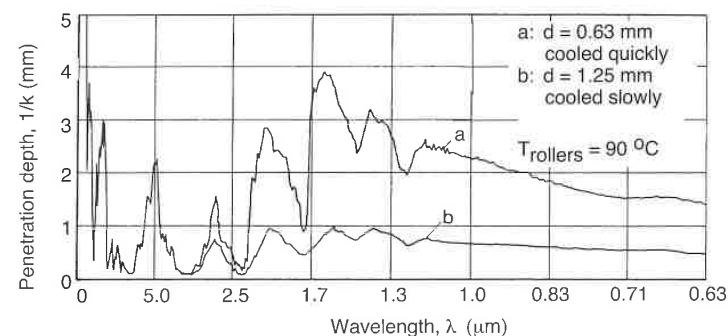


Figure 12.26 Penetration depth of infrared rays into polypropylenes with different morphology.

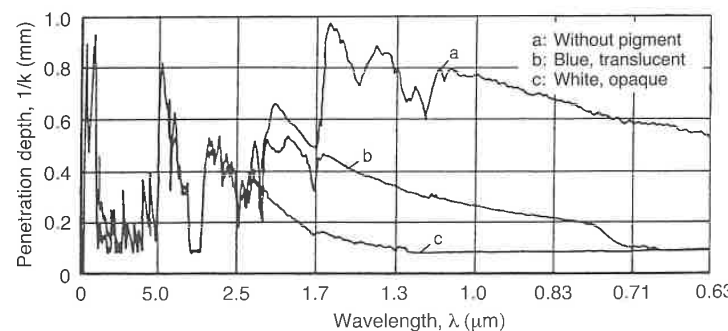


Figure 12.27 Penetration depth of infrared rays into polystyrenes with different pigmentation.

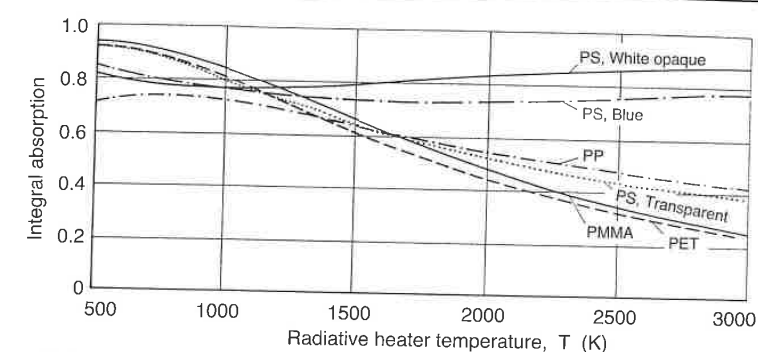


Figure 12.28 Integral absorption as a function of heater temperature for various polymers.

References

1. ASTM Vol 08.02, Plastics (II): ASTM-D4093, (1994).
2. Janeschitz-Kriegl, H., *Polymer Melt Rheology and Flow Birefringence*, Elsevier, Amsterdam, (1984).
3. Isayev, A.I., *Polym. Eng. Sci.*, 23, 271, (1983).
4. Wimberger-Friedl, R., *Polym. Eng. Sci.*, 30, 813, (1990).
5. Lodge, A.S., *Trans. Faraday Soc.*, 52, 120, (1956).
6. Somberger, G., Quantin, J.C., Fajolle, R., Vergnes, B., and Agassant, J.F., *J. Non-Newton. Fluid Mech.*, 23, 123, (1987).
7. Bartoe, W.F., *Engineering Design for Plastics*, E. Baer, Ed., Chapter 8, R.E. Krieger Publishing Co., (1975).
8. ASTM Vol 08.02, Plastics (II): ASTM-D2457, (1994).
9. Adams, J.M., *The Science of Surface Coatings*, Chapter 12, Ed. H.W. Chatfield, D. van Nostrand Co., Inc. Princeton, (1962).
10. Chapman, D., *The Science of Surface Coatings*, Chapter 19, Ed. H.W. Chatfield, D. van Nostrand Co., Inc. Princeton, (1962).
11. Dewitt, D.P., and Richmond, J. C., "Thermal Radiative Properties of Materials," Chapter 2 in *Theory and Practice of Radiation Thermometry*, D.P. Dewitt and G.D. Nutter, Eds., Wiley, New York, (1988).
12. Heimann, W., Communication, Firma W. Heimann, Wiesbaden, Germany.
13. Haberstroh, E., Ph.D. Thesis, IKV, RWTH-Aachen, Germany, (1981).
14. Rietveld, J.X., and Lai, G.-Y., *SPE ANTEC*, 38, 2192, (1992).
15. Lai, G.-Y., Ph.D. Thesis, University of Wisconsin-Madison, Madison, WI, (1993).
16. Rietveld, J.X., and Lai, G.-Y., *SPE ANTEC*, 40, 836, (1994).
17. Weinand, D., Ph.D. Thesis, IKV, RWTH-Aachen, Germany, (1987).

Permeability Properties of Polymers

Because of their low density, polymers are relatively permeable by gases and liquids. A more in-depth knowledge of permeability is necessary when dealing with packaging applications and with corrosive protection coatings. The material transport of gases and liquids through polymers consists of various steps. They are:

- Absorption of the diffusing material at the interface of the polymer, a process also known as *adsorption*,
- *Diffusion* of the attacking medium through the polymer, and
- Delivery or secretion of the diffused material through the polymer interface, also known as *desorption*.

With polymeric materials these processes can occur only if the following rules are fulfilled:

- The molecules of the permeating materials are inert,
- The polymer represents a homogeneous continuum, and
- The polymer has no cracks or voids which channel the permeating material.

In practical cases, such conditions are often not present. Nevertheless, this chapter shall start with these "ideal cases," since they allow for useful estimates and serve as learning tools for these processes.

13.1 Sorption

We talk about adsorption when environmental materials are deposited on the surface of solids. Interface forces retain colliding molecules for a certain time. Possible causes include van der Waals' forces in the case of physical adsorption,

chemical affinity (chemical sorption), or electrostatic forces. With polymers, we have to take into account all of these possibilities.

A gradient in concentration of the permeating substance inside the material results in a transport of that substance which we call *molecular diffusion*. The cause of molecular diffusion is the thermal motion of molecules that permit the foreign molecule to move along the concentration gradient using the intermolecular and intramolecular spaces. However, the possibility to migrate essentially depends on the size of the migrating molecule.

The rate of permeation for the case shown schematically in Fig. 13.1 is defined as the mass of penetrating gas or liquid that passes through a polymer membrane per unit time. The rate of permeation, \dot{m} , can be defined using Fick's first law of diffusion as

$$\dot{m} = -DA\rho \frac{dc}{dx} \quad (13.1)$$

where D is defined as the *diffusion coefficient*, A is the area and ρ the density. If the diffusion coefficient is constant Eq. 13.1 can be easily integrated to give

$$\dot{m} = -DA\rho(c_1 - c_2)/L \quad (13.2)$$

The equilibrium concentrations c_1 and c_2 can be calculated using the pressure, p , and the *sorption equilibrium parameter*, S :

$$c = Sp \quad (13.3)$$

which is often referred to as *Henry's law*.

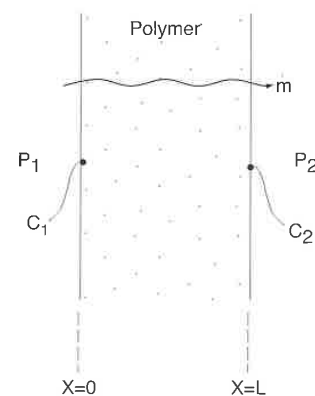


Figure 13.1 Schematic diagram of permeability through a film.

The sorption equilibrium constant, also referred to as *solubility constant*, is almost the same for all polymer materials. However, it does depend largely on the type of gas and on the boiling, T_b , or critical temperatures, T_{cr} , of the gas, such as shown in Fig. 13.2.

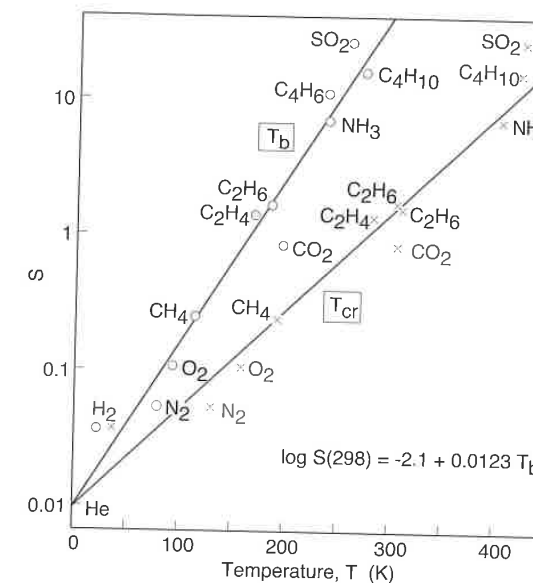


Figure 13.2 Solubility (cm^3/cm^3) of gas in natural rubber at 25 °C and 1 bar as a function of the critical and the boiling temperatures.

13.2 Diffusion and Permeation

Diffusion, however, is only one part of permeation. First, the permeating substance has to infiltrate the surface of the membrane; it has to be absorbed by the membrane. Similarly, the permeating substance has to be desorbed on the opposite side of the membrane. Combining Eq. 13.2 and 13.3 we can calculate the sorption equilibrium using

$$\dot{m} = -DS\rho A(p_1 - p_2)/L \quad (13.4)$$

where the product of the sorption equilibrium parameter and the diffusion coefficient is defined as the *permeability* of a material

$$P = DS = \frac{\dot{m}L}{A\Delta p\rho} \tag{13.5}$$

Equation 13.5 does not take into account the influence of pressure on the permeability of the material and is only valid for dilute solutions. The *Henry-Langmuir model* takes into account the influence of pressure and works very well for amorphous thermoplastics. It is written as

$$P = DS \left(1 + \frac{KR'}{1 + b\Delta p} \right) \tag{13.6}$$

where $K = c'_H b / S$, with c'_H being a saturation capacity constant and b an affinity coefficient. The constant R' represents the degree of mobility, $R'=0$ for complete immobility and $R'=1$ for total mobility. Table 13.1 [1] presents permeability of various gases at room temperature through several polymer films. In the case of multi-layered films commonly used as packaging material, we can calculate the permeation coefficient P_C for the composite membrane using

$$\frac{1}{P_C} = \frac{1}{L_C} \sum_{i=1}^n \frac{L_i}{P_i} \tag{13.7}$$

Table 13.1 Permeability of Various Gases Through Several Polymer Films

Polymer	Permeability (cm ³ mil/100 in ² /24 h/atm)		
	CO ₂	O ₂	H ₂ O
PET	12-20	5-10	2-4
OPET	6	3	1
PVC	4.75-40	8-15	2-3
HDPE	300	100	0.5
LDPE		425	1-1.5
PP	450	150	0.5
EVOH	0.05-0.4	0.05-0.2	1-5
PVDC	1	0.15	0.1

Sorption, diffusion, and permeation are processes activated by heat and as expected follow an Arrhenius type behavior. Thus, we can write

$$S = S_0 e^{-\Delta H_S / RT} \tag{13.8}$$

$$D = D_0 e^{-E_D / RT} \text{ and } \tag{13.9}$$

$$P = P_0 e^{-E_p / RT} \tag{13.10}$$

where ΔH_S is the enthalpy of sorption, E_D and E_p are diffusion and permeation activation energies, R is the ideal gas constant, and T is the absolute temperature. The Arrhenius behavior of sorption, diffusion and permeability coefficients, as a function of temperature for polyethylene and methyl bromine at 600 mm of Hg are shown in Fig. 13.3 [2]. Figure 13.4 [3] presents the permeability of water vapor through several polymers as a function of temperature. It should be noted that permeability properties drastically change once the temperature goes above the glass transition temperature. This is demonstrated in Table 13.2 [4], which presents Arrhenius constants for diffusion of selected polymers and CH₃OH.

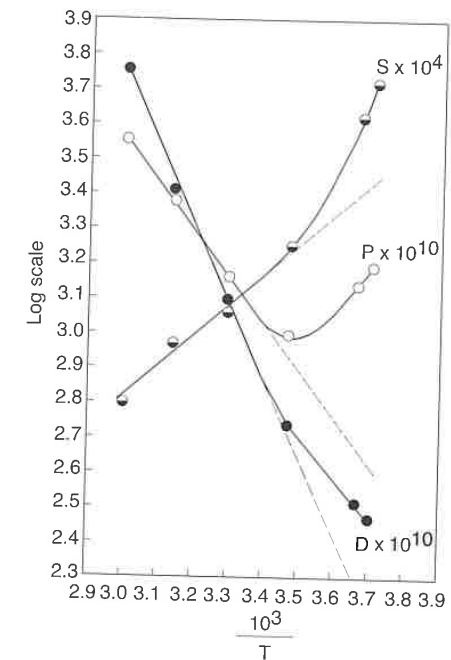


Figure 13.3 Sorption, diffusion, and permeability coefficients, as a function of temperature for polyethylene and methyl bromine at 600 mm of Hg.

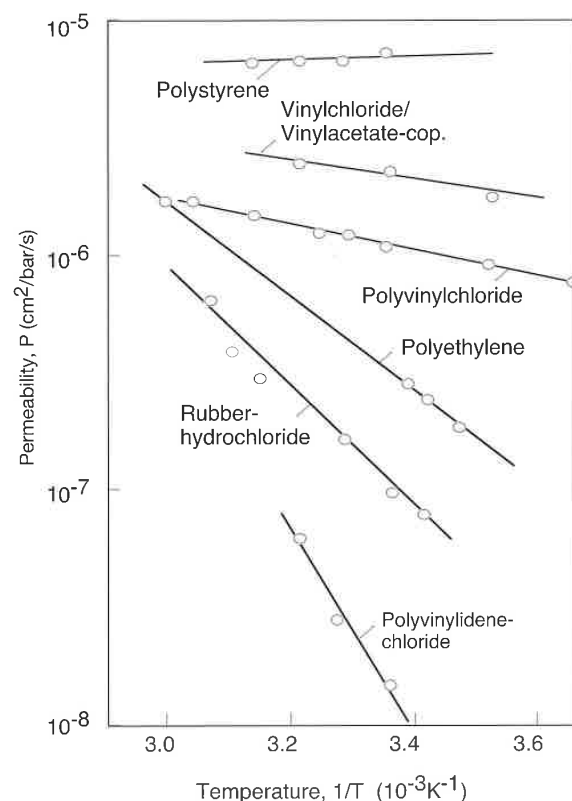


Figure 13.4 Permeability of water vapor as a function of temperature through various polymer films.

The diffusion activation energy E_D depends on the temperature, the size of the gas molecule d_x , and the glass transition temperature of the polymer. This relationship is well represented in Fig. 13.5 [1] with the size of nitrogen molecules, d_{N_2} , as a reference. Table 13.2 contains values of the effective cross section size of important gas molecules. Using Fig. 13.5 with the values from Table 13.1 and using the equations presented in Table 13.3 the diffusion coefficient, D , for several polymers and gases can be calculated.

Table 13.4 also demonstrates that permeability properties are dependent on the degree of crystallinity. Figure 13.6 presents the permeability of polyethylene films of different densities as a function of temperature. Again, the Arrhenius relation becomes evident.

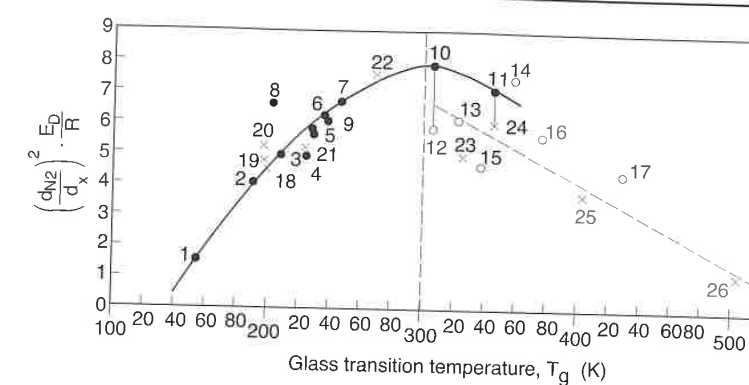


Figure 13.5 Graph to determine the diffusion activation energy E_D as a function of glass transition temperature and size of the gas molecule d_x , using the size of a nitrogen molecule, d_{N_2} , as a reference. Rubbery polymers (\bullet): 1= Silicone rubber, 2= Polybutadiene, 3= Natural rubber, 4= Butadiene/Acrylonitrile K 80/20, 5= Butadiene/Acrylonitrile K 73/27, 6= Butadiene/Acrylonitrile K 68/32, 7= Butadiene/Acrylonitrile K 61/39, 8= Butyl rubber, 9= Polyurethane rubber, 10= Polyvinyl acetate (r), 11= Polyethylene terephthalate (r). Glassy polymers (O): 12= Polyvinyl acetate (g), 13= Vinylchloride/vinyl acetate copolymer, 14= Polyvinyl chloride, 15= Polymethyl methacrylate, 16= Polystyrene, 17= Polycarbonate. Semi-crystalline polymers (X): 18= High-density polyethylene, 19= Low density polyethylene, 20= Polymethylene oxide, 21= Gutta percha, 22= Polypropylene, 23= Polychlorotrifluoroethylene, 24= Polyethyleneterephthalate, 25= Polytetrafluorethylene, 26= Poly(2,6-diphenylphenyleneoxide).

Table 13.2 Diffusion Constants Below and Above the Glass Transition Temperature

Polymer	T_g ($^{\circ}\text{C}$)	D_0 (cm^2/s)		E_D (Kcal/mol)	
		$T < T_g$	$T > T_g$	$T < T_g$	$T > T_g$
Polymethylmethacrylate	90	0.37	110	12.4	21.6
Polystyrene	88	0.33	37	9.7	17.5
Polyvinyl acetate	30	0.02	300	7.6	20.5

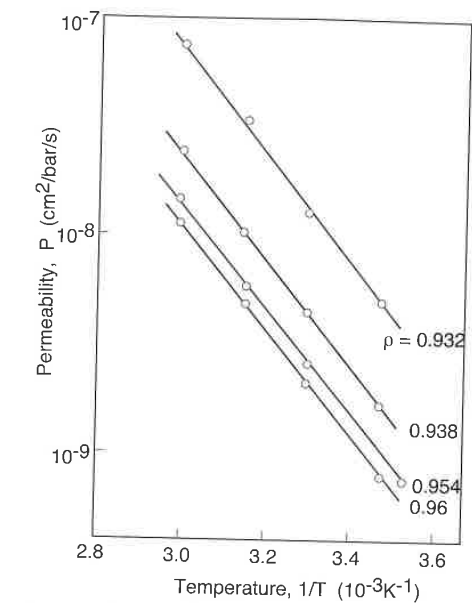
Table 13.3 Important Properties of Gases

Gas	d (nm)	V _{cr} (cm ³)	T _b (K)	T _{cr} (K)	dN ₂ /dx
He	0.255	58	4.3	5.3	0.67
H ₂ O	0.370	56	373	647	0.97
H ₂	0.282	65	20	33	0.74
Ne	0.282	42	27	44.5	0.74
NH ₃	0.290	72.5	240	406	0.76
O ₂	0.347	74	90	55	0.91
Ar	0.354	75	87.5	151	0.93
CH ₃ OH	0.363	118	338	513	0.96
Kr	0.366	92	121	209	0.96
CO	0.369	93	82	133	0.97
CH ₄	0.376	99.5	112	191	0.99
N ₂	0.380	90	77	126	1.00
CO ₂	0.380	94	195	304	1.00
Xe	0.405	119	164	290	1.06
SO ₂	0.411	122	263	431	1.08
C ₂ H ₄	0.416	124	175	283	1.09
CH ₃ Cl	0.418	143	249	416	1.10
C ₂ H ₆	0.444	148	185	305	1.17
CH ₂ Cl ₂	0.490	193	313	510	1.28
C ₃ H ₈	0.512	200	231	370	1.34
C ₆ H ₆	0.535	260	353	562	1.41

Table 13.4 Equations to Compute D Using Data from Table 13.1 and Table 13.2^a

Elastomers	$\log D = \frac{E_D}{2.3R} \left(\frac{1}{T} - \frac{1}{T_R} \right) - 4$
Amorphous thermoplastics	$\log D = \frac{E_D}{2.3R} \left(\frac{1}{T} - \frac{1}{T_R} \right) - 5$
Semi-crystalline thermoplastics	$\log D = \left(\frac{E_D}{2.3R} \left(\frac{1}{T} - \frac{1}{T_R} \right) - 5 \right) (1 - x)$

^a T_R = 435K and X is the degree of crystallinity.

**Figure 13.6** Permeation of nitrogen through polyethylene films of various densities.

13.3 Measuring S, D, and P

The permeability P of a gas through a polymer can be measured directly by determining the transport of mass through a membrane per unit time.

The sorption constant S can be measured by placing a saturated sample into an environment which allows the sample to desorb and measure the loss of weight. As shown in Fig. 13.7, it is common to plot the ratio of concentration of absorbed substance $c(t)$ to saturation coefficient c_∞ with respect to the root of time.

The diffusion coefficient D is determined using sorption curves as the one shown in Fig. 13.7. Using the slope of the curve, a , we can compute the diffusion coefficient as

$$D = \frac{\pi}{16} L^2 a^2 \quad (13.11)$$

where L is the thickness of the membrane.

Another method uses the lag time, t_0 , from the beginning of the permeation process until the equilibrium permeation has occurred, as shown in Fig. 13.8. Here, the diffusion coefficient is calculated using

$$D = \frac{L^2}{6t_0} \tag{13.12}$$

The most important techniques used to determine gas permeability of polymers are the ISO 2556, DIN 53 380 and ASTM D 1434 standard tests.

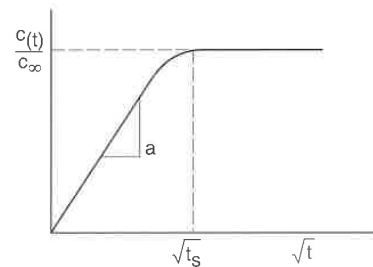


Figure 13.7 Schematic diagram of sorption as a function time.

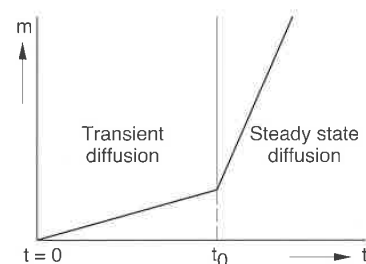


Figure 13.8 Schematic diagram of diffusion as a function of time.

13.4 Corrosion of Polymers and Cracking [5]

In contrast to metallic corrosion, where electrochemical corrosion mechanisms are dominant, several mechanisms play a role in the degradation of polymers. Attacks may occur by physical or chemical means or by combinations of both.

Even without a chemical reaction, the purely physical effect of a surrounding medium can adversely affect the properties of a polymer. Due to the low density of polymers, every surrounding medium that has moveable molecules will infiltrate or permeate the polymer. Experiments have shown that polymer samples under high hydrostatic pressures have even been permeated by silicon oils, which are completely inert at low pressures. The infiltration of silicone oil caused stress cracks and embrittlement in amorphous thermoplastics in the regions of low density, such as particle boundaries, filler material interfaces, and general surface imperfections. If we consider imperfections or particles of characteristic size L , we can perform an energy balance and conclude that the critical strain, ϵ_{crit} , at which a crack will occur is given by [6]

$$\epsilon_{crit} \sim \sqrt{\frac{\gamma}{EL}} \tag{13.13}$$

where E represents Young's modulus and γ the adhesion tension between the individual particles. Crack formation and propagation is shown schematically in Fig. 13.9 [7]. Figure 13.10¹ shows an electron micrograph of permeating media through the inter-spherulitic boundaries of polypropylene.

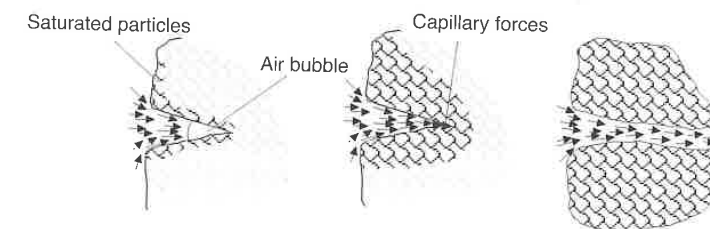


Figure 13.9 Schematic diagram of crack formation and propagation during diffusion.

Desorption, schematically shown in Fig. 13.11, is also undesirable for polymeric components. Similar to soil, which cracks as it dries out too quickly, the stresses that arise as the medium desorbs from the polymer give rise to cracks which may lead to failure of the component. As the absorbed media desorbs, the polymer component shrinks according to the loss of volume. However, inner layers which remain saturated do not shrink, leading to residual stress build-up similar to that which occurs with a cooling component with high temperature gradients. The schematic of the residual stress build-up

¹ Courtesy IKV Aachen.

and concentration of the absorbed media is shown in Fig. 13.12 [8]. The stress history at the edge and center of a desorbing film is shown in Fig. 13.13. The stresses that arise during desorption are easily three times larger than during absorption. The maximum stress, which occurs at the outer edge of the part can be calculated using

$$\sigma_{\max} = \epsilon_{\text{saturation}} \frac{E}{1-\nu} \quad (13.14)$$

The volume change in the immediate surface of the component is caused by the desorption process. The desorbing materials can be auxiliary agents for processing such as coloring agents, softeners, stabilizers, and lubricants, as well as low molecular components of the polymer.



Figure 13.10 Electron micrograph of permeating media through the interspherulitic boundaries of polypropylene.

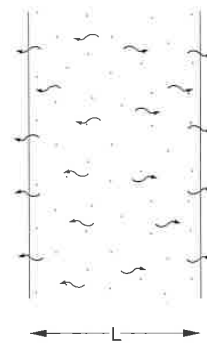


Figure 13.11 Schematic diagram of desorption from a plate.

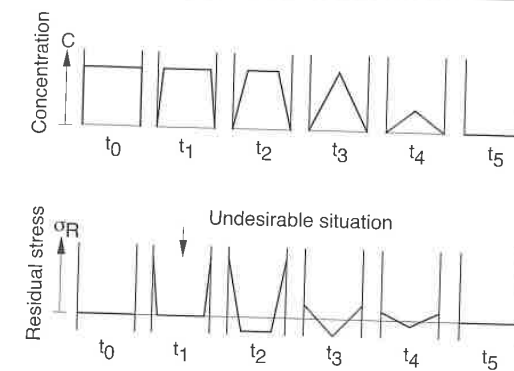


Figure 13.12 Schematic concentration (C) and residual stress (σ_R) as function of time inside a plate during desorption.

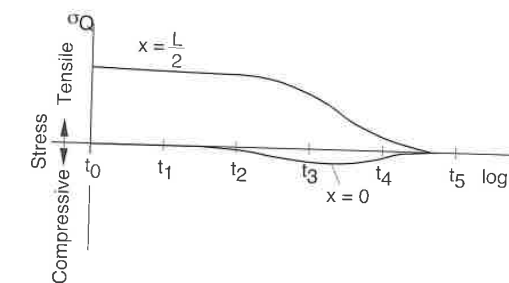


Figure 13.13 Residual stresses inside a plate during desorption.

13.5 Diffusion of Polymer Molecules and Self-diffusion

The ability to infiltrate the surface of a host material decreases with molecular size. Molecules of $M > 5 \times 10^3$ can hardly diffuse through a porous-free membrane. Self-diffusion is when a molecule moves, say in the melt, during crystallization. Also, when bonding rubber, the so-called tack is explained by the self-diffusion of the molecules. The diffusion coefficient for self-diffusion is of the order of

$$D \sim \frac{T}{\eta} \quad (13.15)$$

where T is the temperature and η the viscosity of the melt.

References

1. Rosato, D., and Rosato, D.V., *Blow Molding Handbook*, Hanser Publishers, Munich, (1989).
2. Rogers, C.E., *Engineering Design for Plastics*, Ed. E. Baer, Chapter 9, Robert E. Krieger Publishing Company, Huntington, (1975).
3. Knappe, W., *VDI-Berichte*, 68, 29, (1963).
4. van Krevelen, D.W., and Hoftyzer, P.J., *Properties of Polymers*, 2nd Ed., Elsevier, Amsterdam, (1976).
5. Menges, G., and Löwer, K., *Metallic Corrosion: Proceedings, 8th ICMC*, 2202, Mainz (1981).
6. Menges, G., *Kunststoffe*, 63, 95, (1973).
7. Menges, G. and Suchanek, H., *Kunststoffe, Fortschrittsberichte*, Vol. 3, Hanser Publishers, Munich, (1976).
8. Pütz, D., Ph.D. Thesis, IKV, RWTH-Aachen, Germany, (1977).

Acoustic Properties of Polymers

Sound waves, similar to light waves and electromagnetic waves, can be reflected, absorbed, and transmitted when they strike the surface of a body. The transmission of sound waves through polymeric parts is of particular interest to the design engineer. Of importance is the absorption of sound and the speed at which acoustic waves travel through a body, for example in a pipe, in the form of longitudinal, transversal, and bending modes of deformation.

14.1 Speed of Sound

The speed at which sound is transmitted through a solid barrier is proportional to Young's modulus of the material, E , but inversely proportional to its density, ρ . For sound waves transmitted through a rod, in the longitudinal direction, the speed of sound can be computed as

$$C_L^{\text{rod}} = \sqrt{\frac{E}{\rho}} \quad (14.1)$$

Similarly, the transmission speed of sound waves through a plate along its surface direction can be computed as

$$C_L^{\text{plate}} = \sqrt{\frac{E}{\rho(1-\nu^2)}} \quad (14.2)$$

where ν is Poisson's ratio. The transmission speed of sound waves through an infinite three-dimensional body can be computed using

$$C_{3D} = \sqrt{\frac{E(1-\nu)}{\rho(1+\nu)(1-2\nu)}} \quad (14.3)$$

The transmission of sound waves transversely through a plate (in shear) can be computed using

$$C_r^{\text{plate}} = \sqrt{\frac{G}{\rho}} \quad (14.4)$$

where G is the modulus of rigidity of the material. The transmission speed of sound waves with a frequency f which cause a bending excitation in plates can be computed using

$$C_B^{\text{plate}} = \sqrt{\frac{2\pi fh}{2\sqrt{3}} \frac{E}{\rho(1-\nu^2)}} \quad (14.5)$$

where h is the thickness of the plate.

The speed of sound through a material is dependent on its state. For example, sound waves travel much slower through a polymer melt than through a polymer in the glassy state. Table 14.1 presents orders of magnitude of the speed of sound through polymers in the glassy and rubbery states for various modes of transmission. One can see that the speed of sound through a polymer in the rubbery state is 100 times slower than that through a polymer in a glassy state.

In the melt state, the speed of sound drops with increasing temperature due to density increase. Figure 14.1 [1] presents plots of speed of sound through several polymer melts as a function of temperature. On the other hand, speed of sound increases with pressure as clearly demonstrated in Fig. 14.2 [1].

Table 14.1 Order of Magnitude of Properties Related to Sound Transmission

Modulus (MPa)	Speed of sound (m/s)
	Glassy ($\nu = 0.3$)
$E \cup 10^3 \text{ to } 10^4$	$C_L \cup 2000$ $C_T \cup 1000$ $C_{3D} \cup 2000$
	Rubbery ($\nu = 0.5$)
$E \cup 1 \text{ to } 10^2$	$C_L \cup 10 \text{ to } 400$ $C_T \cup 6 \text{ to } 200$ $C_{3D} \cup 2000$

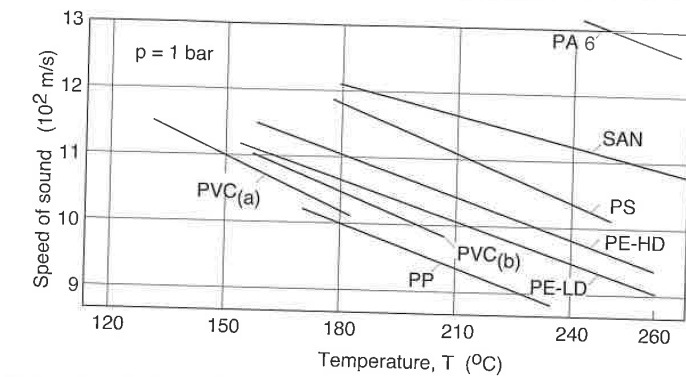


Figure 14.1 Speed of sound as a function of temperature through various polymers.

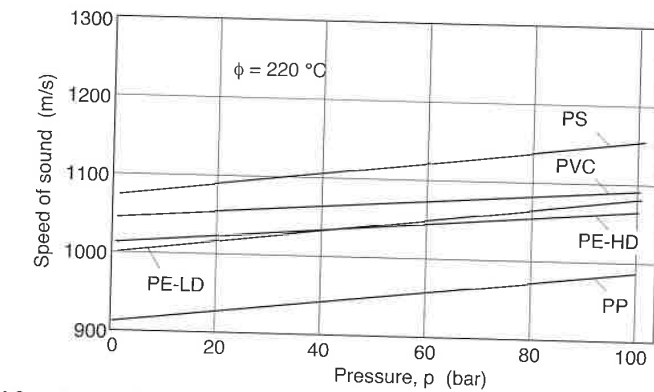


Figure 14.2 Speed of sound as a function of pressure through various polymers.

14.2 Sound Reflection

Sound reflection is an essential property for practical noise reduction. This can be illustrated using the schematic in Fig. 14.3. As sound waves traveling through media 1 strike the surface of media 2, the fraction of sound waves reflected back into media 1 is computed using

$$R = \frac{Z_2 - Z_1}{Z_2 + Z_1} \quad (14.6)$$

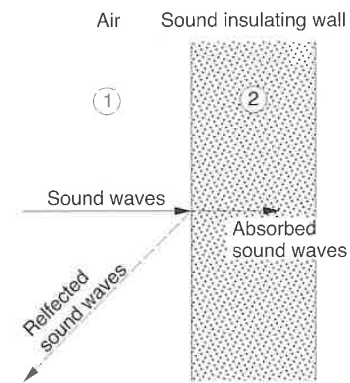


Figure 14.3 Schematic diagram of sound transmission through a plate.

where Z is the impedance or wave resistance, and is defined by

$$Z = \rho C_w \quad (14.7)$$

where C_w is the sound wave speed.

In order to obtain high sound reflection, the mass of the media 2 must be high compared to the mass of media 1 such that $Z_2 \gg Z_1$. The mass of insulating sound walls can be increased with the use of fillers such as plasticized PVC with barium sulfate or by spraying similar anti noise compounds on the insulating walls. Using the mass of the insulating wall, another equation used to compute sound reflectance is

$$R = 20 \log \left(\frac{\pi f M}{Z_0} \right) \quad (14.8)$$

where f is frequency of the sound wave, M the mass of the insulating wall and, Z_0 is the impedance of air. However, doubling the thickness of a wall (media 2) results in only 6 dB of additional sound reduction. It is common practice to use composite plates as insulating walls. This is only effective if walls whose flexural resonance frequencies do not coincide with the frequency of the sound waves are avoided.

14.3 Sound Absorption

Similar to sound reflection, sound absorption is an essential property for practical noise insulation. Materials which have the same characteristic impedance as air ($Z_1 \approx Z_2$) are the best sound-absorbent materials. The sound waves that are not reflected back out into media 1, penetrate media 2 or the sound insulating wall. Sound waves that penetrate a polymer medium are damped out similar to that of mechanical vibrations. Hence, sound absorption also depends on the magnitude of the loss tangent $\tan \delta$, or logarithmic decrement Δ , described in Chapter 9. Table 14.2 presents orders of magnitude for the logarithmic decrement for several types of materials. As expected, elastomers and amorphous polymers have the highest sound absorption properties, whereas metals have the lowest.

Table 14.2 Damping Properties for Various Materials

Material	Temperature range	Logarithmic decrement Δ
Amorphous polymers	$T < T_g$	0.01 to 0.1
Amorphous polymers	$T > T_g$	0.1 to 1
Elastomers		0.1 to 1
Semi-crystalline polymers	$T_g < T < T_m$	≈ 0.1
Fiber reinforced polymers	$T_g < T < T_m$	< 0.01
Wood	$T < T_g$	0.01 to 0.02
Ceramic and glass	$T < T_g$	0.001 to 0.01
Metals	$T < T_m$	< 0.0001

In a material, sound absorption takes place by transforming acoustic waves into heat. Since foamed polymers have an impedance of the same order as air, they are poor reflectors of acoustic waves. This makes them ideal to eliminate multiple reflections of sound waves in *acoustic* or *sound proof rooms*. Figure 14.4 [2] presents the sound absorption coefficient for several foamed polymers as a function of the sound wave frequency. It should be noted that the speed at which sound travels in foamed materials is similar to that of the solid polymers, since foaming affects the stiffness and the density in the same proportion.

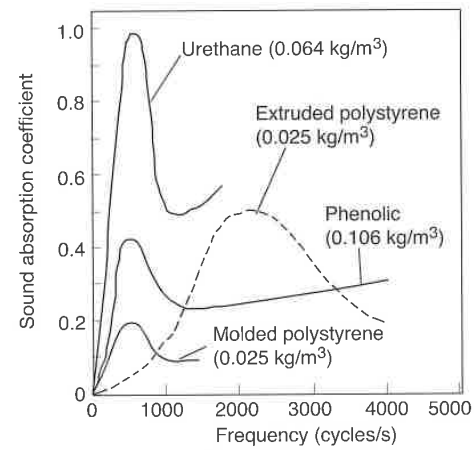


Figure 14.4 Sound absorption coefficients as a function of frequency for various foams.

When compared to wood, even semi-crystalline polymers are considered "sound-proof" materials. Materials with the glass transition temperature lower than room temperature are particularly suitable as damping materials. Commonly used for this purpose are thermoplastics and weakly cross-linked elastomers. Elastomer mats are often adhered on one or both sides of sheet metal, preventing resonance flexural vibrations of the sheet metal such as in automotive applications.

References

1. Offergeld, H., Ph.D Thesis, IKV, RWTH-Aachen, (1990).
2. Griffin, J.D., and Skochdopole, R. E., *Engineering Design for Plastics*, E. Baer, (Ed.), Chapter 15, Robert E. Krieger Publishing Company, Huntington, (1975).

Appendix

Table I Guide Values of the Physical Properties of Plastics

Polymer	Abbreviation	Density		Mechanical properties	
		g/cm ³	lb/in ³	Tensile strength	
				N/mm ²	psi
Low density polyethylene	PE-LD	0.914/0.928	0.0329-0.0330	8/23	1140/3270
High density polyethylene	PE-HD	0.94/0.96	0.0338-0.0345	18/35	2560/4980
EVA	EVA	0.92/0.95	0.0331-0.0341	10/20	1420/2840
Polypropylene	PP	0.90/0.907	0.0324-0.0327	21/37	2990/5260
Polybutene-1	PB	0.905/0.920	0.0325-0.0331	30/38	4270/5400
Polyisobutylene	PIB	0.91/0.93	0.0327-0.0334	2/6	284/853
Poly-4-methylpent-1-ene	PMP	0.83	0.0298	25/28	3560/3980
Ionomers	-	0.94	0.0338	21/35	2990/4980
Rigid PVC	PVC-U	1.38/1.55	0.0496-0.0557	50/75	7110/10670
Plasticized PVC	PVC-P	1.16/1.35	0.0417-0.0486	10/25	1420/3560
Polystyrene	PS	1.05	0.0378	45/65	6400/9240
Styrene/acrylonitrile copolymer	SAN	1.08	0.0392	75	10670
Styrene/polybutadiene graft polymer	SB	1.05	0.0378	26/38	3700/5400
Acrylonitrile/polybut./styrene graft polymer	ABS	1.04/1.06	0.0374-0.0381	32/45	4550/6400
AN/AN elastomers/styrene graft polymer	ASA	1.04	0.0374	32	4550
Polymethylmethacrylate	PMMA	1.17/1.20	0.0421-0.0431	50/77	7110/10950
Polyvinylcarbazole	PVK	1.19	0.0428	20/30	2840/4270
Polyacetal	POM	1.41/1.42	0.0507-0.0511	62/70	8820/9960
Polytetrafluoroethylene	PTFE	2.15/2.20	0.0774-0.0791	25/36	3560/5120
Tetrafluoroethylene/hexafluoropropylene copolymer	FEP	2.12/2.17	0.0763-0.0781	22/28	3130/3980
Polytrifluorochloroethylene	PCTFE	2.10/2.12	0.0755-0.0762	32/40	4550/5690
Ethylene/tetrafluoroethylene	E/TFE	1.7	0.0611	35/54	4980/7680
Polyamide 6	PA 6	1.13	0.0406	70/85	9960/12090
Polyamide 66	PA 66	1.14	0.0410	77/84	10950/11950
Polyamide 11	PA 11	1.04	0.0374	56	7960
Polyamide 12	PA 12	1.02	0.0367	56/65	7960/9240
Polyamide 6-3-T	PA-6-3-T	1.12	0.0403	70/84	9960/11950
Polycarbonate	PC	1.2	0.0432	56/67	7960/9530
Polyethyleneterephthalate	PET	1.37	0.0492	47	6680
Polybutyleneterephthalate	PBT	1.31	0.0471	40	5690
Polyphenyleneether modified	PPE	1.06	0.0381	55/68	7820/9670
Polysulfone	PSU	1.24	0.0446	50/100	7110/14200
Polyphenylenesulfide	PPS	1.34	0.0483	75	10670
Polyarylsulfone	PAS	1.36	0.0490	90	12800
Polyethersulfone	PES	1.37	0.0492	85	12090
Polyarylether	PAE	1.14	0.0411	53	7540
Phenol/formaldehyde, grade 31	PF	1.4	0.0504	25	3560
Urea/formaldehyde, grade 131	UF	1.5	0.0540	30	4270
Melamine/formaldehyde, grade 152	MF	1.5	0.0540	30	4270
Unsaturated polyester resin, grade 802	UP	2.0	0.0720	30	4270
Polydiallylphthalate (GF) molding compound	PDAP	1.51/1.78	0.0543-0.0640	40/75	5690/10670
Silicone resin molding compound	SI	1.8/1.9	0.0648-0.0684	28/46	3980/6540
Polyimide molding	PI	1.43	0.0515	75/100	10570/14200
Epoxy resin, grade 891	EP	1.9	0.0683	30/40	4270/5690
Polyurethane casting resin	PU	1.05	0.0378	70/80	9960/11380
Thermoplastic PU-elastomers	PU	1.20	0.0432	30/40	4270/5690
Linear polyurethane (U ₅₀)	PU	1.21	0.0435	30(σ ₁)	4270(σ ₁)
Vulcanized fiber	VF	1.1/1.45	0.0396-0.0522	85/100	12090/14200
Celluloseacetate, grade 432	CA	1.30	0.0468	38(σ ₁)	5400(σ ₁)
Cellulosepropionate	CP	1.19/1.23	0.0429-0.0452	14/55	7990/7820
Celluloseacetobutyrate, grade 413	CAB	1.18	0.0425	26(σ ₁)	3600(σ ₁)

Elongation at break %	Tensile modulus of elasticity		Ball indentation hardness		Impact strength kJ/m ²	Notched impact strength	
	N/mm ²	kpsi	10-s-value	10-s-value psi		kJ/m ²	ft lb/in of notch
300/1000	200/500	28.4/71.1	13/20	1850/2840	no break	no break	-
100/1000	700/1400	99.6/199	40/65	5690/9240	no break	no break	-
600/900	7/120	0.99/17.1	-	-	no break	no break	-
20/800	11000/1300	156/185	36/70	5120/9960	no break	3/17	no break
250/280	250/350	35.6/49.8	30/38	4270/5400	no break	4/no break	no break
> 1000	-	-	-	-	no break	no break	no break
13/22	1100/1500	156/213	-	-	-	-	0.4/0.6
250/500	180/210	25.6/29.9	-	-	-	-	6/15
10/50	1000/3500	142/498	75/155	10670/22000	no break/>20	2/50	0.4/20
170/400	-	-	-	-	no break	no break	-
3/4	3200/3250	455/462	120/130	17100/18500	5/20	2/2.5	0.25/0.6
5	3600	512	130/140	18500/19900	8/20	2/3	0.35/0.5
25/60	1800/2500	256/356	80/130	11380/18500	10/80	5/13	no break
15/30	1900/2700	270/384	80/120	11380/17100	70/no break	7/20	2.5/12
40	1800	256	75	10670	no break	18	6/8
2/10	2700/3200	384/455	180/200	25600/28400	18	2	0.3/0.5
-	3500	498	200	28400	5	2	-
25/70	2800/3200	398/455	150/170	21300/24200	100	8	1/2.3
350/550	410	58.3	27/35	3840/4980	no break	13/15	3.0
250/330	350	49.8	30/32	4270/4550	-	-	no break
120/175	1050/2100	149/299	65/70	9240/9960	no break	8/10	2.5/2.8
400/500	1100	156	65	9240	-	-	no break
200/300	1400	199	75	10670	no break	no break	3.0
150/300	2000	284	100	14200	no break	15/20	2.1
500	1000	142	75	10670	no break	30/40	1.8
300	1600	228	75	10670	no break	10/20	2/5.5
70/150	2000	284	160	22800	no break	13	-
100/130	2100/2400	299/341	110	15600	no break	20/30	12/18
50/300	3100	441	200	28400	no break	4	0.8/1.0
15	2000	284	180	25600	no break	4	0.8/1.0
50/60	2500	356	-	-	no break	-	4
25/30	2600/2750	370/391	-	-	-	-	1.3
3	3400	484	-	-	-	-	0.3
13	2600	370	-	-	-	-	1/2
30/80	2450	348	-	-	-	-	1.6
25/90	2250	320	-	-	-	-	8.0
0.4/0.8	5600/12000	796/1710	250/320	35600/45500	> 6	> 1.5	0.2/0.6
0.5/1.0	7000/10500	996/1490	260/350	39000/49800	> 6.5	> 2.5	0.5/0.4
0.6/0.9	4900/9100	697/1294	260/410	37000/58300	> 7.0	> 1.5	0.2/0.3
0.6/1.2	14000/20000	1990/2840	240	34100	> 4.5	> 3.0	0.5/16
-	9800/15500	1394/2200	-	-	-	-	0.4/15
-	6000/12000	853/1710	-	-	-	-	0.3/0.8
4/9	23000/28000	3270/3980	-	-	-	-	0.5/1.0
4	21500	3060	-	-	> 8	> 3	2/30
3/6	4000	569	-	-	-	-	0.4
400/450	700	99.6	-	-	no break	no break	no break
35(σ ₁)	1000	140	-	-	no break	3	-
-	-	-	80/140	11380/19900	20/120	-	-
3(σ ₁)	2200	313	50	7110	65	15	2.5
30/100	420/1500	59.7/213	47/79	6680/11240	no break	6/20	1.5
4(σ ₁)	1600	228	35/43	4980/6120	no break	30/35	4/5

(continued on next page)

Table I (cont.) Guide Values of the Physical Properties of Plastics

Polymer	Abbreviation	Density	
		g/cm ³	lb/in ³
Low density polyethylene	PE-LD	0.914/0.928	0.0329-0.0330
High density polyethylene	PE-HD	0.94/0.96	0.0338-0.0345
EVA	EVA	0.92/0.95	0.0331-0.0341
Polypropylene	PP	0.90/0.907	0.0324-0.0327
Polybutene-1	PB	0.905/0.920	0.0325-0.0331
Polyisobutylene	PIB	0.91/0.93	0.0327-0.0334
Poly-4-methylpent-1-ene	PMP	0.83	0.0298
Ionomers	-	0.94	0.0338
Rigid PVC	PVC-U	1.38/1.55	0.0496-0.0557
Plasticized PVC	PVC-P	1.16/1.35	0.0417-0.0486
Polystyrene	PS	1.05	0.0378
Styrene/acrylonitrile copolymer	SAN	1.08	0.0392
Styrene/polybutadiene graft polymer	SB	1.05	0.0378
Acrylonitrile/polybut/styrene graft polymer	ABS	1.04/1.06	0.0374-0.0381
AN/AN elastomers/styrene graft polymer	ASA	1.04	0.0374
Polymethylmethacrylate	PMMA	1.17/1.20	0.0421-0.0431
Polyvinylcarbazole	PVK	1.19	0.0428
Polyacetate	POM	1.41/1.42	0.0507-0.0511
Polytetrafluoroethylene	PTFE	2.15/2.20	0.0774-0.0791
Tetrafluoroethylene/hexafluoropropylene copolymer	FEP	2.12/2.17	0.0763-0.0781
Polytrifluorochloroethylene	PCTFE	2.10/2.12	0.0755-0.0762
Ethylene/tetrafluoroethylene	E/TFE	1.7	0.0611
Polyamide 6	PA 6	1.13	0.0406
Polyamide 66	PA 66	1.14	0.0410
Polyamide 11	PA 11	1.04	0.0374
Polyamide 12	PA 12	1.02	0.0367
Polyamide 6-3-T	PA-6-3-T	1.12	0.0403
Polycarbonate	PC	1.2	0.0432
Polyethyleneterephthalate	PET	1.37	0.0492
Polybutyleneterephthalate	PBT	1.31	0.0471
Polyphenyleneether modified	PPE	1.06	0.0381
Polysulfone	PSU	1.24	0.0446
Polyphenylenesulfide	PPS	1.34	0.0483
Polyarylsulfone	PAS	1.36	0.0490
Polyethersulfone	PES	1.37	0.0492
Polyarylether	PAE	1.14	0.0411
Phenol/formaldehyde, grade 31	PF	1.4	0.0504
Urea/formaldehyde, grade 131	UF	1.5	0.0540
Melamine/formaldehyde, grade 152	MF	1.5	0.0540
Unsaturated polyester resin, grade 802	UP	2.0	0.0720
Polydiallylphthalate (GF) molding compound	PDAP	1.51/1.78	0.0543-0.0640
Silicone resin molding compound	SI	1.8/1.9	0.0648-0.0684
Polyimide molding	PI	1.43	0.0515
Epoxy resin, grade 891	EP	1.9	0.0683
Polyurethane casting resin	PU	1.05	0.0378
Thermoplastic PU-elastomers	PU	1.20	0.0432
Linear polyurethane (U ₅₀)	PU	1.21	0.0435
Vulcanized fiber	VF	1.1/1.45	0.0396-0.0522
Celluloseacetate, grade 432	CA	1.30	0.0468
Cellulosepropionate	CP	1.19/1.23	0.0429-0.0452
Celluloseacetobutyrate, grade 413	CAB	1.18	0.0425

Optical properties		Water absorption	
Refractive index n _D ²⁰	Transparency	mg (4d)	% (24 h)
1.51	transparent	<0.01	<0.01
1.53	opaque	<0.01	<0.01
-	transparent/opaque	-	0.05/0.13
1.49	transparent/opaque	<0.01	0.01/0.03
-	opaque	<0.01	<0.02
-	opaque	<0.01	<0.01
1.46	opaque	-	0.01
1.51	transparent	-	0.1/1.4
1.52/1.55	transparent/opaque	3/18	0.04/0.4
-	transparent/opaque	6/30	0.15/0.75
1.59	transparent	-	0.03/0.1
1.57	transparent	-	0.2/0.3
-	opaque	-	0.05/0.6
-	opaque	-	0.2/0.45
-	translucent/opaque	-	-
1.49	transparent	35/45	0.1/0.4
-	opaque	0.5	0.1/0.2
1.48	opaque	20/30	0.22/0.25
1.35	opaque	-	0
1.34	transparent/translucent	-	<0.1
1.43	translucent/opaque	-	0
1.40	transparent/opaque	-	0.03
1.53	translucent/opaque	-	1.3/1.9
1.53	translucent/opaque	-	1.5
1.52	translucent/opaque	-	0.3
-	translucent/opaque	-	0.25
1.53	transparent	-	0.4
1.58	transparent	10	0.16
-	transparent/opaque	18/20	0.30
-	opaque	-	0.08
-	opaque	-	0.06
1.63	transparent/opaque	-	0.02
-	opaque	-	0.02
1.67	opaque	-	1.8
1.65	transparent	-	0.43
-	translucent/opaque	-	0.25
-	opaque	<150	0.3/1.2
-	opaque	<300	0.4/0.8
-	opaque	<250	0.1/0.6
-	opaque	<45	0.03/0.5
-	opaque	-	0.12/0.35
-	opaque	-	0.2
-	opaque	-	0.32
-	opaque	<30	0.05/0.2
-	transparent	-	0.1/0.2
-	translucent/opaque	-	0.7/0.9
-	translucent/opaque	130	-
-	opaque	-	7/9
1.50	transparent	130	6
1.47	transparent	40/60	1.2/2.8
1.47	transparent	40/60	0.9/3.2

(continued on next page)

Table I (cont.) Guide Values of the Physical Properties of Plastics

Polymer	Abbr- viation	Density		Thermal properties			
		g/cm ³	lb/in ³	Service temperature			
				max./short time		max./continuous	
				°C	°F	°C	°F
Low density polyethylene	PE-LD	0.914/0.928	0.0329-0.0330	80/90	176/194	60/75	140/167
High density polyethylene	PE-HD	0.94/0.96	0.0338-0.0345	90/120	194/248	70/80	158/176
EVA	EVA	0.92/0.95	0.0331-0.0341	65	149	55	131
Polypropylene	PP	0.90/0.907	0.0324-0.0327	140	284	100	212
Polybutene-1	PB	0.905/0.920	0.0325-0.0331	130	266	90	194
Polysisobutylene	PIB	0.91/0.93	0.0327-0.0334	80	176	65	149
Poly-4-methylpent-1-ene	PMP	0.83	0.0298	180	356	120	248
Ionomers	-	0.94	0.0338	120	248	100	212
Rigid PVC	PVC-U	1.38/1.55	0.0496-0.0557	75/100	167/212	65/85	149/185
Plasticized PVC	PVC-P	1.16/1.35	0.0417-0.0486	55/65	131/149	50/55	122/131
Polystyrene	PS	1.05	0.0378	60/80	140/176	50/70	122/158
Styrene/acrylonitrile copolymer	SAN	1.08	0.0392	95	203	85	185
Styrene/polybutadiene graft	SB	1.05	0.0378	60/80	140/176	50/70	122/158
Acrylonitrile/polybut./styrene graft polymer	ABS	1.04/1.06	0.0374-0.0381	85/100	188/212	75/85	167/185
AN/AN elastomers/styrene graft polymer	ASA	1.04	0.0374	85/90	188/194	70/75	158/167
Polymethylmethacrylate	PMMA	1.17/1.20	0.0421-0.0431	85/100	188/212	65/90	149/194
Polyvinylcarbazole	PVK	1.19	0.0428	170	338	160	320
Polyacetal	POM	1.41/1.42	0.0507-0.0511	110/140	230	90/110	194/230
Polytetrafluoroethylene	PTFE	2.15/2.20	0.0774-0.0791	300	572	250	482
Tetrafluoroethylene	FEP	2.12/2.17	0.0763-0.0781	250	482	205	401
hexafluoropropylene copolymer	PCTFE	2.10/2.12	0.0755-0.0762	180	356	150	302
Polytrifluorochlorethylene	E/TFE	1.7	0.0611	220	428	150	302
Ethylene tetrafluoroethylene	-	-	-	-	-	-	-
Polyamide 6	PA 6	1.13	0.0406	140/180	284/356	80/100	176/212
Polyamide 66	PA 66	1.14	0.0410	170/200	338/392	80/120	176/248
Polyamide 11	PA 11	1.04	0.0374	140/150	284/302	70/80	158/176
Polyamide 12	PA 12	1.02	0.0367	140/150	284/302	70/80	158/176
Polyamide 6-3-T	PA-6-3-T	1.12	0.0403	130/140	266/284	80/100	176/212
Polycarbonate	PC	1.2	0.0432	160	320	135	275
Polyethyleneterephthalate	PET	1.37	0.0492	200	392	100	212
Polybutyleneterephthalate	PBT	1.31	0.0471	165	329	100	212
Polyphenyleneether modified	PPE	1.06	0.0381	150	302	80	176
Polysulfone	PSU	1.24	0.0446	200	392	150	302
Polyphenylsulfide	PPS	1.34	0.0483	300	572	200	392
Polyarylsulfone	PAS	1.36	0.0490	300	572	260	500
Polyethersulfone	PES	1.37	0.0492	260	500	200	392
Polyarylether	PAE	1.14	0.0411	160	320	120	248
Phenol/formaldehyde, grade 31	PF	1.4	0.0504	140	284	110	230
Urea/formaldehyde, grade 131	UF	1.5	0.0540	100	212	70	158
Melamine/formaldehyde, grade 152	MF	1.5	0.0540	120	248	80	176
Unsaturated polyester resin, grade 802	UP	2.0	0.0720	200	392	150	302
Polydiallylphthalate (GF) molding compound	PDAP	1.51/1.78	0.0543-0.0640	190/250	374/482	150/180	302/356
Silicone resin molding compound	SI	1.8/1.9	0.0648-0.0684	250	482	170/180	338/356
Polyimide molding	PI	1.43	0.0515	400	752	260	500
Epoxy resin, grade 891	EP	1.9	0.0683	180	356	130	266
Polyurethane casting resin	PU	1.05	0.0378	100	212	80	176
Thermoplastic PU-elastomers	PU	1.20	0.0432	110	230	80	176
Linear polyurethane (U ₅₀)	PU	1.21	0.0435	80	176	60	140
Vulcanized fiber	VF	1.1/1.45	0.0396-0.0522	180	356	105	221
Celluloseacetate, grade 432	CA	1.30	0.0468	80	176	70	158
Cellulosepropionate	CP	1.19/1.23	0.0429-0.0452	80/120	176/248	60/115	140/239
Celluloseacetobutyrate, grade 413	CAB	1.18	0.0425	80/120	176/248	60/115	140/239

min./continuous	Heat deflection temperature				Coefficient of linear expansion		Thermal conductivity		Specific heat		
	°C		°F		K ⁻¹ · 10 ⁶	in/in/°F · 10 ⁻⁶	W/mK	BTU in/ft ² h°F	kJ/kgK	BTU/lb°F	
	VSP (Vicac 5 kg)	1.86/0.45 N/mm ²	VSP (Vicac lb)	264/66 psi							
	°C	°F	°C	°F							
-50	-58	-	35	-	95	250	140	0.32/0.40	2.2/2.8	2.1/2.5	8.8/10.5
-50	-58	60/70	50	140/158	122	200	110	0.38/0.51	2.6/3.5	2.1/2.7	8.8/11.5
-60	-76	-	34/62	-	93/144	160/200	90/110	0.35	2.4	2.3	9.5
0/-30	32/-22	85/100	45/120	185/212	113/248	150	83	0.17/0.22	1.2/1.5	2.0	8.3
0	32	70	60/110	158	140/230	150	83	0.20	1.4	1.8	7.5
-50	-58	-	-	-	-	120	67	0.12/0.20	0.8/1.4	-	-
0	32	-	-	-	-	117	65	0.17	1.2	2.18	9.1
-50	-58	-	38/45	-	100/113	120	67	0.24	1.7	2.20	9.2
-5	21	75/110	60/82	167/230	140/180	70/80	39/45	0.14/0.17	1.0/1.2	0.85/0.9	3.55/3.75
0/-20	32/-4	40	-	104	-	150/210	83/110	0.15	1.05	0.9/1.8	3.75/7.5
-10	14	78/99	110/80	172/210	230/176	70	39	0.18	1.25	1.3	5.4
-20	-4	-	104/90	-	219/194	80	45	0.18	1.25	1.3	5.4
-20	-4	77/95	104/82	171/203	219/180	70	39	0.18	1.25	1.3	5.4
-40	-40	95/110	80/120	203/230	176/248	60/110	33/61	0.18	1.25	1.3	5.4
-40	-40	92	100/110	198	212/230	80/110	44/61	0.18	1.25	1.3	5.4
-40	-40	70/100	60/100	158/212	140/212	70	39	0.18	1.25	1.47	6.15
-100	-148	180	-	356	-	-	-	0.29	2.0	-	-
-60	-76	160/173	110/170	320/344	230/338	90/110	50/61	0.25/0.30	1.7/2.1	1.46	6.1
-200	-328	-	-121	-	-250	100	56	0.25	1.7	1.0	4.20
-100	-148	-	-70	-	-158	80	45	0.25	1.7	1.12	4.65
-40	-40	-	-126	-	-259	60	33	0.22	1.5	0.9	3.75
-190	-310	-	71/104	-	160/219	40	22	0.23	1.6	0.9	3.75
-30	-22	180	80/190	356	176/374	80	44	0.29	2.0	1.7	7.1
-30	-22	200	105/200	392	221/392	80	44	0.23	1.6	1.7	7.1
-70	-94	175	150/130	347	302/266	130	72	0.23	1.6	1.26	5.25
-70	-94	165	140/150	329	284/302	150	83	0.23	1.6	1.26	5.25
-70	-94	145	140/80	293	284/176	80	45	0.23	1.6	1.6	6.70
-100	-148	138	130/145	280	266/293	60/70	33/39	0.21	1.45	1.17	4.90
-20	-4	188	-	280	-	70	39	0.24	1.65	1.05	4.40
-30	-22	178	50/190	352	122/374	60	33	0.21	1.45	1.30	5.40
-30	-22	148	100/140	298	212/284	60	33	0.23	1.60	1.40	5.85
-100	-148	-	175/180	-	347/356	54	30	0.28	1.95	1.30	5.40
-	-	-	137/-	-	277/-	55	31	0.25	1.70	-	-
-	-	-	-	-	-	47	26	0.16	1.10	-	-
-	-	-	-	-	-	55	31	0.18	1.25	1.10	4.6
-	-	-	150/160	-	302/320	65	36	0.26	1.80	1.46	6.1
-	-	-	150/190	-	302/374	30/50	17/28	0.35	2.40	1.30	5.40
-	-	-	130/-	-	266/-	50/60	28/33	0.40	2.75	1.20	5.0
-	-	-	180/-	-	356/-	50/60	28/33	0.50	3.45	1.20	5.0
-	-	-	230/-	-	446/-	20/40	11/22	0.70	4.85	1.20	5.0
-50	-58	-	220/-	-	428/-	10/35	55/19	0.60	4.15	-	5.0
-50	-58	-	480/-	-	896/-	20/50	11/28	0.3/0.4	2.05/2.75	0.8/0.9	3.35/3.75
-200	-239	-	240/-	-	464/-	50/63	28/35	0.6/0.65	4.15/4.50	-	-
-	-	-	200/-	-	392/-	11/35	6.1/19	0.88	6.1	0.8	3.35
-	-	-	90/-	-	194/-	10/20	5.5/11	0.58	4.0	1.76	7.30
-40	-40	-	-	-	-	150	83	1.7	1.15	0.5	2.10
-15	3	100	-	212	-	210	12	1.8	1.25	0.4	1.65
-30	-22	-	-	-	-	-	-	-	-	-	-
-40	-40	50/63	90/-	122/144	194/-	120	67	0.22	1.50	1.6	6.7
-40	-40	100	73/98	212	163/208	110/130	61/72	0.21	1.45	1.7	7.1
-40	-40	60/75	62/71	140/167	144/160	120	67	0.21	1.45	1.6	6.7

(continued on next page)

Table I (cont.) Guide Values of the Physical Properties of Plastics

Polymer	DIN 7728 Bl. 1	Density		Electrical properties	
		g/cm ³	lb/in ³	Volume resistivity Ω cm	Surface resistivity Ω
Low density polyethylene	PE-LD	0.914/0.928	0.0329-0.0330	>10 ¹⁷	10 ¹⁴
High density polyethylene	PE-HD	0.94/0.96	0.0338-0.0345	>10 ¹⁷	10 ¹⁴
EVA	EVA	0.92/0.95	0.0331-0.0341	<10 ¹⁵	10 ¹³
Polypropylene	PP	0.90/0.907	0.0324-0.0327	>10 ¹⁷	10 ¹³
Polybutene-1	PB	0.905/0.920	0.0325-0.0331	>10 ¹⁷	10 ¹³
Polyisobutylene	PIB	0.91/0.93	0.0327-0.0334	>10 ¹⁵	10 ¹³
Poly-4-methylpent-1-ene	PMP	0.83	0.0298	>10 ¹⁶	10 ¹³
Ionomers	-	0.94	0.0338	>10 ¹⁶	10 ¹³
Rigid PVC	PVC-U	1.38/1.55	0.0496-0.0557	>10 ¹⁵	10 ¹³
Plasticized PVC	PVC-P	1.16/1.35	0.0417-0.0486	>10 ¹¹	10 ¹¹
Polystyrene	PS	1.05	0.0378	>10 ¹⁶	>10 ¹³
Styrene/acrylonitrile copolymer	SAN	1.08	0.0392	>10 ¹⁶	>10 ¹³
Styrene/polybutadiene graft polymer	SB	1.05	0.0378	>10 ¹⁶	>10 ¹³
Acrylonitrile/polybut./styrene graft polymer	ABS	1.04/1.06	0.0374-0.0381	>10 ¹⁵	>10 ¹³
AN/AN elastomers/styrene graft polymer	ASA	1.04	0.0374	>10 ¹⁵	>10 ¹³
Polymethylmethacrylate	PMMA	1.17/1.20	0.0421-0.0431	>10 ¹⁵	10 ¹⁵
Polyvinylcarbazole	PVK	1.19	0.0428	>10 ¹⁶	10 ¹⁴
Polyacetal	POM	1.41/1.42	0.0507-0.0511	>10 ¹⁵	10 ¹³
Polytetrafluoroethylene	PTFE	2.15/2.20	0.0774-0.0791	>10 ¹⁸	10 ¹⁷
Tetrafluoroethylene/hexafluoropropylene copolymer	FEP	2.12/2.17	0.0763-0.0781	>10 ¹⁸	10 ¹⁶
Polytrifluoroethoxyethylene	PCTFE	2.10/2.12	0.0755-0.0762	>10 ¹⁸	10 ¹⁶
Ethylene/tetrafluoroethylene	E/TFE	1.7	0.0611	>10 ¹⁶	10 ¹³
Polyamide 6	PA 6	1.13	0.0406	10 ¹²	10 ¹⁰
Polyamide 66	PA 66	1.14	0.0410	10 ¹²	10 ¹⁰
Polyamide 11	PA 11	1.04	0.0374	10 ¹³	10 ¹¹
Polyamide 12	PA 12	1.02	0.0367	10 ¹³	10 ¹¹
Polyamide 6-3-T	PA-6-3-T	1.12	0.0403	10 ¹¹	10 ¹⁰
Polycarbonate	PC	1.2	0.0432	>10 ¹⁷	>10 ¹⁵
Polyethyleneterephthalate	PET	1.37	0.0492	10 ¹⁶	10 ¹⁶
Polybutyleneterephthalate	PBT	1.31	0.0471	10 ¹⁶	10 ¹³
Polyphenyleneether modified	PPE	1.06	0.0381	10 ¹⁶	10 ¹⁴
Polysulfone	PSU	1.24	0.0446	>10 ¹⁶	-
Polyphenylenesulfide	PPS	1.34	0.0483	>10 ¹⁶	-
Polyarylsulfone	PAS	1.36	0.0490	>10 ¹⁶	-
Polyethersulfone	PES	1.37	0.0492	10 ¹⁷	-
Polyarylether	PAE	1.14	0.0411	>10 ¹⁰	-
Phenol/formaldehyde, grade 31	PF	1.4	0.0504	10 ¹¹	>10 ⁸
Urea/formaldehyde, grade 131	UF	1.5	0.0540	10 ¹¹	>10 ¹⁰
Melamine/formaldehyde, grade 152	MF	1.5	0.0540	11 ¹¹	>10 ⁸
Unsaturated polyester resin, grade 802	UP	2.0	0.0720	>10 ¹²	>10 ¹⁰
Polydiallylphthalate (GF) molding compound	PDAP	1.51/1.78	0.0543-0.0640	10 ¹³ /10 ¹⁶	10 ¹³
Silicone resin molding compound	SI	1.8/1.9	0.0648-0.0684	10 ¹⁴	10 ¹²
Polyimide molding	PI	1.43	0.0515	>10 ¹⁶	>10 ¹⁵
Epoxy resin, grade 891	EP	1.9	0.0683	>10 ¹⁴	>10 ¹²
Polyurethane casting resin	PU	1.05	0.0378	10 ¹⁶	10 ¹⁴
Thermoplastic PU-elastomers	PU	1.20	0.0432	10 ¹²	10 ¹¹
Linear polyurethane (U ₅₀)	PU	1.21	0.0435	10 ¹³	10 ¹²
Vulcanized fiber	VF	1.1/1.45	0.0396-0.0522	10 ¹⁰	10 ⁸
Celluloseacetate, grade 432	CA	1.30	0.0468	10 ¹³	10 ¹²
Cellulosepropionate	CP	1.19/1.23	0.0429-0.0452	10 ¹⁶	10 ¹⁴
Celluloseacetobutyrate, grade 413	CAB	1.18	0.0425	10 ¹⁶	10 ¹⁴

Dielectric constant		Dissipation (power) factor tan δ		Dielectric strength		Tracking resistance		
50 Hz	10 ⁶ Hz	50 Hz	10 ⁶ Hz	kV/25 μm	kV/cm	KA	KB	KC
2.29	2.28	1.5 · 10 ⁻⁴	0.8 · 10 ⁻⁴	> 700	-	3b	> 600	> 600
2.35	2.34	2.4 · 10 ⁻⁴	2.0 · 10 ⁻⁴	> 700	-	3c	> 600	> 600
2.5/3.2	2.6/3.2	0.003/0.02	0.03/0.05	-	620/780	-	-	-
2.27	2.25	< 4 · 10 ⁻⁴	< 5 · 10 ⁻⁴	800	500/650	3c	> 600	> 600
2.5	2.2	7 · 10 ⁻⁴	6 · 10 ⁻⁴	700	-	3c	> 600	> 600
2.3	-	0.0004	-	230	-	3c	> 600	> 600
2.12	2.12	7 · 10 ⁻⁵	3 · 10 ⁻⁵	280	700	3c	> 600	> 600
3.5	3.0	0.011	0.015	200/400	350/500	2/3b	600	600
4/8	4/4.5	0.08	0.12	150/300	300/400	-	-	-
2.5	2.5	1/4 · 10 ⁻⁴	0.5/4 · 10 ⁻⁴	500	300/700	1/2	140	150/250
2.6/3.4	2.6/3.1	6/8 · 10 ⁻³	7/10 · 10 ⁻³	500	400/500	1/2	160	150/260
2.4/4.7	2.4/3.8	4/20 · 10 ⁻⁴	4/20 · 10 ⁻⁴	500	300/600	2	> 600	> 600
2.4/5	2.4/3.8	3/8 · 10 ⁻³	2/15 · 10 ⁻³	400	350/500	3a	> 600	> 600
3/4	3/3.5	0.02/0.05	0.02/0.03	350	360/400	3a	> 600	> 600
3.3/3.9	2.2/3.2	0.04/0.06	0.04/0.04	300	400/500	3c	> 600	> 600
-	3	6/10 · 10 ⁻⁴	6/10 · 10 ⁻⁴	500	500	3b	> 600	> 600
3.7	3.7	0.005	0.005	700	380/500	3b	> 600	> 600
< 2.1	< 2.1	< 2 · 10 ⁻⁴	< 2 · 10 ⁻⁴	500	480	3c	> 600	> 600
2.1	2.1	< 2 · 10 ⁻⁴	< 7 · 10 ⁻⁴	500	550	3c	> 600	> 600
2.3/2.8	2.3/2.5	1 · 10 ⁻³	2 · 10 ⁻²	500	550	3c	> 600	> 600
2.6	2.6	8 · 10 ⁻⁴	5 · 10 ⁻³	380	400	3c	> 600	> 600
3.8	3.4	0.01	0.03	350	400	3b	> 600	> 600
8.0	4.0	0.14	0.08	400	600	3b	> 600	> 600
3.7	3.5	0.06	0.04	300	425	3b	> 600	> 600
4.2	3.1	0.04	0.03	300	450	3b	> 600	> 600
4.0	3.0	0.03	0.04	250	350	3b	> 600	> 600
3.0	2.9	7 · 10 ⁻⁴	1 · 10 ⁻²	350	380	1	120/160	260/300
4.0	4.0	2 · 10 ⁻³	2 · 10 ⁻²	500	420	2	-	-
3.0	3.0	2 · 10 ⁻³	2 · 10 ⁻²	500	420	3b	420	380
2.6	2.6	4 · 10 ⁻⁴	9 · 10 ⁻⁴	500	450	1	300	300
3.1	3.0	8 · 10 ⁻⁴	3 · 10 ⁻³	-	425	1	175	175
3.1	3.2	4 · 10 ⁻⁴	7 · 10 ⁻⁴	-	595	-	-	-
3.9	3.7	3 · 10 ⁻³	13 · 10 ⁻³	-	350	-	-	-
3.5	3.5	1 · 10 ⁻³	6 · 10 ⁻³	-	400	-	-	-
3.14	3.10	6 · 10 ⁻³	7 · 10 ⁻³	-	430	-	-	-
6	4.5	0.1	0.03	50/100	300/400	1	140/180	125/175
8	7	0.04	0.3	80/150	300/400	3a	> 400	> 600
9	8	0.06	0.03	80/150	290/300	3b	> 500	> 600
6	5	0.04	0.02	120	250/530	3c	> 600	> 600
5.2	4	0.04	0.03	-	400	3c	> 600	> 600
4	3.5	0.03	0.02	-	200/400	3c	> 600	> 600
3.5	3.4	2 · 10 ⁻³	5 · 10 ⁻³	-	560	1	> 300	> 380
3.5/5	3.5/5	0.001	0.01	-	300/400	3c	> 300	200/600
3.6	3.4	0.05	0.05	-	240	3c	-	-
6.5	5.6	0.03	0.06	-	300/600	3a	> 600	> 600
5.8	4.0	0.12	0.07	330	-	-	-	-
-	-	0.08	-	70/180	-	-	-	-
5.8	4.6	0.02	0.03	320	400	3a	> 600	> 600
4.2	3.7	0.01	0.03	350	400	3a	> 600	> 600
3.7	3.5	0.006	0.021	380	400	3a	> 600	> 600

Table II Permeability of Films Made from Various Polymers

Polymer	Temperature °C	Film thickness μm ¹⁾	Water vapor g/cm ² day	N ₂ cm ³ /m ² day bar	Air	O ₂	CO ₂	H ₂	Ar	He
PE-LD	23	100	1	700	1100	2000	10000	8000	-	-
PE-HD (ρ=0.95 g/cm ³ , unstretched)	25	40	0.9	525	754	1890	7150	6000	-	-
	30	40	1.7	720	960	2270	8600	7600	-	-
	40	40	3.5	1220	1660	3560	13100	11400	-	-
	50	40	8.1	2140	2650	5650	19500	16800	-	-
PE-HD (ρ=0.95 g/cm ³ , stretched)	25	40	1.0	430	680	1210	5900	5000	-	-
	30	40	1.6	560	830	1530	7200	6000	-	-
	40	40	4.3	1050	1490	2650	11200	9400	-	-
	50	40	10.5	1870	2670	4650	18100	14800	-	-
E/VA copolymer, VAC 20%	23	100	455	1400	-	4000	17000	-	-	-
Polypropylene (unstretched)	25	40	2.1	430	700	1900	6100	17700	1480	19200
	30	40	3.2	600	960	2500	8400	18200	2100	21700
	40	40	7.4	1280	1820	5100	14800	28100	4100	29800
	50	40	19.0	2800	3600	9200	27300	46600	8000	43500
Polypropylene (stretched)	25	40	0.81	200	350	1000	3300	6700	-	7300
	30	40	1.2	260	480	1200	3900	8200	-	8500
	40	40	3.3	560	940	2300	7050	12300	-	12100
	50	40	8.4	1200	1850	4150	13200	19800	-	17800
PVC-U (unstretched)	20	40	7.6	12	28	87	200	-	-	-
PVC-U (stretched)	20	40	4.4	13	13	43	110	-	-	-
PVC-P	20	40	20	350	550	1500	8500	-	-	-
Polyvinylidenechloride	25	25	0.1/0.2	1.8/2.3	5/10	1.7/11	60/700	630/1400	-	-
Polystyrene (stretched)	25	50	14.0	27	80	235	800	1260	-	-
Polyacetal	20	40	2.5	10	16	50	96	420	-	-
PFEP copolymers	40	25	2.0	375	-	3000	6500	2000	-	-
	CTFE	40	25	0.38/0.85	39	-	110/230	250/620	3400/5200	-
E/TFE copolymers	23	25	0.6	470	-	1560	3800	-	-	-
	E/CTFE copolymers	23	25	9.0	150	-	39.0	1700	-	-
	PVF	23	25	50.0	3.8	-	4.7	170	900	-
Polyamide 6	25	25	80/110	14	-	40	200	1500	-	-
Polyamide 66	25	25	15/30	11	-	80	140	-	-	-
Polyamide 11	25	25	1.5/4.0	50	-	540	2400	5000	-	-
Polyamide 12	25	25	0.35	200/280	-	800/1400	2600/5300	-	-	-
Polycarbonate	23	25	4	680	-	4000	14500	22000	-	-
Polyethyleneterephthalate (stretched)	23	25	0.6	9/15	-	80/110	200/340	1500	-	-
Polysulfone	23	25	6	630	-	3600	15000	28000	-	-
PU elastomers	23	25	13/25	550/1600	-	1000/4500	6000/22000	-	-	-
Polyimide	23	25	25	94	-	390	700	3800	-	-
Celluloseacetate	25	25	150/600	470/630	-	1800/2300	13000/15000	14000	-	-
Celluloseacetobutyrate	25	25	460/600	3800	-	15000	94000	-	-	-

¹⁾ 1 μm = 0.0394 mil.

Table III General Properties of Selected Polymeric Materials

ABS - Acrylonitrile-Butadiene-Styrene Copolymer

Characteristics: Glossy, high stiffness, impact resistance, scratch resistance, high dimensional stability, ability to be galvanized, poor environmental resistance.

Identified by: Opaque, smells sweet during burn test, yellow flame with soot.

ρ = 1.03 - 1.07 g/cm³

C_p = 1,470 J/kgK

k = 0.3 W/mK

T_{max}^{short term} = 80 - 95°C

T_{max}^{long term} = 75 - 85°C

PA6 - Polyamide 6

Characteristics: Abrasion resistance, impact resistance, absorbs water up to 9.5%, often found as a fiber or filament, often found reinforced.

Identified by: Opaque, cream color, smells of burnt hair during burn test, yellow flame with blue halo.

ρ = 1.12 - 1.15 g/cm³

C_p = 1670 J/kgK

k = 0.24 W/mK

T_{max}^{short term} = 140 - 160°C

T_{max}^{long term} = 80 - 100°C

Table III General Properties of Selected Polymeric Materials (continued)

<p>PA66 - Polyamide 66</p> <p>Characteristics: Abrasion resistance, impact resistance, aging and heat resistance, absorbs water up to 8.5%, often found as a fiber or filament, often found reinforced.</p> <p>Identified by: Opaque, cream color, smells of burnt hair during burn test, yellow flame with blue halo.</p>		
<p>$\rho = 1.13 - 1.16 \text{ g/cm}^3$</p> <p>$C_p = 1670 \text{ J/kg/K}$</p> <p>$k = 0.24 \text{ W/m/K}$</p> <p>$T_{\text{max}}^{\text{short term}} = 140 - 170^\circ\text{C}$</p> <p>$T_{\text{max}}^{\text{long term}} = 80 - 100^\circ\text{C}$</p>		
<p>$\rho = 1.38 \text{ g/cm}^3$</p> <p>$C_p = 1,260 \text{ J/kg/K}$</p> <p>$k = 0.52 \text{ W/m/K}$</p> <p>$T_{\text{max}}^{\text{short term}} = 140 - 170^\circ\text{C}$</p> <p>$T_{\text{max}}^{\text{long term}} = 80 - 100^\circ\text{C}$</p>	<p>PA66 GF30 - Polyamide 66 -30% Glass Reinforced</p> <p>Characteristics: Abrasion resistance, high stiffness, impact resistance, aging and heat resistance.</p> <p>Identified by: Opaque, cream color, smells of burnt hair during burn test, yellow flame with blue halo.</p>	

Table III General Properties of Selected Polymeric Materials (continued)

<p>PC - Polycarbonate</p> <p>Characteristics: Glossy, high optical properties, high dimensional stability, impact resistance, high thermal stability.</p> <p>Identified by: Transparent, dark yellow flame during burn test, soot forming, self extinguishing.</p>		
<p>$\rho = 1.20 - 1.24 \text{ g/cm}^3$</p> <p>$C_p = 1,260 \text{ J/kg/K}$</p> <p>$k = 0.2 \text{ W/m/K}$</p> <p>$T_{\text{max}}^{\text{short term}} = 135^\circ\text{C}$</p> <p>$T_{\text{max}}^{\text{long term}} = 100^\circ\text{C}$</p>		
<p>$\rho = 1.15 - 1.19 \text{ g/cm}^3$</p> <p>$C_p = 1,470 \text{ J/kg/K}$</p> <p>$k = 0.2 \text{ W/m/K}$</p> <p>$T_{\text{max}}^{\text{short term}} = 85 - 95^\circ\text{C}$</p> <p>$T_{\text{max}}^{\text{long term}} = 65 - 80^\circ\text{C}$</p>	<p>PMMA - Polymethylmethacrylate</p> <p>Characteristics: Scratch resistance, stiffness, brittleness, good chemical and environmental stability, susceptible to stress cracking.</p> <p>Identified by: Transparent, flammability, blue flame during burn test, fruity and sweet smell during burn test.</p>	

Table III General Properties of Selected Polymeric Materials (continued)

<p>POM - Polyoxymethylene (Polyacetal)</p> <p>Characteristics: High strength and stiffness, highly flexible, low friction coefficient, high dimensional stability, low susceptibility to stress cracking, sensitive to UV light.</p> <p>Identified by: Opaque, white color, smell of formaldehyde during burn test, blue flame during burn test.</p>		
<p>$\rho = 1.41 - 1.43 \text{ g/cm}^3$</p> <p>$C_p = 1.470 \text{ J/kg/K}$</p> <p>$k = 0.2 \text{ W/m/K}$</p> <p>$T_{\text{max}}^{\text{short term}} = 110 - 140^\circ\text{C}$</p> <p>$T_{\text{max}}^{\text{long term}} = 90 - 100^\circ\text{C}$</p>		
<p>$\rho = 0.90 - 0.91 \text{ g/cm}^3$</p> <p>$C_p = 1.930 \text{ J/kg/K}$</p> <p>$k = 0.24 \text{ W/m/K}$</p> <p>$T_{\text{max}}^{\text{short term}} = 130^\circ\text{C}$</p> <p>$T_{\text{max}}^{\text{long term}} = 90^\circ\text{C}$</p>		
<p>$\rho = 1.41 - 1.43 \text{ g/cm}^3$</p> <p>$C_p = 1.470 \text{ J/kg/K}$</p> <p>$k = 0.2 \text{ W/m/K}$</p> <p>$T_{\text{max}}^{\text{short term}} = 110 - 140^\circ\text{C}$</p> <p>$T_{\text{max}}^{\text{long term}} = 90 - 100^\circ\text{C}$</p>		

Table III General Properties of Selected Polymeric Materials (continued)

<p>PS - Polystyrene</p> <p>Characteristics: High stiffness, brittle, glassy smooth surface, good dimensional stability, susceptibility to stress cracking, limited chemical stability.</p> <p>Identified by: Transparent, sweet smell (styrene) during burn test, yellow flame and soot during burn test.</p>		
<p>$\rho = 1.05 \text{ g/cm}^3$</p> <p>$C_p = 1.340 \text{ J/kg/K}$</p> <p>$k = 0.15 \text{ W/m/K}$</p> <p>$T_{\text{max}}^{\text{short term}} = 90^\circ\text{C}$</p> <p>$T_{\text{max}}^{\text{long term}} = 80^\circ\text{C}$</p>		
<p>$\rho = 1.38 - 1.55 \text{ g/cm}^3$</p> <p>$C_p = 1.000 \text{ J/kg/K}$</p> <p>$k = 0.16 \text{ W/m/K}$</p> <p>$T_{\text{max}}^{\text{short term}} = 70^\circ\text{C}$</p> <p>$T_{\text{max}}^{\text{long term}} = 60^\circ\text{C}$</p>		
<p>$\rho = 0.90 - 0.91 \text{ g/cm}^3$</p> <p>$C_p = 1.930 \text{ J/kg/K}$</p> <p>$k = 0.24 \text{ W/m/K}$</p> <p>$T_{\text{max}}^{\text{short term}} = 130^\circ\text{C}$</p> <p>$T_{\text{max}}^{\text{long term}} = 90^\circ\text{C}$</p>		

Table III General Properties of Selected Polymeric Materials (continued)

PE-HD - High Density Polyethylene	
<p>Characteristics: low density, low strength and stiffness, low dimensional stability, high chemical resistance, inexpensive, high degree of crystallinity (60-80%).</p> <p>Identified by: Milky color, smell of parafin during burn test, yellow flame, drips.</p>	
<p>$\rho = 0.940 - 0.960 \text{ g/cm}^3$</p> <p>$C_p = 2,300 \text{ J/kg/K}$</p> <p>$k = 0.63 \text{ W/m/K}$</p> <p>$T_{\text{max}}^{\text{short term}} = 80 - 110^\circ\text{C}$</p> <p>$T_{\text{max}}^{\text{long term}} = 60 - 80^\circ\text{C}$</p>	
PE-LD - Low Density Polyethylene	
<p>Characteristics: low density, easily processed, high flow stability, low dimensional stability, inexpensive, low degree of crystallinity (40-55%).</p> <p>Identified by: Translucent, smell of parafin during burn test, yellow flame, drips.</p>	
<p>$\rho = 0.914 - 0.928 \text{ g/cm}^3$</p> <p>$C_p = 2,300 \text{ J/kg/K}$</p> <p>$k = 0.33 \text{ W/m/K}$</p> <p>$T_{\text{max}}^{\text{short term}} = 80 - 90^\circ\text{C}$</p> <p>$T_{\text{max}}^{\text{long term}} = 60 - 70^\circ\text{C}$</p>	

Table IV Energy Equation

<p>Tensor notation</p> $\rho C_v \frac{DT}{Dt} = (\nabla \cdot kVT) + \frac{1}{2} \mu (\underline{\dot{\gamma}} : \underline{\dot{\gamma}}) + \dot{Q}$
<p>Expanded equation in rectangular coordinates (x,y,z):</p> $\rho C_v \left(\frac{\partial T}{\partial t} + v_x \frac{\partial T}{\partial x} + v_y \frac{\partial T}{\partial y} + v_z \frac{\partial T}{\partial z} \right) = K \left(\frac{\partial^2 T}{\partial x^2} + \frac{\partial^2 T}{\partial y^2} + \frac{\partial^2 T}{\partial z^2} \right) + 2\mu \left(\left(\frac{\partial v_x}{\partial x} \right)^2 + \left(\frac{\partial v_y}{\partial y} \right)^2 + \left(\frac{\partial v_z}{\partial z} \right)^2 \right) + \mu \left(\left(\frac{\partial v_x}{\partial y} + \frac{\partial v_y}{\partial x} \right)^2 + \left(\frac{\partial v_x}{\partial z} + \frac{\partial v_z}{\partial x} \right)^2 + \left(\frac{\partial v_y}{\partial z} + \frac{\partial v_z}{\partial y} \right)^2 \right) + \dot{Q}$
<p>Expanded equation in cylindrical coordinates (r,θ,z):</p> $\rho C_v \left(\frac{\partial T}{\partial t} + v_r \frac{\partial T}{\partial r} + \frac{v_\theta}{r} \frac{\partial T}{\partial \theta} + v_z \frac{\partial T}{\partial z} \right) = K \left(\frac{1}{r} \frac{\partial}{\partial r} \left(r \frac{\partial T}{\partial r} \right) + \frac{1}{r^2} \frac{\partial^2 T}{\partial \theta^2} + \frac{\partial^2 T}{\partial z^2} \right) + 2\mu \left(\left(\frac{\partial v_r}{\partial r} \right)^2 + \left(\frac{1}{r} \left(\frac{\partial v_\theta}{\partial \theta} + v_r \right) \right)^2 + \left(\frac{\partial v_z}{\partial z} \right)^2 \right) + \mu \left(\left(\frac{\partial v_\theta}{\partial z} + \frac{1}{r} \frac{\partial v_z}{\partial \theta} \right)^2 + \left(\frac{\partial v_r}{\partial z} + \frac{\partial v_z}{\partial r} \right)^2 + \left(\frac{1}{r} \frac{\partial v_r}{\partial \theta} + r \frac{\partial}{\partial r} \left(\frac{v_\theta}{r} \right) \right)^2 \right) + \dot{Q}$

Table V Continuity Equation in Compressible fluids.

<p>Tensor notation</p> $\nabla \cdot \underline{v} = 0$
<p>Expanded equation in rectangular coordinates</p> $\frac{\partial v_x}{\partial x} + \frac{\partial v_y}{\partial y} + \frac{\partial v_z}{\partial z} = 0$
<p>Expanded equation in cylindrical coordinates (r,θ,z)</p> $\frac{1}{r} \frac{\partial}{\partial r} (rv_r) + \frac{1}{r} \frac{\partial v_\theta}{\partial \theta} + \frac{\partial v_z}{\partial z} = 0$

Table VI Equation of Motion in Terms of $\underline{\tau}$

<p>Tensor notation</p> $\rho \frac{Dv}{Dt} = -\nabla p + [\nabla \cdot \underline{\tau}] + \rho \underline{g}$
<p>Expanded equation in rectangular coordinates (x,y,z)</p> $\rho \left(\frac{\partial v_x}{\partial t} + v_x \frac{\partial v_x}{\partial x} + v_y \frac{\partial v_x}{\partial y} + v_z \frac{\partial v_x}{\partial z} \right) = -\frac{\partial p}{\partial x} + \mu \left(\frac{\partial^2 v_x}{\partial x^2} + \frac{\partial^2 v_x}{\partial y^2} + \frac{\partial^2 v_x}{\partial z^2} \right) + \rho g_x$ $\rho \left(\frac{\partial v_y}{\partial t} + v_x \frac{\partial v_y}{\partial x} + v_y \frac{\partial v_y}{\partial y} + v_z \frac{\partial v_y}{\partial z} \right) = -\frac{\partial p}{\partial y} + \mu \left(\frac{\partial^2 v_y}{\partial x^2} + \frac{\partial^2 v_y}{\partial y^2} + \frac{\partial^2 v_y}{\partial z^2} \right) + \rho g_y$ $\rho \left(\frac{\partial v_z}{\partial t} + v_x \frac{\partial v_z}{\partial x} + v_y \frac{\partial v_z}{\partial y} + v_z \frac{\partial v_z}{\partial z} \right) = -\frac{\partial p}{\partial z} + \mu \left(\frac{\partial^2 v_z}{\partial x^2} + \frac{\partial^2 v_z}{\partial y^2} + \frac{\partial^2 v_z}{\partial z^2} \right) + \rho g_z$
<p>Expanded equation in cylindrical coordinates (r,θ,z)</p> $\rho \left(\frac{\partial v_r}{\partial t} + v_r \frac{\partial v_r}{\partial r} + \frac{v_\theta}{r} \frac{\partial v_r}{\partial \theta} - \frac{v_\theta^2}{r} + v_z \frac{\partial v_r}{\partial z} \right) = -\frac{\partial p}{\partial r} + \left(\frac{1}{r} \frac{\partial}{\partial r} (r \tau_{rr}) + \frac{1}{r} \frac{\partial \tau_{r\theta}}{\partial \theta} - \frac{\tau_{\theta\theta}}{r} + \frac{\partial \tau_{rz}}{\partial z} \right) + \rho g_r$ $\rho \left(\frac{\partial v_\theta}{\partial t} + v_r \frac{\partial v_\theta}{\partial r} + \frac{v_\theta}{r} \frac{\partial v_\theta}{\partial \theta} + \frac{v_r v_\theta}{r} + v_z \frac{\partial v_\theta}{\partial z} \right) = -\frac{1}{r} \frac{\partial p}{\partial \theta} + \left(\frac{1}{r^2} \frac{\partial}{\partial r} (r^2 \tau_{r\theta}) + \frac{1}{r} \frac{\partial \tau_{\theta\theta}}{\partial \theta} + \frac{\partial \tau_{\theta z}}{\partial z} \right) + \rho g_\theta$ $\rho \left(\frac{\partial v_z}{\partial t} + v_r \frac{\partial v_z}{\partial r} + \frac{v_\theta}{r} \frac{\partial v_z}{\partial \theta} + v_z \frac{\partial v_z}{\partial z} \right) = -\frac{\partial p}{\partial z} + \left(\frac{1}{r} \frac{\partial}{\partial r} (r \tau_{rz}) + \frac{1}{r} \frac{\partial \tau_{\theta z}}{\partial \theta} + \frac{\partial \tau_{zz}}{\partial z} \right) + \rho g_z$

Table VII Equation of Motion in terms of \underline{y} (Navier-Stokes Equations),

<p>Tensor notation</p> $\rho \frac{Dv}{Dt} = -\nabla p + \mu \nabla^2 \underline{y} + \rho \underline{g}$
<p>Expanded equation in rectangular coordinates (x,y,z)</p> $\rho \left(\frac{\partial v_x}{\partial t} + v_x \frac{\partial v_x}{\partial x} + v_y \frac{\partial v_x}{\partial y} + v_z \frac{\partial v_x}{\partial z} \right) = -\frac{\partial p}{\partial x} + \mu \left(\frac{\partial^2 v_x}{\partial x^2} + \frac{\partial^2 v_x}{\partial y^2} + \frac{\partial^2 v_x}{\partial z^2} \right) + \rho g_x$ $\rho \left(\frac{\partial v_y}{\partial t} + v_x \frac{\partial v_y}{\partial x} + v_y \frac{\partial v_y}{\partial y} + v_z \frac{\partial v_y}{\partial z} \right) = -\frac{\partial p}{\partial y} + \mu \left(\frac{\partial^2 v_y}{\partial x^2} + \frac{\partial^2 v_y}{\partial y^2} + \frac{\partial^2 v_y}{\partial z^2} \right) + \rho g_y$ $\rho \left(\frac{\partial v_z}{\partial t} + v_x \frac{\partial v_z}{\partial x} + v_y \frac{\partial v_z}{\partial y} + v_z \frac{\partial v_z}{\partial z} \right) = -\frac{\partial p}{\partial z} + \mu \left(\frac{\partial^2 v_z}{\partial x^2} + \frac{\partial^2 v_z}{\partial y^2} + \frac{\partial^2 v_z}{\partial z^2} \right) + \rho g_z$
<p>Expanded equation in cylindrical coordinates (r,θ,z)</p> $\rho \left(\frac{\partial v_r}{\partial t} + v_r \frac{\partial v_r}{\partial r} + \frac{v_\theta}{r} \frac{\partial v_r}{\partial \theta} - \frac{v_\theta^2}{r} + v_z \frac{\partial v_r}{\partial z} \right) = -\frac{\partial p}{\partial r} + \mu \left(\frac{\partial}{\partial r} \left(\frac{1}{r} \frac{\partial}{\partial r} (r v_r) \right) + \frac{1}{r^2} \frac{\partial^2 v_r}{\partial \theta^2} - \frac{2}{r^2} \frac{\partial v_\theta}{\partial \theta} + \frac{\partial^2 v_r}{\partial z^2} \right) + \rho g_r$ $\rho \left(\frac{\partial v_\theta}{\partial t} + v_r \frac{\partial v_\theta}{\partial r} + \frac{v_\theta}{r} \frac{\partial v_\theta}{\partial \theta} + \frac{v_r v_\theta}{r} + v_z \frac{\partial v_\theta}{\partial z} \right) = -\frac{1}{r} \frac{\partial p}{\partial \theta} + \mu \left(\frac{\partial}{\partial r} \left(\frac{1}{r} \frac{\partial}{\partial r} (r v_\theta) \right) + \frac{1}{r^2} \frac{\partial^2 v_\theta}{\partial \theta^2} - \frac{2}{r^2} \frac{\partial v_r}{\partial \theta} + \frac{\partial^2 v_\theta}{\partial z^2} \right) + \rho g_\theta$ $\rho \left(\frac{\partial v_z}{\partial t} + v_r \frac{\partial v_z}{\partial r} + \frac{v_\theta}{r} \frac{\partial v_z}{\partial \theta} + v_z \frac{\partial v_z}{\partial z} \right) = -\frac{\partial p}{\partial z} + \mu \left(\frac{1}{r} \frac{\partial}{\partial r} \left(r \frac{\partial v_z}{\partial r} \right) + \frac{1}{r^2} \frac{\partial^2 v_z}{\partial \theta^2} + \frac{\partial^2 v_z}{\partial z^2} \right) + \rho g_z$

Subject Index

A

Abbreviations 6
abs 99,102,105,450,464,476,494,497,509,510
absorption 468,469,535,543,553,555,556,563,564
absorption index 554
acoustic properties 585
acrylic materials 547
additives 71
alternating copolymers 68
amorphous thermoplastics 56,58,84,85,88,382,386,393,409,410,413,414
anisotropic strain-stress relation 422
anisotropy induced curvature change 357
Anisotropy 283,285,294,345,537,418
aramid fiber 416
arrangement of polymer molecules 55
atactic 51,53
Avrami equation 327
azodicarbonamide 262

B

Baekeland 25,26,27
Bagley Equation 162
bakelite 22,25,26,27
Banbury Mixer 214,216
Beer's law 554
Bingham Fluid 140
biot number 347,348,351,352
bipolymer 68
birefringence 284,285,287,545,548,551,552
blackbody radiation 565
blends 203,204
block copolymers 68
blow molding 129,140,156,169,245,249
blowing agents 262
Boltzmann Superposition Principle 76,80,83,398
Bourger's law 555
brittle failure 456,469,475,484,492-495
brittle fracture 455,456,464,484

C

calendering 185,222,224,255
caoutchouc 15,17

capacitance 521,522,528,530
capillary viscometer 149,159
Carothers 20,31-35
Castro-Macosko curing model 340
cavity transfer mixing section 219
cellulose acetate 285,286
Charpy test 473,478,482
chemical degradation 511
chewing gum 76
China 39
chromaticity diagram 561,562,563
cis-1,4- polybutadiene 53
clamping unit 233,239,240
closed cell 262
co-rotating twin screw extruder 187,221-224
cokneader 220
cold feed rubber extruder 218
Colombia 39
Color 560
common polymer blends 204
compatibilizers 203
compatible polymers 204
complex current 528
complex dielectric coefficient 530
complex capacitance 530
complex modulus 401
composite laminate properties 426
compression molding 140,244,260,261,292,293,295,297,303,308,310
condenser 521-523,528,529,542
conformation and configuration of polymer molecules 51
consistency index 138
continuity equation 608
continuum mechanics 129
convected derivative 151
corrosion of polymers 580
Couette flow 204,205
Couette Rheometer 166
Coulomb's law of friction 499
counter-rotating twin screw extruder 221,223,259
crack growth 448,450,451,487,498
crack pinning 465
cracking 496,506,513
crazes 457,458,464,469,470,513
crazing 457,458,459,465,486,513

creep compliance 389,390
 creep modulus 389,391,400,402
 creep response 389,390,392,400,402,404
 creep rupture 447,456,483,485,487,489
 creep rupture test 484,511
 creep test 388,389,392,400,404,484
 critical capillary number 211,212,213
 critical energy release rate 452
 critical stress intensity factor 448,516
 critical surface tension 171
 cross-linked elastomers 67
 cross-linked polymers 418
 cross-linking 67
 crystalline growth rate 328,329
 crystallinity 53,54,58,59,61
 crystallinity for high density polyethylene 59
 crystallinity for low density polyethylene 59
 crystallization 322,323,326,332
 cure Kinetics 336,339
 curing reaction 321,334,336,337,353
 curtain coating 257,259

D

damage of polymers 447
 debonding 466,496
 Deborah number 134
 deformation dependent tensor 154
 degree of crystallization 322
 degree of cure 142-145,336,337
 density 54,55,58,59,78,97,100,101,109,111,122
 density measurements 122
 desorption 571,581,582,583
 deviatoric stress 131,133,140,151,176
 diamagnetic substances 543
 dielectric behavior 521
 dielectric coefficient 521,523,524,527,530
 dielectric dissipation factor 528,531,538
 dielectric strength 537,538,540
 dielectric susceptibility 524
 dielectrical polarization 524
 differential scanning calorimeter (DSC) 118, 328,336
 differential thermal analysis (DTA) 117
 differential viscoelastic models 151
 diffusion 571,574,575,576,577,583
 diffusion coefficient 572,576,579,580,583
 dioctylphthalate 227
 dip coating 257
 dispersed melting 220
 dispersion index 225,226

dispersive mixing 203,208,246,266
 displacement gradient tensors 155
 displacement polarization 524,526
 distributive mixing 203,204,211,214,219
 double refractance 548
 double refraction 284
 drop break-up 211
 ductile failure 459,484
 ductile fracture 455
 dynamic fatigue 488
 dynamic mechanical test 393

E

effect of orientation 205
 efficiency 207,214,225
 Einstein's model 146
 elastic energy release rate 452
 electrets 542
 electric breakdown 537
 electric breakdown resistance 537
 electric conductivity 523,531,532,534,535
 electric field intensity 522
 electric resistance 532,534,542
 electrical loss in a dielectric 532
 electrical properties 521
 electromagnetic interference shielding (EMI Shielding) 542
 electron spinning resonance (ESR) 543
 electrostatic charge 540
 elongational viscosity 140
 emulsions 140
 endurance stress 486
 energy balance 97
 energy consumption 224
 energy equation 608
 engineering elastic constant 427
 enthalpy 322
 environmental effects 500,505
 Epoxy 5,450,465,466,490
 Erwin's ideal mixer 207
 ethylene 43,44,55,68
 ethylene propylene rubber 5
 ethylene-propylene 68,70
 ethylene-propylene copolymer 70
 extensional rheometry 167
 extrudate swell 135
 extruder dimensions 188
 extrusion 185,249
 extrusion dies 199

F

failure of composites 464
 failure of polymers 447
 falling dart test 477,
 fatigue 483,488
 fatigue failure 496,498
 fatigue test method 488
 fiber attrition 312
 fiber damage 312,314
 fiber density continuity equation 299
 fiber orientation 429
 fiber reinforced polymer (FRP) 421
 fiber spinning 129,140,141,245,246
 fibers 4,8,10,246,260
 filled polymers 378,422
 fillers 225
 film 243,245
 film blowing 247
 film casting 246,247
 finger strain tensors 154
 finite strain tensors 155
 first contravariant convected time derivative 151
 first normal stress differences 134,156
 first-order particle interactions 146
 flexural strength 49,50
 flow induced birefringence 552
 foaming 140,262
 Folgar-Tucker Model 303,304,308,310
 fountain flow effect 289-291,306
 Fourier's Law 97
 fracture mechanics 447,498
 fracture prediction (energy balance) 448
 fracture toughness 448,477,478,479
 friction 490,499
 fringe order 549,550,551
 frozen-in flow 346

G

Geisbüsch model 146
 general properties 3
 generalized Maxwell model 83
 generalized Newtonian fluid 131
 geometrical crack factor 479
 Gibbs free energy equation 229
 Giesekus model 152
 glass fiber 102-106,108,109,111,112
 glass filled polyester mat 496
 glass transition 45,57,59,60,63-66,86
 glass transition temperature

45,47,57,59,60,76,79,86,88
 gloss 559
 glossmeter 559
 goniophotometer 559
 graft copolymers 68
 Griffith's hypothesis 452
 grooved feed extruder 187,192,193,194,198
 gummi elasticum 15,17
 gummi plasticum 18
 Guth equation 378
 Guth's model 146
 gutta-percha 18,23

H

Halpin-Tsai model 424
 haze measurement 558
 heat activated cure 334
 heat of crystallization 322,332
 heat of fusion 107,119,123,322,332
 heat transfer during cure 340
 heat transfer during solidification 329
 heat-distortion temperature 429
 Hele-Shaw model 306
 Henry's law 572
 Henry-Langmuir model 574
 high density polyethylene 5,135,156,374,383,384,477,484,485,501,506
 high impact polystyrene 69,73,395,459,464,469,470,481,553
 hookean model 399
 hue 562

I

immiscible fluid 208
 impact failure 478
 impact strength 447,464,467,506
 impact test method 473
 incompatible polymers 204
 index of refraction 545
 infrared pyrometry 565
 infrared radiation 567
 infrared spectrometer 564,565,
 infrared spectroscopy 565,563
 infrared spectrum 545,564
 injection molding 233,306,312,313,316
 injection molding cycle 234
 injection molding machine 202,238,239,240, 241,273
 injection unit 238
 integral viscoelastic model 154

inter-molecular attraction 45
 intrinsic viscosity 48
 introduction to processing 185
 isochromatic 284,285,286,551
 isochronous creep plots 391
 isometric creep plots 391
 isotactic 52,53,63,64
 izod impact test 473,474,479,481
 izod-type impact machine 473

J

J-integrals 447,453
 Jeffrey Model 401

K

Kelvin model 399
 Kenics static mixer 215
 kinetic theory of rubber elasticity 375
 Kirchhoff's law 566
 Knappe's model 106
 knife coating 257,258
 knitlines 293,295

L

lamellar crystal 58
 linear coefficient of thermal expansion 110, 113
 linear elastic fracture mechanics (LEFM) 447, 478
 linear viscoelastic fracture 448, 453
 linear viscoelasticity 76,80,81
 liquid crystalline polymers 416
 logarithmic decrement 394,395,410
 long fiber composites 421
 long-term tests 388
 loss modulus 87,394,398,401,407
 loss tangent 395
 low density polyethylene 5,54,58,102,132,134
 lubricating squeezing flow 167
 luminance 562
 lustremeter 559

M

Maddock mixing section 220
 magnetic properties 543
 magnetic resonance 543
 magnetic susceptibility 543
 magnetizability 543

Mark-Houwink relation 48
 Martens temperature test 429
 material derivative 130
 Maxwell model 81-86
 Maxwell-Wiechert Model 405
 mechanical behavior 371
 melamine 5
 melt flow indexer 159
 melt fracture 135,136
 melting temperature 102,109,113,114,116
 melting zone 195
 memory function 154,155,156
 metering zone 197
 methane 51,52
 methyl bromine 575
 microcracks 456,457,460,466,486 513
 Mixing 202
 mixing activated cure 334,336,340
 mixing devices 202,210,214
 mixing in single screw extruder 218
 mixing processes 185,202,225
 mixing quality 202,214,223,225
 mixing section 192,218,219,220
 molding diagram 236,237
 molecular bonds 45
 molecular diffusion 572
 molecular weight 45,56,57,61
 Mooney plot 377
 Mooney-Rivlin equation 376
 morphological structure 325,414
 morphology development 203,222
 morphology development of polymer blends 203
 motion equation 609
 multi-layered films 574

N

natural rubber 5,374,376,377,378,379,577, 581
 necking 460,462,463
 Neumann solution can 330
 non-linear viscoelasticity 76
 normal stresses 133
 notched Charpy test 473
 nuclear magnetic resonance (NMR) 543
 nucleating agents 262
 number average 46-48,50
 nylon 66 497

O

open cell 262
 optical properties 545
 optimal orientation 206
 orientation 206,207,208,215,219,243,245,246, 251, 261,283,295,297,298
 orientation (planar) 298
 orientation (predicting) 297,306
 orientation distribution function 298,300,310
 orientation polarization 524,526
 oriented thermoplastic 412

P

p-v-T diagram 109,110-114,324
 particle motion 300
 particulate agglomerates 208
 penetration depth 568,569
 permeability 575,578,579,580
 permeability properties 571,575
 permeation 572,573,575
 Phan-Thien Tanner models 152
 phenol-formaldehyde 67
 phenolic 5,67,72
 photoelasticity 548
 pin barrel extruder 218,219
 pin mixing 219
 pineapple mixing section 219
 Planck's law 565
 plane strain 372,373
 plane stress 372
 plasticating extruder 188,189
 plasticating unit 202,233,238,239,244,255,262
 plasticization 227
 plasticized polyvinyl chloride 5
 plasticized PVC 382,384,385,386,390,409
 plasticizers 228,229,233
 PMMA 380,390,391,413,431,547,557,569,573
 Poincaré sections 227
 Poisson's ratio 391,433
 polariscope 549,550,552
 polyamide 5
 polyamide 6 102,104,107,227-229,231
 polyamide 66 107,109,111,126,228,229,231, 277,329,450,322
 polybutadiene rubber particles 553
 polybutadiene 5
 polybutylene terephthalate 420,421
 polycarbonate 5,102,104,108,109,110,204,231, 374,408,450,477,494,563,564
 polydispersed polymer 48

polydispersity index 48
 polyethylene 43,44,49,54,55,58,61,132,156,168,575
 polyisobutylene 8, 76,406,407
 polymethyl methacrylate 5,101,114
 polyoxymethylene 506
 polypropylene 5,43,53,63,72,101,107,136,139, 140,173,322,326,327,329,332,334,388,392,395,39 6,408,412,419,450, 459,460,462,467,470,471,477, 577,581,582
 polypropylene copolymer 388,450
 polystyrene 5,37,40,43,45,50,69,75,83,84,85,86,108, 131,132,139,140,148,152,152,173,204,231,234,24 9,262,322,329,352,395,408, 410,411,450,569
 polytetrafluoroethylene 5
 polyurethane 5
 polyvinyl chloride 43,57,58,72,73,75,477
 power law index 138,139,149,164,166
 power law model 137
 predicting orientation 297,306
 processing thermoplastic polymers 283
 processing thermoset polymers 292
 pumping systems 186
 PVC fabric 121
 PVC pipes 507

Q

QSM-extruder 218
 quality 223,225,239

R

random copolymers 70
 ratcheting 495
 rate of deformation 131,141,176
 Rayleigh disturbances 246
 reactive end-groups 55,56
 reduced stress 377
 Reduced viscosity 133
 Reflection 553,556
 refractive index 545,547,557
 reinforced polymer 420
 relative dielectric coefficient 522,524,527
 relaxation test 381,386
 relaxation time 77,83-87,90,91
 representative viscosity method 163
 residence time distribution 226
 residual stress 341,343,344,346,349,350
 resistive current 529

retardation 549,550
 rheology 129
 rheometry 159
 roll coating 257,258
 rotational molding 264
 rubber 3,16
 rubber elasticity 373

S

S-N curves 488,493,494
 saturation 562
 Schottky-Barriers 534
 screw characteristic curves 190,192,194,197,198
 secant modulus 381
 second normal stress differences 133,134
 second-order orientation 304
 self-cleaning 220
 self-diffusion 583
 Semi-Crystalline Thermoplastics 58,381,382,
 385,393,408,410,414
 shark skin 135
 shear modulus 57,59,61
 shear thinning effect 131
 sheet inflation 170
 sheet molding compound (SMC) 260
 sheeting dies 199
 shish-kebab 326,328
 short fiber composites 421
 short-term tensile strength 455
 short-term tensile test 371,373
 silicone rubber 5
 single crystals 326
 single screw extruder 187,188,190,192,218,
 220,239
 sink marks 343,358
 sinusoidal disturbance 213
 sinusoidal oscillatory test 397
 slurries 140
 solidification 321,329
 solidification of thermoplastics 322
 solidification of thermosets 334
 solids conveying zone 188,191
 solubility constant 573
 solubility parameters 230,512
 solutions 574
 sorption 574,575,579
 sorption constant 579
 sorption equilibrium constant 573
 sound absorption 589
 sound proof rooms 589

sound reflection 587,589
 specific heat 97,98,107,119
 specific resistance 535,536
 spectral radiance 565,566
 specular gloss 559
 speed of sound 585
 spherulites 58,325,326
 spring-forward effect 357
 spurt flow 135
 squeezing flow 167,168
 stabilizers 255
 standard linear solid model 403
 static fatigue 483
 static mixers 215
 Staudinger 29,32,34,35
 stefan condition 332
 stick-slip effect 135
 storage modulus 87,398,401,407
 strain 371,373,422
 strain-optical coefficient 548
 strength stability under heat 429
 stress 371,373,400,403,405
 stress cracking 344
 stress intensity factor 487,498,516
 stress relaxation 380,381,388,389,400,405,406
 stress relaxation test 76,392,391
 stress whitening 460,461
 stress-optical coefficient 548
 striation thickness 204
 structural units 63-66
 Structure of Polymers 43
 styrene-butadiene-rubber (SBR) 5,374
 substantial derivative 130
 surface tension 170
 suspension rheology 146
 swelling 229,230
 syndiotactic 52,53

T

tacticity 51,53
 tangent modulus 381
 tensile test 379
 tensor representation of fiber orientation 304
 terpolymer 68,69
 thermal conductivity 100
 thermal conductivity of ABS 105
 thermal conductivity of LDPE 103
 thermal conductivity of polyamide 6 104
 thermal conductivity of polycarbonate 104
 thermal degradation 119,227,237,513

thermal diffusivity 98,112
 Thermal Expansion 113
 thermal fatigue 491,495,496
 Thermal Penetration 115
 thermodynamics during cooling 322
 thermoforming 130,140,169,245,253
 thermogravimetry (TGA) 121,514
 thermomechanical analysis (TMA) 120
 thermoplastic polymers 51,55,58,379
 thermosets 55,67
 tie molecules 414
 time-temperature superposition 76
 torsion pendulum 393
 total stress 131,141
 toughness 448,450,452,453,464,479
 trans-1,4- polybutadiene 53
 translucent 58
 transmissivity 557,558,566
 transmittance 553,556,567
 transparency 545,553
 transparent 56,58
 treeing 539
 trichromatic coefficients 561
 tristimulus values 561
 Trouton viscosity 141
 tubular dies 201
 twin screw extruders 187,188,202,214,221,222

U

ultra high molecular weight polyethylene
 fibers 416
 ultra-drawn, ultra-high molecular weight high
 density polyethylene 8
 ultra-violet radiation 505
 Union Carbide mixing section 220
 United States 19,20,22,26,29,30,40
 unplasticized PVC (uPVC) 5,382,383,386
 unsaturated polyester 334,335,342,361
 unsaturated polyester 5
 unsaturated polyester/aligned glass fiber
 composite laminate 425
 upper convective model 151

V

Van-der-Waals forces 45
 Vicat temperature test 429
 vinyl ester 142-144,336,337
 viscoelastic flow models 151
 Viscosity average 46,48
 viscosity curves 132,142

viscosity ratios 215
 viscous flow models 137
 volume conductivity 535,536
 volume-specific energy absorption 469
 volume-specific energy to fracture 496
 vulcanization 18

W

warpage (predicting) 354
 warpage 323,325,330,344,354,359
 wavelength disturbance amplitude 213
 wear 499
 weathering 505
 weight average 46
 Weissenberg-Rabinowitsch Equations 162
 White-Metzner model 151
 Wien's law 565
 Williams-Landel-Ferrey (WLF) equation
 78,79,80,85-87,90,91
 wire coating 257

X

X groups 43,51,53

Y

yield point 462
 yield strength 462
 yield stresses 140
 Young's modulus 585

Z

zero shear rate viscosity 139

Author Index

A

Adams, J.M. 569
 Advani, S.G. 319
 Agassant, J.F. 180,569
 Aklonis, J.J. 94
 Alam, M. 180
 Alf, E. 518
 Andersen, O. 367
 Andrews, E.H. 519
 Anturkar, N.R. 281
 Araujo, F.F.T. 128
 Armstrong, R.C. 180, 181
 Avenas, P. 180
 Avrami, M. 367

B

Baaijens, F.P.T. 367
 Baaijens, J.P.W. 181
 Baer, E. 13,544
 Bagley, E.B. 182
 Bailey, R. 319
 Bannantine, J.A. 518
 Barone, M.R. 319,367
 Bartoe, W.F. 569
 Batchelor, G.K. 181
 Bay, R.S. 318
 Beahan, P. 518
 Becker, H. 319,445
 Bellehumeur, C.T. 281
 Benham, P.P. 519
 Bentley, B.J. 280
 Berezhnaya, G.V. 180
 Berg, H. 544
 Bernier, G.A. 519
 Bernstein, B. 181
 Berry, G.C. 94
 Bird, R.B. 180,280,281
 Birtz, L.F. 519
 Biswas, A. 280
 Boden, H.E. 519
 Bogetti, T.A. 367
 Boonstra, B.B. 280
 Borisenkova, E.K. 180
 Boyer, R.F. 519
 Brandrup, J. 367
 Brintrup, H. 445

Bucknall, C.B. 519
 Burgers, J.M. 319
 Bushko, W.C. 367

C

Carreau, P.J. 95,180,181
 Castiff, E. 95
 Castro, J.M. 180
 Catič, I. 128
 Caulk, D.A. 319,367
 Chapman, D. 569
 Chatrei, Sh. 182
 Chen, C.Y. 319
 Cheng, J.J. 280
 Chhabra, R.P. 95, 180
 Chiang, H.H. 367
 Cintra, J. S. 319
 Co, A. 281
 Cohen, R.E. 181
 Comer, J.J. 519
 Cox, R.G. 280
 Crawford, R.J. 128,281,445,518,519,544
 Crochet, M.J. 181,319,367
 Crouthamel, D.L. 367
 Crowder, M.L. 94

D

Dalke, B.D. 94
 Davies, A.R., 181
 Davis, A. 519
 de la Condamine, C.M. 41
 De Kee, D.C.R. 95, 180
 de Waale, A. 181
 Dealy, J.M. 180, 181
 Debbaut, B. 181
 Denn, M.M. 181
 Denton, D.L. 281,519
 Dewitt, D.P. 569
 DiBenedetto, A.T. 367
 Diedrich, G. 519
 Dietsche, L. 181
 Dietz, W. 128
 Dillon, R.D. 180
 Dominghaus, H. 94,445,519,544
 Dooley, J. 181

DuBois, J.H. 41
 Dukes, R. 519
 Dupret, F. 319
 Dusek, K. 367

E

E. Gaube 519
 Eder, G. 128,367
 Ehrenstein, G.W. 13,367,445,5519
 Einstein, A. 181
 Elemans, P.H.M. 280
 Engel, L. 519
 Erns, J.B. 368
 Erwin, L. 280

F

Fajolle, R. 569
 Faupel, J. H. 367
 Ferry, J.D. 95
 Fillers, R.W. 95
 Fischer, F.E. 128,367
 Folgar, F.P. 319
 Fox, T.G. 94
 Frisch, K.C. 95
 Fujimoto, T. 95

G

Gaube, E. 519
 Geisbüsch, P. 181, 318
 Gillespie, J.W. 367
 Gillham, J.K. 367
 Godovsky, Y.K. 128
 Gogos, C.G. 41,128, 280,367
 Gordon, G.V. 180
 Gotham, K.V. 519
 Grace, H.P. 280
 Gramann, P.J. 280,319
 Green, J. 94
 Greener, J. 280
 Griffin, J.D. 590
 Griffith, A.A. 518
 Gumbrell, S.M. 445
 Gupta, R.K. 181,319
 Guth, E. 181,445

H

Haberstroh, E. 569
 Hadley, D.W. 445

Hagen, G.H.L. 181
 Halpin, J.C. 445
 Han, C.D. 181
 Handrock, J.L. 519
 Harms, E. 280
 Hassager, O. 180
 Hatzikiriakos, S.G. 180,181
 Havlicek, I. 368
 Heimann, W. 569
 Hele-Shaw H.S. 319
 Henning, F. 445
 Herrmann, H. 42
 Hertzberg, R.W. 519
 Hieber, C.A. 368
 Hildebrand, J. 182,281
 Hiltner, A. 13
 Himasekhar, K. 368
 Hoftzyer, P.J. 94,128,182,281,367
 Hosemann, R. 445
 Hrymak, A.N. 319
 Huer, W. 94
 Hughes, K. 181

I

Ihm, D.W. 13
 Immergut, E.H. 368
 Isayev, A.I. 180,368,569

J

Jackson, W.C. 319
 Janeschitz-Kriegl, H. 128,368,569
 Janssen, J.M.H. 281
 Jeffery, G.B. 319

K

Kabanemi, K.K. 368
 Kamal, M.R. 368
 Kambour, R.P. 519
 Kanamoto, T. 445
 Karbhari, V.M. 366
 Kaufman, M. 41
 Kausch, H.H. 519
 Kaye, A. 181
 Kearsley, E. 181
 Keunings, R. 181
 Kinloch, A.J. 518
 Kiriakidis, D.G. 181
 Kleinemeier, B. 519
 Klemm, A. 41

Klempner, D. 95
 Klingele, H. 519
 Knappe, W. 128,584
 Knausenberber, R. 445
 Kraft, H. 319
 Krämer, S. 445
 Krieger, S. W. 368
 Krishnamachari, S.I. 445
 Krobath, G. 368

L

Lai, G.-Y. 569
 Landel, R.F. 95,445
 Laun, H.M. 180
 Lauterbach, M. 280
 Leal, L.G. 280
 Lee, C.-C. 319,368
 Leibfried, D. 319
 Lem, K.W. 181
 Levi, P. 41
 Liebig's Ann. 42
 Liedauer, S. 368
 Lightfoot, E.N. 280
 Lim, S. 280
 Lodge, A.S. 181,569
 Löwer, K. 590
 Luo, X.-L. 181

M

MacKnight, W.J. 94
 Macosko, C.W. 180,181,280,368
 Malkin, A.Y., 180
 Manas-Zloczower, I. 280
 Manson, J.A. 519
 Marchal, J.M. 181
 Mascia, L. 281
 Mathot, V.B.F.128
 Mavrides, H. 319
 Maxwell, J.C. 128
 McPherson, A.T. 41
 Medalia, A.I. 280
 Meissner, J. 182
 Menges, G. 181,280,281,318,367,444,445,519,
 590
 Meredith, R.E. 128
 Michaeli, W. 181,280
 Milliken, W.J. 181
 Mitsoulis, E. 181
 Mittal, R.K. 319
 Mooney, M. 445

Moore, E.R. 94
 Mullins, L. 445
 Münstedt, H. 95,181

N

Nagasawa, M. 95
 Ng, K.Y. 280
 Nicolay 519
 Nielsen, L.E. 445
 Nir, A. 280
 Noriega M. del P. 42

O

O'Neill, J.M. 368
 O'Toole, J.L. 445
 Offergeld, H. 590
 Ogale, A.M. 94
 Orbey, N. 181
 Osswald, T.A. 280,281,319,367,368
 Ostwald, W. 181
 Ott, S. 319
 Owen, M.J. 519
 Owens, D.K. 182
 Ozaki, M. 95

P

Pagano, N.J. 445
 Palmese, G.R. 368
 Papanastasiou, A.C. 181
 Paulik, Ch. 128
 Pazek, D.J. 95
 Perry, S.J. 181
 Plati, E. 519
 Poiseuille, L.J. 181
 Powell, P.C. 445
 Powell, R.L. 181
 Progelhof, R.C. 42
 Pütz, D. 590

Q

Quantin, J.C. 569

R

Rabinowitch, E. 368
 Rabinowitsch, B. 182
 Randell, D.R. 368
 Rauwendaal, C. 280
 Reboul, J.-P. 545

Regnault, H.V. 42
 Rest, H. 519
 Retting, W. 445
 Rice, J.R. 518
 Richard, K. 519
 Richmond, J. C. 569
 Riddell, M.N. 519
 Rietveld, J.X. 569
 Rivlin, R.S. 445
 Rogers, C.E. 590
 Rogers, T.G. 367
 Rosato, D.V. 281,590
 Rosen, S.L. 94,281
 Rosenberg, H.M. 128
 Roskothen, H.J. 519
 Ruhnke, G.M. 519

S

Santhanam, N. 368
 Saunders, D.W. 445
 Schacht, T. 319
 Schaper, H. 519
 Schmachtenberg, E. 445
 Schultz, J.M. 519
 Schümmer, P. 182
 Scott, R.L. 182,280,281
 Scriven, L.E. 181
 Sharma, P.K. 319
 Sharples, A. 368
 Shaw, M.T. 180
 Shutov, F.A. 281
 Simha, R. 181,445
 Sims, D. 519
 Skibo, M.D. 519
 Skochdopole, R.E. 590
 Smallwood, H.M. 445
 Smith P. 13
 Smith, T.R. 519
 Sonntag, R. 41
 Sornberger, G. 569
 Spencer, A.J.M. 368
 Spencer, R.S. 180
 Staudinger, H. 94
 Stefan, J. 368
 Stern, H.J. 41
 Stevenson, J.F. 280
 Steward, W.E. 280
 Stokes, V.K. 368
 Stone, H.A. 280
 Stradins, L. 280

Suchanek, H. 590
 Suetsugu 280
 Sun, E.M. 319
 Sundararaj, U. 280

T

Tadmor, Z. 41,128,280,281,367
 Termonia, Y. 13
 Thieltges, H.-P. 319
 Thimm, Th. 445
 Throne, J.L. 42
 Timoshenko, S. P. 368
 Tobias, C.W. 128
 Tobin, N.R. 445
 Tobolsky, A.V.J. 95
 Treloar, L.R.G. 445
 Trouton, F.T. 181
 Tsai, S.W. 445
 Tschoegl, N.W. 95
 Tseng, S.C. 367,368
 Tucker III, C.L. 180,319
 Turng, L.S. 280

U

Ulrich, H. 42
 Utracki, L.A. 42,280

V

van Krevelen, D. W. 94,128,182,281,367,590
 Vergnes, B. 569
 Verleye, V. 319
 Vincent, P.I. 518
 Vinogradov, G.V. 180
 Vlachopoulos, J. 180,281,319

W

Wagner, H. 367,544
 Wagner, M.H. 181
 Walters, K. 181
 Wang, K.K. 368
 Ward, I.M. 445
 Weinand, D. 569
 Wende, A. 445
 Wendt, R.C. 182
 Weng, M. 445
 White, J.L. 280
 Wiest, J.M. 180
 Williams, M.L. 95

Williams, J.G. 519
Wimberger-Friedl, R. 318, 368, 569
Winkel, E. 367
Winter, H.H. 182
Wippel, H. 128
Wissbrun, K.F. 180
Wobken, W. 318
Wortberg, F. 181
Worthoff, R.H. 182
Wu, C.H. 128
Wu, S. 182
Wübken, G. 95, 319, 368
Wübken, W. 318

Y

Yanovskii, Y.G. 180
Yarlykov, B.V. 180
Yasuda, K. 181
Young, R.J. 518

Z

Zachariades, A.E. 445
Zapas, L. 181
Zisman, W.A. 182



This unified approach to polymer materials science is divided in three major sections:

- *Basic Principles* – covering historical background, basic material properties, molecular structure, and thermal properties of polymers
- *Influence of Processing on Properties* – tying processing and design by discussing rheology of polymer melts, mixing and processing, the development of anisotropy, and solidification processes.
- *Engineering Design Properties* – covering the different properties that need to be considered when designing a polymer component – from mechanical properties to failure mechanisms, electrical properties, acoustic properties, and permeability of polymers.

A new chapter introducing polymers from a historical perspective not only makes the topic less dry, but also sheds light on the role polymers played, for better and for worse, in shaping today's industrial world.

The first edition was praised for the vast number of graphs and data that can be used as a reference. A new table in the appendix containing material property graphs for several polymers further strengthens this attribute.

The most important change made to this edition is the introduction of real-world examples and a variety of problems at the end of each chapter.

ISBN 1-56990-348-4
Hanser Gardner Publications
<http://www.hansergardner.com>

ISBN 3-446-22464-5
Carl Hanser Verlag
<http://www.hanser.de>



97815691903483